Physical properties of clusters relevant for the dust formation process in oxygen–rich astrophysical environments

vorgelegt von
Dipl. Phys. Marcus John
aus Berlin

von der Fakultät II (Mathematik und Naturwissenschaften)
der Technischen Universität Berlin
zur Erlangung des akademischen Grades

Doktor der Naturwissenschaften (Dr. rer. nat.)

genehmigte Dissertation

Berlin 2003
D 83

Promotionsausschuß

Vorsitzender: Prof. Dr. A.Knorr
Berichter: Prof. Dr. E. Sedlmayr
Priv. Doz. Dr. J. P. Kaufmann

Tag der mündlichen Prüfung: 25.7.2003

Gewidmet meiner Familie
In Erinnerung an
Großmutter und Opa.

Die Welt zerdacht. Und Raum und Zeiten
und was die Menschheit wob und wog,
Funktion nur von Unendlichkeiten –,
die Mythe log.

G.Benn

Zusammenfassung

Die Bildung kleiner Festkörperpartikel (Staubteilchen) aus der Gasphase heraus, wie sie in den zirkumstellaren Hüllen später Riesensterne oder den Atmosphären Brauner Zwerge beobachtet wird, kann nur unter ganz bestimmten, relativ eng begrenzten physikalischen und chemischen Bedingungen stattfinden. Nur dann ist eine effiziente Bildung kleiner und mittelgroßer Cluster möglich, die genau diesen Übergang vom Molekül zum Festkörper markieren. Neben den chemischen Reaktionsraten bestimmt die Gibbs'sche freie Bildungsenergie im wesentlichen die Effektivität dieses Prozesses. Diese wiederum läßt sich mittels der physikalischen Eigenschaften (Atomisierungsenergie, Geometrie und Vibrationsfrequenzen) der Cluster im Rahmen der Thermodynamik berechnen. Daher ist die genaue Kenntnis dieser Größen eine notwendige Voraussetzung für ein detailliertes Verständnis des Nukleationsprozesses. Im Falle der anorganischen Staubbildung, wie sie in sauerstoffreichen, astrophysikalischen Situationen auftritt, ist ferner davon auszugehen, daß der Nukleationsprozess nur unzureichend durch die klassische *homogene* Nukleationstheorie beschrieben wird. Stattdessen ist eine Beschreibung vorzuziehen, die *nicht stöchiometrische* Bildungsreaktionen miteinbezieht. Eine solche Beschreibung mittels einer Mastergleichung wird im Rahmen dieser Arbeit vorgestellt.

Ein weiterer Schwerpunkt dieser Arbeit widmet sich der Untersuchung der physikalischen Eigenschaften kleiner und mittelgroßer Siliziumoxidcluster. Dabei wird zunächst untersucht, inwieweit sich diese mittels eines empirischen Potentialmodells bestimmen lassen. Die für solche Untersuchungen notwendigen numerischen Methoden, insbesondere geeignete Verfahren zur lokalen und globalen Optimierung reellwertiger Funktionen, werden diskutiert und auf ihre Effizienz hin untersucht. Es wird ferner skizziert, wie sich vorhandene Verfahren unter Umständen verbessern lassen.

Da das verwendete Potentialmodell lediglich die Untersuchung homogener SiO_2–Cluster erlaubt, werden heterogene Siliziumoxidcluster (Si_xO_y, $x = 1, \ldots, 15$, $y = 0, \ldots, 45$) mittels dichtefunktionaltheoretischer Methoden untersucht. Zu diesem Zweck wird zunächst getestet, welche Kombination aus verschiedenen Funktionalen und Basissätzen die experimentell bestimmten spektroskopischen Daten für das SiO Molekül, insbesondere die Dissoziationsenergie, möglichst gut reproduziert. Mittels des auf der Basis dieser Untersuchung ausgewählten Methode werden dann die eigentlichen Untersuchungen durchgeführt und die Geometrien, Atomisierungsenergien und Vibrationsfrequenzen von etwas über 100 verschiedenen Clustern und etwa doppelt so vielen Isomeren bestimmt. Dabei wird auch auf die Ergebnisse der Potentialmodellrechnungen zurückgegriffen. Mit Hilfe der so bestimmten Daten werden die thermodynamischen Funktionen dieser Cluster berechnet. Die Ergebnisse dieser Rechnungen werden unter unterschiedlichen Aspekten analysiert, wobei ein besonderes Augenmerk auf die möglichen Kondensationsprozesse in einem Silizium–Sauerstoff–Gemisch gelegt wird. Es zeigt sich an Hand eines einfachen, stationären Windmodells, daß die homogene Nukleation von SiO_2 in einem Abstand von etwa $7.8\,R_*$ vom

Stern bei einer Temperatur von ca. 660 K sehr effektiv einsetzt, womit dieser Prozess allerdings für die Staubbildung in sauerstoffreichen, astrophysikalischen Situationen von eher untergeordneter Bedeutung ist. Die berechneten Daten legen jedoch die Vermutung nahe, daß die Kondensation über nicht–stöchiometrische Bildungsreaktionen sehr effektiv ablaufen könnte. Die Arbeit wird mit einer kurzem Erläuterung, in welche Richtung zukünftige Arbeiten auf diesem Gebiet zielen sollten, abgeschlossen.

Abstract

The formation of small solid particles (dust grains) from the gas phase in the circumstellar environments of evolved stars or the atmospheres of substellar objects (brown dwarfs) requires suitable physical and chemical conditions. The temperature and density of the gas have to be confined to a certain regime, the *dust formation window*, in order to allow the formation of clusters, which bridge the gap between small molecules and the solid. Apart from reaction kinetics the efficiency of this process is mainly governed by the Gibbs free energy of formation, which in turn can be calculated from the properties of the clusters. Hence, a detailed knowledge of the atomization energies, the geometries and the vibrational frequencies of the ground states of inorganic clusters is a necessary prerequisite for the understanding and modelling of the nucleation process. In case of the inorganic dust formation in oxygen–rich astrophysical environments strong evidence exists, that this process is not reasonable well described by means of the classical *homogeneous* nucleation theory. Instead a description, which takes *non–stoichiometric* reactions into account is more appropriate. In the context of this thesis a master equation is presented, which incorporates such type of reactions.

Further emphasis is put on the investigation of small and medium sized silicon oxide clusters. In a first step, these are studied by means of an empirical potential model. The necessary numerical methods, in particular those for the local and global optimization of real valued functions are discussed with respect to their efficiency. It is further outlined, how existing global optimization algorithm could be improved.

Since the used empirical force field is only applicable to homogeneous SiO_2 clusters, the more general case of heterogeneous silicon oxide clusters (Si_xO_y, $x = 1, \ldots, 15$, $y = 0, \ldots, 45$) is investigated by means of density functional methods. To this end we first assess the quality of different combinations of various DFT functionals and basis sets by comparing the theoretically determined spectroscopic constants of the SiO molecule with those known from experiment. Using the thus selected level of theory, we determined the atomization energies, geometries and vibrational frequencies of about 100 different clusters and approximately twice as much isomers. Thereby, we make use of the previous results obtained with the empirical potential model. With the help of these data, the thermodynamic functions of the clusters are calculated. The results are analysed under different aspects, with special emphasis on the possible condensation processes in a mixture of silicon and oxygen. Concluding the consequences of these results for astrophysical dust formation are discussed. Using a simple stationary wind model it is demonstrated, that effective homogeneous nucleation of SiO_2 starts at a distance of about $7.8\,R_*$ from the star at a temperature of $\approx 660\,\mathrm{K}$. Thus, this process is only of minor importance for the onset of dust formation in circumstellar envelopes of oxygen–rich AGB stars. On the other hand confirm these results the necessity to describe the condensation of silicon oxide by means of a non–stoichiometric nucleation theory. At the end of this thesis, it is outlined, in which directions future research should be directed.

Contents

List of Figures

List of Tables

Chapter 1

Introduction

The formation of solid particles is observed to occur in the (more or less) steady outflows of different types of mass–losing stars, as e.g. cool M–giants (Hagen, 1978), hot stars like η Carinae (Andriesse et al., 1978) or the hostile environments of Wolf–Rayet stars (Hackwell et al., 1979). It is further observed in the sporadic occultation events of RCB stars (see e.g. Woitke, 1997, for an overview) and the cataclysmic events of novae (Hyland & Neugebauer, 1970) or supernovae (Moseley et al., 1989). Recent observations also show, that dust is found in certain sub-stellar objects called brown dwarfs (Lüttke, 2002).

The process, which is responsible for the appearance of dust in these environments is quite different from the corresponding formation process of the dust, one gets angry about in everyday life. The latter one is a destructive process, which decomposes an already existing macroscopic solid like stones or chalk into tiny little dust grains, whereas the dust formation in circumstellar environments starts from the gas phase. Following Sedlmayr (1997), one might sketch the following scenario (see also figure 1.1):

1. The process starts with a hot and dense gas, which consists solely of atoms or ions.

2. This gas element is cooled and diluted by different physical processes, which depend on the characteristics of the astrophysical object, thus defining a *cooling trajectory* in the pressure-temperature plane (pT).

3. As the temperature is lowered, ions recombinate first forming neutral atoms. These then form at still lower temperatures diatomic molecules.

4. If the gas temperature is decreased even further, the consecutive formation of larger molecules and clusters with more then 2 atoms starts. Such clusters represent the intermediate species between a single atom and the solid. Thus, if the gas reaches conditions, which favour the effective formation of such clusters, they then can grow further, until small dust grains are formed.

The description of the last of these phases suggests, that the condensation of dust out of the gas phase can be conceived as a two–step process. The first of these steps comprises

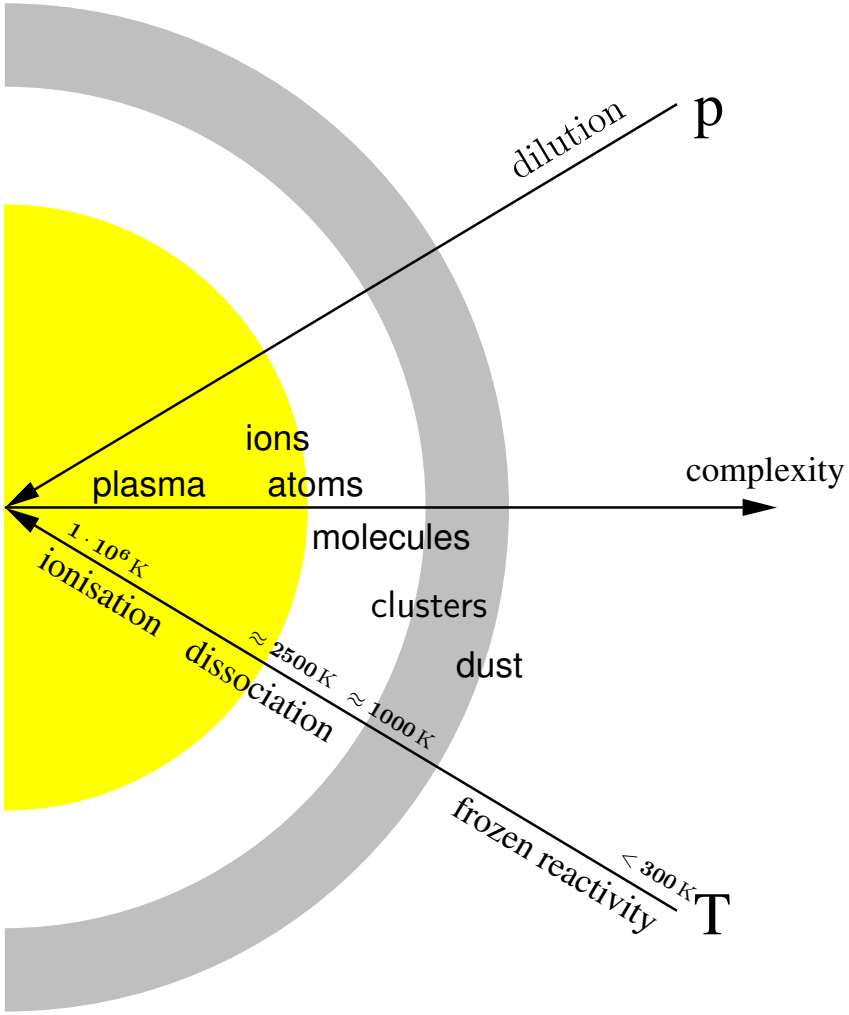

Figure 1.1: The dust formation window in AGB stars.

the formation of a *critical cluster* which is stable against dissociation. Smaller clusters will evaporate, while larger clusters will grow to macroscopic particles in the second step.

The sketched scenario of dust formation imposes some general limiting factors for the gas-solid transition (e.g. Sedlmayr, 1997, Woitke, 1999):

1. The formation of dust is inhibited by temperatures so high, that the possible solid evaporates or the molecules and clusters dissociate.

2. On the other hand low temperatures do not favour the (effective) dust formation either, since the collision and reaction time scales become larger than the characteristic time scales of the astrophysical object (frozen reactivity).

3. A similar argument applies to the density: If the density is too low, collisions between molecules are so infrequent, that the necessary growth process becomes ineffective.

As a consequence, the formation of dust is confined to certain parts of the pT-plane, which are referred to as the *dust formation window* (Sedlmayr, 1997). These conditions for the thermodynamic properties of a dust forming system are complemented by some constraints on the physical properties of the condensating substance. Gail & Sedlmayr (1986) particularise three different restrictive properties, that allow an assortment of different *primary dust condensates* in oxygen-rich asymptotic giant branch (AGB) stars:

- **Abundance constraints**: The first constraint concerns the abundances of the elements, which are involved in the dust formation process. The rate, at which the necessary reactions between the involved species proceed, is proportional to their particle density. Thus, only those compounds have to be considered, for which the abundances of the constituting elements are sufficiently high.

- **Reactivity constraints**: Some molecules like CO or N_2 exhibit an exceptional high dissociation energy *and* are non–reactive. Thus in case of an oxygen–rich composition of the gas almost all carbon is blocked in CO and will not participate in the dust formation process[1]. Such elements can be excluded as primary dust condensates.

- **Stability constraints**: It is generally accepted, that the dust formation in the circumstellar shells of AGB stars starts at about 1000 K (Gail & Sedlmayr, 1986). Thus, only substances which have a solid (or fluid) phase, which is stable at such high temperatures – so called *high temperature condensates* – can form the primary dust condensate.

In this thesis we focus on the case of *oxygen–rich* astrophysical environments. Whereas the condensation in C–rich environments is simple in that sense, that solely solid carbon (some kind of soot) is formed[2] and observed, the situation in the oxygen–rich is a little bit more complicated. This has mainly two reasons. At first, there exists a great variety of molecules, like different types of oxides, sulfides etc. in the gas phase. There are also many different solids, which have been identified in the circumstellar environments of AGB–stars (see d'Hendecourt et al., 1999, for an overview). Furthermore, the necessary molecular data for the inorganic chemistry in such a system are mostly missing.

Further investigations of different candidates for the primary condensate excluded the onset of dust formation by the nucleation of magnesium oxide (Köhler et al., 1997) or iron (John, 1995). In both cases the small dissociation energy of the monomer (MgO, $D_0 = 2.7$eV) or the dimer (Fe_2, $D_0 = 1.14$eV) prevents an effective nucleation, because these molecules have to be formed during the nucleation process. They thus form a kind of narrow bottle neck, which leads to small nucleation rates. Another possible candidate

[1] The opposite is true for carbon-rich environments. There, all oxygen is blocked. This explains the different nature of dust observed in C– and M–stars.

[2] Of course, the microscopic details of this process are non–trivial, but are a little bit better understood, than in the O–rich case, because this process if of great technical importance e.g. for combustion. As a consequence the chemistry is known in greater detail. The case of (approximate) equal abundance of O and C we exclude here from the discussion.

is corundum Al_2O_3, as this solid is very stable and it has also been detected in presolar dust grains found in meteorites (e.g. Nittler et al., 1994, 1997). Chang et al. (1998, 2000) performed an *ab initio* study of some Al_xO_y clusters, and the thermodynamic properties of different Al_2O_3 have been calculated by Patzer et al. (1999). The resulting equilibrium densities of Al_2O_3, calculated by means of these data, are so low, that the homogeneous nucleation of corundum under astrophysical conditions seems to be unlikely. However, Al_2O, AlOH, and Al_2O_2 prove to be abundant molecules at temperatures below ca. 1150 K. Therefore the condensation of aluminium oxides could proceed via a non–stoichiometric nucleation process at temperatures below $\approx 1150\,\mathrm{K}$ (Patzer, 1998). The most promising candidate for the primary condensate at the moment is titanium oxide, which has been investigated by means of density functional theory calculations by Jeong et al. (2000).

Usually, the homogeneous condensation of silicon oxides (either SiO or SiO_2) is also excluded, but there are two main objections against this. At first, this conjecture is *not* based on the molecular data of silicon oxide clusters. And secondly, there is strong evidence by laboratory experiments, that the condensation of silicon oxides is similar to the case of aluminium oxides a non–stoichiometric nucleation process (c.f. section 5.1). Hence, it is the aim of this thesis to elucidate the dust formation process in circumstellar environments on an atomistic level. To this end it is necessary to develop a suitable method for the description of a non–stoichiometric nucleation process. Another prerequisite is the detailed knowledge of the physical properties of silicon oxide clusters which represent the key species in the transition from atoms to solids.

We close this section with a short outline of the structure of this thesis. The next chapter discusses the derivation of a master equation, which describes the non–stoichiometric nucleation in a gas, that consists of two different elements.

The third chapter gives a brief overview of different theoretical methods, which can be used, to determine the physical properties of atomic and molecular clusters, thereby concentrating on some aspects of the applicability of these techniques. In order to introduce some concepts, which are useful for the discussions in the further course of this thesis, the properties of Lennard–Jones clusters and some topological aspects of the underlying potential energy surface are reviewed. At the end of this chapter, it is explicated, how the thermodynamic properties of molecules and clusters can be calculated by means of the so called *rigid-rotor harmonic-oscillator* (RRHO) approximation. The methods are exemplarily applied to some diatomic molecules of astrophysical interest.

Chapter 4 is solely devoted to the numerical methods used to investigate the potential energy surface of clusters. Although most of these methods are applied to empirical force fields, the methods can in principle also be applied to potential energy surfaces, which are based on *ab initio* calculations. The first part of this chapter deals with the theory of local minimization, whereas the second part is about global optimization. In both cases the necessary theory is briefly recapitulated and some algorithms are introduced, which are suitable to solve the corresponding problem. Additionally, we discuss the performance of the introduced algorithms, in order to motivate our selection of a certain method. The third part of this chapter gives an overview over some techniques, which are suitable for the quantitative analysis of molecular conformations. The chapter closes with a short

description of molecular dynamics simulations in the microcanonical ensemble.

In chapter 5, the results of an investigation of silicon oxide clusters by means of the introduced methods is presented. The first part of this chapter concentrates on homogeneous $(SiO_2)_N$ clusters, modelled by an empirical force field, whereas small and medium sized Si_xO_y ($x = 1, \ldots, 15$, and $y = 0, \ldots, 30$) are studied in the next part. The results of this calculations are used to discuss the possibility of silicon oxide condensation in the circumstellar environments of AGB stars.

The thesis closes with some concluding remarks and an outlook on possible future research direction in chapter 6. For the sake of better readability, some further informations and data are given in the appendix.

Chapter 2

Remarks on non–stoichiometric nucleation

2.1 Introduction

It is the aim of this thesis to elucidate the dust formation process in circumstellar environments. As discussed in chapter 1 this process might be split into two different parts, where different types of descriptions are appropriate. It was further explicated, that the first of these two steps, the formation of condensation seeds by molecular reactions, is only poorly understood. One of the reasons mentioned is, that this nucleation process probably is *not* a homogeneous nucleation process, but instead a *non–stoichiometric* process, which involves the reaction between molecules and clusters of diverse stoichiometric composition. Therefore, it is the aim of this chapter, to present a kinetic description of this process.

Throughout this chapter we restrict the discussion to the special case, where the gas phase consists of only two substances A and B. The number of possible solids formed by these two elements shall be limited to three modifications, viz. pure A(bulk), pure B(bulk), and the mixed solid $\mathsf{A}_{\bar{x}}\mathsf{B}_{\bar{y}}$(bulk), where $\bar{x}$ and $\bar{y}$ are the stoichiometric coefficients of A and B. The possible existence of further solids with different stoichiometric coefficients or crystal modifications are neglected here. The conditions in such a gas are determined by the following quantities:

1. The temperature of the gas T_{gas}.

2. The total particle density n_{ges}.

3. The abundances of the elements A and B, denoted with ε_{A} and ε_{B}, respectively:

$$\varepsilon_{\mathsf{A}} = \frac{n_{<\mathsf{A}>}}{n_{tot}} \qquad \varepsilon_{\mathsf{B}} = \frac{n_{<\mathsf{B}>}}{n_{tot}} \tag{2.1}$$

   where $n_{<\mathsf{A}>}$ and $n_{<\mathsf{B}>}$ are the *total density* of A, and B, respectively, when all molecules are dissociated into atoms (Dominik, 1992).

4. The (time dependent) particle density $f(x, y; t)$ of a clusters $\mathsf{A}_x\mathsf{B}_y$ $(x, y = 0, 1, \ldots)$. As a consequence of the conservation of mass, it holds:

$$n_{tot} = \sum_{x=0} \sum_{y=0} f(x, y; t) \tag{2.2}$$

with $f(0, 0; t) \equiv 0 \; \forall \; t$.

Depending on the abundances ε_A and ε_B of the two elements, different types of solids are stable (see also the discussion of some condensation experiments of silicon oxide in section 5.1). If e.g. $\varepsilon_\mathsf{A} \gg \varepsilon_\mathsf{B}$, all atoms will form bulk A, whereas the small amount of B is either still in the gas phase or incorporated as impurities into the solid or on its surface. The details of the stability limits depend on the thermodynamic properties of the considered species.

2.2 Derivation of a master equation

The time evolution of the particle densities $f(x, y; t)$ is determined by the microscopic growth and evaporation processes, changing the size of a cluster $\mathsf{A}_x\mathsf{B}_y$. The classical theory of homogeneous nucleation considers only growth and evaporation of monomers, viz.:

$$\mathsf{A}_x + \mathsf{A} \leftrightharpoons \mathsf{A}_{x+1} \tag{2.3}$$

Here more general condensation and evaporation processes are considered, which can be written as:

$$\mathsf{A}_x\mathsf{B}_y + \mathsf{A}_u\mathsf{B}_v \leftrightharpoons \mathsf{A}_{x+u}\mathsf{B}_{y+v} \qquad \text{with } u, v, x, y = 0, 1, \ldots \tag{2.4}$$

This type of reactions additionally includes the possibility of cluster-cluster collisions and the growth via non-stoichiometric species. This *ansatz* is among others motivated by the observation, that despite the high stability of bulk corundum, Al_2O_3 has a rather low nucleation rate (Patzer, 1998, Lüttke, 2002, Jeong et al., 2003), since only a low equilibrium abundance of the nominal molecule is predicted (Chang et al., 1998, Patzer et al., 1999). Since other aluminium–oxides as e.g. AlO, Al_2O, or Al_2O_2 are quite abundant in the gas phase, it seems possible, that the formation of Al_2O_3 seeds proceeds via reactions of type (2.4).
For the reactions rates, describing these processes the following notation is introduced:

- The rate for a growth process like:

$$\mathsf{A}_x\mathsf{B}_y + \mathsf{A}_u\mathsf{B}_v \longrightarrow \mathsf{A}_{x+u}\mathsf{B}_{y+v} \tag{2.5}$$

  is designated by $\mathcal{G}_{x,y}^{u,v}$ or more generally by $\mathcal{G}_{\text{initial cluster}}^{\text{growth cluster}}$.

- The rate for a evaporation process like:

$$\mathsf{A}_x\mathsf{B}_y \longrightarrow \mathsf{A}_{x-u}\mathsf{B}_{y-v} + \mathsf{A}_u\mathsf{B}_v \tag{2.6}$$

  is designated by $\mathcal{E}_{x,y}^{u,v}$ or more generally by $\mathcal{E}_{\text{initial cluster}}^{\text{evaporated cluster}}$.

Note, that the left-hand side of equation (2.5), and the right-hand side of equation (2.6) imply a kind of symmetry, since it holds:

$$\mathcal{G}_{x,y}^{u,v} = \mathcal{G}_{u,v}^{x,y} \qquad \text{and} \qquad \mathcal{E}_{x,y}^{u,v} = \mathcal{E}_{x,y}^{x-u,y-v} \tag{2.7}$$

Using this notation one can now derive a master equation, which describes the temporal evolution of the particle density $f(x, y; t)$ of a cluster $\mathsf{A}_x\mathsf{B}_y$. If one denotes the sum of all gain reactions yielding an $\mathsf{A}_x\mathsf{B}_y$ cluster with Γ, and the sum of all loss reactions destroying an $\mathsf{A}_x\mathsf{B}_y$ cluster with Λ, one can simply write:

$$\frac{d}{dt} f(x, y; t) = \Gamma - \Lambda = \Gamma_g + \Gamma_e - \Lambda_e - \Lambda_g \tag{2.8}$$

A cluster of a certain size can be created either by growing on a smaller cluster or by destroying a larger cluster (see figure 2.1). Thus the sum of all gain processes can be divided into two contributions, one due to growth (Γ_g in equation 2.8), and one due to evaporative processes (Γ_e in equation 2.8). Similar arguments apply to the loss processes, since a cluster of a given size can be destroyed either by evaporation (subsumed in Λ_e) or growing (subsumed in Λ_g).

Up to now no assumptions about the type of the growth and evaporation processes entered the derivation of the master equation. In the form presented here equation (2.8) is also valid for the case of homogeneous nucleation.

Next one has to explicate the gain and loss processes in equation (2.8). Using the notation introduced above one gets the following expressions for the four different terms on the right-hand side of this equation:

1. For the term Γ_g, describing the gain due to collisions of type (2.5) it holds:

$$\Gamma_g = \sum_{u=0}^{I_u} \sum_{v=0}^{I_v} \mathcal{G}_{x-u,y-v}^{u,v} \, f(x-u, y-v; t) \tag{2.9}$$

   where the upper limits of the sums (I_u, I_v) and the explicit form of the growth rates will be discussed later. Note, that both sums may start at 0, since it was similar to equation (2.2) assumed, that $\mathcal{G}_{x,y}^{0,0} \equiv 0 \; \forall \; t, x,$ and y.

2. The term Γ_e, which accounts for (positive) change of the particle density due to evaporation of cluster larger then $\mathsf{A}_x\mathsf{B}_y$, one finds:

$$\Gamma_e = \sum_{u=0}^{I_u} \sum_{v=0}^{I_v} \mathcal{E}_{x+u,y+v}^{u,v} \, f(x+u, y+v; t) \tag{2.10}$$

   Again the assumption is made, that $\mathcal{E}_{x,y}^{0,0} \equiv 0$.

3. Similar to equation (2.9) one gets for the loss of $\mathsf{A}_x\mathsf{B}_y$ clusters due to the growth towards larger clusters:

$$\Lambda_g = \sum_{u=0}^{I_u} \sum_{v=0}^{I_v} \mathcal{G}_{x,y}^{u,v} \, f(x, y; t) \tag{2.11}$$

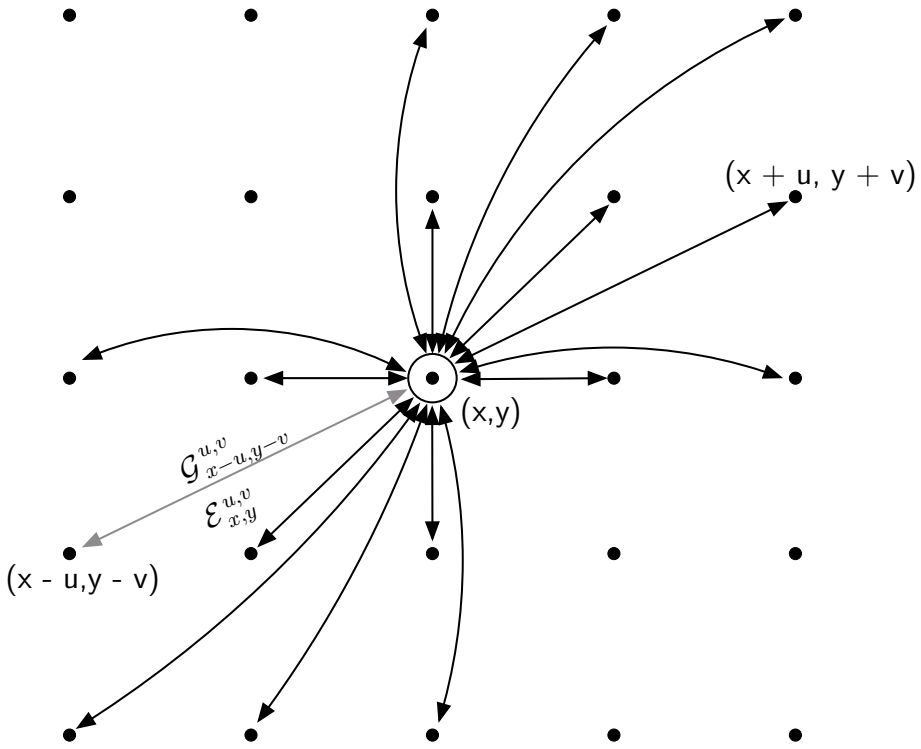

Figure 2.1: Schematic representation of the different reactions in the two dimensional cluster space, changing the size of a $\mathsf{A}_x\mathsf{B}_y$ cluster. Only reactions of the type of equation 2.4 are considered.

4. The destruction of $\mathsf{A}_x\mathsf{B}_y$ clusters due to evaporation (or dissociation) into smaller clusters is described by:

$$\Lambda_e = \sum_{u=0}^{I_u} \sum_{v=0}^{I_v} \mathcal{E}^{u,v}_{x,y}\, f(x,y;t) \tag{2.12}$$

The upper indices I_u and I_v of the sums in equations (2.9) to (2.12) can be determined in two different ways. At first one could sum over all possible reactions. In this case one has to keep in mind, that due to the symmetric properties of $\mathcal{G}^{u,v}_{x,y}$ and $\mathcal{E}^{u,v}_{x,y}$ (c.f. Eq. 2.7) some reactions are taken into account twice. Since this would complicate the expressions and make them rather confusing, a second approach is used here. It is based on the assumption that mainly small molecules and clusters are abundant enough to contribute significantly to the growth process and that larger clusters are only of minor importance, as they rapidly grow to macroscopic size. In the case of corundum, for example, one might restrict the list of *growth species* to Al, O, AlO, Al_2, O_2 Al_2O, AlO_2, and Al_2O_2[1]. Additionally, it is assumed, that evaporation involves the decomposition of the clusters into a bigger and into

[1]A short coming of this approach, is the neglect of any hydrides, see section 2.3.

a smaller aggregate. Formally these assumptions are expressed by restricting the indices I_u and I_v, respectively, to certain values, e.g. $I_u, I_v = 0, 1, 2$ for the case of aluminium oxides, listed above.

If one introduces an *effective transition rate* $\mathcal{J}^{\text{final cluster}}_{\text{initial cluster}}$ as the net rate for the transition of $\mathsf{A}_{x-u}\mathsf{B}_{y-v}$ clusters to $\mathsf{A}_x\mathsf{B}_y$ clusters and vice versa:

$$\mathcal{J}^{x,y}_{x-u,y-v} = \mathcal{G}^{u,v}_{x-u,y-v}\, f(x-u, y-v; t) - \mathcal{E}^{u,v}_{x,y}\, f(x, y; t) \tag{2.13}$$

one can transform equation (2.8) using the equations (2.9) to (2.12) into the following form:

$$\begin{aligned}\frac{d}{dt} f(x,y;t) = & \sum_{u=0}^{I_u}\sum_{v=0}^{I_v} \left(\mathcal{G}^{u,v}_{x-u,y-v}\, f(x-u, y-v; t) - \mathcal{E}^{u,v}_{x,y}\, f(x,y;t)\right) \\ & - \sum_{u=0}^{I_u}\sum_{v=0}^{I_v} \left(\mathcal{G}^{u,v}_{x,y}\, f(x,y;t) - \mathcal{E}^{u,v}_{x+u,y+v}\, f(x+u, y+v; t)\right) \\ = & \sum_{u=0}^{I_u}\sum_{v=0}^{I_v} \mathcal{J}^{u,v}_{x,y} \quad - \quad \sum_{u=0}^{I_u}\sum_{v=0}^{I_v} \mathcal{J}^{u,v}_{x+u,y+v}\end{aligned} \tag{2.14}$$

having the typical form of a master equation (e.g. Patzer, 1998). The effective transition rate $\mathcal{J}^{x,y}_{x-x,y-v}$ is marked as a gray arrow in figure 2.1. Depending on the sign of $\mathcal{J}$, the population of $\mathsf{A}_x\mathsf{B}_y$ clusters is either increasing ($\mathcal{J} > 0$) or decreasing ($\mathcal{J} < 0$). A stationary state in attained, if $\mathcal{J} = 0$ for all clusters!

2.2.1 The growth and evaporation rates

After the derivation of a master equation describing the time dependence of the particle densities $f(x, y; t)$ it is now necessary to give explicit expressions for the growth and evaporation rates, $\mathcal{G}^{u,v}_{x,y}$ and $\mathcal{E}^{u,v}_{x,y}$, respectively.

Since events leading to the growth of a cluster always require the collision with another cluster[2], it is evident to describe the growth rate $\mathcal{G}^{u,v}_{x,y}$ using the gas–kinetic theory. In this case one finds for the growth rate:

$$\mathcal{G}^{u,v}_{x,y} = A(x,y;u,v)\; \alpha(x,y;u,v)\; \langle\, v_{rel}(x,y;u,v)\,\rangle\; f(u,v;t) \tag{2.15}$$

Here $A(x, y; u, v)$ is the collision cross section of the clusters $\mathsf{A}_x\mathsf{B}_y$ and $\mathsf{A}_u\mathsf{B}_v$. For spherical clusters it holds:

$$A(x,y;u,v) = \pi\; (r_{x,y} + r_{u,v})^2 = \pi\; r^2_{x,y;u,v} \tag{2.16}$$

with $r_{x,y}$ denoting the radius of a $\mathsf{A}_x\mathsf{B}_y$ cluster. For the mean relative velocity $\langle\, v_{rel}\,\rangle$ between the two collision partners if follows (e.g. Atkins, 1989):

$$\langle\, v_{rel}(x,y;u,v)\,\rangle = \sqrt{\frac{8\; k\; T}{\pi\; \mu}} \qquad \text{and} \quad \mu = \frac{m_{x,y}\; m_{u,v}}{m_{x,y} + m_{u,v}} \tag{2.17}$$

[2]As the densities in astrophysical objects are quite low, three–body collisions seem to be unlikely.

with μ the reduced mass of the two collision partners. The factor α is the reaction efficiency. It is noteworthy, that the growth rate (2.15) depends on the density $f(u,v;t)$ of the collision partner $\mathsf{A}_u\mathsf{B}_v$. It is convenient to split $\mathcal{G}_{x,y}^{u,v}$ into two factors: a '*geometric*' factor, which depends solely on the physical properties of the reacting clusters (i.e. their masses, and reaction cross section), and the density $f(.)$, for which the time evolution is described by the master equation (2.14). If one denotes the first factor with $\widehat{\mathcal{G}}_{x,y}^{u,v}$:

$$\widehat{\mathcal{G}}_{x,y}^{u,v} = A(x,y;u,v)\ \alpha(x,y;u,v)\ \langle\, v_{rel}(x,y;u,v)\,\rangle \tag{2.18}$$

one rewrites the equation (2.13) for the transition rate $\mathcal{J}_{x,y}^{u,v}$ as follows:

$$\mathcal{J}_{x-u,y-v}^{x,y} = \widehat{\mathcal{G}}_{x-u,y-v}^{u,v}\ f(u,v;t)\ f(x-u,y-v;t) - \mathcal{E}_{x,y}^{u,v}\ f(x,y;t) \tag{2.19}$$

Note, that it is mainly a matter of taste, whether one prefers the expression in equation (2.13) or that in (2.19) for $\mathcal{J}_{x,y}^{u,v}$.

For the calculation of the evaporation rates one makes use of the principle of *detailed balance*. Evaporation, i.e the spontaneous emission of atoms or molecules from a cluster $\mathsf{A}_x\mathsf{B}_y$ only depends on its properties, namely its size, atomization energy and frequencies, and its internal state or temperature. As a consequence, the rate at which such evaporative events occur should be independent of the properties of the surrounding gas. Hence if one assumes, that the system is in a state of local thermodynamic equilibrium (LTE–state), where for each microscopic growth process and its inverse the principle of detailed balance holds, one is able to express the evaporation rate in terms of the growth rate. Using the effective transition rate introduced in equation (2.13), the principle of detailed balance means, that:

$$\mathcal{J}_{x-u,y-v}^{x,y} \equiv 0 \tag{2.20}$$

for each cluster. If the particle densities in the LTE–state are denoted with $\overset{\circ}{f}$, it follows that:

$$\begin{aligned} \mathcal{E}_{x,y}^{u,v}\ \overset{\circ}{f}\,(x,y) \ &=\ \widehat{\mathcal{G}}_{x-u,y-v}^{u,v}\ \overset{\circ}{f}\,(u,v)\ \overset{\circ}{f}\,(x-u,y-v) \\ \Longleftrightarrow \qquad \mathcal{E}_{x,y}^{u,v} \ &=\ \widehat{\mathcal{G}}_{x-u,y-v}^{u,v}\ \frac{\overset{\circ}{f}\,(u,v)\ \overset{\circ}{f}\,(x-u,y-v)}{\overset{\circ}{f}\,(x,y)} \end{aligned} \tag{2.21}$$

Since the quotient in equation (2.21) can be expressed using the Gibbs energy of formation of the reaction partners

$$\frac{\overset{\circ}{f}\,(x-u,y-v)\ \overset{\circ}{f}\,(u,v)}{\overset{\circ}{f}\,(x,y)} = \exp\left(\frac{\Delta_r G^{\ominus}(\mathsf{A}_{x-u}\mathsf{B}_{y-v},\mathsf{A}_u\mathsf{B}_v;T)}{RT}\right) \tag{2.22}$$

with

$$\Delta_r G^{\ominus} = \left(\frac{\Delta_f G^{\ominus}(\mathsf{A}_x\mathsf{B}_y;T) - \Delta_f G^{\ominus}(\mathsf{A}_{x-u}\mathsf{B}_{y-v};T) - \Delta_f G^{\ominus}(\mathsf{A}_u\mathsf{B}_v)}{R\,T}\right) \tag{2.23}$$

one finally gets for the evaporation rate:

$$\mathcal{E}_{x,y}^{u,v} \;=\; \mathcal{G}_{x-u,y-v}^{u,v}\;\exp\left(\frac{\Delta_r G^{\ominus}(\mathsf{A}_{x-u}\mathsf{B}_{y-v},\mathsf{A}_u\mathsf{B}_v;T)}{R\,T}\right) \tag{2.24}$$

As the Gibbs free energy $\Delta_f G^{\ominus}$ enters the calculation of the evaporation rate exponentially, it is evident, that this quantity is decisive for the effectiveness of the nucleation process.

2.3 Discussion

Up to now, the derivation of a master equation describing the process of non–stoichiometric nucleation was straight forward. However, there exist some drawbacks, that require some further considerations. The most problematic point seems to be the existence of the proposed equilibrium state necessary for the application of the principle of detailed balance. Following Patzer (1998) this equilibrium state can be defined as a phase equilibrium not only between the monomers and bulk solid but between N–mers and the solid as well. There it was demonstrated that if the monomer is in a phase equilibrium with the bulk, meaning that:

$$\mathcal{S}_1 = \frac{\overset{\circ}{p}\,(1)}{\overset{\circ}{p}_{sat}\,(1)} = 1 \tag{2.25}$$

where $\overset{\circ}{p}_{sat}\,(1)$ is the vapour saturation pressure above the solid, this holds true for N–mers also. If one defines the supersaturation ratio $\mathcal{S}_N$ of an N–cluster similar to (2.25) as:

$$\mathcal{S}_N = \frac{\overset{\circ}{p}\,(N)}{\overset{\circ}{p}_{sat}\,(N)} \qquad \text{with } \overset{\circ}{p}_{sat}\,(N) = p^{\ominus}\;\exp\left(\frac{N\;\Delta_f G^{\ominus}(\text{bulk}) - \Delta_f G^{\ominus}(N)}{R\,T}\right) \tag{2.26}$$

this equilibrium state is expressed by the following relationship:

$$\mathcal{S}_N = (\mathcal{S}_1)^N = 1 \tag{2.27}$$

Unfortunately a similar expression can not be derived for the more general case of non–stoichiometric nucleation and heterogeneous cluster considered here. Of course equation (2.27) is valid for the supersaturation ratio of an $(\mathsf{A}_{\bar{x}}\mathsf{B}_{\bar{y}})_N$–cluster, if $\mathsf{A}_{\bar{x}}\mathsf{B}_{\bar{y}}$ is the stoichiometric composition of the bulk. But from this one can not conclude whether the *vapour pressure* of an arbitrary cluster $\mathsf{A}_u\mathsf{B}_v$ in equilibrium with a solid $\mathsf{A}_{\bar{x}}\mathsf{B}_{\bar{y}}$. The reason for this is simply, that equation (2.27) is based on the fact, that the continuous addition of N–mers finally will lead to the same solid, as if adding continuously monomers. Formally one could this express by writing

$$\underbrace{\mathrm{C}_N + \mathrm{C}_N + \ldots + \mathrm{C}_N}_{\times\, L,\text{ with } L\to\infty} \;\longrightarrow\; \mathrm{C(bulk)} \;\longleftarrow\; \underbrace{\mathrm{C}_1 + \mathrm{C}_1 + \ldots + \mathrm{C}_1}_{\times\, L',\text{ with } L'\to\infty} \tag{2.28}$$

or alternatively

$$\sum_{l=0}^{\infty} \mathrm{C}_1 = \sum_{l'=0}^{\infty} \mathrm{C}_N = \mathrm{C(bulk)} \tag{2.29}$$

For the case of heterogeneous nucleation preceding via reactions of type (2.4), where the intermediate products are not necessary of the same stoichiometric composition as the final solid, this is no longer true. This can be expressed, using the notation introduced above, as:

$$\sum_{l=0}^{\infty} \mathsf{A}_u\mathsf{B}_v \neq \mathsf{A}_{\bar{x}}\mathsf{B}_{\bar{y}}\mathrm{(bulk)} \qquad \text{for } u \neq n\bar{x} \text{ and } v \neq m\bar{y} \text{ with } n, m \in \mathbb{N} \tag{2.30}$$

The discussion is further complicated by the fact that, as pointed out above, more than one solid may be stable.

Another drawback of the derived master equation is the neglect of any further elements involved in the nucleation process. As already mentioned, it might be necessary to take also reactions with e.g. hydrates like AlH or AlOH into account. Such reactions are of the following type:

$$\mathsf{A}_x\mathsf{B}_y\mathsf{M} + \mathsf{A}_u\mathsf{B}_v \rightleftharpoons \mathsf{A}_{x+u}\mathsf{B}_{y+v} + \mathsf{M}^* \tag{2.31}$$

Since the unchanged reaction partner M might be able to carry away the released reaction heat, indicated by M^* on the right hand side of reaction (2.31), the efficiency of the corresponding growth reactions might be increased.

2.3.1 Concluding remark

The outlined theory of non–stoichiometric nucleation is not yet complete, although a direction, in which future work should go, is given. The main quantity, which is essential for the efficiency of this process is, as in the case of homogeneous nucleation (see Patzer, 1998), the Gibbs free energy of formation $\Delta_f G^{\ominus}$. The next chapter will, among others, be devoted to the question, how this quantity can be calculated using the molecular data of a cluster, which are determined either by experiment or by theoretical calculations.

Chapter 3

Physical properties of clusters with special emphasis on their relevance for the astrophysical dust formation process

Although rather young, the physics and chemistry of clusters is a rapidly growing area of research. From the very beginning the development of cluster science is closely connected to astrophysical problems, especially the problem of dust formation. The experiments of Kroto et al. (1985) in order to elucidate the formation of large carbon chains in the

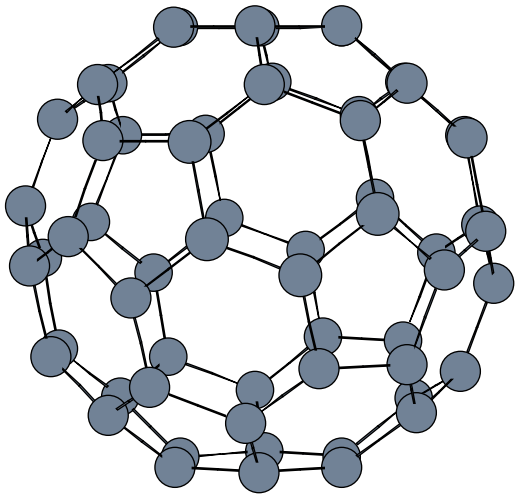

Figure 3.1: The C_{60} cluster or buckminsterfullerene, one of the most prominent and perhaps most beautiful molecules.

interstellar medium (ISM) or circumstellar environments (CSE) of evolved stars revealed the existence of a highly stable and symmetric cluster, consisting of 60 carbon atoms: A

truncated icosahedron with 12 pentagonal and 20 hexagonal faces christened '*buckminsterfullerene*', which is shown in figure 3.1. The history of the investigations, which finally led to the discovery of C_{60} and its structure are described in Kroto (1997). At about the same time[1] as C_{60} was discovered, the investigation of clusters consisting of other atoms or molecules started. For example, Harris et al. (1984) report the first well resolved rare-gas mass spectrum generated in a free jet expansion. Since then our knowledge about the physics and chemistry of C_{60} and other fullerenes, rare gas clusters, metal clusters and molecular clusters etc. has grown considerably, which makes it impossible to give a complete survey about this fascinating field. Instead, the reader might refer to some of the numerous publications dealing with the physics and chemistry of clusters, as e.g. the books by Haberland (1995a), Jellinek (1999), Guet et al. (2001) or Johnston (2002).

The main motivation for the investigation of clusters is the fact, that clusters bridge the gap between small molecules and the solid state. Thus a major concern of cluster science is the question, how large a cluster must be, before its properties resemble those of the corresponding solid. The answer to this question depends strongly on the considered properties and on the atoms, the cluster consists of. Next to the investigation of such size effects, clusters are often used as models for the surfaces of bulk matter, because a high percentage of atoms lie at the surface of a cluster.

On the next pages, a short overview over different approaches to determine the physical properties of clusters is given.

3.1 Theoretical methods to calculate the properties

The theory of quantum mechanics enables one in principle, to calculate the properties of any atom, molecule or solid by means of one *first principle* - the Schrödinger equation:

$$\hat{\mathcal{H}}\,\Psi = E\,\Psi \tag{3.1}$$

where $\hat{\mathcal{H}}$ is the Hamiltonian operator of the system under consideration, Ψ is its wave function and E the energy. For molecular systems, the Hamiltonian operator can be written as:

$$\hat{\mathcal{H}} = -\sum_i \frac{\hbar^2}{2\,m_e}\nabla_i^2 - \sum_k \frac{\hbar^2}{2\,m_k}\nabla_k^2 - \sum_i\sum_k \frac{Z_k\,e^2}{r_{ik}} + \sum_{i<j}\frac{e^2}{r_{ij}} + \sum_{k<l}\frac{Z_k\,Z_l\,e^2}{r_{kl}} \tag{3.2}$$

where i and j run over electrons, k and l run over nuclei and $\hbar$ is the Planck constant, divided by $2\,\pi$. The masses of the electron and the nuclei are denoted as m_e, and m_k, respectively; e is the charge of the electron and Z is the atomic number. The distance

[1]The '*history*' of cluster science given here is of course abbreviated. For example Kreibig & Vollmer (1995) point out, that Mies's study about the optical properties of gold particles, which gave rise to the well known '*Mie theory*' describing the scattering of light at small particles, can be regarded as one of the first publications about clusters. Johnston (2002) gives a citation of Boyle in 1661 as the earliest reference of the word 'cluster' in a chemistry publication.

between two particles is r_{ab}. The first two terms describe the kinetic energy of the electron, and the nuclei, respectively. The third term is the potential energy of the attraction between the electrons and nuclei. The potential energy of the repulsion between two electrons is expressed by the fourth term, while the fifth term is the corresponding quantity for the nuclei. Note, that the Hamiltonian operator (3.2) neglects spin–orbit and other relativistic interactions (Levine, 2000).

The Hamiltonian operator in equation (3.2) can be simplified by means of the Born–Oppenheimer approximation, which is described in most textbooks about quantum chemistry (e.g. Levine, 2000, Leach, 2001). The approximation is based on the fact, that electrons are much lighter then the nuclei and thus move much faster then those. This means, that it is possible to decouple these two motions, and compute the electronic energy for *fixed* nuclear positions. This is expressed by the following equation (Cramer, 2002):

$$(\hat{\mathcal{H}}_{el} - V_N)\ \Psi_{el}(\vec{\mathbf{q}}_i; \vec{\mathbf{q}}_k) = E_{el}\ \Psi_{el}(\vec{\mathbf{q}}_i; \vec{\mathbf{q}}_k) \tag{3.3}$$

The new Hamiltonian operator of the Born–Oppenheimer approximation comprises only the first, third, and fourth term of the original operator (3.2). The coordinates $\vec{\mathbf{q}}_i$ of the electrons are independent variables, whereas the nuclear coordinates $\vec{\mathbf{q}}_k$ are parameters. The term V_N is a constant for a given set of fixed nuclear coordinates $\vec{\mathbf{q}}_k$.

Thus, one equation (either 3.2 or 3.3) is sufficient to determine the physical and chemical properties of the simplest molecule, the H_2^+ ion, as well as of the most complex molecules like the desoxyribosenucleic acid (DNA) or proteins. In other words, as stated by Dirac (1929): "*The underlying physical laws necessary for the mathematical theory of a large part of physics and the whole of chemistry are thus completely known and the difficulty is only that exact application of the laws leads to equations much to complicated to be solved*[2]." Whereas it is possible to find an analytic solution of the Schrödinger equation in the case of the hydrogen molecule ion H_2^+ (explicated e.g in Levine, 2000, p. 376 ff) this is impossible for molecules with more then one electron. One thus has to introduce further approximations. It is beyond the scope of this thesis to give an overview of the different approaches introduced in order to solve equation (3.3). Concise presentations can be found in different publications about quantum chemistry as e.g. by Hehre et al. (1985), Levine (2000), Leach (2001), or Cramer (2002). Instead of this we give a short overview over different concepts, which can be used to calculate the physical properties of clusters, consisting of N atoms. For this discussion we refer to the sketch in figure 3.2, where we display the applicability of different methods on the x–scale. On the y–scale we try to illustrate, how computational demanding a certain method is. As one expects, is the range of applicability inverse proportional to the computational effort of a method. It is difficult to assess the quality of the results obtained by different methods in a general manner, since it is strongly influenced by the following factors:

- The considered cluster system. The discussion on page 38ff will demonstrate, that

[2]It is a fascinating question, whether such a reduction is also possible for the biological *laws*. Authors like Mayr (1988) refuse such a possibility for principal reasons.

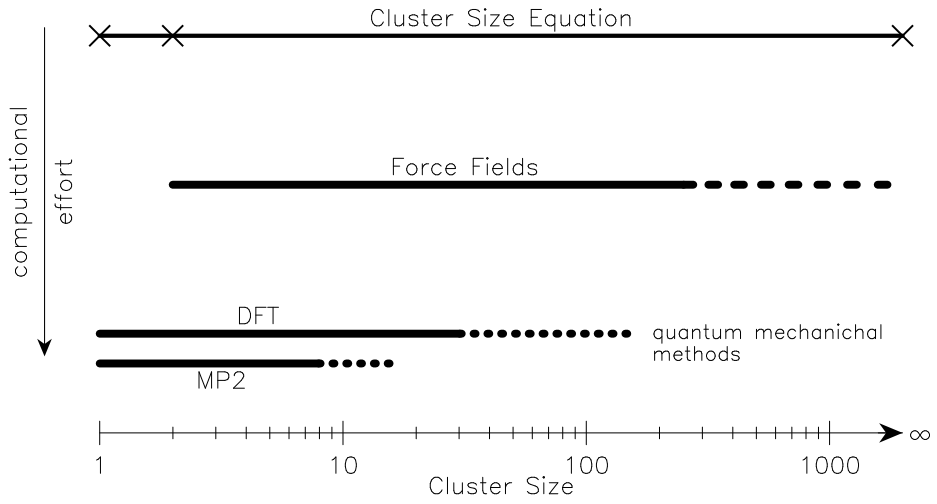

Figure 3.2: Overview over different computational methods for the calculation of cluster properties. Note, that solids can be treated on all levels of theory, because the periodic boundary conditions allow some simplifications, which make the problem solvable.

homogeneous transition metal clusters are only poorly described by means of density functional theory (DFT).

- The details of the used method. In section 5.3.1.1 it will be demonstrated, that the quality of the calculated data depends decisively on the chosen functional for the DFT method and the chosen basis set.

- The considered quantity. Different quantities like geometries, vibrational frequencies or atomization energies are not reproduced with the same accuracy by a specific method (c.f. section 5.3.1.1).

Nevertheless one can give as a rule of thumb, that the more elaborate a method is, the more reasonable the results should be.

Methods like the Hartree–Fock (HF), Møller–Plesset perturbation theory of N–th order (MPN), or the density functional theory (DFT) provide a suitable quantum mechanical description of atoms, molecules, clusters or even solids. They are all based on an approximate solution of the Schrödinger equation and mostly yield comparable results as it is e.g. discussed for the Al_4O_4 cluster by Chang et al. (2000). It is generally accepted, that density functional theory is the method of choice to achieve a reliable level of accuracy at lowest cost (Cramer, 2002). The discussion in section 5.3.1.1 will validate this. Thus, density functional methods represent a suitable method to investigate the physical and chemical properties of clusters, since they allow the treatment of aggregates with a huge number[3] of atoms.

[3]Chang et al. (2001b) for example studied semiconductor clusters with up to 120 atoms.

Even larger particles can be treated by means of empirical force fields. This concept is a direct consequence of the Born–Oppenheimer approximation: The potential energy Φ of a molecule or cluster is calculated as a function of the coordinates $\vec{\mathbf{r}}_i$ of the N atoms in the cluster[4]. One usually decomposes this energy into a sum of n-body interactions (Erkoç, 1997):

$$\Phi(\vec{\mathbf{R}}) = \Phi(\vec{\mathbf{r}}_i, \vec{\mathbf{r}}_2, \ldots, \vec{\mathbf{r}}_N) = \varphi_2 + \varphi_3 + \cdots + \varphi_n + \cdots \tag{3.4}$$

with:

$$\varphi_2 = \sum_{i<j} \phi_2(\vec{\mathbf{r}}_i, \vec{\mathbf{r}}_j) \tag{3.5}$$

$$\varphi_3 = \sum_{i<j<k} \phi_3(\vec{\mathbf{r}}_i, \vec{\mathbf{r}}_j, \vec{\mathbf{r}_\mathbf{k}}) \tag{3.6}$$

$$\vdots$$

$$\varphi_n = \sum_{i<j<\ldots<n} \phi_n(\vec{\mathbf{r}}_i, \vec{\mathbf{r}}_j, \ldots, \vec{\mathbf{r}_\mathbf{n}}) \tag{3.7}$$

where ϕ_2, ϕ_3, ϕ_n represent two–, three–, and n–body interactions, respectively. In most cases this many–body expansion of Φ converges quickly, and terms of higher order can be neglected. Most empirical force fields are restricted solely to two–body interactions with a view exceptions, which also take three–body interactions into account (Erkoç, 1997).

The choice of the functional form used for the different interaction terms is a non–trivial problem, which requires sufficient informations about the physical and chemical nature of the bond. The necessary parameterisation of these functions is achieved by a general least–square fit, where different types of data (e.g. experimental, theoretical data for molecules or solids) can be used to determine the quality of the fit (Cramer, 2002, Gastreich, 2001). The quality of the results obtained by such force fields depends next to the elaborateness of the fit procedure also on the considered system. In some cases, as e.g. the simulation of proteins in aqueous solutions, such force fields are currently the only possibility to perform such investigations (Leach, 2001).

Regardless, whether the energy of a cluster is computed by means of *ab initio* methods or empirical force fields, the problem in both cases is aggravated by the necessity to locate its *ground state*, i.e. the global minimum on the potential energy surface. While for small and organic molecules chemistry provides models, allowing the construction of structures, which nearly represent its ground state, such principles are (mostly) unknown for clusters (see e.g. Hartke, 2002). Although some rules of thumb can be derived, they do not guarantee to construct the ground state configuration (c.f. the discussion section 3.2 and 5.3.2). The closely connected problem of global optimization will be discussed in 4.2.

Cluster size equations circumvent this problem, because they provide an analytic formula, which allows the calculation of a generic cluster property $\mathcal{G}$ as a function of the

[4]Throughout this thesis we use the following convention: The 3-dimensional vector of the Cartesian coordinates of the i–th atom in cluster is denoted as $\vec{\mathbf{r}}_i$, whereas the $3 \times N$ dimensional vector of the coordinates of all atoms, the configuration, is written as $\vec{\mathbf{R}}$.

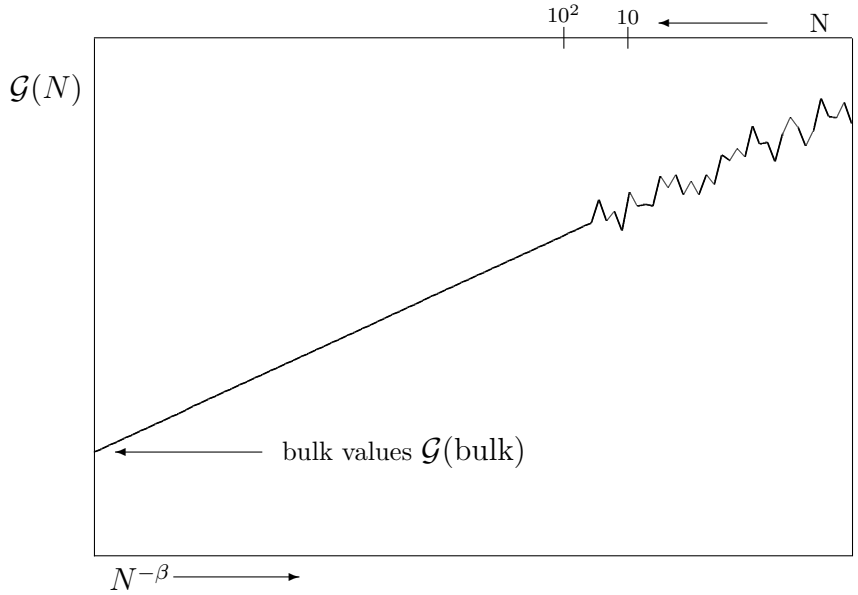

Figure 3.3: Schematic illustration of the size–dependence of a cluster property, plotted as a function of $N^{-\beta}$. The figure has been adopted from Jortner (1992)

cluster size N. In the large cluster regime ($N > 10^4$) many such properties like the ionization potential I_p or the cohesive energy E_{coh}, show a smooth, regular variation with the cluster size. Due to quantum and surface effects, $\mathcal{G}(N)$ exhibits for small cluster sizes a irregular or oscillating curve (c.f. fig. 3.3). A general *ansatz* for a cluster size equation is (Müller et al., 1995):

$$\mathcal{G}(N) = c_0 + c_1\ N^{-1/3} + c_2\ N^{-2/3} + \ldots \tag{3.8}$$

The dependence on $N^{-1/3}$ is motivated by the fact, that most properties depend on the ratio F_s of surface to volume atoms, which is proportional to $N^{-1/3}$. Since for $N \to \infty$, equation (3.8) has to reproduce the bulk value, it follows that:

$$c_0 = \lim_{N\to\infty} \mathcal{G}(N) = \mathcal{G}(\text{bulk}) \tag{3.9}$$

In most cases only the first two terms in equation (3.8) are considered, which means, that the parameter c_1 is given by:

$$c_1 = \Big(\mathcal{G}(\widehat{N}) - \mathcal{G}(\text{bulk})\Big)\ \widehat{N}^{1/3} \tag{3.10}$$

where $\widehat{N}$ is a cluster size, for which the property $\mathcal{G}$ is also known. Thus, the knowledge of $\mathcal{G}$ for the bulk and for a cluster with $\widehat{N}$ atoms, provides a simple interpolation formula, which in some cases describes the general trend of the data astonishingly well (see Müller et al., 1995, for some examples). On the other hand, if $\mathcal{G}$ is known for more then one cluster size, one might determine either one or both parameters by a least square fit.

The size dependence of the cohesive energy E_{coh} (for a definition see page 31) is often expressed by the following equation (Bachels & Schäfer, 2000):

$$E_{coh}(N) = E_{coh}(\text{bulk}) - 4\,\pi\,r_w^2\,\widetilde{\sigma}\,N^{-1/3} \tag{3.11}$$

where r_w is the Wigner–Seitz radius $r_w = (3\,m)/(4\,\pi\,\rho)^{1/3}$ (m the mass of the monomer and ρ the density of the solid). The parameter $\widetilde{\sigma}$ has the physical meaning of a surface tension. For large clusters, which have a spherical geometry this interpretation of $\widetilde{\sigma}$ is comprehensible. On the other hand, for small clusters, with only a few atoms, it is not possible to identify a surface, and hence this interpretation becomes a little bit imprecise. Thus, in order to emphasise, that $\widetilde{\sigma}$ is mainly a parameter, we use the notation $\widetilde{\sigma}$ instead of the usually used σ.

3.2 Lennard–Jones clusters

Lennard–Jones clusters represent a classical prototypical system for studying the properties of potential energy surfaces (see e.g. the review articles by Berrry, 1993; or Berry, 1996). It is beyond the scope of this section to give a complete overview over all features and properties of this well studied system, as there exists a vast amount of literature (e.g. Honeycutt & Andersen, 1987, Amon & Reinhardt, 2000, ten Wolde et al., 1999, Moore & Al-Quraishi, 2000, Neirotti et al., 2000, Frantz, 2001, and references therein). Here we only want to review some basic facts, which are important in the context of this thesis. In view of the problem of finding the lowest energy configuration (see next chapter), we confine the discussion here to the minima of the potential energy surface and omit any dynamical aspects, which are discussed e.g. in Garzón et al. (1989), Salian et al. (1996), Doye & Wales (2002), and some papers of Berry and coworkers (e.g. Kunz & Berry, 1993, 1994, 1995).

Lennard–Jones clusters are bound by a potential energy function which was first proposed by Lennard-Jones (1924) to explain the experimental temperature variation of viscosity in gases (see Torrens, 1972, chapter 4 for details). The original expression for the potential energy function reads as follows:

$$\phi(r_{ij}) = \varepsilon\left(\frac{\sigma_n}{r_{ij}^n} - \frac{\sigma_m}{r_{ij}^m}\right) \tag{3.12}$$

but the most commonly used form is the (6-12) Lennard-Jones potential, where $n = 12$ and $m = 6$. The potential energy of a cluster, consisting of N atoms bound by the Lennard–Jones potential is given by:

$$\Phi_{\text{LJ}}(N) = 4\,\varepsilon\,\sum_{i<j}^{N}\left\{\left(\frac{\sigma}{r_{ij}}\right)^{12} - \left(\frac{\sigma}{r_{ij}}\right)^{6}\right\} \tag{3.13}$$

where $2^{1/6}\,\sigma$ is the pair equilibrium distance and ε is the pair equilibrium well depth. In most cases reduced units are employed, i. e. $\varepsilon = \sigma = 1$. Equations for the gradient and the Hessian matrix can be found in appendix (A.3)

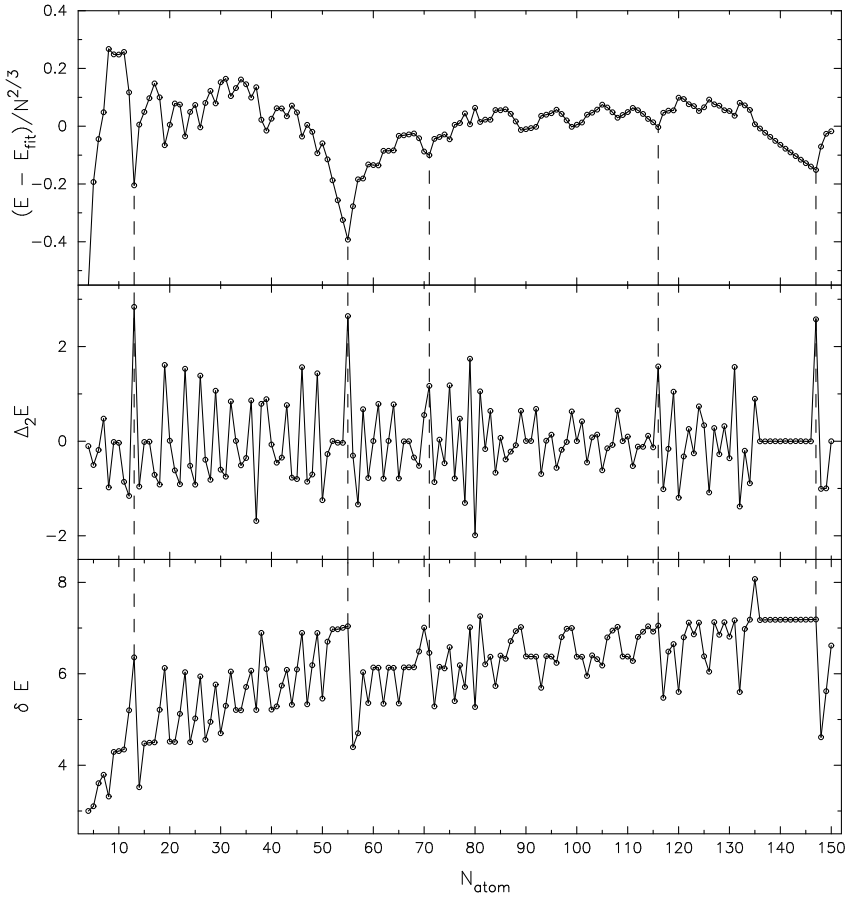

Figure 3.4: Binding energy of Lennard–Jones clusters LJ_N (N = 3 - 150). The lower panel shows the *first energy difference* δE (cf. Eq. 3.14). The *second energy difference* (3.16) is plotted in the middle panel, while in the upper panel the deviation of the potential energy from a fit defined by equation (3.18) is depicted (normalised to remove the nonspecific size dependence). The dashed lines mark the following cluster sizes: 13, 55, 71, 116 and 147.

Generally any van der Waals like interaction, especially between rare gas atoms, can be described using this potential energy function (see e.g. Leach, 2001, Haberland, 1995b). Values for the parameters ε and σ for various substances like Ar, Ne or Xe can be found in Hirschfelder et al. (1954).

3.2.1 Energetic and structural aspects of Lennard–Jones clusters

A complete list of putative global minima for Lennard–Jones clusters containing up to 150 atoms, can be found in the *Cambridge Cluster Database* (Wales et al., 2002). The data presented there are a compilation from various sources. As Lennard–Jones clusters serve as a popular test case for global optimization, some of these publications will be

mentioned, when the problem of global minimization is discussed in section 4.2. A few examples for possible global minima structures of larger cluster (up to 309) have been reported by Barrón et al. (1999)[5]. Using the data published by Wales et al. (2002) for the potential energy $\Phi_{\mathrm{rLJ}}(N)$ of Lennard–Jones clusters, we first discuss the stability of theses aggregates. As the function Φ_{rLJ} decreases monotonically, it is difficult to infer anything about the enhanced stability of certain cluster sizes, which might be observable in mass spectroscopic investigations as *magic numbers*. One of the first mass spectra of argon clusters was presented by Harris et al. (1984). They observed, that the fine structure of the spectrum is nearly proportional to the first energy difference[6], defined as:

$$\delta E(N) = \Phi_{\mathrm{rLJ}}(N) - \Phi_{\mathrm{rLJ}}(N-1) \tag{3.14}$$

which is plotted in the lower panel of figure 3.4. For example the peaks at $N = 13, 49$, and 55 in the $\delta E(N)$–curve correspond to peaks in the mass spectrum of Harris et al. (1984). Some of the peaks can be explained in terms of geometric shell closures. The dominant structural motive of Lennard–Jones clusters are icosahedral based configurations (see e.g. Johnston, 2002, p. 39 ff). Complete icosahedra with K shells exist for clusters, containing I_K atoms, where the *icosahedral numbers* I_k are given by Smirnov (1999, p. 123f):

$$I_K = \frac{1}{3}\left(10\,K^3 + 15\,K^2 + 11\,K + 3\right), \tag{3.15}$$

which explain the peaks at $N = 13$ ($K = 1$), $N = 55$ ($K = 2$), and $N = 147$ ($K = 3$). These numbers are marked with a dashed line in figure 3.4 and the structures are shown in figure (3.5). Note however, that the details of the mass spectra depend on the experimental conditions used to generate the clusters (see e.g. Johnston, 2002, for an overview). Thus it is not guaranteed, that the observed magic numbers arise solely due to the size–dependence of the binding energy of rare gas cluster cations.

Another indicator for the stability of clusters was introduced by Clemenger (1985) in order to explain the magic numbers in the mass spectra of sodium clusters. He defined the *second energy difference* $\Delta_2 E$ as follows:

$$\begin{aligned} \Delta_2 E(N) &= \delta E(N+1) - \delta E(N) \\ &= \Phi_{\mathrm{rLJ}}(N+1) + \Phi_{\mathrm{rLJ}}(N-1) - 2\,\Phi_{\mathrm{rLJ}}(N) \end{aligned} \tag{3.16}$$

The middle panel of figure 3.4 depicts this quantity for Lennard–Jones clusters. In order to interpret the physical meaning of the second energy difference it is useful to consider the successive evaporation of an atom from a cluster with $N + 1$ atoms, viz:

$$\mathrm{LJ}_{N+1} \xrightarrow[\delta E(N+1)]{\text{evaporation of an atom}} \mathrm{LJ}_N \xrightarrow[\delta E(N)]{\text{evaporation of an atom}} \mathrm{LJ}_{N-1} \quad \cdots \tag{3.17}$$

[5]For a visualization of the structures see `http://www.vcl.uh.edu/~cbarron/LJ_cluster/researchpot.html`

[6]Harris et al. (1984) use the term successive binding energy difference.

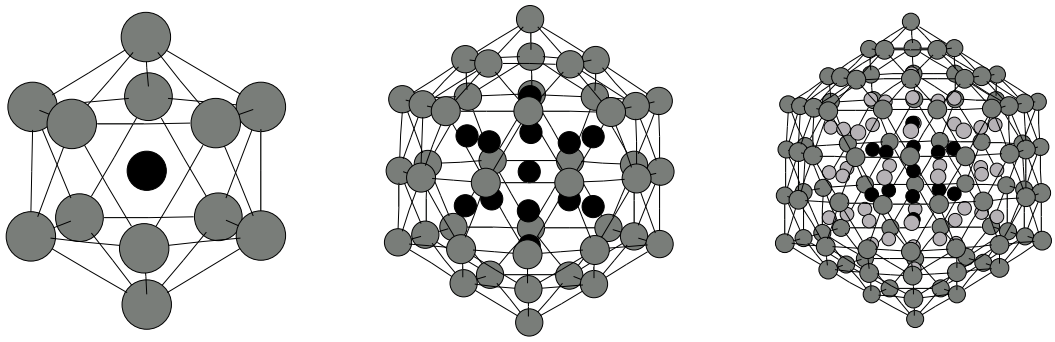

LJ_{13} LJ_{55} LJ_{147}

Figure 3.5: Structures of the first three complete Lennard–Jones icosahedra. All configurations have I_h symmetry. For clearness the inner atoms have been plotted in different colours. The 42 surface atoms of LJ_{55} enclose the icosahedron of the LJ_{13}–cluster (plotted in black). For the LJ_{147}–cluster one can discern an inner most icosahedron with 13 atoms, plotted in black, and as the next shell the 42 surface atoms of a LJ_{55}–cluster, plotted in light grey. On the surface of this cluster 92 atoms are situated.

At each step one requires $\delta E(N)$ to remove an atom from an N–mer . If $\Delta_2 E(N) > 0$, it is energetically more favourable to form an N–mer by removing one atom from the LJ_{N+1}–cluster, then to proceed further in the evaporation sequence. As can be seen in figure 3.4 some of the peaks of the $\Delta_2 E$ curve are more pronounced than in the $\delta E(N)$ curve (e.g. for LJ_{55}). Additionally some peaks appear, which are observable also in the mass spectrum, but not in the plot of the binding energy difference δE, e.g. for $N = 71$. The enhanced stability of this cluster can be explained by the closure of subshells, while filling the third icosahedral shell (see Sugano & Koizumi, 1998, p. 151ff for details).

A last method to analyse the size dependence of the potential energy of Lennard–Jones clusters is to fit $E(N)$ using a polynomial in $N^{1/3}$:

$$E_{\text{fit}}(N) = a\,N + b\,N^{2/3} + c\,N^{1/3} + d \tag{3.18}$$

$$a = -9.667361 \qquad b = 26.017789 \quad c = -39.115640 \qquad d = 30.608246$$

and measure the deviation $E(N) - E_{\text{fit}}(N)$ from this *general trend*. Cluster sizes, for which this difference is negative are more stable than could be expected from this trend[7]. The plot of this quantity in the upper panel of figure 3.4 reveals some further interesting aspects of the discussed size dependence of the potential energy $E(N)$. First of all it becomes apparent, that the complete icosahedra at $N = 13, 55$ and 147 exhibit an exceptional stability compared to other cluster sizes as it can be seen from the deep drops in the curve. The increase in the energy after $N = 13$ is due to the addition of another layer

[7]Doye & Calvo (2002) use a similar approach by considering the deviation of $E(N)$ from an interpolation formula through the energies of the four complete icosahedra at $N = 13, 55, 147$ and 309.

to the complete 13–atom icosahedron. As this overlayer is almost complete, the energy decreases again and reaches at another minimum $N = 55$ (see also figure 3.5). The smaller features (e.g. at $N = 19$) arise from the formation of particularly stable overlayers with no low–coordinate atoms (Doye et al., 1999a; and Sugano & Koizumi, 1998). The same trend is observed between the second and third complete icosahedra ($N = 55$ and 149, respectively).

As already mentioned, most Lennard–Jones clusters have structures, which are based on the so called Mackay icosahedra. This observation was utilised by Northby (1987) in his pioneering work in order to determine the ground state structures of Lennard–Jones clusters. However there exist some notable exceptions from this general rule, which have been found since then. The first one occurs at $N = 38$, where the global minimum is a face–centred–cubic truncated octahedron with O_h symmetry (see figure 3.6(a)), first found by Pillardy & Piela (1995) and Doye et al. (1995). The second lowest minium represents an incomplete Mackay icosahedron (see figure 3.6(b)), first found by Deaven et al. (1996). The other thirteen exceptions are the icosahedral structures with incomplete core (found

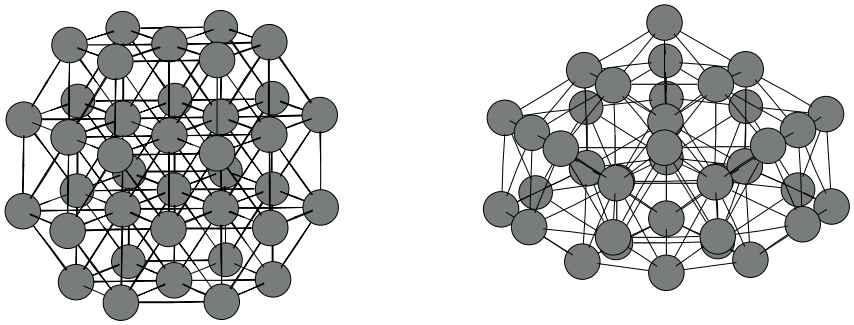

(a) FCC LJ_{38} structure (b) Icosahedral LJ_{38} structure

Figure 3.6: The two lowest energy structures of the LJ_{38} cluster. The energies of the two structures are $-173.928427\,\varepsilon$, and $-173.252378\,\varepsilon$, respectively. The difference is only 0.676049, which is $\approx 0.4\%$ of the ground state energy.

for $N = 69, 78, 88, 107, 113$, and 115), the Marks decahedral structures for $N = 75 - 77$ and $N = 102 - 104$, and the Leary tetrahedron found only recently by Leary & Doye (1999). Since most of these non-icosahedral minima are difficult to find by (unbiased) global optimization algorithms, they serve as popular test cases (see section 4.2). The reasons for these difficulties will be mentioned briefly in the next section.

Furthermore, icosahedral–based structures possess a five-fold symmetry axis. Such pentagonal symmetries are impossible for the infinite lattice of the solid state, because one

cannot construct a complete filling of the space with such a symmetry. Hence five–fold symmetry is restricted to the cluster regime, where it is ubiquitous with some remarkable exceptions as discussed above. For the Lennard–Jones system the transition form icosahedral based structures to FCC based structures of the bulk system occurs in the range between $N = 1000$ and $N = 10.000$. The concrete value depends on the theoretical and experimental methods (see e.g. Northby et al., 1989; Haberland, 1995b; or Doye & Calvo, 2002 and references therein) used to ascertain it.

3.2.2 The roughness of the potential energy surface

Another important characteristic of a potential energy surface is its *roughness*. Although this concept might be quite intuitive, if one thinks of a *landscape* with hills (transition states) and valleys (local minima with their basins of attraction), its not straightforward to quantify this conception. A first *ansatz* might be, to simply count the number of minima and transition states, which would imply, that all minima have been found. Tsai & Jordan (1993) demonstrated that this task becomes already intractable for quite small clusters. The number of local minima and first order transition states found by Tsai & Jordan are summarised in table 3.1 together with the results of a more exhaustive search by Doye & Wales (2002). Based on theoretical considerations (Stillinger & Weber, 1983, Stillinger, 1999), one expects the number of local minima in an N–cluster to increase exponential with the number of atoms. Since the data given in table 3.1 confirm this, the number of local minima n_{min}, has been fitted using an exponential function:

$$n_{min} = \beta \exp(\alpha N) \qquad \text{with } \beta = 0.0012 \quad \text{and } \alpha = 1.078 \tag{3.19}$$

The extrapolated numbers of local minima for some exemplary cluster sizes are given in the last row of table 3.1. It is obvious, that the vast amount of local minima for clusters of even moderate size, makes the location of the lowest energy structure a formidable task, like finding the proverbial needle in a haystack. Assume, as an example, one had an algorithm at hand, which for a given cluster size N constructs a list of *all* configurations representing a local minimum and computes its potential energy. Assume further, one could have started the computation right after the Big Bang, approximately $4.7 \cdot 10^{17}$ seconds ago. For the LJ_{100} cluster with an estimated number of $8.0 \cdot 10^{43}$ local minima, one had $\approx 6 \cdot 10^{-27}$ seconds time for constructing each structure and to calculate Φ. Since the latter depends on the distance of each atom i to all other atoms j ($j \neq i$), it requires at least the $N(N-1)/2 \approx 5000$ arithmetic operations, which reduces the time the computer may need for each floating point operation to $1.2 \cdot 10^{-30}$ seconds. In other words, one would have to build[8] a computer, which can perform approximately $1 \cdot 10^{30}$ floating point operations per second - a *mega-tera-teraflop* machine. For comparison: The fastest machine currently[9]

[8]The extremely short time scales occurring in such a kind of computer make it very unlikely that it is realisable.

[9]As at November, 2002. See `http://www.top500.org` for an up to date list of the 500 fastest supercomputers.

Table 3.1: Number of local minima and first order transition states of Lennard-Jones clusters. The data have been take from Tsai & Jordan (1993, TJ93) and Doye & Wales (2002, DW02), respectively. In order to illustrate, how fast the number of minima grows, some extrapolated values are given in the last row. Note, that the age of the universe is about $4.7 \cdot 10^{17}$ seconds!

cluster	LJ_4	LJ_5	LJ_6	LJ_7	LJ_8	LJ_9	LJ_{10}	LJ_{11}	LJ_{12}	LJ_{13}
					Number of minima					
TJ93	1	1	2	4	8	21	64	152	464	1328
DW02	1	1	2	4	8	21	64	170	515	1509
					Number of first order transition states					
TJ93				12	40	152	584	911	2803	8453
DW02	1	2	3	12	42	165	635	2424	8607	28 756
					Extrapolations using equation (3.19)					
cluster	LJ_{15}		LJ_{20}		LJ_{25}		LJ_{50}		LJ_{100}	LJ_{250}
	13 030		$2.9 \cdot 10^6$		$6.3 \cdot 10^8$		$3.2 \cdot 10^{20}$		$8.0 \cdot 10^{43}$	$1.3 \cdot 10^{114}$

existent is the *Earth Simulator* (Yokohama, Japan) with about 36 TFlops. The problem sketched above is severely aggravated by the fact, that an algorithms, which constructs a list of all structures representing local minima of a cluster is not at hand.

The demonstration given above is a modification of the *Levinthal's paradox* (see Levinthal, 1969), which is known in the context of protein folding and the problem, how to predict the native structure of a protein from its amino acid sequence. In this case as well the number of possible conformations is too big, to find the native state by a random search within reasonable time, i.e. the age of the universe. Paradoxically it can be demonstrated, that denaturated proteins in a test tube regain their native structure on laboratory time scales (see Wales, 2001, and references therein). As this paradox is closely connected with global optimization, we will come back to it in a following chapter.

Another more visually orientated method to examine the topography of the potential energy surface of a cluster or protein is the *disconnectivity graph* introduced by Becker & Karplus (1997) and further applied to Lennard–Jones clusters (Doye et al., 1999b), Morse clusters (Miller et al., 1999) and sodium chloride clusters (Doye & Wales, 1999a,b), just to state a few examples. More applications can be found in a recent review by Wales et al. (2000).

The construction of such a graph requires the knowledge of the minima of the potential energy surface and of the transition states, which connect two such minima. Methods used to locate the first kind of stationary points are extensively discussed in section 4.1. Since the methods discussed there are improper to locate transition states, one has to use other methods like the eigenvector following technique developed by Cerjan & Miller (1981).

Two examples for the 38-atom and the 55-atom Lennard–Jones cluster are reproduced

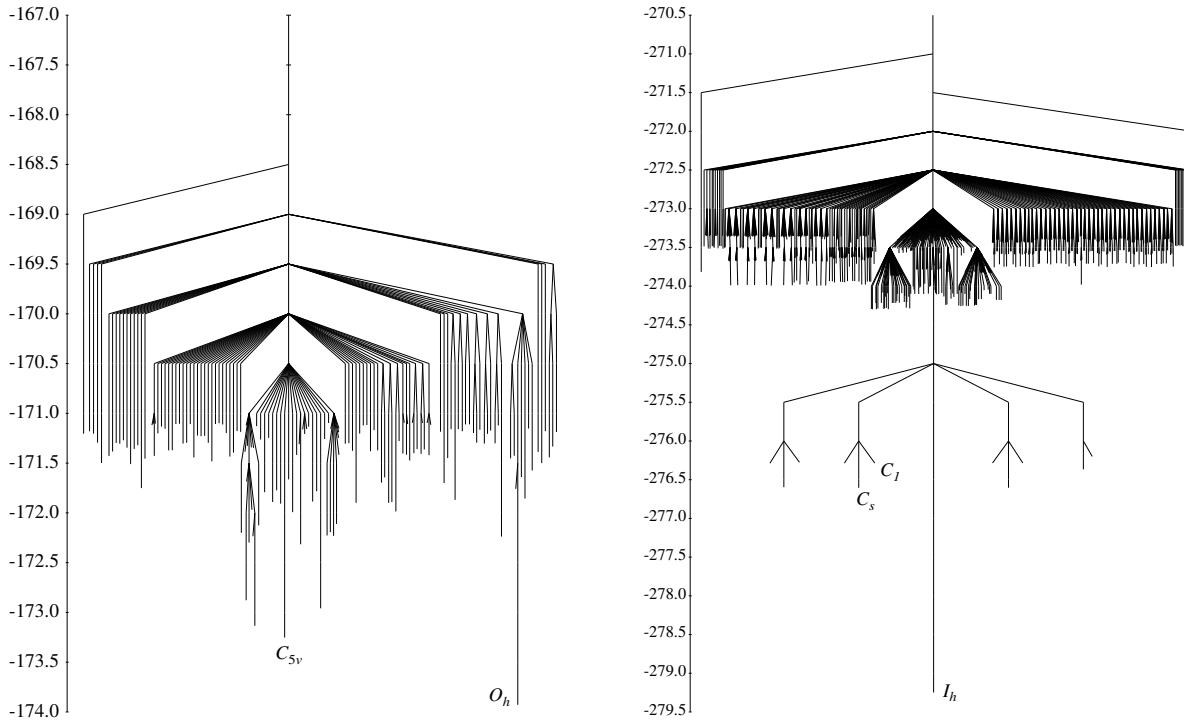

(a) LJ_{38} (b) LJ_{55}

Figure 3.7: Disconnectivity graphs for LJ_{38} and LJ_{55}. The graph for LJ_{38} has been taken from Doye et al. (1999b) and uses a sample with 6000 minima and 8633 transition states. For clarity only 150 minima are shown. For the graph of the LJ_{55} cluster (taken from Doye et al., 1999a) a sample with 6000 minima and 13125 transition states has been used. Only the 900 lowest minima are represented. Note, that these samples are far from being complete.

in figure 3.7. Using a sample of local minima and related transition states, connecting these minima, a disconnectivity graph is constructed as follows: At a given total energy one has to determine, which minima are connected by pathways that lie below that specific energy. At a finite energy value the minima are thus divided into disjoint sets of mutually accessible structures, separated by insurmountable barriers. Now one increases the energy in regular steps along a vertical axis. While the vertical height of the beginning of the lines is determined by the energy at the bottom of the corresponding well, the horizontal placement of the lines can be chosen arbitrarily to give a clear representation. Two lines are joined by a node at an energy, for which both minima become mutually accessible. In other words, the vertical position of the nodes approximately corresponds to the energy of the (lowest) transition state, connecting two minima or two sets of minima. Since graphs constructed in this way contain no cycles, they are called *trees* (Wales et al., 1998), for

reasons which are apparent from figure 3.7.

The disconnectivity graph of LJ_{38} has an archetypal[10] double funnel. One funnel is associated with the global minimum, the face-centred-cubic truncated octahedron (O_h) shown in figure 3.6(a). The other, centrally placed funnel, belongs to the energetically second lowest structure, the icosahedral minimum depicted in figure 3.6(b). As is evident from figure 3.7, the funnel associated with the icosahedral minimum is much larger, than that of the fcc minimum. Doye et al. (1999b) specify, that 446 minima in the sample used to construct the graph in figure 3.7, belong to the icosahedral funnel, while only 28, i.e. an order of magnitude fewer, minima belong to the fcc funnel. For a detailed discussion of the potential energy surface of the LJ_{38}–cluster the interested reader might refer to the already mentioned article by Doye et al. (1999b). The Lennard–Jones cluster with 75 atoms is another example of a disconnectivity tree with two funnels (Doye et al., 1999a).

The most striking difference between the disconnectivity graphs of LJ_{38} and LJ_{55} is the existence of a single funnel in the latter case. Another interesting feature is the separation of the minima into bands, which is due to different numbers and types of defects in the Mackay icosahedron (Doye et al., 1999a). The first band above the global minimum at about $-276.0\ \varepsilon$ includes all minima with a missing vertex and an atom on the surface. The second band at $\approx -274.3\ \varepsilon$ consists of those Mackay icosahedra, which have two missing vertices and two adatoms. The connection of these features with the dynamics of the cluster are investigated in Doye & Wales (1995).

Although in both graphs only a cut-out of all minima and transition states in the sample is plotted, it is discernible, that the density of branch–ends is rapidly increasing as the energy rises past $-171.5\ \varepsilon$ for LJ_{38} and $-274.5\ \varepsilon$ for LJ_{55}, respectively. The fact that the number of states available to the cluster increases as the energy becomes large, is usually interpreted as the onset of the liquid–like part of the potential energy surface (Doye et al., 1999b). It is noteworthy for the problem of global optimization, that in the case of the 38–atom Lennard-Jones cluster, the system *must* enter this part of the configuration space in order to pass between the two distinct funnels, that of the icosahedra–based structures and that of the fcc–like structures.

Since both clusters serve as prototypes for the problem of global optimization, we will refer to the topology of the underlying potential energy surfaces discussed here in section 4.2 again.

[10]For a illustration of further archetypal graphs like the *weeping willow* or the *banyan tree* see Wales et al. (1998).

3.3 Thermodynamic properties

Once the basic molecular properties (i.e. the geometry, the vibrational frequencies, the dissociation energy) are known either from experiment or *ab initio* calculation, it is possible to calculate the thermodynamic properties needed by means of the molecular partition function $Q(T, V)$. As the necessary equations and basic assumptions have been discussed in detail elsewhere (e.g. John, 1995, Patzer, 1998, Jeong, 2000) or can be found in each textbook about thermodynamics (e.g. Lewis & Randall, 1961, Mayer & Mayer, 1977, Landau & Lifschitz, 1987, Diu et al., 1994) or physical chemistry (Atkins, 1989, Berry et al., 2000), we only give a short summary of the necessary expressions.

3.3.1 Some remarks about energies

Before discussing the partition function it is beneficial to introduce the energy scale and to clarify some terms used in what follows. Figure 3.8 gives a sketch of the potential energy curve of a diatomic molecule. Mostly the ground states of the neutral atoms at infinite separation define the zero point of the energy scale. The depth of the potential energy well measured with respect to this point is often called *equilibrium dissociation energy* (Levine,

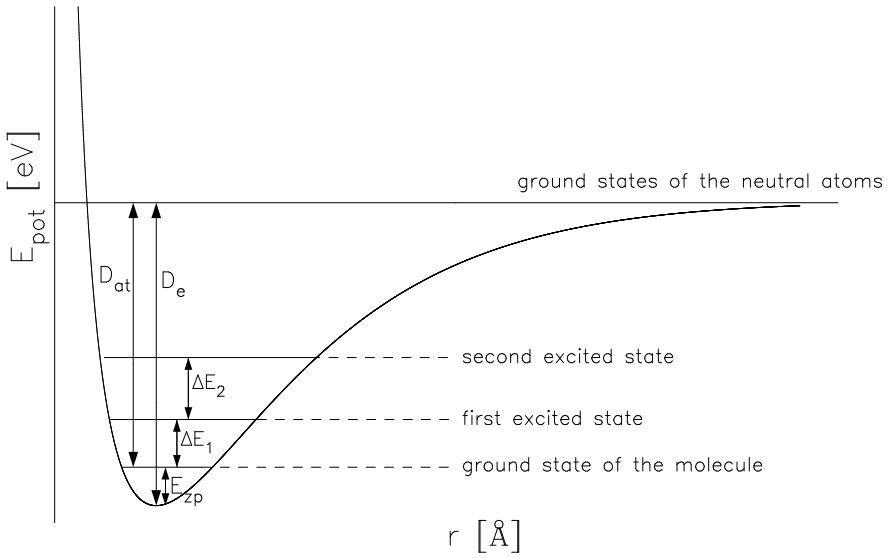

Figure 3.8: Definition of the energy scale.

2000) or *bond dissociation energy* (Atkins, 1989). It is denoted with D_e in figure 3.8 and can be calculated by *ab initio* methods according to:

$$D_e = \left(\sum_{j=\text{atoms}} \nu_j \, E_{tot}(\text{El}_j) \right) - E_{tot}(\text{molecule}) \tag{3.20}$$

where ν_j is the number of atoms El_j in the cluster or molecule. For the sake of brevity we shall call D_e *bond* or *binding energy*. While this quantity is of purely theoretical nature

and cannot be measured by experiments, the *dissociation energy* D_0 of diatomic molecules is indeed accessible by experimental methods. It differs from bond dissociation energy D_e by the *zero point vibrational energy* E_{zp}:

$$E_{zp} = \frac{1}{2} \sum_{i=1}^{f_{vib}} h\,\nu_i \tag{3.21}$$

where f_{vib} is the number of vibrational degrees of freedom, and ν_i is the frequency of the i–th vibrational mode.

For larger molecules or clusters one can often measure the energy required to dissociate the aggregate into certain parts or sub-units. Loh et al. (1989) e.g. investigated the collision induced dissociation of Fe_N^+–clusters (see also Loh et al., 1988, Lian et al., 1992). The authors give the energy $D_0(Fe_{N-1}^+ - Fe)$ required to remove one neutral iron atom from a positively charge Fe_N–cluster. Combined with the ionization energy of Fe_N clusters (taken e.g. from Rohlfing et al., 1984; or Yang & Knickelbein, 1990) it is possible to calculate the dissociation energy $D_0(Fe_N - Fe)$ for neutral iron clusters. As further demonstrated in John (1995) one can use these data to calculate the energy required to dissociation a Fe_N cluster completely into N atoms:

$$D_{at} = \sum_{m=1}^{N-1} D_0(Fe_m - Fe) \tag{3.22}$$

which is consequently called *atomization energy*. For a diatomic molecule the dissociation energy is equivalent to the atomization energy. While the atomization energy is not directly inferable from experiment for molecules containing more then 2 atoms, it can be calculated either using equation (3.22) or by means of:

$$D_{at} = D_e - E_{zp} \tag{3.23}$$

from electronic structure calculations. Unfortunately there seems to be no common use of the different terms for the energies within the literature. Jeong (2000) e.g. uses the term *atomization energy* for what is called here *binding energy* and vice versa. But since we think, that the *atomization* of a cluster, i.e. its decomposition into its constituting atoms, is a real physical process, which could be realised by experimental methods, we use the nomenclature as described above.

As one is often interested in the emergence of bulk properties when clusters are studied, it is useful to monitor the atomization energy per atom, called *cohesive energy* E_{coh}

$$E_{coh} = \frac{D_{at}}{N}, \tag{3.24}$$

which converges for $N \to \infty$ to the corresponding bulk value (see e.g. Bréchignac, 1995).

Finally we note, that the *atomization enthalpy* $\Delta_{at}H$ is simply the atomization energy D_{at} expressed in units of $\mathrm{kJ\,mol^{-1}}$, viz.:

$$\Delta_{at}H[\mathrm{kJ\,mol^{-1}}] = \frac{N_A\ e}{1000}\ D_{at}[\mathrm{eV/atom}] = 96.485307\ D_{at}[\mathrm{eV/atom}] \tag{3.25}$$

where N_A is the Avogadro constant, and e the elementary charge[11].

3.3.2 Basic equations - the partition function

The *molecular* partition function Q represents the connection between the microscopic properties of a molecule or cluster and its macroscopic thermodynamic quantities, like the Gibbs free energy of formation $\Delta_f G^{\ominus}$ or the entropie $S^{\ominus}$. The starting point for all further exemplifications is the following definition of the canonical partition function Q:

$$Q(T,V) = \sum_i \; g_i \exp\left(-\frac{E_i}{kT}\right) \tag{3.26}$$

where g_i is the statistical weight of the i–th (quantum) state with energy E_i. In order to evaluate equation (3.26) one would have to compute all states of by solving the Schrödinger equation, which of course is out of reach for most molecules (for an exception see e.g. Jørgensen & Larsson, 1990). Instead of this one has to make certain assumptions, in order to simplify the problem. First of all one separates the energy E_i into four different contributions for each degree of freedom, namely the translational energy E_{tr}, the electronic energy E_{el}, the vibrational energy E_{vib}, and the rotational energy E_{rot}. Besides the translational energy, which is always independent from the so called *internal motions* of the molecule, this separation is an assumption, which is justified by the Born–Oppenheimer approximation. As the energy of the i–th state is written as:

$$E_i = E^i_{tr} + \underbrace{E^i_{elec} + E^i_{vib} + E^i_{rot}}_{E^i_{int}} \tag{3.27}$$

it follows for the partition function:

$$Q(T,V) = Q_{tr}(T,V) \sum_i \; Q^i_{elec}(T)\; Q^i_{vib}(T)\; Q^i_{rot}(T) \tag{3.28}$$

where the rotational, vibrational, and electronic partition function depend on the spectroscopic constants of the i–th –state of the molecule. As a consequence one now can calculate the molecular partition function for each degree of freedom separately.

Since one is interested in the thermochemical properties of a gas consisting of $N_A \approx 6 \cdot 10^{23}$ particles, one has to calculate the partition function Q_{ens} of an ensemble of the appropriate number of particles. As the particles are indistinguishable one gets the following expression, which connects the partition function of a (one-component) gas with the molecular partition function:

$$Q_{ens}(T,V,N_A) = \frac{Q(T,V)^{N_A}}{N_A!} \tag{3.29}$$

[11] The product $N_A\, e$ is also known as Faraday constant F.

It is noteworthy, that equation (3.29) is only valid for *weakly* interacting particles, which means, that the interaction energy of two particles is small compared to the other energy terms. This assumption is generally justified in the temperature and pressure range considered here.

The explicit formulas for the different contributions to the partition function discussed in the following sections are all obtained in the same way. One first has to derive an expression for the energy of the degree of freedom under consideration. Under certain assumptions one then can transform the sum in equation (3.26) into an analytic formula, which can be easily evaluated, if the necessary molecular data are given.

3.3.2.1 The translational partition function

The translational partition function can be treated either classically or quantum mechanically (see Reif, 1987, p. 282ff and p. 423ff, respectively). Under the assumption that the mean free pathway of the particle is much larger than its de Broglie wavelength, one finds for the translational partition function of a particle in a box with volume V:

$$Q_{trans}(T,V) = V\left(\frac{2\pi\, m\, k\, T}{h^2}\right)^{3/2} \tag{3.30}$$

Here m is the mass of the molecule. As discussed in John (1995), the mentioned condition is fulfilled over a broad range of pressure and temperature.

As one refers for practical applications to a specific standard state, one has to choose the volume in equation (3.30) appropriately. Since one considers 1 mol with N_A (Avogadro's number) particles, it is consistent to identify V with the molar volume $V^{\ominus}_{mol}$:

$$V^{\ominus}_{mol} = \frac{N_A\, k\, T}{p^{\ominus}} \tag{3.31}$$

where $p^{\ominus} = 1$ bar is the standard pressure[12].

3.3.2.2 The rotational partition function

For the calculation of the rotational partition function it is convenient to start with an expression for the energy of a diatomic quantum mechanical *rigid-rotor*. The latter one means, that the equilibrium distance r_e is assumed to be constant and any coupling between rotational and vibrational motions is neglected. In this case the solution of the Schrödinger equations yields the following energy values for the rigid-rotor:

$$E_{rot} = j\,(j+1)\,\frac{h^2}{8\,\pi^2\, I} \tag{3.32}$$

where j is the rotational quantum number, taking only integer values. The moment of inertia I can be calculated from the geometry of the molecule or it can be deduced from

[12]Some older publications (e.g. Stull & Prophet, 1971) use 1 atm = 1.01325 bar as the standard pressure.

spectroscopic experiments by means of the molecular rotational constant B:

$$B = \frac{h}{8\,\pi^2\,I} \tag{3.33}$$

mostly given in cm^{-1}. Finally one has to specify the degeneracy g_j of the rotational state:

$$g_j = 2\,j + 1 \tag{3.34}$$

Equations (3.32) and (3.34) have to be inserted into equation (3.26), which gives a sum over all positive integers for the quantum number j. As for most molecules the difference between the rotational energy levels are very small compared to the thermal energy[13] (Berry et al., 2000), it is possible to replace the sum in equation (3.26) by an integral over all energy levels. This leads to:

$$Q_{rot} = \frac{8\,\pi^2\,k\,T}{\sigma\,h^2}\;I = \left(\frac{k\,T}{h}\right)\;\frac{1}{\sigma\,B} \tag{3.35}$$

where the rotational symmetry number σ accounts for the fact, that indistinguishable orientations of the molecule in space are repeatedly counted. It is defined as the number of pure rotations, that transform the molecule into itself. Symmetry numbers for the relevant points groups are given in table (C.1) in appendix C.

A generalisation for the case of non–linear molecules can be found in Landau & Lifschitz (1987). One finds for this case the following expression:

$$Q_{rot} = \frac{(8\,\pi\,k\,T)^{3/2}}{\sigma\,h}\;\sqrt{\pi\;I_A\;I_B\;I_C} = \left(\frac{k\,T}{h}\right)^{3/2}\;\frac{1}{\sigma}\,\sqrt{\frac{\pi}{A\;B\;C}} \tag{3.36}$$

where I_A, I_B, and I_C are the principal moments of inertia of the molecule, with which the rotational constants A, B, and C are calculated using equation (3.33).

3.3.2.3 The vibrational partition function

As the atoms in a molecule or cluster oscillate around their equilibrium position one assumes, that each vibrational normal mode contributes independently to the thermodynamic functions. Each of these normal modes with a frequency ν_i is treated as *harmonic oscillator* with an energy which is given by:

$$E_{osc} = h\,\nu_i\;\left(n + \frac{1}{2}\right) \tag{3.37}$$

A linear molecule with N atoms has $f_{vib} = 3\,N - 5$ vibrational degrees of freedom, whereas a non–linear molecule has $3\,N - 6$. Using again the general definition of the partition function (c.f. Eq. 3.26), one obtains for the vibrational partition function:

$$Q_{vib} = \prod_{i=1}^{f_{vib}} \left(1 - \exp\left(-\frac{h\,\nu_i}{k\,T}\right)\right)^{-1} \tag{3.38}$$

[13] An exception are diatomic molecules containing hydrogen.

Here one assumes, that the zero point energy E_{zp} has been separated from the vibrational partition function and is contained in the dissociation energy.

The assumption, that each vibrational mode can be treated as a *harmonic oscillator*, and the molecule can be treated as a *rigid rotator* coined the name *rigid rotator harmonic oscillator* (RRHO) approximation for the introduced expressions. This approach is generally considered to be excellent at low temperatures (e.g. Lewis & Randall, 1961). But for higher temperatures the vibrations become anharmonic and the rotation non–rigid. Consequently one would have to use higher order approximations. These start with the following (empirical) expression for the energy levels of a diatomic molecule (see e.g. Lewis & Randall, 1961, p .430 ff):

$$\begin{aligned} E(n,J) \;=\; & \omega_e \left(n+\tfrac{1}{2}\right) && \text{| harmonic vibration} \\ & + B_e\, J(J+1) && \text{| rigid rotation} \\ & - x_e\, \omega_e \left(n+\tfrac{1}{2}\right)^2 && \text{| anharmonicity} \\ & - D_e\, J^2(J+1)^2 && \text{| centrifugal bond stretch} \\ & - \alpha_e\, n\, J(J+1) && \text{| rotation–vibration interaction} \end{aligned} \tag{3.39}$$

Here the first two terms are part of the common RRHO approximation. The next term arises from the deviation of the potential energy curve from the assumed ideal harmonic form. The vibrational *anharmonicity constant* $\omega_e\, x_e$ can be determined spectroscopically. The fourth correction term accounts for the stretch of the interatomic distance due to the centrifugal forces of rotation. For the corresponding centrifugal-force constant D_e it holds that (e.g. Mayer & Mayer, 1977, p. 187):

$$D_e = \frac{4\, B_e}{\omega_e}$$

If the interatomic forces are not harmonic, the mean distances between atoms might depend on the vibrational energy, which leads to the correction in the last term. The (first order) *rotation–vibration interaction* constant α_e is also determinable by spectroscopy.

The rather lengthy but straightforward evaluation of some additive correction terms Q_{cor} to the partition function is sketched in Lewis & Randall (1961, p.432 ff). Unfortunately the necessary data are mostly unknown for molecules, which are not yet listed in the JANAF tables. A computation by means of quantum mechanical *ab initio* methods is also rather difficult.

3.3.2.4 The electronic partition function

For most molecules the excitation energy ΔE_1 of the first electronic state is about 1 eV or higher. Thus for temperatures of about 3000 K or below, only the ground state is considerably populated and one might omit higher levels. If one defines the ground state of the particle as the zero point of the energy scale (see 3.3.1) one obtains for the electronic

partition function:

$$Q_{el} = \sum_{i=0} g_i \ \exp\left(-\frac{\Delta E_i}{k\,T}\right) = g_0 + \sum_{i=1} g_i \ \exp\left(-\frac{\Delta E_i}{k\,T}\right) \tag{3.40}$$

An exception are for example transition metals. As discussed in John (1995), the excitation energy of the first electronic state of the iron atom is $\Delta E_1 = 415.9\ \mathrm{cm}^{-1} = 0.052$ eV (Corliss & Sugar, 1982) and the condition $\Delta E_1 \gg k\,T$ is not fulfilled. For the Fe_2–molecule it was shown by Shim & Gingerich (1982), that the first excitation energy $\Delta E_1 \approx 0.007\,\mathrm{eV}$, which corresponds to an excitation temperature of about 80 K. In such a case the neglect of higher electronic state might lead to severe errors in the calculated thermodynamic data (see John, 1995, for an illustrative example). It should be noted, that different electronic states have, in general, different spectroscopic constants, which enter the calculation of the rotational and vibrational partition function. Thus one has to calculate Q_{rot} and Q_{vib} separately for each known electronic state using the previously discussed expressions (3.35) and (3.38). The total partition function is then obtained via equation (3.28).

3.3.3 Calculation of thermodynamic functions

By means of the partition function it is possible to calculate the thermodynamic data for a molecule or cluster. Here we adhered to the reference system of the JANAF tables (Chase, 1998) for an ideal gas at $p^{\ominus} = 1$ bar and $T_r = 298.15$ K. In order to evaluate the necessary data needed for the determination of the gas phase abundances of molecules and clusters, we additionally used auxiliary thermodynamic data for the elements from Chase (1998). Next a short recipe of the procedure used to calculate the thermochemical functions for molecules and clusters is presented:

1. Get the molecular data, namely the atomization energy D_{at} (or D_0 for diatomic molecules), the geometry, vibrational frequencies ω_e either from experiment or *ab initio* calculations.

2. Calculate the enthalpy of formation $\Delta_f H^{\ominus}$ at $T = 0$ K using the atomization enthalpy $\Delta_{at}H$ and the enthalpy of formation $\Delta_f H^{\ominus}(0\,\mathrm{K})$ of the neutral atoms:

$$\Delta_f H^{\ominus}(0\,\mathrm{K}) = \left\{ \sum_{\text{elements}} \nu_{\mathrm{el}}\ \Delta_f H^{\ominus}(0\,\mathrm{K}, \mathrm{el(g)}) \right\} - \Delta_{at}H \tag{3.41}$$

   where the sum is taken over all elements, the molecule consists of. ν_{el} is the stoichiometric coefficient of an element.

3. Determine the enthalpy of formation at $T_r = 298.15$ K by evaluating:

$$\begin{aligned} \Delta_f H^{\ominus}(T_r) = \quad & \Delta_f H^{\ominus}(0\,\mathrm{K}) \ - \ \left(H^{\ominus}(0\,\mathrm{K}) - H^{\ominus}(T_r)\right)_{\text{compound}} \\ + \quad & \sum_{\substack{\text{elements in their} \\ \text{reference state}}} \nu_{\mathrm{el}} \left(H^{\ominus}(0\,\mathrm{K}) - H^{\ominus}(T_r)\right) \end{aligned} \tag{3.42}$$

In the JANAF tables the *reference state* of an element is defined as the most stable thermodynamic state at a given temperature and a pressure of $p^\ominus = 1$ bar. The enthalpy $H^\ominus(T) - H^\ominus(T_r)$ of the elements in the reference state is taken from the JANAF tables, whereas it must be calculated for the compound under consideration pursuant to:

$$H^\ominus(T) - H^\ominus(0\ \mathrm{K}) = R\,T^2\,\frac{d\ln Q}{dT} \tag{3.43}$$

Here $R = N_A\,k$ is the molar gas constant. This step is necessary, since the JANAF tables use $T = 298.15$ K as the reference temperature and not 0 K. The necessary expressions for the various contributions to the partition function can be obtained by differentiation of the formulas given in the previous section.

4. At this point one is able to calculate the data at each temperature of interest. The standard enthalpy of formation $\Delta_f H^\ominus$ is determined by:

$$\begin{aligned}\Delta_f H^\ominus(T) = \quad & \Delta_f H^\ominus(T_r) + \big(H^\ominus(T) - H^\ominus(T_r)\big)_{compound} \\ - & \sum_{\substack{\text{elements in their}\\ \text{reference state}}} \nu_{\mathrm{el}}\,\big(H^\ominus(T) - H^\ominus(T_r)\big)\end{aligned} \tag{3.44}$$

and for the entropy one gets:

$$S^\ominus = R\,T\,\frac{d\ln Q}{dT} + R\,\ln Q \tag{3.45}$$

Using the calculated values $\Delta_f H^\ominus(T)$, $S^\ominus(T)$ of the molecule and the entropy of the elements in their reference state, one obtains the Gibbs free energy of formation $\Delta_f G^\ominus$ by:

$$\Delta_f G^\ominus(T) = \Delta_f H^\ominus(T) - T\left\{S^\ominus(T)_{\mathrm{compound}} - \sum_{\substack{\text{elements in their}\\ \text{reference state}}} \nu_{\mathrm{el}}\,S^\ominus(T)\right\} \tag{3.46}$$

This last step has to be performed at each temperature of interest.

These calculations were done by a computer program, that was originally developed by John (1995) and subsequently improved. It has been tested for some molecules using the data given in Chase (1998). The thermodynamic functions are reproduced up to the second digit. Further application of the program will be presented in Barth (2004).

3.3.4 Thermodynamic data for some molecules

In this section we will illustrate the calculation of thermodynamic data by discussing some concrete examples. The data for the molecules discussed below are missing in the standard compilations of equilibrium constants and partition functions usually used, namely that

of Tsuji (1973), Irwin (1981, 1988), Sauval & Tatum (1984), Sharp & Huebner (1990) or Fegley & Lodders (1994). They are also not present in the latest available edition of the JANAF tables (Chase, 1998). Some preliminary results have been already used by Lüttke (2002), where it is also discussed, that the lack of data might influence the reliability of chemical equilibrium calculations.

3.3.4.1 Transition metal hydrides

The hydrides of various transition metals, viz. TiH, VH, CrH, and FeH, contribute significantly to the opacity of the gas phase in cool stellar and substellar objects. TiH e.g. has been identified by Yerle (1979) in the spectra of the M–stars α Orionis, α Scorpii, and δ Virginis. More recently, the hydrides of iron and chromium have been identified in the spectra of brown dwarfs (Kirkpatrick et al., 1999). We are not aware of any published thermodynamic functions or equilibrium constants of these species[14]

The spectroscopic data from various sources for the ground states of the transition metal hydrides TiH, VH, CrH and FeH, respectively, are summarised in table 3.2. We abstain here from an in-depth discussion of the data and methods. The values actually used for the subsequent calculation of the thermodynamic functions are underlined. Where ever possible experimental values for the molecular constants have been used, since theoretical calculations for transition metals are still rather difficult and erroneous (see e.g. Barone & Adamo, 1997). Here we give some additional remarks, in order to justify the choices made:

- For TiH we have chosen the data from Launila & Lindgren (1996) and not those given by Andersson et al. (2003). The latter give an equilibrium distance r_e which is not consistent with the rotational constant B_e. Since the moment of inertia of a diatomic molecule is given by:

  $$I = \mu_{red}\, r_e^2$$

  with μ_{red} being the reduced mass, one gets the following expression for the equilibrium distance, if one uses equation (3.33):

  $$r_{eq}\ [\text{Å}] = \sqrt{\frac{h}{8\,\pi\,\mu_{red}\,B_e}} = 4.1058/\sqrt{\mu_{red}[\text{amu}]\ B_e[\text{cm}^{-1}]} \tag{3.47}$$

  While the data of Launila & Lindgren (1996) can be reproduced using this formula, this is not the case for the data of Andersson et al. (2003).

- In the case of vanadium hydride we are not aware of any experimental work, which determines its spectroscopic constants. Consequently one has to use theoretical work. Our choice is motivated by the following observations:

[14] Burrows & Sharp (1999) present some chemical equilibrium calculations for the atmospheres of brown dwarfs and giant planets, which include FeH. Unfortunately the authors do not mention the source of the thermodynamic data of this species.

1. As density functional methods reproduce the experimental data for transition metals only poorly, those methods were not considered.
2. The calculated values for the dissociation energy D_0 presented by Walch & Bauschlicher (1983) compare quite well with the experimental value. On the other hand, the agreement between calculated and measured spectroscopic constants is only reasonable.
3. Although the dissociation energies calculated by Chong et al. (1985) are slightly more worse than those of Walch & Bauschlicher (1983), they reproduce the spectroscopic constants clearly better.

For this reason, the calculated data by Chong et al. (1985) has been used for the calculation of the thermodynamic data of VH.

- For most species the value for the rotation-vibration interaction constant α_e is unknown. An exception is CrH for which Bauschlicher et al. (2001) give a value of $\alpha_e = 0.18098\text{cm}^{-1}$, which has been used for the calculation of the thermodynamic functions.

- The aforementioned paper by Bauschlicher et al. (2001) is a combined computational and experimental approach. A noteworthy result of the *ab initio* calculations is the difficulty to obtain simultaneously satisfactory results for both, the geometric and energetical properties of a molecule. While the results given in table 3.2, regarded as the best values by the authors, reproduce the equilibrium length, the vibrational frequency and the anharmonicity very well, the calculated value for the dissociation energy D_0 clearly lies outside the presumed error range for the experimental value (Chen et al., 1993). On the other hand, these authors carried out some similar calculations using a different basis set, which yield a dissociation energy of 1.98 eV, close to the experimental value, whereas the values for $r_e = 1.673$ Å and $\omega_e = 1595\ \text{cm}^{-1}$ are notably worse.

The collection of experimental data should be fairly complete, as e.g. no further data are listed in a recent review about transition metal diatomics by Harrison (2000). Although it is generally accepted that transition metal hydrides have many low-lying states of high spin multiplicity (Tanaka et al., 2001), they have not been taken into account since accurate data for those states are (mostly) missing.

Table 3.2: A compilation of the molecular constants of the transition metal hydrides TiH, CrH, FeH, and VH collected from various sources. The data used for the calculation of the thermodynamic properties are underlined. μ_{red} is the reduced mass of the molecule.

source	r_e [Å]	ω_e [cm^{-1}]	$\omega_e x_e$ [cm^{-1}]	B_e [cm^{-1}]	D_0 [eV]	method
	Titanium hydrid TiH ($^4\Phi$)		$\mu_{red} = 0.98715$ amu			
Ref. 1	–	–	–	–	$\underline{2.08 \pm 0.09}$	GIBMS [a]
Ref. 2	–	$\underline{1405 \pm 10}$	–	–	–	MIS [b,c]
Ref. 3	$\underline{1.7847}$	–	–	$\underline{5.3621}$	–	FTS [d]
Ref. 4	1.779	–	–	5.3564	–	FTS [d]
	Ab initio calculations					
Ref. 15	1.83	1407	–	–	2.03	CASSCF/CI [e,f]
Ref. 16	1.781	1407	–	–	1.96	MCPF [n,f]
Ref. 5	1.8362	1498	22.2	5.08	1.96	MRD-CI [g,f]
Ref. 6	1.744	1601	–	–	2.61	B3LYP
Ref. 7	1.767	1559	–	–	2.08	CCSD(T) [h]
Ref. 8	1.760	1557	–	–	–	BLYP [i]
	Vanadium hydrid VH ($^5\Delta$)		$\mu_{red} = 0.98838$ amu			
Ref. 12	–	–	–	–	$\underline{2.13 \pm 0.07}$	GIBMS [a]
	Ab initio calculations					
Ref. 15	1.74	1590	–	–	2.20	CASSCF/CI [g,f]
Ref. 16	$\underline{1.719}$	$\underline{1635}$	–	–	2.23	MCPF [n,f]
Ref. 6	1.677	1658	–	–	2.77	B3LYP
	Chromium hydrid CrH ($^6\Sigma^+$)		$\mu_{red} = 0.98877$ amu			
Ref. 12	–	–	–	–	$\underline{1.93 \pm 0.07}$	GIBMS [a]
Ref. 13	1.656	1581	30	6.22	–	compilation [j]
Ref. 14	$\underline{1.6554}$	$\underline{1656.1}$	$\underline{30.49}$	$\underline{6.2222}$	–	FTS [d]
	Ab initio calculations					
Ref. 15	1.70	1465	–	–	2.01	CASSCF/CI [g,f]
Ref. 16	1.694	1647	–	–	2.03	MCPF [n,f]
Ref. 6	1.654	1637	–	–	2.34	B3LYP
Ref. 13	1.654	1653.8	31.0	–	2.17	MRCI [k] + correction
	Iron hydrid FeH ($^4\Delta$)		$\mu_{red} = 0.99007$ amu			
Ref. 9	–	–	–	–	$\underline{1.63 \pm 0.08}$	GIBMS [a]
Ref. 10	$\underline{1.63 \pm 0.01}$	$\underline{1774 \pm 10}$	$\underline{47 \pm 5}$	–	–	PES [l]
	Ab initio calculations					
Ref. 6	1.561	1829	–	–	1.76	B3LYP

Table 3.2: (continued)

source	r_e [Å]	ω_e [cm^{-1}]	$\omega_e x_e$ [cm^{-1}]	B_e [cm^{-1}]	D_0 [eV]	method
Ref. 11	1.596	1735	–	–	1.80	MRCPA [m]

Ref. 1: Chen et al. (1991); Ref. 2: Chertihin & Andrews (1994); Ref. 3: Launila & Lindgren (1996); Ref. 4: Andersson et al. (2003); Ref. 5: Anglada et al. (1990); Ref. 6: Barone & Adamo (1997); Ref. 7: Bauschlicher (1999); Ref. 8: Pápai (2000); Ref. 9: Schultz & Armentrout (1991); Ref. 10: Stevens et al. (1983); Ref. 11: Tanaka et al. (2001); Ref. 12: Chen et al. (1993); Ref. 13: Radzig & Smirnov (1985); Ref. 14: Bauschlicher et al. (2001); Ref. 15: Walch & Bauschlicher (1983); Ref. 16: Chong et al. (1985)

[a] Guided ion beam mass spectroscopy
[b] Matrix isolation spectroscopy
[c] Chertihin & Andrews (1994) actually measured a value of $\omega_e = 1385.3\,cm^{-1}$. The value given in the table has been corrected by the authors in order to take the effect of the matrix into account.
[d] Fourier transform spectroscopy
[e] Complete active space self–consistent field calculation.
[f] The value for D_0 has been calculated from the given value for D_e and the vibrational frequency.
[g] Mulitreference configuration interaction calculation.
[h] Coupled cluster calculations using a newly developed correlation-consistent basis set for Ti (see Bauschlicher, 1999, for the details).
[i] Pápai (2000) gives also the values using B3LYP and BP86, which are worse than those given in the table.
[j] The data given in Huber & Herzberg (1979) are the same as in Radzig & Smirnov (1985). For the other hydrides no data are given in either compilations.
[k] Multireference configuration interaction approach.
[l] Photoelectron spectroscopy
[m] Multireference coupled pair approximation
[n] Modified coupled pair functional method

A clear periodic trend for the data is evident. As the molecules in table 3.2 are ordered according to the position in the periodic table starting with the most left one (titanium) and ending with the most right one (iron), one deduces the following rules of thumb:

1. The equilibrium distance in transition metal hydrides decreases from left to right.

2. The vibrational frequency increases from left to right.

Taking into account the other first–row transition metals (Sc, Mn, Co, Ni and Cu) such trends are still discernible but less clear (see Stevens Miller et al. (1987) and Harrison (2000) for a detailed discussion).

The thermodynamic properties of the transition metal hydrides TiH, VH, Cr, and Fe have then been calculated using the molecular data marked in table 3.2. Since the molecular data are all of the same order of magnitude, no distinct differences between the calculated partition function and entropy are observed (data not shown here).

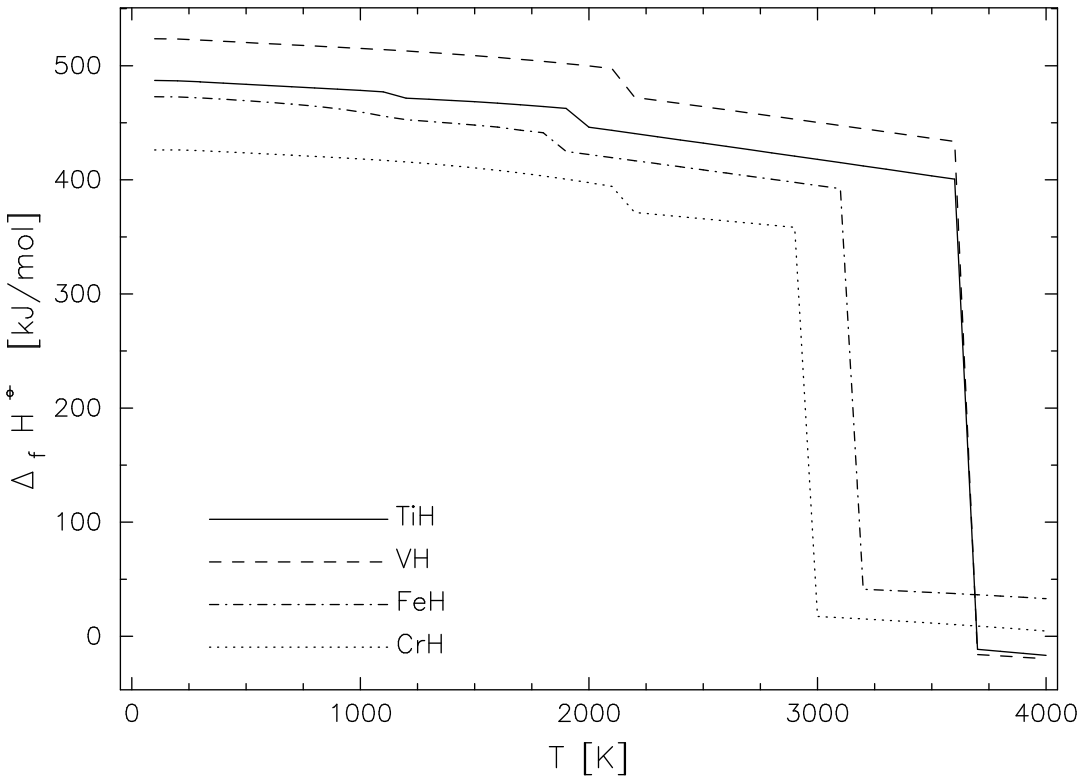

Figure 3.9: Heat of formation $\Delta_f H^\ominus$ of the transition metal hydrides TiH, VH, CrH, and FeH as a function of temperature.

While the entropy $S^\ominus$ of a molecule is a smooth function, the enthalpy of formation $\Delta_f H^\ominus$ (see figure 3.9) and the Gibbs free energy of formation $\Delta_f G^\ominus$ (see figure 3.10) shows some discontinuities, which reflect the phase transition of the reference state at certain temperatures. For the four transition metals under consideration here these are:

metal	solid $\leftrightarrow$ liquid transition	liquid $\leftrightarrow$ gas transition
titanium	1939 K	3630.96 K
vanadium	2190 K	3690.08 K
chromium	2130 K	2952.08 K
iron	1809 K	3133.35 K

While the solid/liquid transition causes a distinct but not large jump of $\approx$ 25 kJ mol^{-1} in the $\Delta_f H^\ominus$–curve, the liquid/gas transition manifests itself as a huge jump of $\approx$ 400kJ mol^{-1}. Additionally some of the bulk metals possess different modifications. For example iron has three different modification, named α, γ, and δ, with transition temperature at 1184 K, 1665 K, and 1809 K, respectively. They are discernible as small kinks in the curve of FeH.

Recall that VH has the highest dissociation energy D_0, followed by TiH, CrH, and finally FeH, which is most loosely bound. In case of the Al_2O_3 molecule studied by Patzer (1998) the different atomization energies of the seven found isomers cause a similar ordering of the $\Delta_f H^\ominus$ curves. For the transition metal hydrides the picture is less clear which is due to the fact, that the shown data refer to the reference states, i.e. most stable phases at a given temperature, of *different* elements.

The mentioned discontinuities at the phase transition temperature are still recognisable in the $\Delta_f G^\ominus(T)$ curve shown in figure 3.10 but less perspicuous, except for the gas/liquid transition, where the curves change the sign of their slope. Since the entropy $S^\ominus(T)$ for the four considered molecules are very similar, the temperature dependence of $\Delta_f G^\ominus$ is for all roughly the same.

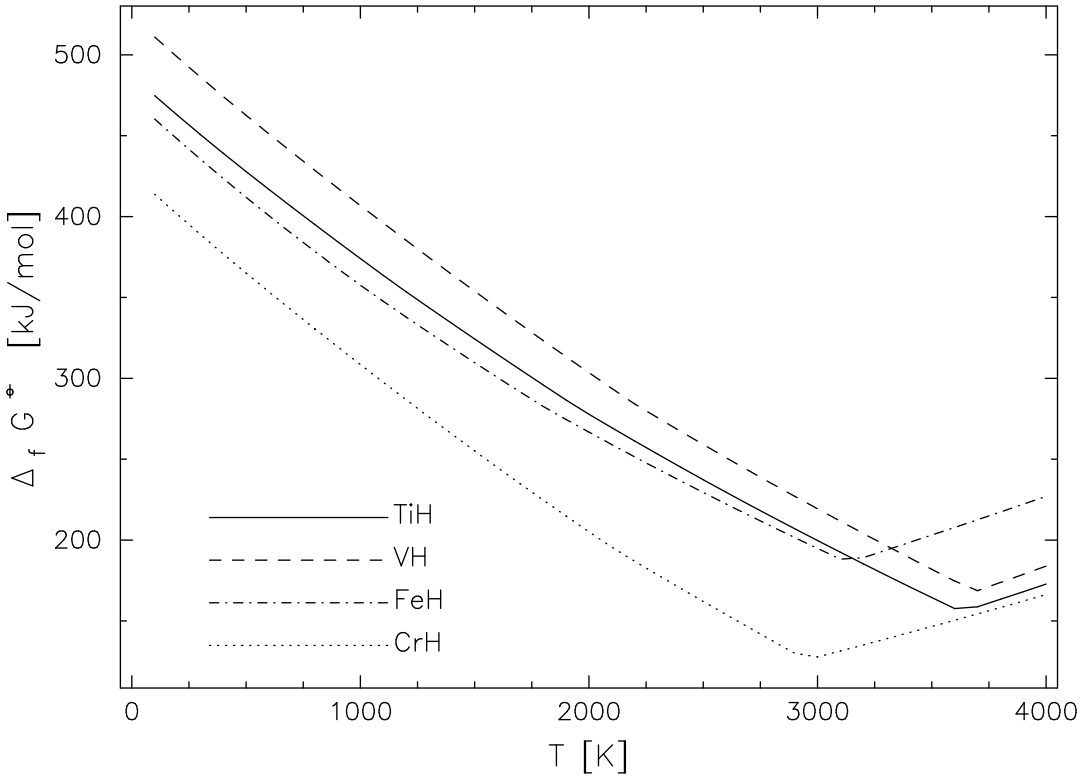

Figure 3.10: Gibbs free energy of formation $\Delta_f G^\ominus$ of the transition metal hydrides TiH, VH, Cr, and FeH as a function of temperature.

Note that a similar concept has been used by Patzer et al. (1999) to compute the thermodynamic functions of Al_2O_3 using the *ab initio* data presented by Chang et al. (1998).

3.3.4.2 Other titanium compounds

Gail & Sedlmayr (1998) proposed, that titanium oxide might play an important role in the dust formation process and serve as the primary condensate in M–stars. The investigations

of small Ti_xO_y clusters presented by Jeong et al. (2000) (see also Jeong, 2000) support this hypothesis. Since the thermodynamic data of many diatomic titanium species are not known, we try to fill this gap, at least for compounds involving titanium and other abundant elements, namely hydrogen (see previous section), carbon, sulfur and titanium itself. The data of the ground states of TiC, TiN, TiS and Ti_2 are summarised in table 3.3. As in the case of transition metal hydrides the underlined data have been used for the thermodynamic calculations. Some short comments are given here:

- For titanium carbide we are not aware of any experimental work trying to determine its molecular constants. Two papers by Chupka & Berkowitz (1958), and Kohl & Stearns (1974), respectively, present some mass spectrometric studies of gaseous metal carbides. Both only give an upper bound for the dissociation energy of TiC of $D_0 \leq 5.50$ eV, and 4.48 eV, respectively. So in this case one has to rely solely on the results of *ab initio* calculations. Since the binding energy $D_e = 6.44$ eV calculated by Sosa et al. (1997) by means of density functional methods falls outside this range, this work is not considered further here.

- McFeaters et al. (1994) give an implausible high dissociation energy for TiC with $D_0 = 531\ \mathrm{kJ\,mol^{-1}} = 5.50$ eV, which lies at the upper bound of the experimentally determined range for D_0. Since McFeaters et al. cite the paper by Bauschlicher & Siegbahn (1984) as the source of their data, one must conclude that these data are a typo[15].

- Hack et al. (1996) investigated the electronic structure of TiC by means of *ab initio* calculations on various levels of theory ranging from simple Hartree–Fock (ROHF) up to multireference configuration interaction (MRCI) calculations, which are regarded as the highest used level of theory. The results indicate, that the calculated properties are very sensitive to the level of theory used. Table 3.3 lists only the values regarded as the best by the authors.

- There are mainly two arguments, which favour the selection of the data given by Kalemos & Mavridis (2002) for the thermodynamic calculations of TiC. At first Kalemos & Mavridis use the basis set of Bauschlicher (1999) for the Ti atom, which proved to reproduce the experimental values for TiH very well (see table 3.2). Secondly these data lie close to those, obtain by the quantum Monte-Carlo computations of Sokolova & Lüchow (2000). These methods have been proven to yield very accurate dissociation or atomization energies, e.g. for silicon clusters (Grossman & Mitáš, 1995) or diatomic molecules of some first–row atoms (Lu, 2003). The results of Bauschlicher & Siegbahn (1984) strengthen these arguments, since they obtain similar values for r_e and ω_e. Furthermore Bauschlicher & Siegbahn note, that their dissociation energy might be too small.

[15] Assuming that the energy is not given in $\mathrm{kJ\,mol^{-1}}$ but in $\mathrm{kcal\,mol^{-1}}$ make the discrepancy even worse. Astonishingly the given values for D_0 and $\Delta_f H^{\ominus}$ are consistent. As a consequence of this typo the data for the equilibrium constant given in Helling et al. (2000) are erroneous, too.

- For TiS and TiN we are not aware of any further data, then those given by Radzig & Smirnov (1985) and Harrison (2000), respectively, but we feel, that using these data may be better then nothing.

- Although there exist some *ab initio* calculations of the titanium dimer (e.g. Bauschlicher et al., 1991; or Pápai, 2000) we do not consider them here. For example the MRCI calculations of Bauschlicher et al. (1991) do not find a $^3\Delta$ state as the ground state of Ti_2, which contradicts the experimental finding of Doverstål and coworkes (Doverstål et al., 1992, 1997). Additionally the systematic study of homonuclear transition metals dimers using density functional methods by Barden et al. (2000) clearly demonstrates that it is rather difficult to describe such species correctly on a DFT level of theory. The best results for bond length and harmonic vibrational frequencies are obtained with the BLYP and the BP86[16] functionals. Dissociation energies are severely overestimated for some cases and negative in others. A similar study by Yanagisawa et al. (2000) confirms these findings also for the use of a larger basis set.

- The way the dissociation energy has been computed by Russon et al. (1994) deserves some remarks. The experimental technique yields only a value for the dissociation energy of the charged molecule ($D_0(Ti_2^+) = 2.435 \pm 0.02$eV). Using a Born–Haber type thermochemical cycle, one gets the following equation, connecting the dissociation energy of the neutral and charged species with the ionization energies of the atom and the molecule:

$$D_0(Ti_2) + I_p(Ti) = D_0(Ti_2^+) + I_p(Ti_2) \tag{3.48}$$

  First Russon et al. derive a lower limit for $I_p(Ti_2) \leq 5.742$ eV by using the ionization potential of the Ti atom ($I_p = 6.82817$ eV) and the lower bound for the dissociation energy of Ti given by Doverstål et al. (1992, see table 3.3). These authors give an upper bound for the ionization energy of the molecule of $I_p(Ti_2) \leq 6.125$ eV. By simply taking the mean of these two values, Russon et al. (1994) obtain an ionzation energy of 5.93 eV for Ti_2, which inserted into equation (3.48) yields the value given in table 3.3 for the dissociation energy of Ti_2.

The data presented here for some titanium compounds are not as ensured as those presented for the transition metal hydrides discussed in the previous section 3.3.4.1. Especially the lack of any experimental data for TiC makes it difficult to assess the quality of the molecular constants and thus the quality of the calculated thermodynamic data. But since the data result from high-level *ab initio* methods, the error should not be too large. Due to the lack of any informations about the (likely) existence of low-lying states, these were not taken into account.

[16] This finding is rather interesting with respect to the comparison of different density functional methods to be presented in a subsequent chapter.

Table 3.3: A compilation of the molecular constants of the titanium compounds TiC, TiN, TiS, and Ti_2 collected from various sources. The data used for the calculation of the thermodynamic properties are underlined. μ_{red} is the reduced mass of the molecule.

source	r_e [Å]	ω_e [cm^{-1}]	$\omega_e x_e$ [cm^{-1}]	B_e [cm^{-1}]	D_0 [eV]	method
	Titanium carbide TiC ($^3\Sigma^+$)		$\mu_{red} = 9.6015$ amu			
Ref. 1	1.76	860	–	–	3.17	CASSCF [a,c]
Ref. 2	1.733	704	–	–	2.77	MRCI [b,c]
Ref. 3	1.70	–	–	–	3.52	FN-DQMC [d]
Ref. 4	<u>1.716</u>	<u>861</u>	–	–	<u>3.55</u>	MRCI+Q [e,c]
	Titanium nitride TiN ($^2\Sigma^+$)		$\mu_{red} = 10.8359$ amu			
Ref. 5	<u>1.582</u>	<u>1039</u>	–	–	<u>4.9</u>	compilation [f]
	Titanium sulfide TiS ($^3\Delta_1$)		$\mu_{red} = 19.20205$ amu			
Ref. 6	<u>2.083</u>	<u>558.4</u>	<u>1.9</u>	<u>0.2018</u>	<u>4.7</u>	compilation
	Titanium dimer Ti_2 ($^3\Delta_g$)		$\mu_{red} = 23.9335$ amu			
Ref. 7	–	<u>407.9</u>	<u>1.08</u>	–	–	MIS [g]
Ref. 8	<u>1.9422 ± 0.0008</u>	–	–	–	≥ 1.349	R2PI [h]
Ref. 9	–	–	–	–	<u>1.54 ± 0.19</u>	REPD [i]

Ref. 1: Bauschlicher & Siegbahn (1984); Ref. 2: Hack et al. (1996) Ref. 3: Sokolova & Lüchow (2000); Ref. 4: Kalemos & Mavridis (2002); Ref. 5: Harrison (2000); Ref. 6: Radzig & Smirnov (1985); Ref. 7: Cossé et al. (1980); Ref. 8: Doverstål et al. (1992); Ref. 9: Russon et al. (1994)

[a] Complete active space self–consistent field calculation.
[b] Multireference configuration interaction
[c] The value for D_0 has been calculated from the given value for D_e and the vibrational frequency.
[d] Fixed–node diffusive quantum Monte Carlo calculations. Since Sokolova & Lüchow (2000) did not compute the vibrational frequency of TiC, the given value is the bond energy D_e.
[e] Multireference configuration interaction + Davidson correction.
[f] Only the experimental values listed in Harrison (2000) are reproduced, since they are only poorly reproduced by the mentioned *ab initio* values.
[g] Matrix isolation spectroscopy
[h] Resonance two–photon ionisation spectroscopy. In a later paper Doverstål et al. (1997) found for the bond length $r_{eq} = 1.9429$ Å.
[i] Resonance-enhanced photodissociation spectroscopy.

Since the calculated thermodynamic functions show all the features already discussed in connection with the hydrides, we do not present the resulting data here. The values for $S^{\ominus}$, $\Delta_f H^{\ominus}$, and $\Delta_f G^{\ominus}$ at the reference temperature T_r are given in table C.2.

3.3.4.3 Silicon compounds

Since in the further course of this thesis we will focus on silicon–oxide clusters, we calculated the thermodynamic data for some silicon–containing molecules, namely the diatomics SiP, SiB, AlSi, MgSi and the enstatite molecule $MgSiO_3$. The necessary molecular constants are summarised below in table 3.4.

As can be seen from that table, there exist only one experimental paper dealing with the determination of the spectroscopic constants of SiX molecules. This may be due to the rather reactive character of many diatomic molecules containing elements from the first and second row of the periodic table (Boldyrev et al., 1994). On the other hand the available experimental data are quite well reproduced by the elaborate *ab initio* methods listed in table 3.4. Since all methods also yield similar results, the used data can be considered as quite reliable.

Table 3.4: Molecular constants of some silicon–containing molecules collected from various sources. The data used for the calculation of the thermodynamic properties are underlined. μ_{red} is the reduced mass of the molecule.

source	r_e [Å]	ω_e [cm^{-1}]	$\omega_e x_e$ [cm^{-1}]	B_e [cm^{-1}]	D_0 [eV]	method
	Silicon phosphide SiP ($^2\Pi_i$)			$\mu_{red} = 14.7295$ amu		
Ref. 1	<u>2.0775</u>	<u>615.7</u>	<u>2.34</u>	–	–	LIFS [a]
	Ab initio calculations					
Ref. 2	2.087	754	–	–	3.31	QCISD(T) [e]
Ref. 3	1.9678	653	–	–	388.8 [c]	BAC–MP4 [b]
Ref. 4	2.089	608	2.886	0.2630	<u>3.602</u>	CASSCF/CMRCI [d]
	Silicon boride SiB ($^4\Sigma$)			$\mu_{red} = 7.8062$ amu		
Ref. 5	1.905	772	–	–	3.10	QCISD(T) [e]
Ref. 6	<u>1.918</u>	<u>733</u>	<u>2.81</u>	–	<u>3.22</u>	CASSCF/CMRCI [d]
	Aluminium Silicide AlSi ($^4\Sigma$)			$\mu_{red} = 13.7612$ amu		
Ref. 5	2.430	383	–	–	2.43	QCISD(T) [e]
Ref. 7	<u>2.424</u>	<u>385</u>	<u>1.31</u>	<u>0.2093</u>	<u>2.51</u>	CASSCF/CMRCI [d]

Table 3.4: (continued)

source	r_e [Å]	ω_e [cm^{-1}]	$\omega_e x_e$ [cm^{-1}]	B_e [cm^{-1}]	D_0 [eV]	method
Magnesium Silicide MgSi ($^3\Sigma$)					$\mu_{red} = 13.0294$ amu	
Ref. 5	2.561	316	–	–	0.94	QCISD(T) [e]

Ref. 1: Jakubek et al. (2002); Ref. 2: Boldyrev & Simons (1993a); Ref. 3: Zachariah & Melius (1997); Ref. 4: Ornellas et al. (2000); Ref. 5: Boldyrev & Simons (1993b); Ref. 6: Ornellas & Iwata (1997); Ref. 7: Ornellas & Iwata (1998)

[a] Laser induced fluorescence spectroscopy.

[b] BAC–MP4 is based on *ab initio* molecular orbital calculations followed by an application of bond additivity corrections (see Zachariah & Melius, 1997, and references therein for details). The frequency has been calculated at the HF/6-31G(D) level of theory and scaled by 0.89.

[c] The value given in the column for the dissociation energy is the enthalpy of formation $\Delta_f H^\ominus(T = 298.15\text{K})$ in kJ mol^{-1}.

[d] Complete active space self-consistent field calculations followed by internally contracted multireference configuration interaction calculations. The spectroscopic constants have been obtained by applying a fitting procedure to the calculated potential energy curve (see Ornellas et al., 2000, and references therein for details).

[e] Quadratic configuration interaction calculations. The frequencies have been calculated at the MP2/6-311+G* level of theory.

The thermodynamic data of some phosphorus compounds deserve some short remarks. As noted by Zachariah & Melius (1997) the data listed in the 3rd edition of the JANAF tables (1985) for phosphinidene (PH), phosphino (PH_2), and phosphine (PH_3) are erroneous. This is due to the change of the reference state for phosphorus in this edition of the JANAF tables (Chase et al., 1985) from red to white phosphorus. Obviously this change has not been taken into account for all phosphorus–containing species listed in the JANAF tables. This error still affects the electronic edition but not the latest (4-th) printed edition (Chase, 1998), so it was necessary, to correct the data, namely the values for the enthalpy and Gibbs energy of formation. Note, that the entropie $S^\ominus$ and the enthalpy difference $H^\ominus(T) - H^\ominus(T_r)$ are unaffected by a change of the reference state. This was attained in the following way:

- For PH it sufficed to add an offset $\delta = -19.939$ kJ mol^{-1} to the $\Delta_f H^\ominus$ and $\Delta_f G^\ominus$ values. Additionally we calculated the thermodynamic data using the molecular constants given in Chase (1998). The data by these two procedures differ by less then 0.002 kJ mol^{-1}.

- For PH_2 it was necessary to calculate the thermodynamic data using the molecular data given in the JANAF tables. As in the case of PH, the difference between our data for $S^\ominus$, $\Delta_f H^\ominus$, and $\Delta_f G^\ominus$, and those in the printed tables does not exceed 0.001 and can be ascribed to rounding errors.

- In the case of phosphine the data listed in the newest edition of the JANAF tables (Chase, 1998) are still erroneous. Using the given molecular constants, we calculated

the thermodynamic data for PH_3. The resulting values for the entropie $S^{\ominus}$ deviate at most by 0.002 J $K^{-1}mol^{-1}$ from those given in the Chase (1998). The enthalpy difference $H^{\ominus}(T) - H^{\ominus}(T_r)$ is exactly reproduced by our program. But despite this accord between our data and and those of Chase (1998) in this case, there is a significant deviation in $\Delta_f H^{\ominus}$ and $\Delta_f G^{\ominus}$, respectively. A closer inspection reveals, that equation (3.41) is not valid for the data given in Chase (1998). Unfortunately it was not possible to find out, at which point of the calculations the error was introduced. Since the used program reproduced in all tested cases the data very well, the newly calculated data for PH_3 are used.

The corrected thermodynamic ($S^{\ominus}$, $\Delta_f H^{\ominus}$, and $\Delta_f G^{\ominus}$ at $T_r = 298.15$ K) data for the molecules discussed above are given in table C.2.

Additionally the molecular constants calculated at the B3P86/6-31G(d) level of theory for the ground state of $MgSiO_3$ (see Patzer et al., 2002, for the details) have been used to calculate its thermodynamic data (see table C.2 and C.3 for a summary).

3.3.5 Equilibrium constants

The abundances of molecules in the gas phase are usually determined by the solution of a nonlinear system of equations which goes back to Russel (1934). More recent derivations of these equations can be found in Dominik (1992), John (1995) or Lüttke (2002). It is noteworthy in the context of this thesis, that the underlying physical principal can also be stated as a *minimization* problem, namely the minimization of the system's Gibbs free energy (Sharp & Huebner, 1990, Burrows & Sharp, 1999). As a consequence the problem is tackled by some authors using appropriate minimization algorithms (see e.g. Sharp & Huebner, 1990, similar to those, which will be discussed in chapter 4.

For the system of equations one needs for each molecule $\mathcal{M}$ considered the *equilibrium constant* $K_p(T;\mathcal{M})$, which is defined as:

$$K_p(T;\mathcal{M}) = \left(\frac{1}{p^{\ominus}}\right)^{b-1} \exp\left(-\frac{\Delta_r G^{\ominus}(T;\mathcal{M})}{R\,T}\right) \tag{3.49}$$

Here the exponent b is the number of atoms in the molecule $\mathcal{M}$, which is simply the sum of the stoichiometric coefficients of all elements in the molecule. The *Gibbs free energy of reaction* $\Delta_r G^{\ominus}(T;\mathcal{M})$ is given by:

$$\Delta_r G^{\ominus}(T;\mathcal{M}) = \Delta_f G^{\ominus}(T;\mathcal{M}) - \sum_{\substack{\text{elements}\\ \text{in}\,\mathcal{M}}} \nu_{el}\,\Delta_f G^{\ominus}(T;\mathrm{el}(g)) \tag{3.50}$$

For practical purposes the natural logarithm of the equilibrium constant is often fitted by a polynomial of N–th order. The most frequently used form is that introduced by Tsuji (1973):

$$\ln K_p = \sum_{i=0}^{4} a_i\,\Theta^i \qquad \text{with } \Theta = \frac{5040\text{ K}}{T} \tag{3.51}$$

An alternative approach is used by Lüttke (2002), who introduced a rational polynomial fit of second order:

$$\ln K_p = \frac{a_0 + a_1\,T + a_2\,T^2}{b_0 + b_1\,T + b_2\,T^2} \tag{3.52}$$

Since it was found that, especially for temperatures above 300 K, there are only negligible differences of mostly below 0.5% between the two fit functions (data not shown), the calculated data have been fitted using equation (3.51). The resulting coefficients, their mean error, and the values for $S^{\ominus}(T_r)$, $\Delta_f H^{\ominus}(T_r)$, and $\Delta_f G^{\ominus}(T_r)$ are given in table C.3 in appendix C (p. 189 ff).

3.3.6 Application to a stationary wind model

As an application a chemical equilibrium calculation in a stationary wind model introduced by Dominik (1992) is presented here. The temperature and the total hydrogen density are calculated analytically. It is further assumed, that the outflow has a solar element mixture, where the elemental abundances are taken from Cox (1999)[17]. The non linear system of equations, determining the equilibrium abundances of the 46 elements and 785 molecules considered, is solved using the damped Newton-Raphson algorithm described in Lüttke (2002). The stellar parameters used are:

$$L_* = 1 \cdot 10^4\ L_\odot \qquad T_{\text{eff}} = 2500\ \text{K}$$
$$\dot{M} = 1 \cdot 10^{-6}\ M_\odot/\text{yr} \qquad v_{\text{wind}} = 1\ \text{km/s}$$

They are typical for a late–type star. The resulting local concentrations of some molecules are presented in figure 3.11. The equilibrium densities of SiB, SiP, AlSi, and MgSi are almost vanishing, while the abundance of $MgSiO_3$ increases with increasing distance from the star. Due to its low dissociation energy, it is unlikely, that MgSi is an important intermediate product for the formation of $MgSiO_3$.

The hydrides of vanadium and titanium show small but significant abundances in the innermost regions of the wind and vanish rather rapidly with growing distance from the star. Contrary the concentration of FeH and CrH remain almost constant. The rather high abundance of CrH is a little bit astonishing, since the elemental abundance of chromium is approximately 2 orders of magnitude lower, than that of iron. One might suspect, that this is an artefact due to the limited number of chromium–containing species considered in the chemical equilibrium calculation; only 6 compared to 18 Fe–compounds.

Titanium sulfide proves to be the most abundant molecule considered in this section, while the equilibrium densities of TiN and TiC are almost negligible. The latter one is caused by the oxygen-rich chemistry considered here and may change in a C–rich environment.

It is noteworthy, that the resulting density of the cooling trajectory is many orders of magnitude lower than that in the atmosphere of a brown dwarf (see e.g. Lüttke, 2002).

[17] Note that this is the 4th edition of Allen (1973) and that there are some differences between the data given in the 3rd and the 4th edition (see Cox, 1999, p. 28ff).

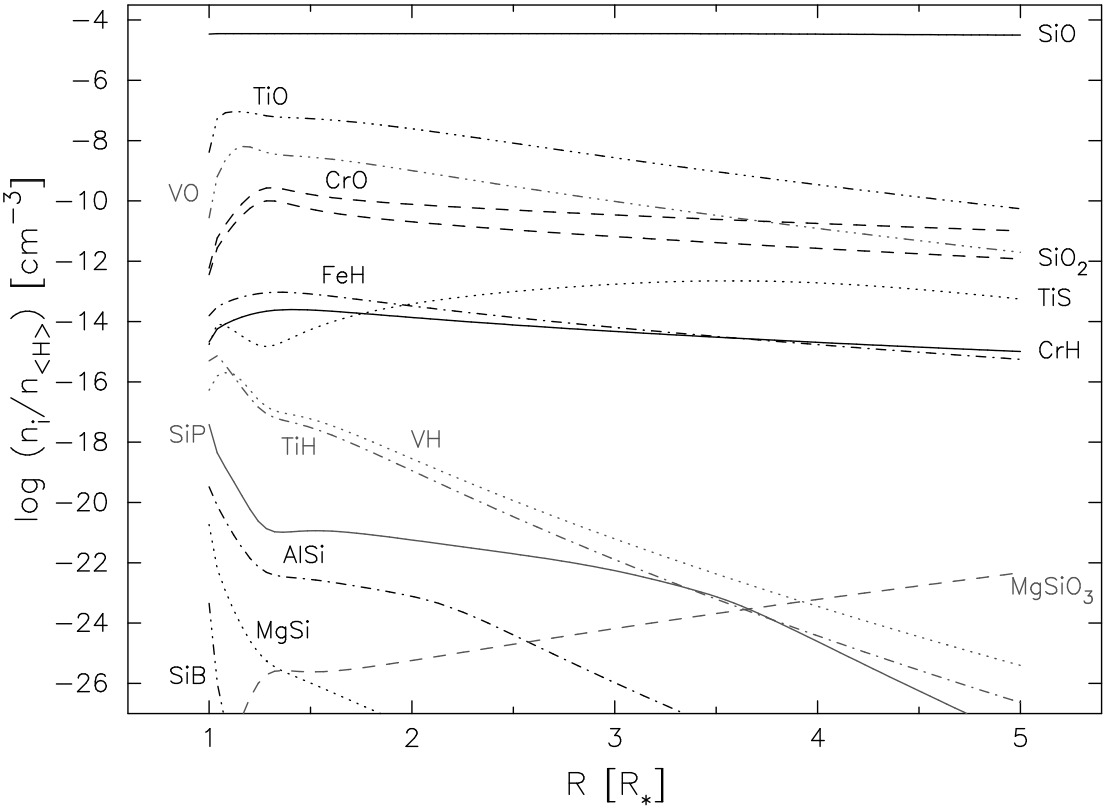

Figure 3.11: Chemical equilibrium abundances of some molecules in a stationary wind model with solar element mixture.

Thus the results discussed here may change significantly, if the chemistry in the denser atmospheres of these substellar objects is investigated.

In summary it was demonstrated, that it is feasible to obtain consistent thermodynamic data for molecules or clusters relying on molecular constants obtained by either experiments and/or theoretical *ab initio* calculations. It was further explained that especially dissociation energies computed by means of *ab initio* methods have to be used cautiously, since some molecules, especially those containing transition metals, are not accurately described at some levels of theory, e.g density functional methods.

Chapter 4

Numerical methods for the investigation of potential energy surfaces

Following the discussion in the last chapter, the physical and chemical properties of clusters, which determine the efficiency of the dust formation process, may be understood by analysing the topology of the underlying potential energy surface, regardless whether this is calculated by means of empirical potential functions or quantum mechanical techniques. In this chapter the numerical methods used for such an analysis in the course of this thesis are introduced and discussed.

The first two sections try to give a short overview over the broad field of optimization. After having recapitulated some results from the theory of optimization, we focus on the problem of local minimisation and discuss the functionality and performance of three different algorithms. The next section will deal with the problem of global optimization, which plays a crucial role throughout this thesis. It is followed by some remarks about the analysis of structural properties of cluster configurations. We then discuss how to investigate the dynamical properties of a potential energy surface by means of microcanonical molecular dynamic simulations.

Finally some remarks about the notation used throughout this chapter are given. Vectors are marked with bold Latin letters with an arrow (e.g. $\vec{\mathbf{x}}$), while letters like $\underline{\mathsf{H}}$ are used for matrices[1]. Any set of real numbers is denoted by calligraphic letters like $\mathcal{A}$ or $\mathcal{U}$. Additionally N–dimensional vectors are assumed to be *column* vectors, which can be considered as $N \times 1$ matrices. In the literature, especially those publications concerned with optimization, one often finds for the inner product of two vectors a notation like $\vec{\mathbf{a}}^T \vec{\mathbf{b}}$, where $\vec{\mathbf{a}}^T$ means the transposed (row) vector. Note however the different meaning of the (outer) product $\vec{\mathbf{b}}\,\vec{\mathbf{a}}^T$ which yields an $N \times N$ matrix $\underline{\mathsf{G}}$, whose elements are given by $\mathsf{G}_{ij} = b_i a_j$. For the sake of clarity henceforth the usual notation is used for the scalar product (viz. $\vec{\mathbf{a}} \cdot \vec{\mathbf{b}}$) while the other product is explicitly written as $\vec{\mathbf{b}}\,\vec{\mathbf{a}}^T$.

[1]For a specific element i, j of this matrix, the underscore is omitted, e.g. H_{ij}

4.1 Local Optimization

Optimization is a common problem in science, engineerings, business, administration, politics, and everyday life. Engineers try to construct machines with an energy or material consumption as efficient as possible. Managers try to maximise the profit and minimise the loss of their companies. In fact one of the most famous problems in the theory of optimization, that of the *travelling salesman* (see e.g. Press et al., 1992), arose from an economical problem: Given N cities and their locations (x_i, y_i), the proverbial sales man (Miller, 1949) has to choose the *shortest* route of transportation, visiting each city once and ending up at the starting point.

But optimization is also common in nature or at least in the description of natural phenomena, as we shall illustrate with the following examples:

- The rays of light in a medium follow a path which minimises the travel time.
- One fundamental result of thermodynamics states, that the equilibrium state of a system is characterised by the extremum of a specific thermodynamic potential (e.g. Schlögl, 1989, p. 97). The type of thermodynamic potential depends only on the constraints used to prepare the system, e.g. whether one uses isobaric, isothermic, isochoric or other conditions.
- Each stable configuration of a molecule or cluster represents a minimum of the potential energy with the ground state corresponding to the global minimum, i.e. the deepest minimum of all.

One also encounters an optimization problem by interpreting experimental data if one has to decide, which model and which parameters describe the data best[2].

Finally in biology Darwin's paradigm of the *survival of the fittest* (Darwin, 1859) interprets the origin of species as an optimization process. The success of evolutionary and genetic algorithms, which mimic the natural processes of mutation and selection, demonstrate unambiguously the strength of this concept[3].

After these preliminary remarks we next try to introduce the necessary concepts for the numerical solution of optimization problems from a more mathematical point of view.

4.1.1 Outline of the problem

Consider a smooth function $f(\vec{\mathbf{x}})$: $\mathbb{R}^N \to \mathbb{R}$, which is in the following often called *objective*, *cost* or *fitness* function. In the theory of optimization one generally distinguishes between three different types of optimization problems:

[2]It is worth noting, that the question, which model or theory is best suited to describe a physical problem, might be a *meta-physical* question in that sense, that the criteria used to decide for one theory in favour of an other competing theory, do not solely rely on experimental facts, if these are explained by both (see Huber, 2000).

[3]It might be fruitful to invert the problem: Instead of asking "What is the optimal solution to a given problem?", one could try to answer the question: "Given a - presumably optimal - solution, what is the problem?"

1. If there are no restrictions on the variables $\vec{\mathbf{x}}$, the problem is called *unconstrained* optimization, and one writes:

$$\min_{\vec{\mathbf{x}}\in\mathcal{U}} f(\vec{\mathbf{x}}) \qquad \mathcal{U} \subset \mathbb{R}^N \tag{4.1}$$

   In chemistry and physics one is mostly confronted with this type of problems.

2. If however the variables have to satisfy certain constraints one speaks of *constrained* optimization problems:

$$\min_{\vec{\mathbf{x}}\in\mathcal{U}} f(\vec{\mathbf{x}}) \qquad \text{subject to} \begin{cases} c_i(\vec{\mathbf{x}}) = 0, & i \in \mathcal{E} \\ c_j(\vec{\mathbf{x}}) \geq 0, & j \in \mathcal{I} \end{cases} \tag{4.2}$$

   where c_i are scalar-valued functions and $\mathcal{E}$, $\mathcal{I}$ are sets of indices.

3. The last category can be viewed as a constrained optimization problem with a further constraint, restricting the variables to certain, discrete values:

$$\min_{\vec{\mathbf{x}}\in\mathcal{U}} f(\vec{\mathbf{x}}) \qquad \text{subject to} \begin{cases} c_i(\vec{\mathbf{x}}) = 0, & i \in \mathcal{E} \\ c_j(\vec{\mathbf{x}}) \geq 0, & j \in \mathcal{I} \end{cases} \quad \text{and} \quad x_i \in \mathbb{Z} \tag{4.3}$$

   and is consequently called a *discrete* optimization problem.

The previously mentioned problem of the travelling salesman falls into the last category. The discrete character of the variable set implies, that the objective function f is no longer smooth! Thus, the solution of such problems is often more demanding, than that of continuous problems, because in the latter case the smoothness of the function makes it possible to infer from the functional properties at any point $\vec{\mathbf{x}}_0$ to that of any other point $\vec{\mathbf{x}}_i$ close to $\vec{\mathbf{x}}_0$.

In this thesis we are mainly concerned with *unconstrained continuous* optimization problems (4.1). Constrained and discrete optimization problems will be therefore only shortly mentioned.

Another distinctive feature of optimization problems is the availability of the first derivative of the function $f(\vec{\mathbf{x}})$ one has to minimise. As we shall discuss in the next section, the gradient of an N-dimensional function defines quite naturally a direction, which points *downwards*. Thus, informations about the first derivative serve as a guiding line towards the (next) local minimum. Algorithms utilising such informations will be presented in sections 4.1.3 and 4.1.4 respectively. If on the other hand it is not possible or computational expensive to calculate the gradient, an optimization algorithm can only use the function itself. Since all minimization algorithms require a search direction, this implies that in this case one has to use more than one point. Examples for such algorithms are the downhill simplex algorithm presented in section 4.1.5 and the broad class of evolutionary algorithms, which make use of several individuals.

4.1.2 Theory of local minimization

Before one can try to examine algorithms which find a solution for the problem stated in equation (4.1), it is necessary to discuss some properties of this problem and its solution. For a detailed overview the reader might refer to the books of Polak (1997) or Nocedal & Wright (1999), or the review article by Nocedal (1992). A vast amount of informations about this broad field also can be found in the *Encyclopedia of Optimization* by Floudas & Pardalos (2001).

First of all one has to clarify, what one means, if one states, that $\vec{\mathbf{x}}_{\min}$ is a (global or local) minimum of f. Following Polak (1997) we define:

Definition 4.1 Global and local minimum
Consider a function $f : \mathbb{R}^N \longrightarrow \mathbb{R}$.
(a) A point $\vec{\mathbf{x}}_{\min}$ *is called a* global minimum *of f, if*

$$f(\vec{\mathbf{x}}_{\min}) \leq f(\vec{\mathbf{x}}), \qquad \forall\, \vec{\mathbf{x}} \in \mathbb{R}^N \tag{4.4}$$

(b) A point $\vec{\mathbf{x}}_{\min}$ *is called a* local minimum *of f, if there exists a* $\rho > 0$ *such that*

$$f(\vec{\mathbf{x}}_{\min}) \leq f(\vec{\mathbf{x}}), \qquad \forall\, \vec{\mathbf{x}} \in \mathcal{B}(\vec{\mathbf{x}}_{\min}, \rho) \tag{4.5a}$$

where

$$\mathcal{B}(\vec{\mathbf{x}}_{\min}, \rho) = \left\{ \vec{\mathbf{x}} \in \mathbb{R}^N \mid \|\vec{\mathbf{x}} - \vec{\mathbf{x}}_{\min}\| \leq \hat{\rho} \right\} \tag{4.5b}$$

(c) A point $\vec{\mathbf{x}}_{\min}$ *is called* strict local minimum *of f, if there exists a* $\hat{\rho} > 0$ *such that* $f(\vec{\mathbf{x}}_{\min}) < f(\vec{\mathbf{x}})$ *for all* $\vec{\mathbf{x}} \in \mathcal{B}(\vec{\mathbf{x}}_{\min}, \hat{\rho})$, *with* $\vec{\mathbf{x}} \neq \vec{\mathbf{x}}_{\min}$.

In this section the discussion will focus on local minima and techniques to find them. A short discussion about global minimization algorithms is presented in section 4.2.

Of course it would be impractical to examine all points in the vicinity of an assumed minimum $\vec{\mathbf{x}}_{\min}$ in order to verify, that no other point has a smaller function value[4]. In the case of a smooth function f there exist much more efficient and practical ways to identify local minima. The main mathematical tool to study such cases is Taylor's theorem (Nocedal & Wright, 1999, p. 15):

Theorem 4.1 Taylor's Theorem
Suppose that $f : \mathbb{R}^N \to \mathbb{R}$ *is continuously differentiable and that* $\vec{\mathbf{p}} \in \mathbb{R}^N$. *Then it holds that:*

$$f(\vec{\mathbf{x}} + \vec{\mathbf{p}}) = f(\vec{\mathbf{x}}) + \nabla f(\vec{\mathbf{x}} + t\ \vec{\mathbf{p}}) \cdot \vec{\mathbf{p}} \tag{4.6}$$

for some $t \in (0, 1)$. *Moreover, if f is twice continuously differentiable, one has:*

$$\nabla f(\vec{\mathbf{x}} + \vec{\mathbf{p}}) = \nabla f(\vec{\mathbf{x}}) + \int_0^1 \nabla^2 f(\vec{\mathbf{x}} + t\ \vec{\mathbf{p}})\ \vec{\mathbf{p}}\ dt \tag{4.7}$$

and that

$$f(\vec{\mathbf{x}} + \vec{\mathbf{p}}) = f(\vec{\mathbf{x}}) + \nabla f(\vec{\mathbf{x}}) \cdot\ \vec{\mathbf{p}} + \frac{1}{2}\vec{\mathbf{p}} \cdot \nabla^2 f(\vec{\mathbf{x}} + t\ \vec{\mathbf{p}})\ \vec{\mathbf{p}} \tag{4.8}$$

for some $t \in (0, 1)$.

[4] In the case of global minima this type of search strategy is the only possibility (see section 4.2)

A proof for this theorem can be found in any textbook about analysis (e.g. Heuser, 1990). For the Hessian matrix $\nabla^2 f$ in equation (4.8) the notation $\underline{\mathsf{H}}$ is used throughout this thesis and equation (4.8) reads as follows:

$$f(\vec{\mathbf{x}} + \vec{\mathbf{p}}) = f(\vec{\mathbf{x}}) + \nabla f(\vec{\mathbf{x}}) \cdot \vec{\mathbf{p}} + \frac{1}{2}\, \vec{\mathbf{p}} \cdot (\underline{\mathsf{H}}(\vec{\mathbf{x}} + t\, \vec{\mathbf{p}})\, \vec{\mathbf{p}}) \tag{4.9}$$

There are mainly two reasons for the importance of Taylor's theorem for the theory of minimization. At first it allows the derivation of some *necessary conditions* a point $\vec{\mathbf{x}}$ must or might fulfil, in order to be recognised as local minimum. This is achieved by assuming, that $\vec{\mathbf{x}}$ indeed is a local minimum $\vec{\mathbf{x}}_{\min}$ and then proving some facts about $\nabla f(\vec{\mathbf{x}}_{\min})$ and $\underline{\mathsf{H}}(\vec{\mathbf{x}}_{\min})$. Furthermore equation (4.9) is the starting point for the development of most local minimization algorithms.

Before we turn to the question, how one can find a minimum, we want to recall some conditions for $\vec{\mathbf{x}}$ being a local minimum. The first theorem makes a statement about a property, a minimum *has to* fulfil:

Theorem 4.2 First-Order Necessary Condition
If $\vec{\mathbf{x}}_{\min}$ is a local minimum and f is continuously differentiable in an open neighbourhood of $\vec{\mathbf{x}}_{\min}$, then $\nabla f(\vec{\mathbf{x}}_{\min}) = \vec{\mathbf{0}}$.

A prove can be found in Nocedal & Wright (1999, p. 15). Theorem 4.2 does not distinguish between minima, maxima or turning-points. In all these cases, the gradient of the function vanishes and such points are called *stationary points*. Each minimum of a function is a stationary point, but not all stationary points are minima.

The next two theorems additionally make some statements about the Hessian matrix and its positive semidefiniteness. Any matrix $\underline{\mathsf{B}}$ is called *positive semidefinite* if for all $\vec{\mathbf{p}} \neq \vec{\mathbf{0}}$ it holds $\vec{\mathbf{p}} \cdot \underline{\mathsf{B}}\, \vec{\mathbf{p}} \geq 0$. As a consequence all eigenvalues λ_i of a positive semidefinite matrix are greater or equal zero.

Theorem 4.3 Second-Order Necessary Conditions
If $\vec{\mathbf{x}}_{\min}$ is a local minimum of f and $\underline{\mathsf{H}}$ is continuous in an open neighbourhood of $\vec{\mathbf{x}}_{\min}$, then $\nabla f(\vec{\mathbf{x}}_{\min}) = \vec{\mathbf{0}}$ and $\underline{\mathsf{H}}(\vec{\mathbf{x}}_{\min})$ is positive semidefinite.

The next theorem describes a *sufficient* condition on the derivatives of f, which guarantees, that $\vec{\mathbf{x}}_{\min}$ is a *strict* local minimum.

Theorem 4.4 Second-Order Sufficient Conditions
Suppose that $\underline{\mathsf{H}}$ is continuous in an open neighbourhood of $\vec{\mathbf{x}}_{\min}$ and that $\nabla f(\vec{\mathbf{x}}_{\min}) = \vec{\mathbf{0}}$ and $\underline{\mathsf{H}}(\vec{\mathbf{x}}_{\min})$ is positive definite. Then $\vec{\mathbf{x}}_{\min}$ is a strict local minimum of f.

Theorem 4.2 and 4.3 describe *necessary* properties of a minimum. Hence they can be used to locate the minimum $\vec{\mathbf{x}}_{\min}$ of a function f starting at an arbitrary point $\vec{\mathbf{x}}_0$. Theorem 4.4 then allows to test, whether this stationary point is a minimum. Note however, that one can think of cases, where a strict local minimum fails this test. The function $f(x) = x^4$ is

an example for such a case: Although the point $x = 0$ is a strict minimum, the Hessian matrix at this points vanishes.

Starting at an arbitrary point $\vec{\mathbf{x}}_0$ each minimization algorithm will generate a sequence of iterates $\{\vec{\mathbf{x}}_i\}_{i=0}^{\infty}$. The procedure is stopped, when either no more progress can be made or when a solution is approximated with sufficient accuracy. A suitable stopping criterion is easily derived from the first–order necessary condition 4.2: The norm of the gradient has to be lower than a given parameter ε:

$$\|\nabla f(\vec{\mathbf{x}}_i)\| \;\leq\; \varepsilon \qquad \varepsilon \in \mathbb{R} \tag{4.10}$$

where the norm has not necessarily to be the Euclidean norm. In the case of molecules, one often monitors the *root–mean–square* gradient[5], which is simply the norm of the gradient multiplied with $1/\sqrt{3\,N}$, where N is the number of atoms (see e.g. Leach, 2001, p. 273).

The following discussion will solely concentrate on so called *line search methods*, where iterations of the form

$$\vec{\mathbf{x}}_{k+1} = \vec{\mathbf{x}}_k + \alpha_k\, \vec{\mathbf{d}}_k \tag{4.11}$$

are considered. Here $\vec{\mathbf{d}}_k$ is a search direction and α_k is the length of step $\vec{\mathbf{d}}_k$, which is obtained by means of a one-dimensional minimization problem along the direction $\vec{\mathbf{d}}_k$:

$$\min_{\alpha_k > 0} f(\vec{\mathbf{x}}_k + \alpha_k\, \vec{\mathbf{d}}_k) \tag{4.12}$$

It is not necessary and also computational expensive to find an exact solution of problem (4.12), but instead one might accept a step length α_k, that only loosely approximates the minimum of (4.12). On the other hand, α_k has to suffice certain conditions, which are known as *Wolfe conditions* (Nocedal & Wright, 1999, p. 37 ff for a detailed discussion). The first one states, that α_k should yield a *sufficient decrease* of the objective function f, which is expressed by the following inequality:

$$f(\vec{\mathbf{x}}_k + \alpha_k\, \vec{\mathbf{d}}_k) \;\leq\; f(\vec{\mathbf{x}}_k) + c_1\, \alpha_k\, \nabla f(\vec{\mathbf{x}}_k) \cdot \vec{\mathbf{d}}_k \qquad \text{for } c_1 \in (0, 1) \tag{4.13}$$

The second (curvature) condition prevents the steps from being too small, by requiring α_k to satisfy:

$$\nabla f(\vec{\mathbf{x}}_k + \alpha_k\, \vec{\mathbf{d}}_k) \cdot \vec{\mathbf{d}}_k \;\geq\; c_2\, \nabla f(\vec{\mathbf{x}}_k) \cdot \vec{\mathbf{d}}_k \qquad \text{for } c_2 \in (c_1, 1) \tag{4.14}$$

One often modifies this curvature condition to force α_k to lie in a closer neighbourhood of the minimum of $\phi(\alpha_k) = f(\vec{\mathbf{x}}_k - \alpha_k\, \vec{\mathbf{d}}_k)$, than it can be achieved by the fulfilling equation (4.14). This *strong* Wolfe condition requires α_k to satisfy equation (4.13) and:

$$\left|\nabla f(\vec{\mathbf{x}}_k + \alpha_k\, \vec{\mathbf{d}}_k) \cdot \vec{\mathbf{d}}_k\right| \;\leq\; c_2 \left|\nabla f(\vec{\mathbf{x}}_k) \cdot \vec{\mathbf{d}}_k\right| \tag{4.15}$$

with $0 < c_1 < c_2 < \frac{1}{2}$. The difference from the normal Wolfe condition is that equation (4.15) prevents the derivative of $\phi(\alpha_k)$ from being too positive. Note however that each

[5] In a physical context this quantity is called *root-mean-square force*, since the gradient of a potential energy function has the meaning of a force.

step length α_k satisfying the *strong* Wolfe condition also satisfies the usual Wolfe condition (Nocedal, 1992). Such a step length exists for all smooth functions f, that are bounded from below. A line search algorithm, which fulfils both Wolfe conditions (4.13) and (4.14) is given by Moré & Thuente (1994). Other one–dimensional minimization algorithms are discussed in Press et al. (1992, chapter 10.4).

The other broad class of minimization algorithms, so called *trust–region* methods, will be omitted from the discussion here. The interested reader might refer to Nocedal & Wright (1999, chapter 4).

4.1.3 Conjugate gradient method

After the discussion of some conditions for the step length α_k (equations 4.13 and 4.14), one next has to choose a suitable search direction $\vec{\mathbf{d}}_k$. The most obvious choice it the *steepest descent direction* $\nabla f(\vec{\mathbf{x}}_k)$. Using Taylor's Theorem (4.1), one can show, that this search direction is the one along which f most rapidly decreases (see Nocedal & Wright, 1999, p. 21 f). But a closer inspection of this procedure shows, that in most cases it is only slowly converging to the local minimum (see section 4.1.6 for an example). As Press et al. (1992) point out, this is due to the fact, that the search directions $\vec{\mathbf{d}}_k$ and $\vec{\mathbf{d}}_{k+1}$ of two consecutive iterations are perpendicular to each other. The problem is tackled by constructing the new search direction $\vec{\mathbf{d}}_{k+1}$ to be *conjugate* to the previous search directions $\vec{\mathbf{d}}_k, \vec{\mathbf{d}}_{k-1}, \ldots$. Methods accomplishing this way of constructing a new search direction are called *conjugate gradient* methods[6]. A set of vectors $(\vec{\mathbf{d}}_0, \vec{\mathbf{d}}_1, \ldots, \vec{\mathbf{d}}_l)$ is called conjugate with respect to a symmetric, positive definite matrix $\underline{\mathsf{A}}$ if:

$$\vec{\mathbf{d}}_i \cdot \underline{\mathsf{A}}\, \vec{\mathbf{d}}_j = 0 \qquad \forall\, i \neq j \tag{4.16}$$

With these prerequisites the conjugate gradient algorithm for the minimization of nonlinear functions is given in algorithm 4.1 on page 60. It is completed by specifying the choice of the line search parameter α_k. As demonstrated by Nocedal & Wright (1999, p.121), the problem is that due to the second term in equation (4.17b) the search direction $\vec{\mathbf{d}}_k$ may fail to be a descent direction for ill chosen values of α_k. In order to ensure this, the step length α_k has to satisfy the *strong* Wolfe conditions (4.13) and (4.15).

One might show, that the search directions $\vec{\mathbf{d}}_k$ $(k = 0, 1, \ldots)$ resulting from algorithm 4.1 are conjugate to each other with respect to the Hessian matrix $\underline{\mathsf{H}}$ of f *without* knowing the matrix (see e.g. Chong & Żak, 1996, p.140 ff; or Miller, 2000, p.359 ff)! This holds true not only for quadratic functions f, but also for nonlinear functions by interpreting the quadratic form as a second-order Taylor series approximation (c.f. Eq. 4.9).

There exist numerous alternatives for the parameter β_k in the conjugate gradient algorithm 4.1. The formula given in equation (4.17a) is the original expression used by Fletcher & Reeves (1964), who presumably applied the conjugate gradient method to the minimiza-

[6] This kind of methods was first introduced by Hestenes & Stiefel (1952) for the numerical solution of linear equation systems (see also Press et al., 1992, chapter 2.7)

Algorithm 4.1 Conjugate Gradient method of Fletcher & Reeves

Require: Starting point $\vec{\mathbf{x}}_0$, convergence tolerance $\varepsilon > 0$
  Evaluate $f_0 = f(\vec{\mathbf{x}}_0)$ and $\nabla f_0 = \nabla f(\vec{\mathbf{x}}_0)$
  Set $\vec{\mathbf{d}}_0 = -\nabla f_0$ and $k \leftarrow 0$
  while $\|\nabla f_k\| > \varepsilon$ do
    Compute α_k
    Set $\vec{\mathbf{x}}_{k+1} = \vec{\mathbf{x}}_k + \alpha_k \vec{\mathbf{d}}_k$
    Calculate

$$\beta_{k+1}^{\mathrm{FR}} = \frac{\nabla f_{k+1} \cdot \nabla f_{k+1}}{\|\nabla f_k\|^2} \tag{4.17a}$$

    Calculate

$$\vec{\mathbf{d}}_{k+1} = -\nabla f_{k+1} + \beta_{k+1}^{FR}\, \vec{\mathbf{d}}_k \tag{4.17b}$$

    Set $k \leftarrow k + 1$
  end while

tion of nonlinear function for the first time. Another choice[7], which is often regarded as the best choice (Nocedal, 1992) was introduced by Polak & Ribière (1969):

$$\beta_k^{\mathrm{PR}} = \frac{\nabla f_{k+1} \cdot (\nabla f_{k+1} - \nabla f_k)}{\|\nabla f_k\|^2} \tag{4.18}$$

It is noteworthy, that for exact line searches and quadratic functions both forms of the quantity β_k are identical, i.e. $\beta_k^{\mathrm{FR}} = \beta_k^{\mathrm{PR}}$.

Many practical implementations of the conjugate gradient algorithm restart the iteration (4.17b) at every N_{reset} steps by setting $\beta_k = 0$ in equation (4.17a) or (4.18) taking a steepest descent step instead. This restarting refreshes the algorithm by erasing old information that may not be beneficial any more. It also ensures the global convergence of the algorithm (see Nocedal, 1992, and section 4.1.6).

The conjugate gradient is a rather simple and elegant algorithm for nonlinear minimization. Additionally this method is storage–efficient as it requires only a few N–dimensional vectors to be stored a part from the informations needed to specify the problem it self. To be more precise, the original form of Fletcher & Reeves needs to store the 3 N–dimensional vectors (the gradient, the search direction, and the point $\vec{\mathbf{x}}_k$). The modification due to Polak & Ribière (1969) requires the storage of an additional vector, namely the gradient of the preceding iteration. For an overview over the storage requirement of the different minimization algorithms see table 4.2 in section 4.1.7.

For this thesis the implementation of the conjugate gradient minimization method given by Press et al. (1992) was used. It utilises Brent's method of parabolic interpolation using first derivatives for the line minimization (see Press et al., 1992, chapter 10.2 and 10.3 for details).

[7]Further alternatives are given in the article of J. L. Nazareth about conjugate gradient methods in Floudas & Pardalos (2001).

4.1.4 Quasi–Newton methods

Consider the Taylor approximation of the objective function f in equation (4.9) and assume for one moment, that the Hessian $\underline{\mathsf{H}}$ of f is positive definite. By defining a function μ of the vector $\vec{\mathbf{d}}$ one locally approximates the function f by a quadratic function:

$$\mu(\vec{\mathbf{d}}) := f(\vec{\mathbf{x}}) + \nabla f(\vec{\mathbf{x}}) \cdot \vec{\mathbf{p}} + \frac{1}{2}\, \vec{\mathbf{d}} \cdot \underline{\mathsf{H}}(\vec{\mathbf{x}})\, \vec{\mathbf{d}} \approx f(\vec{\mathbf{x}} + \vec{\mathbf{d}}) \tag{4.19}$$

The vector $\vec{\mathbf{d}}$ which minimizes $\mu(\vec{\mathbf{d}})$ is obtained by using the first order necessary condition (4.2) and setting the derivative of μ to zero:

$$\mathbf{0} = \nabla\mu(\vec{\mathbf{d}}) = \nabla f(\vec{\mathbf{x}}) + \underline{\mathsf{H}}(\vec{\mathbf{x}})\, \vec{\mathbf{d}} \tag{4.20}$$

yielding the following, explicit expression for the so called *Newton direction*:

$$\vec{\mathbf{d}}^{\,\mathrm{N}} = -\underline{\mathsf{H}}^{-1}(\vec{\mathbf{x}})\, \nabla f(\vec{\mathbf{x}}) \tag{4.21}$$

which is another important search direction next to the steepest descent direction (see section 4.1.3). If the Hessian matrix is positive definite, the Newton direction is indeed a descent direction, which means that the angle θ between the gradient ∇f and the search direction is $\cos\theta < 0$ (Nocedal & Wright, 1999, p.22ff):

$$\nabla f \cdot \vec{\mathbf{d}}^{\,\mathrm{N}} = -\vec{\mathbf{d}}^{\,\mathrm{N}} \cdot \underline{\mathsf{H}}\, \vec{\mathbf{d}}^{\,\mathrm{N}} \leq -\sigma \left\| \vec{\mathbf{d}}^{\,\mathrm{N}} \right\|^2 \qquad \text{for } \sigma > 0 \tag{4.22}$$

If the Hessian matrix is *not* positive definite, it might happen that the Newton direction is either not defined or that is not a descent direction.

Methods using the Newton direction exhibit a fast rate of convergence. In the neighbourhood of the minimum such methods converge within a few iterations yielding a high accuracy of the solution. A major drawback of using the Newton step is the necessity to evaluate the Hessian matrix $\underline{\mathsf{H}}$, which for large N might be computationally expensive and error–prone. Furthermore one has to invert this matrix, which is often computational demanding too (see Nocedal & Wright, 1999, chapter 6, p. 135ff, for a discussion of *practical* Newton methods). The method to be presented in this section aims to alleviate this difficulty by approximating the inverse of the Hessian using solely the gradient of the function, which is used to update a matrix $\underline{\mathsf{B}}_k$ after each iteration step. Due to the proximity of these methods to the Newton methods, the name *quasi–Newton* methods has been coined for this class of algorithms, which are sometimes also called *variable metric methods*. Since the changes of the gradient at each step provide information about the curvature of the function f (i.e. the second derivative), it is possible to construct a sequence of matrices $\underline{\mathsf{B}}_k$ such that:

$$\lim_{k\to\infty} \underline{\mathsf{B}}_k = \underline{\mathsf{H}}^{-1} \tag{4.23}$$

Using this approach, one circumvents both disadvantages of the Newton method, namely the calculation of the Hessian matrix *and* its inversion. The main difference between

the different proposed methods is the way of updating the matrix $\underline{\mathsf{B}}_k$. Here we mainly introduce the different expressions but do not motivate them in detail. For a derivation of the formulas see for example Nocedal & Wright (1999, chapter 8) or Polak (1997, p. 104 ff).

The first variable metric method was introduced by Davidon (1959)[8] and was improved by Fletcher & Powell (1963). The so called *DFP* update formula reads as follows:

$$\underline{\mathsf{B}}_{k+1} = \underline{\mathsf{B}}_k - \frac{\underline{\mathsf{B}}_k \, \vec{\mathbf{y}}_k \, (\underline{\mathsf{B}}_k \vec{\mathbf{y}}_k)^T}{\vec{\mathbf{y}}_k \cdot \underline{\mathsf{B}}_k \, \vec{\mathbf{y}}_k} + \frac{\vec{\mathbf{s}}_k \, \vec{\mathbf{s}}_k^T}{\vec{\mathbf{y}}_k \cdot \vec{\mathbf{s}}_k} \tag{4.24}$$

where the quantities $\vec{\mathbf{s}}_k$ and $\vec{\mathbf{y}}_k$ are defined by

$$\vec{\mathbf{s}}_k = \vec{\mathbf{x}}_{k+1} - \vec{\mathbf{x}}_k \; , \qquad \vec{\mathbf{y}}_k = \nabla f_{k+1} - \nabla f_k \; . \tag{4.25}$$

Equation (4.24) illustrates the fundamental idea of quasi–Newton updating: Instead of recomputing the Hessian matrix $\underline{\mathsf{H}}_k$ (respectively its inverse $\underline{\mathsf{B}}_k$) at every iteration from scratch, quasi–Newton methods apply simple modifications, which make use of the already existing informations embedded in the current Hessian approximation *and* the knowledge about the objective function and its curvature gained during the last iteration stored in the vectors $\vec{\mathbf{s}}_k$ and $\vec{\mathbf{y}}_k$, respectively.

Although the DFP formula is quite efficient, it was soon replaced by an updating scheme, that was simultaneously but independently proposed by Broyden, Fletcher, Goldfarb, Shanno (all in 1970), and which is consequently called *BFGS* formula. The starting point for the deduction of the DFP formula (4.24) was the approximation of the Hessian matrix $\underline{\mathsf{H}}_k$ itself, which thereafter was transformed into an expression for the inverse Hessian matrix $\underline{\mathsf{B}}_k$ using the so called Sherman–Morrison–Woodbury formula (see Nocedal & Wright, 1999, p. 605). Contrary the BFGS formula is deduced starting with the inverse Hessian $\underline{\mathsf{B}}_k$, and imposing similar conditions on it, as has been done for the Hessian matrix (see Nocedal & Wright, 1999, p. 195ff for details). Then the BFGS update formula reads as follows:

$$\underline{\mathsf{B}}_{k+1} = \left(\underline{\mathsf{I}} - \rho_k \, \vec{\mathbf{s}}_k \, \vec{\mathbf{y}}_k^T\right) \, \underline{\mathsf{B}}_k \, \left(\underline{\mathsf{I}} - \rho_k \, \vec{\mathbf{y}}_k \, \vec{\mathbf{s}}_k^T\right) + \rho_k \, \vec{\mathbf{s}}_k \, \vec{\mathbf{s}}_k^T \tag{4.26}$$

where the scalar ρ_k is defined as:

$$\rho_k = \frac{1}{\vec{\mathbf{y}}_k \cdot \vec{\mathbf{s}}_k} \tag{4.27}$$

The description of the algorithm is completed by specifying how to choose the initial guess for the approximation $\underline{\mathsf{B}}_0$. Unfortunately, there exists no fail safe method, which works equally well for all cases. One possibility is to exploit some knowledge about the problem e.g. by calculating the Hessian matrix at the starting point either analytically or numerically. Henceforth we adopt a much simpler way by just using the identity matrix $\underline{\mathsf{I}}$ as the starting point. The complete algorithm is listed below (see algorithm 4.2).

[8] A short historical note: Davidon developed this method in the mid 1950s, because computers at that time were not stable enough to carry out long minimization calculations. So he developed the first quasi–Newton method, which turned out to be one of the most revolutionary ideas in nonlinear optimization. Ironically his original paper (Davidon, 1959) was not accepted for publication and remained a technical report until it appeared in the first issue of the *SIAM Journal on Optimization* (Davidon, 1991).

Algorithm 4.2 BFGS method

Require: A starting point $\vec{\mathbf{x}}_0$, convergence tolerance $\varepsilon > 0$,
approximation $\underline{\mathsf{B}}_0$ of the inverse Hessian
$k \leftarrow 0$
while $\|\nabla f_k\| > \varepsilon$ do
Calculate the search direction $\vec{\mathbf{d}}$:

$$\vec{\mathbf{d}}_k = -\underline{\mathsf{B}}_k \, \nabla f_k \tag{4.28}$$

Set $\vec{\mathbf{x}}_{k+1} = \vec{\mathbf{x}}_k + \alpha_k \vec{\mathbf{d}}_k$ where α_k is computed from a line search algorithm,
which satisfies the Wolfe conditions (4.13) & (4.14)
Define $\vec{\mathbf{s}}_k = \vec{\mathbf{x}}_{k+1} - \vec{\mathbf{x}}_k$ and $\vec{\mathbf{y}}_k = \nabla f_{k+1} - \nabla f_k$
Compute $\underline{\mathsf{B}}_{k+1}$ by means of equation (4.26)
$k \leftarrow k + 1$
end while

It is worth mentioning, that the BFGS update formula (4.26) for the *inverse* Hessian matrix $\underline{\mathsf{B}}_k$ can be converted to an expression for the Hessian matrix $\underline{\mathsf{H}}_k$ itself by means of the already mentioned Sherman–Morrison–Woodbury formula. One obtains:

$$\underline{\mathsf{H}}_{k+1} = \underline{\mathsf{H}}_k - \frac{\underline{\mathsf{H}}_k \, \vec{\mathbf{s}}_k \, (\underline{\mathsf{H}}_k \, \vec{\mathbf{s}}_k)^T}{\vec{\mathbf{s}}_k \cdot \underline{\mathsf{H}}_k \, \vec{\mathbf{s}}_k} + \frac{\vec{\mathbf{y}}_k \, \vec{\mathbf{y}}_k^T}{\vec{\mathbf{y}}_k \cdot \vec{\mathbf{s}}_k} \tag{4.29}$$

The similarity between equation (4.24) and (4.29) is rather striking[9] if one keeps in mind that by construction $\underline{\mathsf{H}}_k$ and $\underline{\mathsf{B}}_k$ changed their roles. This observation gave reason to define the *Broyden* class of quasi–Newton methods by introducing the following general update formula:

$$\underline{\mathsf{B}}_{k+1} = \underline{\mathsf{B}}_k - \frac{\underline{\mathsf{B}}_k \, \vec{\mathbf{s}}_k \, (\underline{\mathsf{B}}_k \, \vec{\mathbf{s}}_k)^T}{\vec{\mathbf{s}}_k \cdot \underline{\mathsf{B}}_k \, \vec{\mathbf{s}}_k} + \frac{\vec{\mathbf{y}}_k \, \vec{\mathbf{y}}_k^T}{\vec{\mathbf{y}}_k \cdot \vec{\mathbf{s}}_k} + \phi_k \, (\vec{\mathbf{s}}_k \cdot \underline{\mathsf{B}}_k \, \vec{\mathbf{s}}_k) \, \vec{\mathbf{v}}_k \, \vec{\mathbf{v}}_k^T \tag{4.30}$$

where the vector $\vec{\mathbf{v}}_k$ is defined by:

$$\vec{\mathbf{v}}_k = \left[\frac{\vec{\mathbf{y}}_k}{\vec{\mathbf{y}}_k \cdot \vec{\mathbf{s}}_k} - \frac{\underline{\mathsf{B}}_k \, \vec{\mathbf{s}}_k}{\vec{\mathbf{s}}_k \cdot \underline{\mathsf{B}}_k \, \vec{\mathbf{s}}_k} \right] \tag{4.31}$$

and ϕ_k is a scalar value, which in case of the *restricted* Broyden class is restricted to the interval $[0, 1]$. For $\phi_k = 0$ one gets the BFGS formula (4.26) and the DFP case is recovered by setting $\phi_k = 1$. At this point of the discussion it is beneficial to recall, that quasi–Newton methods compute the search direction $\vec{\mathbf{d}}_k$ in (4.11) pursuant to:

$$\vec{\mathbf{d}}_k = -\underline{\mathsf{G}}_k \, \nabla f_k \tag{4.32}$$

where the matrix $\underline{\mathsf{G}}_k$ has either the meaning of the Hessian or its inverse.

[9] The same similarity can be seen, if the DFP update formula (4.24) for the inverse Hessian matrix $\underline{\mathsf{B}}_k$ is transformed into one for the Hessian matrix $\underline{\mathsf{H}}_k$, which yields a expression similar to (4.26).

If one make use of an update formula for the inverse Hessian matrix, each iteration is performed at a computational cost of $\mathcal{O}(N^2)$ arithmetic operations (except for the computation of the function and its gradient). Using the Hessian instead raises the computational effort considerably due to the required matrix–matrix operations and the solution of a linear systems. In this case the computational effort scales with $\mathcal{O}(N^3)$.

Since quasi–Newton methods require the storage of the Hessian matrix (or its inverse), their memory requirement grows proportional to N^2, which in most cases prevent their application to large scale optimization problems like minimizing the potential energy of a cluster or protein with more than 100 atoms. Some methods, which elude this unfavourable scaling of the storage requirement, make use of the separability of the fitness function f. For example consider a function, which can be decomposed into N_e simpler functions g_i like:

$$f(\vec{\mathbf{x}}) = \sum_{i=1}^{N_e} g_i(x_k, \ldots, x_u) \tag{4.33}$$

where each function g_i depends only on a few components of $\vec{\mathbf{x}}$. As a consequence the gradient ∇f_i and the Hessian matrix contain only a few elements, which are not zero. Algorithms which utilise this properties are described in Nocedal & Wright (1999, chapter 9.5 & 9.6). Unfortunately the potential energy functions of clusters or molecules lack this property of separability. In this case, the functions g_i have to be interpreted as the potential energy of atom within the cluster, which on the other hand depends on the coordinates of all other atoms. Thus this kind of algorithms is not applicable to the optimization of cluster configurations.

Another method to reduce the memory requirement, is to choose a compact, implicit representation of the Hessian matrix. The most widely used method, the *limited–memory* BFGS, or L–BFGS algorithm for short, was introduced by Nocedal (1980).

In order to explicate the L–BFGS algorithm, equation (4.26) is rewritten as follows:

$$\underline{\mathsf{B}}_{k+1} = \underline{\mathsf{V}}_k^T \, \underline{\mathsf{B}}_k \, \underline{\mathsf{V}}_k + \rho_k \, \vec{\mathbf{s}}_k \, \vec{\mathbf{s}}_k^T \tag{4.34}$$

where

$$\underline{\mathsf{V}}_k = \underline{\mathsf{I}} - \rho_k \, \vec{\mathbf{y}}_k \, \vec{\mathbf{s}}_k^T \tag{4.35}$$

and ρ_k is defined as in equation (4.27). The main idea of Nocedals L–BFGS method is to store a prefixed number (M_{up}) of vector pairs $\{\vec{\mathbf{s}}_i,\ \vec{\mathbf{y}}_i\}$ (cf. Eq. 4.25), which *implicitly* define the matrix $\underline{\mathsf{B}}_k$. This would reduce the storage requirement from N^2 for the full matrix $\underline{\mathsf{B}}_k$, to $2\,M_{up}\,N$, for the two vectors $\vec{\mathbf{s}}_k$ and $\vec{\mathbf{y}}_k$. At each iteration, $\underline{\mathsf{B}}_k$ is calculated using ∇f_k and the M_{up} vectors $\vec{\mathbf{s}}_i$ and $\vec{\mathbf{y}}_i$. At the end of the iteration the oldest pair in $\{\vec{\mathbf{s}}_i,\ \vec{\mathbf{y}}_i\}$ is deleted and replaced by the new pair $\{\vec{\mathbf{s}}_k,\ \vec{\mathbf{y}}_k\}$ computed during the current step. It is generally accepted that modest values for M_{up} between 3 and 20 yield satisfactory results (see also section 4.1.6). The recursive updating scheme is the only difference to the original BFGS algorithm 4.2.

Nocedal (1980) derived a recursion formula for the matrix $\underline{\mathsf{B}}_k$ solely using the vectors $\{\vec{\mathbf{s}}_i,\ \vec{\mathbf{y}}_i\}$ and the current gradient ∇f_k. Presumed the initial guess for the matrix $\underline{\mathsf{B}}_k^0$

is positive definite, Nocedals expression ensures the positive definiteness of all following matrices $\underline{\mathsf{B}}_k$. The L–BFGS approximation of $\underline{\mathsf{B}}_k$ is given by:

$$\begin{aligned}\underline{\mathsf{B}}_{k+1} \;=\; & (\,\underline{\mathsf{V}}_{k-1}^T \cdots \underline{\mathsf{V}}_{k-M_{up}}^T\,)\,\underline{\mathsf{B}}_k^0\,(\,\underline{\mathsf{V}}_{k-M_{up}} \cdots \underline{\mathsf{V}}_{k-1}\,) \\ & + \rho_{k-M_{up}}\,(\,\underline{\mathsf{V}}_{k-1}^T \cdots \underline{\mathsf{V}}_{k-M_{up}+1}^T\,)\,\vec{\mathbf{s}}_{k-M_{up}}\,\vec{\mathbf{s}}_{k-M_{up}+1}^T(\,\underline{\mathsf{V}}_{k-M_{up}+1} \cdots \underline{\mathsf{V}}_{k-1}\,) \\ & + \rho_{k-M_{up}+1}\,(\,\underline{\mathsf{V}}_{k-1}^T \cdots \underline{\mathsf{V}}_{k-M_{up}+2}^T\,)\,\vec{\mathbf{s}}_{k-M_{up}+1}\,\vec{\mathbf{s}}_{k-M_{up}+1}^T(\,\underline{\mathsf{V}}_{k-M_{up}+2} \cdots \underline{\mathsf{V}}_{k-1}\,) \\ & + \ldots \\ & + \rho_{k-1}\,\vec{\mathbf{s}}_{k-1}\,\vec{\mathbf{s}}_{k-1}^T \end{aligned} \tag{4.36}$$

A procedure for the concrete computation of the product $\underline{\mathsf{B}}_k\,\nabla f_k$ is listed in algorithm 4.3 as pseudo–code.

Algorithm 4.3 L–BFGS two–loop recursion for the computation of the inverse Hessian

Require: $M_{up} > 0$
  Set $\vec{\mathbf{q}} \leftarrow \nabla f_k$
  for $i = k-1,\ k-2,\ \ldots,\ k-M_{up}$ do
    Set $\alpha_i \leftarrow \rho_i\,\vec{\mathbf{s}}_i^T\,\vec{\mathbf{q}}$
    Set $\vec{\mathbf{q}} \leftarrow \vec{\mathbf{q}} - \alpha_i\,\vec{\mathbf{y}}_i$
  end for
  Set $\vec{\mathbf{r}} \leftarrow \underline{\mathsf{B}}_k^0\,\vec{\mathbf{q}}$
  for $i = k-M_{up},\ k-M_{up}+1,\ \ldots,\ k-1$ do
    Set $\beta \leftarrow \rho_i\,\vec{\mathbf{y}}_i^T\,\vec{\mathbf{r}}$
    Set $\vec{\mathbf{r}} \leftarrow \vec{\mathbf{r}} + \vec{\mathbf{s}}_i\,(\alpha_i - \beta)$
  end for
  end with the result $\underline{\mathsf{B}}_k\,\nabla f_k = \vec{\mathbf{r}}$

If one does not consider the multiplication $\underline{\mathsf{B}}_k^0\,\vec{\mathbf{q}}$, the recursion scheme requires only $4\,M_{up}\,N$ multiplications, which is rather inexpensive, compared to the $\mathcal{O}(N^2)$ of the full BFGS algorithm. As a matter of principle one could vary the initial guess $\underline{\mathsf{B}}_k^0$ of the inverse Hessian matrix from iteration to iteration, which is unconsidered here. The complete L–BFGS algorithm is given as algorithm 4.4.

As it is evident from the description, the L–BFGS algorithm 4.4 and the BFGS method 4.2 are equivalent during the first $M_{up}-1$ iterations provided both use the same initial guess $\underline{\mathsf{B}}_0$. As Nocedal & Wright (1999) point out, it is possible to mimic the BFGS method by choosing a very high value for M_{up}, which is larger than the number of iterations actually needed until convergence is reached. Of course, as M_{up} gets larger than $N/2$, the memory required to store the vectors $\vec{\mathbf{s}}_k$ and $\vec{\mathbf{y}}_k$ gets larger, than that needed for $\underline{\mathsf{B}}_k$. The question, how the choice of M_{up} affects the performance of the L–BFGS minimization procedure is addressed in section 4.1.6. Next to the M_{up} vectors $\vec{\mathbf{s}}_k$ and $\vec{\mathbf{y}}_k$, the algorithm requires the storage of four additional vectors of length N, namely the current iterate $\vec{\mathbf{x}}_k$, the current and previous gradient ∇f_k and the current search direction $\vec{\mathbf{d}}_k$. Furthermore it is useful to store the auxiliary quantities ρ_i and α_i needed in algorithm 4.3, so that the total amount of storage is $2\,M_{up}\,N + 2\,M_{up} + 4\,N$ (cf. table 4.2).

Algorithm 4.4 Complete L–BFGS algorithm

Require: Starting point $\vec{\mathbf{x}}_0$, convergence tolerance $\varepsilon > 0$, and $M_{up} > 0$
  Set $k \leftarrow 0$
  while $\|\nabla f_k\| > \varepsilon$ do
    Chose $\underline{\mathsf{H}}_k^0$ /* *not considered here* */
    Calculate $\vec{\mathbf{d}}_k \leftarrow -\underline{\mathsf{B}}_k \nabla f_k$ using Algorithm 4.3
    Calculate $\vec{\mathbf{x}}_{k+1} \leftarrow \vec{\mathbf{x}}_k + \alpha_k \vec{\mathbf{d}}_k$, where α_k must satisfy the Wolfe conditions
    if $k > M_{up}$ then
      Discard the vector pair $\{\vec{\mathbf{s}}_{k-M_{up}}, \vec{\mathbf{y}}_{k-M_{up}}\}$ from storage
    end if
    Calculate and save $\vec{\mathbf{s}}_k \leftarrow \vec{\mathbf{x}}_{k+1} - \vec{\mathbf{x}}_k$ and $\vec{\mathbf{y}}_k \leftarrow \nabla f_{k+1} - \nabla f_k$.
    $k \leftarrow k + 1$
  end while

For this thesis a slightly modified implementation of the L–BFGS algorithm developed by Liu & Nocedal (1989) was used. The routine makes use of the line search algorithm by Moré & Thuente (1994, see also appendix D).

4.1.5 The downhill simplex algorithm

The *downhill simplex algorithm*[10] proposed by Nelder & Mead (1964) is an example for a multidimensional local minimization algorithm requiring only function evaluations and no derivatives. Its key idea can be easily explained, if one considers the one-dimensional case, as depicted in figure 4.1. A *first order* algorithm would start using two points a and b, with

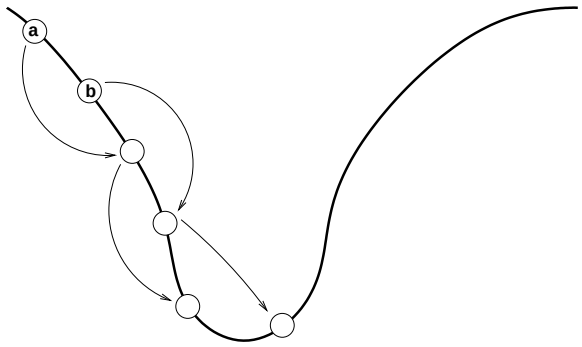

Figure 4.1: A simple minimization algorithm for the one dimensional case.

$f(a) > f(b)$, for which one assumes, that the minimum lies outside the interval (a, b). It will become clear later, what has to be done, if this is not true. The algorithm now moves the interval (a, b) along the graph of the function, until the minimum is bracketed by the two points a and b. This can be accomplished in several ways, e.g. by simply moving the

[10] Sometimes also called *sequential simplex method*.

point b (using e.g. a predefined step size δ) until the function value $f(b)$ starts raising. The drawback of this method, the enlargement of the interval (a, b), can be circumvented by reflecting point a with the higher functional value at point b, viz.:

$$a_{\text{new}} = b + \rho\,(b - a_{\text{old}}) \qquad \text{with } \rho > 0 \tag{4.37}$$

and swapping the two points afterwards, so $f(a) > f(b)$ holds again. This movement, illustrated by the arrows in figure 4.1, is repeated, until the reflection of point a moves upwards, indicating that no further improvement can be made by this operation. At this points of the algorithm one knows, that the minimum of $f(x)$ lies within the interval (a, b). One proceeds by reducing the size of the interval (a, b), contracting it into the direction of the lowest point. Suppose this is b, a new point a could be calculated according to:

$$a_{\text{new}} = b - \gamma\,(b - a_{\text{old}}) \qquad \text{with } 0 < \gamma < 1 \tag{4.38}$$

After this contraction the procedure of moving the interval and contracting is repeated until its size falls below a certain tolerance ε. In summary, this algorithm can be written in pseudo-code as shown in algorithm 4.5 on page 67.

Algorithm 4.5 A simple, one-dimensional minimization algorithm

```
Require: a, b, f(a) > f(b)  /* otherwise simply swap a and b */
  repeat
    a_new ← reflect point a at point b
    if f(a_new) < f(b) then
      a ← b
      b ← a_new
    else
      Contract interval using equation 4.38
    end if
  until Convergence criterion met
```

Of course this simple algorithm is not the best method one can think of for minimising a one-dimensional function. For more elaborate see e.g. Press et al. (1992, chapter 10.1 and 10.2) or Nocedal & Wright (1999, chapter 3). But while the more efficient algorithms can not be generalised to the N–dimensional case, this can be done for algorithm 4.5 quite naturally. The interval used in this algorithm consists of $2 = N + 1$ points, which define a geometric object called *simplex* $\mathcal{S}_N$ (see figure 4.2). Thus in N dimensions one only has to move this simplex properly, using similar operations (reflection and contraction) in order to minimise a N–dimensional function. Nelder & Mead (1964) introduced four different operations on an initial simplex consisting of $N + 1$ points, called *vertices* $\vec{\mathbf{p}}_i$ (see figure 4.2). Further ingredients of the algorithms are the function values $f(\vec{\mathbf{p}}_i)$ at the vertices, which are ordered according to their function values. The point $\vec{\mathbf{p}}_h$ is the point with the highest, $\vec{\mathbf{p}}_{sh}$ that one with the second highest, and $\vec{\mathbf{p}}_l$ that one with the lowest function

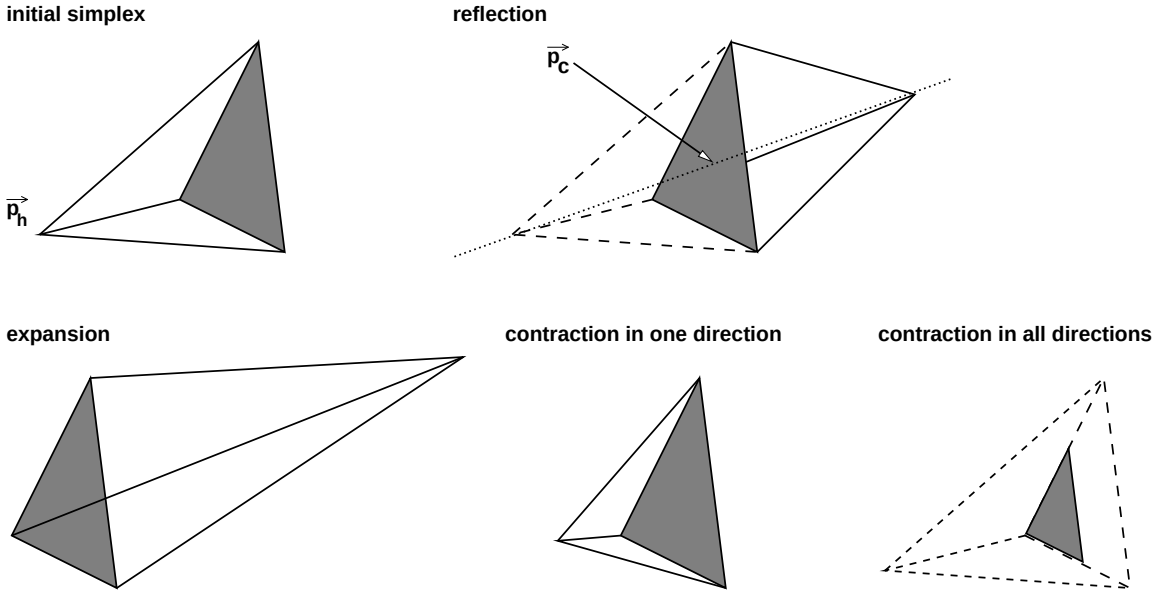

Figure 4.2: Elementary operations of a simplex $\mathcal{S}_N$ in 3 dimensions, which is a tetrahedron, not necessarily a regular one. The point $\vec{\mathbf{p}}_h$ indicates the point with the highest function value. The point $\vec{\mathbf{p}}_c$ defines the centre of mass of the 3 remaining points (without $\vec{\mathbf{p}}_h$), which in this case form the shaded triangle.

value. It is useful to define the *centroid of the simplex* $\mathcal{S}_N$ (excluding the highest function value vertex) by:

$$\vec{\mathbf{p}}_c = \frac{1}{N} \sum_{\substack{i=1 \\ \vec{\mathbf{p}}_i \neq \vec{\mathbf{p}}_h}}^{N+1} \vec{\mathbf{p}}_i \tag{4.39}$$

With this Nelder & Mead (1964) introduced the following basic simplex operations, which are additionally visualised in figure 4.2:

1. **Reflection** of the point $\vec{\mathbf{p}}_h$ with the highest function value through the opposite face of the simplex, creating a new point $\vec{\mathbf{p}}_r$. The reflected point is constructed by:

$$\vec{\mathbf{p}}_r = \vec{\mathbf{p}}_c + \rho\,(\vec{\mathbf{p}}_c - \vec{\mathbf{p}}_h) \tag{4.40}$$

   with $\rho > 0$ the *reflection coefficient*. The new point $\vec{\mathbf{p}}_r$ lies on a line joining the points $\vec{\mathbf{p}}_c$ and $\vec{\mathbf{p}}_h$.

2. **Expansion** of the simplex in the direction of the new point $\vec{\mathbf{p}}_r$, away from the highest point $\vec{\mathbf{p}}_h$. This operation is performed, when the function value of the new vertex $\vec{\mathbf{p}}_r$, obtained by the reflection operation, is better then the best value of the starting simplex, i.e. $f(\vec{\mathbf{p}}_r) < f(\vec{\mathbf{p}}_l)$. The new point $\vec{\mathbf{p}}_e$ is calculated according to:

$$\vec{\mathbf{p}}_e = \vec{\mathbf{p}}_c + \chi\,(\vec{\mathbf{p}}_r - \vec{\mathbf{p}}_c) \tag{4.41}$$

with $\chi > 1$ the *expansion coefficient*[11].

3. **Contraction** of the simplex in one direction from the highest point. If for the function value of the new point $\vec{\mathbf{p}}_r$ it holds, that $f(\vec{\mathbf{p}}_r) > f(\vec{\mathbf{p}}_{sh})$, a point $\vec{\mathbf{p}}_{cc}$ is calculated according to:
$$\vec{\mathbf{p}}_{cc} = \vec{\mathbf{p}}_c - \gamma\,(\vec{\mathbf{p}}_c - \vec{\mathbf{p}}_h) \tag{4.42}$$
with $0 < \gamma < 1$ the *contraction coefficient*.

4. **Contraction** along all directions towards the lowest point. If the algorithm still did not touchdown an improvement, the simplex $\mathcal{S}_N$ is contracted as a whole, viz.:
$$\vec{\mathbf{p}}_i = \vec{\mathbf{p}}_l + \sigma\,(\vec{\mathbf{p}}_i - \vec{\mathbf{p}}_l) \qquad \forall\ \vec{\mathbf{p}}_i \neq \vec{\mathbf{p}}_l \tag{4.43}$$
with $0 < \sigma < 1$ the *shrinkage coefficient*.

Using these basic moves the simplex tries to adjust itself to the local topology of the function to be optimised. A detailed overview of the algorithm is given below (see listing for algorithm 4.6).

It is noteworthy, that especially regarding the conditions for the contraction operations, exist some ambiguities in the original paper of Nelder & Mead (1964). They are clarified in the paper by Lagarias et al. (1998). Particularly these authors introduce a second kind of contraction, they call *outside contraction*, which is omitted here. The standard values of the coefficients ρ, χ, γ and σ are:

$$\rho = 1\,, \quad \chi = 2\,, \quad \gamma = \frac{1}{2}\,, \quad \text{and} \quad \sigma = \frac{1}{2}$$

Comparing equations (4.40) to (4.43) with the corresponding expressions (4.37) and (4.38), the similarity between the one-dimensional minimization algorithm sketched above and the Nelder–Mead procedure becomes evident!

Because the algorithm does not require any derivatives, one can not use the condition discussed in section 4.1.2 to terminate the minimization process. Instead of this one has to use the function values at the $N+1$ vertices in order to estimate how close to the minimum one might be. Press et al. (1992) e.g. simply compare the highest and the lowest function values. This method sometimes proved to be impractical, because it led to a nearly degenerate simplex (i.e. a simplex, where all points are (almost) equal), before the tolerance indicated the convergence of the algorithm. Instead of this the original convergence criterion introduced by Nelder & Mead (1964) was used throughout the following discussion. They calculate the standard deviation of the function values, according to:

$$\varepsilon_{\mathrm{NM}} = \sqrt{\frac{1}{N+1}\sum_{i=1}^{N+1}\left(f(x_i) - \langle\, f \,\rangle\right)^2} \tag{4.44}$$

[11] If $\chi = 1$ the expansion and reflection operations are identical.

Algorithm 4.6 Pseudo-code for the downhill simplex algorithm by Nelder & Mead (1964).

```
Require: N + 1 points p_i in R^N forming a simplex, f(p_i)
  repeat
    Sort p_i according to their function values, determine p_h, p_sh, and p_l
    p_try ← reflection of p_h using equation (4.40)
    if f(p_try) < f(p_l) then
      p_h ← p_try
      p_try ← expansion of the simplex using equation (4.41)
      if f(p_try) < f(p_l) then
        p_h ← p_try
      end if
    else
      if f(p_try) > f(p_sh) then
        p_try ← one-dimensional contraction using equation (4.42)
        if f(p_try) > f(p_h) then
          Contraction of the whole simplex using equation (4.43)
        else
          p_h ← p_try
        end if
      else
        p_h ← p_try
      end if
    end if
  until convergence criterion met or maximum number of iterations exceeded
```

and require to fall $\varepsilon_{\mathrm{NM}}$ below an predefined value within a certain number of iterations.

An analysis of the performance of the downhill simplex algorithm will be given in the following section, where it will be compared with the two other minimization algorithms presented in section 4.1.3 and 4.1.4, respectively. One main advantage of the outlined algorithm is, that it is not necessary to compute the gradient of the function. Furthermore the Nelder–Mead method is appealing because its steps are simple to program. This benefits are counteracted by the rather large memory requirement of the algorithm: The storage of the $N + 1$ vertices (each is a N–dimensional vector) and the same number of function values, add up to $N(N + 2) \approx N^2$ numbers, which is appreciable more, than the other algorithms met so far. An application of this method to the parametrisation of force–fields for liquids is presented by Faller et al. (1999).

4.1.6 On the convergence of local minimization algorithms

After we discussed, how the different minimization algorithms work, we next want to address the question, how well they work. This comprises two different aspects:

1. Global convergence: Starting at an arbitrary point $\vec{\mathbf{x}}_0$, will the iterates converge to a solution of the minimization problem?

2. Rate of convergence: How fast converges an algorithm to the solution?

The first question is of rather theoretical interest and can only be answered by using an elaborate machinery from analysis, because it is impossible to try all possible starting points. In contrast the second question is of great practical importance, if one has to choose a suitable algorithm for a given problem. In some cases one might find analytical expressions for an asymptotic rate of convergence (as discussed e.g. in Nocedal, 1992). Otherwise one has to fall back on numerical tests.

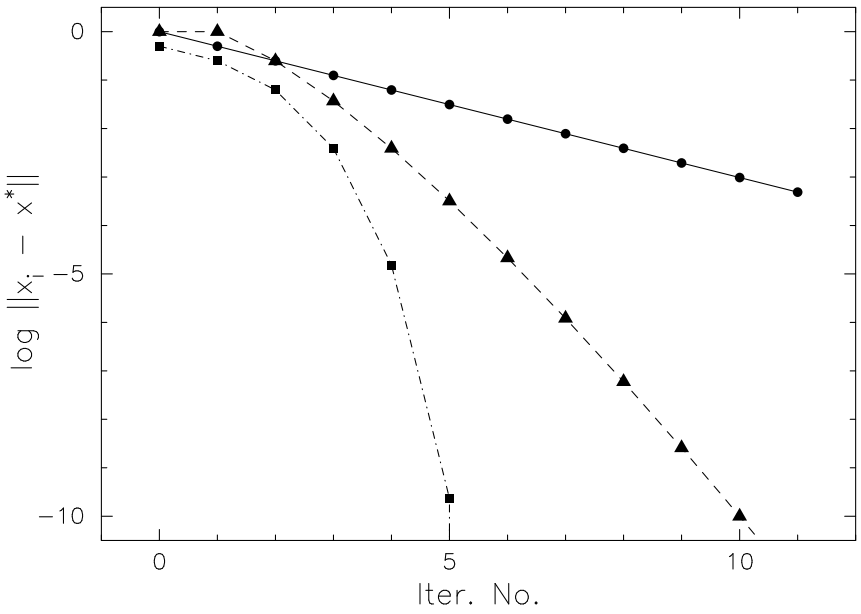

Figure 4.3: Illustration of the three different convergence rates. For three different sequences, which all converge to $x^* = 1$, the logarithmic error $\|x_i - x^*\|$ has been plotted. •: The *linear* convergent sequence $1 + (0.5)^k$. ▲: The *superlinear* convergent sequence $1 + k^{-k}$. ■: The *quadratic* convergent sequence $1 + (0.5)^{2^k}$. The examples have been taken from Nocedal & Wright (1999, p.29).

The convergence rate of the algorithms is often described in terms like *linear* or *quadratic* convergence. What does this mean? Consider a sequence of points $\{\vec{\mathbf{x}}_k\} \in \mathbb{R}^N$ that converges to $\vec{\mathbf{x}}^*$. If the distance to the solution $\vec{\mathbf{x}}^*$ decreases at each iteration by at least a constant factor, the convergence is called *linear*, viz.:

$$\frac{\|\vec{\mathbf{x}}_{k+1} - \vec{\mathbf{x}}^*\|}{\|\vec{\mathbf{x}}_k - \vec{\mathbf{x}}^*\|} \leq c \qquad \text{for all } k \text{ sufficiently large and } c \in (0,1) \tag{4.45}$$

To be more precisely equation (4.45) defines a Q-linear convergent sequence, but following Nocedal & Wright (1999) the letter Q is omitted throughout this thesis[12].

[12]Polak (1997) additionally defines the term R-linear convergent which is not used here.

The convergence is called *superlinear* if

$$\lim_{k\to\infty} \frac{\|\vec{\mathbf{x}}_{k+1} - \vec{\mathbf{x}}^*\|}{\|\vec{\mathbf{x}}_k - \vec{\mathbf{x}}^*\|} = 0 \tag{4.46}$$

Superlinear convergence is faster than linear convergence but not as fast as *quadratic* convergence, which is obtained if:

$$\frac{\|\vec{\mathbf{x}}_{k+1} - \vec{\mathbf{x}}^*\|}{\|\vec{\mathbf{x}}_k - \vec{\mathbf{x}}^*\|^2} \leq M \qquad \text{for all } k \text{ sufficiently large and } M > 0 \tag{4.47}$$

where M is a positive constant. Note that the speed of convergence depends on c and (more weakly) on M, and that the precise values for these constants depend not only on the algorithm but also on the properties of the particular problem. Figure 4.3 illustrates the three different convergence rates, so one might see at a first glance on the progress of the function values, what kind of convergence rate is at hand.

Before some practical aspects of the performance of the different minimization algorithms are discussed, some results about their global convergence and their convergence rates are summarised. For details, the reader might be referred to the already mentioned publications by Nocedal & Wright (1999), Nocedal (1992) or Polak (1997).

4.1.6.1 Convergence properties of the steepest descent and the conjugate gradient method

The discussion first focuses onto the steepest descent and the related conjugate gradient method by stating an important theorem due to Zoutendijk (see Nocedal & Wright, 1999, page 43).

Theorem 4.5 Zoutendijk's Theorem
Consider any line search method, where the iteration is of the form (4.11), where $\vec{\mathbf{d}}_k$ *is a descent direction and* α_k *satisfies the Wolfe conditions (4.13) & (4.14). Suppose that* f *is bounded below in* $\mathbb{R}^N$ *and that* f *is continuously differentiable in an open set* $\mathcal{N}$ *containing the level set* $\mathcal{L} := \{\vec{\mathbf{x}} \mid f(\vec{\mathbf{x}}) \leq f(\vec{\mathbf{x}}_0)\}$*, where* $\vec{\mathbf{x}}_0$ *is the starting point of the iterations. Assume also that the gradient* ∇f *is Lipschitz continuous on* $\mathcal{N}$*, that is, there exists a constant* $L > 0$ *such that:*

$$\|\nabla f(\vec{\mathbf{x}}) - \nabla f(\vec{\mathbf{x}}^*)\| \leq L \|\vec{\mathbf{x}} - \vec{\mathbf{x}}^*\|, \qquad \text{forall } \vec{\mathbf{x}},\ \vec{\mathbf{x}}^* \in \mathcal{N} \tag{4.48}$$

Then

$$\sum_{k\geq 0} \cos^2\theta_k \, \|\nabla f_k\|^2 < \infty. \tag{4.49}$$

Remember, that θ_k is the angle between the steepest descent direction $-\nabla f_k$ and the current search direction $\vec{\mathbf{d}}_k$, defined by:

$$\cos\theta_k = \frac{-\nabla f_k \cdot \vec{\mathbf{d}}_k}{\|\nabla f_k\| \, \|\vec{\mathbf{d}}_k\|} \tag{4.50}$$

Theorem 4.5 has far reaching consequences. The most appealing one is obtained, if one assures, that the search direction $\vec{\mathbf{d}}_k$ is *never* perpendicular or almost perpendicular to the gradient. With this if follows that $\cos\theta_k \geq \delta > 0$ for all k, and consequently:

$$\lim_{k\to\infty} \|\nabla f_k\| = 0 \tag{4.51}$$

which means, that the sequence of gradients converges to zero. In particular this holds true for the steepest descent method, where the search direction is identical to the gradient and thus the angle is zero. Note however, that theorem 4.5 does not make any statements about how *fast* the steepest descent method will converge. It only states, that it *will* converge, provided that one waits long enough. How long one has to wait is stated by the following theorem given by Nocedal & Wright (1999, p. 49), which quantifies the rate of convergence of the steepest descent algorithm in terms of the eigenvalues of the Hessian matrix:

Theorem 4.6
Suppose that $f : \mathbb{R}^N \to \mathbb{R}$ is twice continuously differentiable, and that the iterates generated by the steepest descent method with exact line searches converge to a point $\vec{\mathbf{x}}^*$, where the Hessian matrix $\underline{\mathsf{H}}(\vec{\mathbf{x}}^*)$ is positive definite. Then:

$$f(\vec{\mathbf{x}}_{k+1}) - f(\vec{\mathbf{x}}^*) \leq \left(\frac{\lambda_N - \lambda_1}{\lambda_N + \lambda_1}\right)^2 [f(\vec{\mathbf{x}}_k) - f(\vec{\mathbf{x}}^*)] \tag{4.52}$$

where $\lambda_1 \leq \ldots \leq \lambda_N$ are the eigenvalues of $\underline{\mathsf{H}}(\vec{\mathbf{x}}^*)$.

Nocedal (1992) notes, that this is the worst–case global behaviour of the steepest descent method. It is apparent from equation (4.52), that the asymptotic rate of convergence of the sequence $\{f(\vec{\mathbf{x}}_k)\}_{k=0}^{\infty}$ is linear (c.f. Eq. 4.45), with a constant, that depends on the largest and smallest eigenvalues of the Hessian matrix. The ratio $\kappa = \lambda_{max}/\lambda_{min}$ is the so called condition number of the Hessian matrix (e.g. Golub & van Loan, 1996). Obviously, if κ is large, the term inside the brackets of equation (4.52) is close to 1 and the convergence will be slow.

Unfortunately things are not that easy for the conjugate gradient method. Under the same assumptions as in Zoutendijk's theorem one can prove the following statement (Nocedal & Wright, 1999, p. 128ff) about the convergence of the Fletcher–Reeves conjugate gradient method:

Theorem 4.7
Suppose that the assumptions of theorem 4.5 hold, and that algorithm 4.1 is implemented with a line search that satisfies the strong Wolfe condition (4.15). Then

$$\liminf_{k\to\infty} \|\nabla f_k\| = 0 \tag{4.53}$$

which means, that the sequence of gradients $\{\nabla f_k\}$ is at least not *bounded away from zero.*

A similar theorem for the Polak–Ribière method can be proved only for the case of convex functions and an exact line search. This is rather surprising, since it is generally accepted, that this conjugate gradient variant performs better in practise than the original Fletcher–Reeves form. On the other hand it can be shown by using Zoutendijk's theorem, that each algorithm, which is periodically restarted by taking a steepest descent step, is globally convergent.

As for the global convergence it is not possible to make any general statements about the convergence rate of the conjugate gradient algorithm. Depending on the assumptions made concerning the applied line search method etc. different convergence rates can be deduces Nocedal (see 1992). In most cases at least a linear convergence is obtained.

4.1.6.2 Convergence properties of quasi–Newton methods

The situation is similar for the BFGS method, although the method has been proved to be remarkably robust in many practical applications (see also the overview given in section 4.1.7): Global convergence can be only proved under certain, rather restrictive assumptions as e.g. the convexity of the cost function f. In this case the rate of convergence is superlinear. This applies to all update formulas in the restricted Broyden class (c.f. Eq. 4.30) as has been shown by Byrd et al. (1987). To make things worse, Dai (2002) gives a constructed example of a non-convex function f, for which the BFGS method using a line search method satisfying the Wolfe conditions *can not* converge but instead cycles around six non-stationary points. On the other hand Li & Fukushima (2001) propose a modified, *cautious* BFGS update formula, for which they can prove global convergence. Their main idea is to modify the matrix $\underline{\mathsf{B}}_k$ only, if a cautious rule is fulfilled. Otherwise $\underline{\mathsf{B}}_k$ is left unchanged. Li & Fukushima (2001) observe by numerical experiments, that their rule is generally satisfied, implying that the BFGS methods is indeed mostly *cautious*, which explains, why it seldom fails in practical applications.

It was shown by Dennis & Moré (1974) that a necessary condition for the superlinear convergence of a line search method (4.11) is, that the search direction $\vec{\mathbf{d}}_k$ asymptotically approximates the Newton direction $\vec{\mathbf{d}}_k^{\mathrm{N}}$:

$$\alpha_k \, \vec{\mathbf{d}}_k = \vec{\mathbf{d}}_k^{\mathrm{N}} + o(\|\vec{\mathbf{d}}_k^{\mathrm{N}}\|) \tag{4.54}$$

Equation (4.54) can be rewritten as follows (Nocedal & Wright, 1999, p. 50):

$$\lim_{k\to\infty} \frac{\|(\underline{\mathsf{B}}_k - \underline{\mathsf{H}}(\vec{\mathbf{x}}^*)) \, \vec{\mathbf{d}}_k\|}{\|\vec{\mathbf{d}}_k\|} = 0 \tag{4.55}$$

where $\vec{\mathbf{x}}^*$ denotes a stationary point ($\nabla f(\vec{\mathbf{x}}^*) = 0$). Thus, for a superlinear convergence it is *not* necessary, that the sequence of quasi–Newton matrices $\underline{\mathsf{B}}_k$ converges to the Hessian matrix $\underline{\mathsf{H}}(\vec{\mathbf{x}}^*)$. Instead of this it suffices that *along the search direction* $\vec{\mathbf{d}}_k$ the Hessian matrix is approximated with increasing accuracy by the matrices $\underline{\mathsf{B}}_k$. This condition is normally satisfied by quasi–Newton methods as discussed by Nocedal & Wright (1999,

p. 214 ff). They show, that under the additional assumption, that the Hessian matrix is Lipschitz continuous at $\vec{\mathbf{x}}^*$, the BFGS algorithm attains a superlinear convergence rate.

The only publication we are aware of, which investigates the convergence properties of the limited–memory BFGS method, is the paper by Liu & Nocedal (1989), where they show, that the L–BFGS method is globally convergent and that its convergence rate is linear[13]. Unfortunately their prove premises that the function is uniformly convex and thus is not applicable to more general cases.

4.1.6.3 Convergence properties of the downhill simplex algorithm

The downhill simplex algorithm belongs to the class of *direct search methods*, which among others have been studied by Torczon (1991). While most of the algorithms in this class explore at every iteration each of N linearly independent directions, the Nelder–Mead algorithm searches only in one single direction each iteration. Because all known proves of convergence for this class of minimization algorithms rely on the linear independence of the search directions, a prove is still missing for the downhill simplex algorithm for all dimensions except for the case $N = 1$ (Lagarias et al., 1998). To make things worse, McKinnon (1998) gave an example, where the algorithm converged to a non-stationary point.

4.1.6.4 Two concrete examples

Subsequent to this theoretical discussion, we now turn to some more practical considerations and compare the performance of the different local minimization algorithms presented previously (namely steepest descent, conjugate gradient, L–BFGS method, and downhill simplex). To this end we first focus on two different test functions commonly used for investigating the convergence behaviour of optimization algorithms (see Moré et al., 1981, for more examples).

The first function can be viewed as a generalisation of the well know sphere function (see e.g Bäck, 1996), which is defined as:

$$f_{\text{sphere}}(\vec{\mathbf{x}}) = \sum_{i=1}^{N} x_i^2 \qquad \text{with } \vec{\mathbf{x}} \in \mathbb{R}^N \tag{4.56}$$

and is an example of a continuous, convex, unimodal function. By introducing N parameters a_i one deforms the sphere into an ellipsoid and the corresponding test function reads as follows:

$$f_{\text{ellipsoid}}(\vec{\mathbf{x}}) = \sum_{i=1}^{N} a_i \, x_i^2 \qquad \text{with } \vec{\mathbf{x}} \in \mathbb{R}^N \tag{4.57}$$

For the gradient of this function it holds:

$$\frac{\partial}{\partial x_i} f_{\text{ellipsoid}} = 2 \, a_i \, x_i \tag{4.58}$$

[13] To be exact, it is R–linear, see Polak (1997)

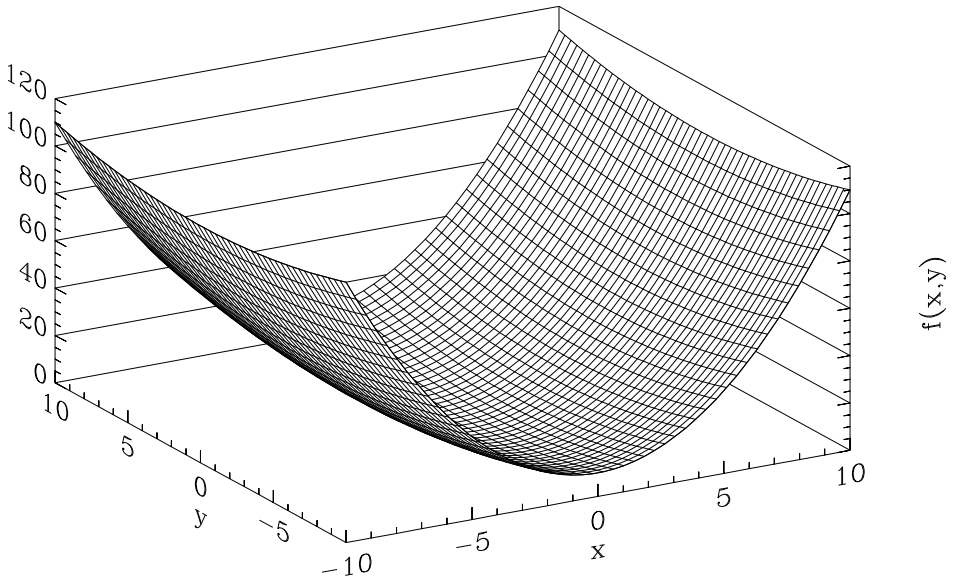

Figure 4.4: A three dimensional view of the ellipsoid function (4.57) with the parameters $a_1 = 1.0$ and $a_2 = 0.1$

With this one easily shows, that the point $(0, 0, \ldots, 0)$ is the global minimum of the function. The Hessian matrix, needed for the convergence analysis of the steepest descent method according to theorem 4.6, reads as follows:

$$\underline{\mathsf{H}}(f_{\text{ellipsoid}}) = \begin{pmatrix} 2a_x & 0 \\ 0 & 2a_y \end{pmatrix} = \begin{pmatrix} 2 & 0 \\ 0 & 0.2 \end{pmatrix} \qquad \text{if } a_x = 1.0 \ \wedge \ a_y = 0.1$$

Thus one has for the condition number and the factor in equation (4.52):

$$\kappa = \frac{a_x}{a_y} = 10 \qquad \left(\frac{\lambda_N - \lambda_1}{\lambda_N + \lambda_1}\right)^2 = \left(\frac{a_x - a_y}{a_x + a_y}\right)^2 = 0.6694$$

A three dimensional view is depicted in figure 4.4. As one sees, the function resembles a long valley along the axis with the lower coefficient a_i, in this case the y-axis. Such valleys with a small gradient are generally difficult to handle for most local minimization algorithms, which is demonstrated in figure 4.5, where the results of an optimization calculation for the four different algorithms discussed above, are illustrated.

Obviously the L–BFGS method is the fastest method. Comparing the upper panel of figure 4.5 with the illustrative example of the different types of convergence in figure 4.3 one might presume, that in this case the L–BFGS method exhibits at least a superlinear or even quadratic convergence rate, while the other all are linearly convergent. Note, that theoretically predicted convergence rates display the worst case behaviour! Interestingly the simple steepest descent method is not significantly worse than the conjugate gradient method. The performance of the downhill simplex algorithm is similar to that of the steepest descent method, although it does not reach as low function values as the other

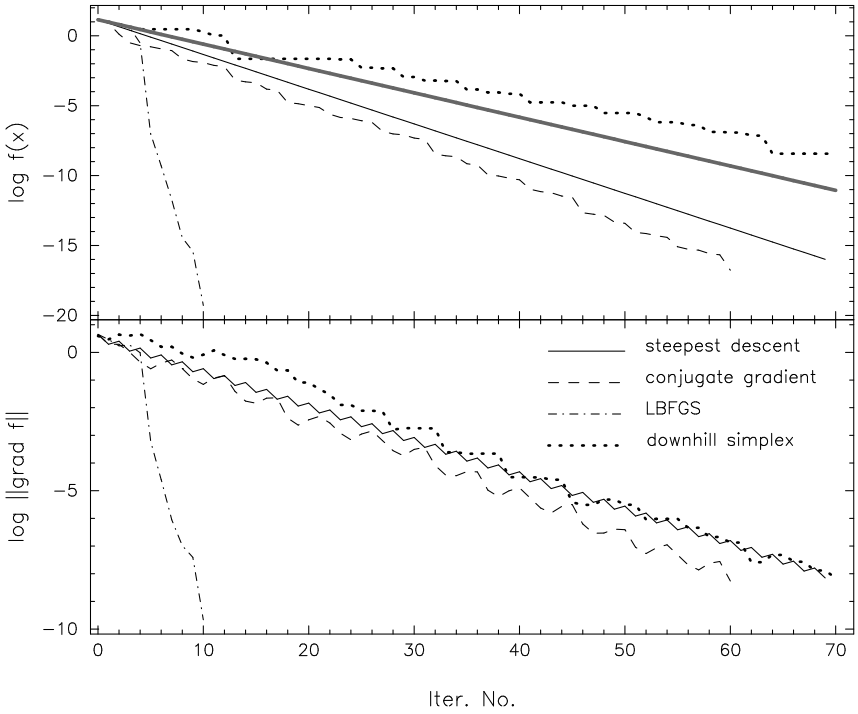

Figure 4.5: Comparison of the convergence behaviour of four different local minimization algorithms for the ellipsoid function (4.57) starting at the point $(2, 2)$. The parameters for the function are $a_x = 1$ and $a_y = 0.1$ (see figure 4.4). The upper panel shows the evolution of the function values during a minimisation run, while the lower panel monitors the norm of the gradient $\|\nabla f\|$. The thick, dark grey line in the upper panel shows the theoretical convergence behaviour of the steepest descent algorithm as determined by equation (4.52).

minimization algorithms. Remember, that the convergence in this case is not monitored using the gradient but the standard deviation of the function values (c.f. Eq. 4.44).

It is intriguing to analyse the *minimization trajectory*. With this term the way of an algorithm on the hypersurface, which leads from a starting point to a (possible) solution, is meant. Consider for example the steepest descent algorithm, where the search direction is defined solely by the gradient through:

$$\vec{\mathbf{r}}_{i+1} = \vec{\mathbf{r}}_i - \alpha_{i+1}\, \nabla f(\vec{\mathbf{r}}_i) \qquad \text{with} \quad \min_{\lambda>0} f(\vec{\mathbf{r}}_i - \alpha_{i+1}\, \nabla f(\vec{\mathbf{r}}_i)) \tag{4.59}$$

In case of the ellipsoid function (4.57) one can calculate the minimization trajectory analytically, which is briefly demonstrated, restricting the discussion without the loss of generality to two dimensions. Using equation (4.58) and (4.59) one finds for the function value at the point $\vec{\mathbf{r}}_{i+1}$:

$$f(\vec{\mathbf{r}}_i, \lambda) = a_x\, x_i^2\, (1 - 2\lambda a_x) + a_y\, y_i^2\, (1 - 2\lambda a_y) \tag{4.60}$$

Using standard techniques from analysis one finds for the minimum $\lambda_{\min}$ of this equation:

$$\lambda_{\min} = \frac{a_x^2 x_i^2 + a_y^2 y_i^2}{2(a_x^3 x_i^2 + a_y^3 y_i^2)} \tag{4.61}$$

With this result and equation (4.59) and (4.58) the coordinates $\vec{\mathbf{r}}_{i+1} = (x_{i+1}, y_{i+1})$ of the next iteration step are given by:

$$x_{i+1} = \frac{a_y(a_y^2 - a_x\, a_y)x_i\, y_i^2}{a_x^3 x_i^2 + a_y^3 y_i^2} \tag{4.62a}$$

$$y_{i+1} = \frac{a_x(a_x^2 - a_x\, a_y)x_i^2\, y_i}{a_x^3 x_i^2 + a_y^3 y_i^2} \tag{4.62b}$$

For a *perfect* sphere (i.e. $a_x = a_y$) it follows that the steepest descent algorithm hits the minimum in one step, which of course holds true for each algorithm, using the gradient of a function. On the other hand, equation (4.62) shows, that for the ellipsoid function (i.e. $a_x \neq a_y$) the steepest descent algorithm needs more than one iteration.

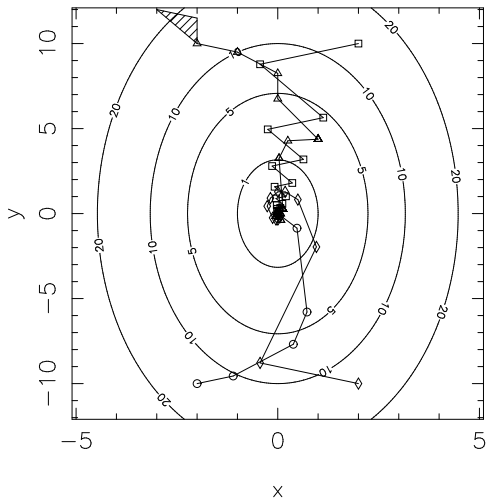

Figure 4.6: Minimization trajectories for the ellipsoid function with the parameters $a_x = 1$ and $a_y = 0.1$ using four different minimization algorithms. △: downhill simplex algorithm; □: steepest descent; ♢: conjugate gradient; ◯: L–BFGS method. The minimization runs started at the points $(-2, 10)$, $(2, 10)$, $(2, -10)$, and $(-2, -10)$ respectively. Due to the symmetry of the function these four points are in that sense *equivalent*, that a minimization starting at any of these points goes through the same functions values and the coordinates of the trajectories have the same absolute values $|x_i|$.

In figure 4.6 the minimization trajectory for the four different algorithms under consideration are presented[14]. Note, that the y– and x–axis have different scales, which distorts

[14] Although one could use equation (4.62) to calculate the trajectory for the steepest descent method, the data shown in figure 4.6 where obtained numerically. They agree with the analytic trajectory within $\approx 10^{-9}$.

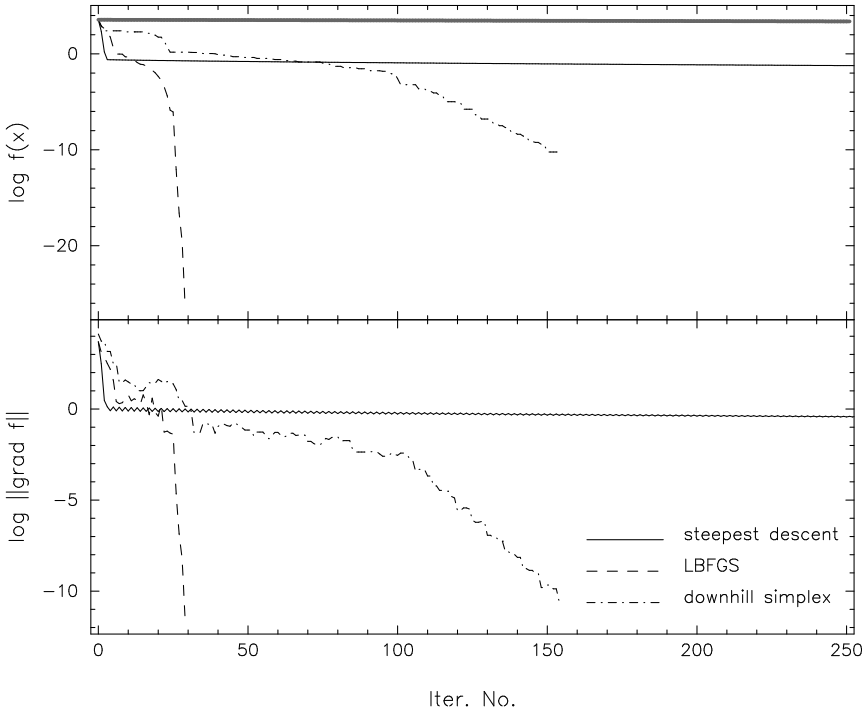

Figure 4.7: Comparison of the convergence behaviour of different local minimization algorithms for Rosenbrock's function (A.31). The minimization for each method started at the point $\vec{\mathbf{x}}_0 = (-2, -2)$. The thick, dark grey line in the upper panel shows the theoretical convergence behaviour of the steepest descent algorithm as determined by equation (4.52).

the plot a little bit, so that the angles between the search direction and the contour lines are not reproduced correctly. For example, the consecutive search directions of the steepest descent method (□) are orthogonal, which indeed can be seen, if both axes are scaled equally.

A striking property of the L–BFGS method (◯) seen in figure 4.6 is the rather direct movement of the algorithm towards the minimum while all other methods display a more or less pronounced zigzag course. This is due to the continuous improvement of the second order approximation of the function, which is superior to that of the conjugate gradient algorithm and clearly outperforms the first order approximation used by the steepest descent method.

Rosenbrocks test function, introduced in section A.6 is treated as a second example. Here again the minimum lies within a flat, bent valley (c.f. figure A.1). The corresponding condition number $\kappa = 2.508 \cdot 10^3$ is approximately 3 orders of magnitude larger, then in the case of the ellipsoid function. Consequently one expects, that gradient based methods converge only slowly to the minimum, which is confirmed in figure 4.7.

It can be seen in this plot, that the steepest descent algorithm fails to reach the minimum within 250 iterations. Even after 2000 steps the norm of the gradient is reduced only

to $\|\nabla f\| \approx 4 \cdot 10^{-2}$, a value which is reached by the L–BFGS method after ≈ 35 iterations. Again, this method clearly outperforms the other algorithms. Since the conjugate gradient shows a similar performance as the steepest descent technique, we omitted the data from figure 4.7.

While the downhill simplex algorithm performed approximately as good as the steepest descent and the conjugate gradient method for the ellipsoid function, it performs obviously better for the Rosenbrock function. One clearly sees two different plateaus in the course of the tolerance ε_{NM} shown in the upper panel of figure 4.7. The first between iteration number 5 and 20, and the second between iteration number 30 and 100. While the function value during these stages of the optimization procedure decreases only slowly, it shows significant progress towards the minimum in the intermediate phases. If one recalls the details of the algorithm discussed in section 4.1.5, it becomes evident, that in these phases of slow progress, seen as plateaus in figure 4.7, the simplex $\mathcal{S}_N$ adjusts itself to the local conditions of the functions. After this adjustment is completed it proceeds with a linear convergence rate towards the minimum. It is this self-adjusting property and the simplicity of the procedure, which makes the downhill simplex algorithm an interesting optimization technique for functions, for which the gradient is very small and/or very expensive to evaluate.

4.1.7 A detailed benchmark investigation

In this section we want to address two different questions. At first it shall be clarified, how the performance of a local minimization technique depends on the parameters of the algorithm. This will be exemplified for the parameters N_{reset} of the conjugate gradient and M_{up} of the L–BFGS method, respectively. Second we try to elucidate how the performance of these two algorithms scales with the dimension of the problem. The aim of this analysis is to put the choice of a local minimization technique on a firm basis.

4.1.7.1 Parameter dependence of the performance

In section 4.1.3 it was mentioned that many practical implementations of the conjugate gradient restart the algorithm at every N_{reset} steps, by setting $\beta_k = 0$ in equation (4.18) and thus switch to the steepest descent step for one iteration. As a rule of thumb it is often mentioned, that N_{reset} should be of the same order of magnitude, as the dimension of the problem (Press et al., 1992). This is confirmed by figure 4.8, which displays the performance of the conjugate gradient algorithm for different values of the parameter N_{reset}, viz. 4 (dotted line), 20 (dash-dotted line), and the case, that the algorithms is not reset (dashed line). For comparison the data for the L–BFGS and the steepest descent method are repeated. The pure conjugate gradient minimization (i.e. without reset) performs only slightly better then the steepest descent method, which can be viewed as a conjugate gradient calculation with $N_{reset} = 1$. Setting $N_{reset} = 20$ yields only a minor improvement, while setting $N_{reset} = 4$, i.e. twice the dimension of the problem, gives a performance, which is similar to that of the L–BFGS method. This confirms the mentioned rule of thumb. It also

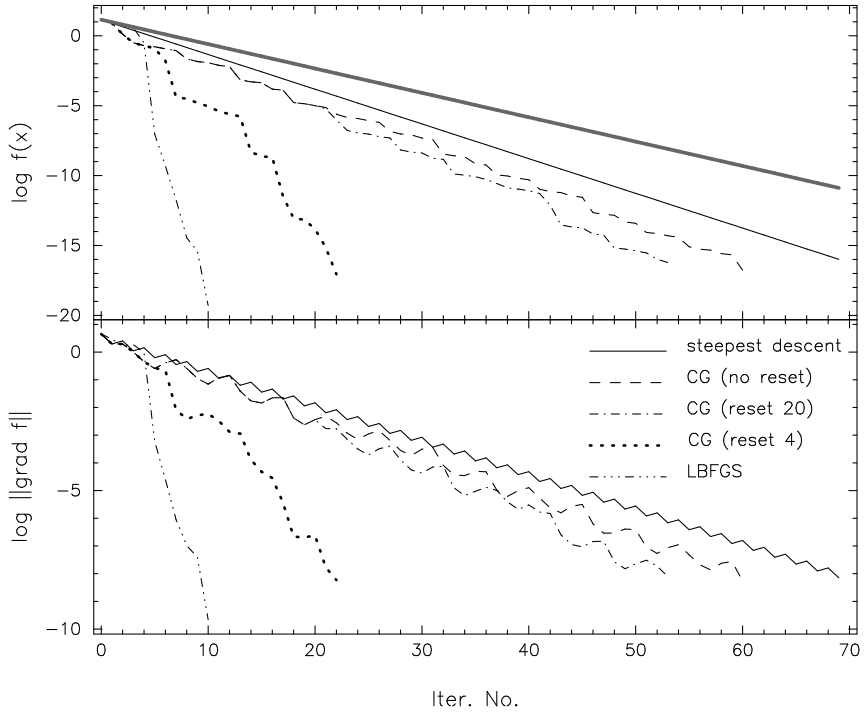

Figure 4.8: Comparison of different gradient based minimization algorithms for the ellipsoid function (4.57). Next to the L–BFGS and the steepest descent method, the conjugate gradient algorithm is presented for different choices of the parameter N_{reset}. The thick, dark grey line in the upper panel shows the theoretical convergence behaviour of the steepest descent algorithm as determined by equation (4.52).

reveals an interesting similarity between the L–BFGS and the conjugate gradient method: For both methods it seems essential to *forget* after some time the informations gathered during the minimization procedure in order to perform effectively. This is plausible, since the slope and the curvature of the function at a point far away from the minimum may have no influence on the slope and curvature near the minimum.

Due to this mentioned similarity between the parameter N_{reset} and M_{up}, it seems appropriate to discuss now the influence of the latter parameter on the performance of the L–BFGS algorithm. As is apparent from the exemplifications in section 4.1.4, the L–BFGS method during the first M_{up} iterations is identical to the BFGS quasi–Newton method (see Liu & Nocedal, 1989). Equivalently one could say, that for $M_{up} \to \infty$ the limited version resembles the unlimited version. Although most authors agree in that the number of iterations needed by the L–BFGS methods decreases, as the number of updates M_{up} is increased (e.g. Zou et al., 1993, Liu & Nocedal, 1989, Nash & Nocedal, 1991), we are not aware of any quantitative investigation which confirms this conjecture. To address this question we performed a systematic benchmark study for two different cluster sizes, $N = 80$ and $N = 150$, respectively. As the potential model for these calculations a simple

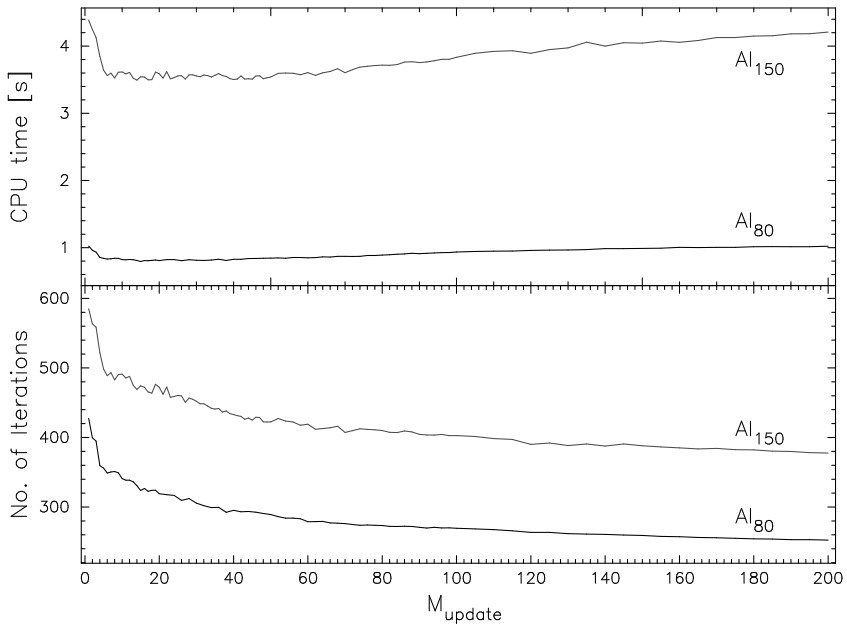

Figure 4.9: Influence of the parameter M_{up} on the performance of the L–BFGS algorithm. As a test case the Al_{80} and Al_{150} clusters, bound by a Morse potential, have been used. The upper panel displays the mean CPU time needed to reach a local minimum. The lower panel shows the corresponding mean number of iterations used.

Morse potential has been employed, using parameters, which have been calculated using the molecular data of the aluminium dimer Al_2 – a totally arbitrary choice. For each cluster we varied the parameter M_{up} between 1 and 200, performed 500 minimization runs and determined the mean number of iterations $\langle N_{iter} \rangle$ and CPU time $\langle \tau_{CPU} \rangle$ required to reach a stationary point. A convergence criterion of $\varepsilon = 1 \cdot 10^{-6}$ has been applied. The results are presented in figure 4.9.

As can be seen in the lower panel of that figure, the mean number of iterations required to reach a local minimum decreases as the the parameter M_{up} is increased. One might deduce form figure 4.9 that $\langle N_{iter} \rangle \propto M_{up}^{-1}$. Whether for the limit $M_{up} \to \infty$ actually the performance of the BFGS algorithm is attained, i.e. $\lim_{M_{up}\to\infty} \langle N_{iter} \rangle_{\mathrm{L-BFGS}} = \langle N_{iter} \rangle_{\mathrm{BFGS}}$ cannot be concluded, since no implementation of the BFGS algorithm is at hand.

The optimal choice for the parameter M_{up} for practical applications is not only influenced by the mean number of iterations it takes to reach a stationary point. Instead of this one also has to into account the storage requirement. As discussed in section 4.1.4 the L–BFGS algorithm needs for $M_{up} > N/2$ more memory, then the BFGS algorithm. Thus, it seems not favourable to use values larger then this upper bound. Furthermore it is necessary to consider, that due to the two–loop recursion used for the computation of the inverse Hessian matrix (see algorithm 4.3), the number of arithmetic operations increases, as M_{up} is increased. The consequence can be seen in the upper panel of figure 4.9 where

the mean CPU time is depicted. After a first drop between $M_{up} = 1$ and $M_{up} \approx 5 - 7$, $\langle \tau_{CPU} \rangle$ remains almost constant until it slowly starts rising for $M_{up} \gtrsim 40$ for Al_{80} and $M_{up} \gtrsim 70$ for Al_{150}, respectively.

To sum up it can be concluded, that choosing M_{up} between 5 and $\approx N/2$ gives the best performance of the L–BFGS algorithm in terms of CPU time. Although one could lower $\langle N_{iter} \rangle$ further by increasing M_{up} to larger values, this seems not appropriate due to the enhanced storage requirement and the longer duration of each minimization. Throughout this thesis $M_{up} = 5$ was set, otherwise it is mentioned explicitly.

4.1.7.2 Dependence on the dimension of the problem

In the previous section we discussed the influence of various parameters on the performance of the minimization algorithms, while the dimension of the test functions was kept fixed. Now we want to address the question, how the performance of the conjugate gradient and the L–BFGS algorithms scales with the dimension of the problem. To this end we conducted a simple benchmark test. For cluster sizes between $N = 15$ and $N = 200$ a randomly generated configuration was quenched using as a convergence criterion the *root mean square force* to fall below $1 \cdot 10^{-4}$. As the potential model for these calculations the simple Morse potential already introduced in the previous section 4.1.7.1. The CPU time has been measured and averaged over 500 successful quenches. In case of the conjugate gradient method, the search direction was reset after every 20 iterations. For the L–BFGS method $M_{up} = 5$ was set. As a second example the reduced Lennard–Jones potential has been used in conjunction with the L–BFGS method. In this case the required convergence criterion has been varied between $\varepsilon = 1 \cdot 10^{-4}$ (tight) and $\varepsilon = 1 \cdot 10^{-2}$ (sloppy). All calculations have been performed on an AMD Athlon XP with 1400 MHz and 524 MB RAM. The results are presented as a double logarithmic plot figure 4.10 and summarised in table 4.1.

For both methods the data points lie along a straight line, indicating a power law for the function $t_{lm}(N)$:

$$t_{lm}(N) = A_{lm}\, N^{b_{lm}} \tag{4.63}$$

The coefficients A_{lm} and b_{lm} have been determined using a standard least square fit technique and are given in table 4.1. It is apparent that the L–BFGS method clearly outperforms the conjugate gradient algorithm. While the latter one needs about one minute to minimise a Morse cluster with 200 atoms, the variable metric method only takes about 6 seconds, i.e. one tenth of that time. Since many global optimization techniques require many (in the order magnitude of about 10^3 up to 10^5) local minimization runs or *quenches* (see section 4.2), the *suitable* choice of the minimization technique determines, whether one has to wait about one month or only 3 day for the results.

A further interesting feature evident from the data shown in figure 4.10 and table 4.1 is the fact, that the performance of the L–BFGS algorithm depends only moderately on the type of the potential energy model used. It would be intriguing to investigate further, whether this is generally true for other empirical potential functions.

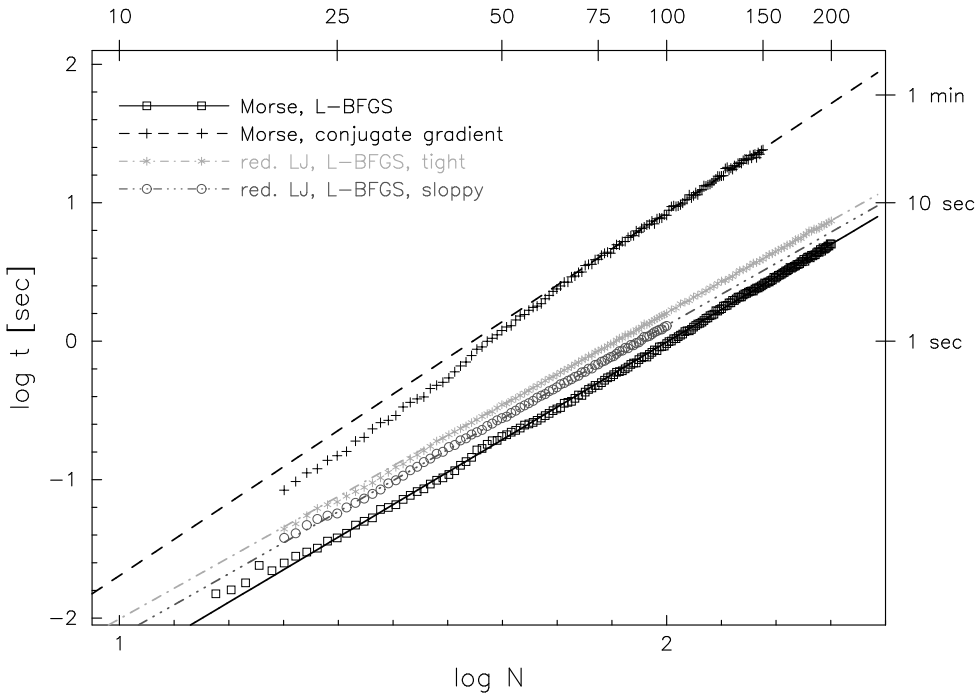

Figure 4.10: Benchmark test for the L–BFGS and the conjugate gradient local optimization algorithm. The calculations have been performed on AMD Athlon XP with 1400 MHz. The straight lines display equation (4.63), where the parameters have been obtained using a least–square fit.

The main idea of the quasi–Newton methods discussed in section 4.1.4 is the step wise approximation of the Newton direction. Such methods generally show a very fast convergence rate, once the algorithm is near the minimum. This can be seen in figure 4.5 and 4.7, where after the first iterations with a moderate, approximately linear progress, the norm of the gradient suddenly drops by many orders of magnitude, to reach the minimum within a few additional steps. Thus, one expects only a slight dependence of the performance on the required tolerance ε, which indeed can be seen in figure 4.10 and table 4.1, respectively.

In summary it can be presumed, that the pre–exponential factor A_{lm} is mainly determined by the used potential or test function, the required tolerance, and - of course - the speed of the computer facility used for the calculations. Whereas the exponent b_{lm} seems to depend mainly on the details of the algorithm, though it can not be excluded, that it also depends on the objective function and its *non–linearity*. Additionally it is obvious, that for the test cases considered here, the L–BFGS method clearly outperforms the implemented conjugate gradient method.

We next try to discuss, how the performance of the limited–memory BFGS method of Nocedal (1980) compares with other minimization techniques. Since it is impossible to implement all known algorithms, we refer to some published comparative studies. Some of the algorithms mentioned below have not been introduced in the previous sections. In such a case, a detailed description of the method can be found in the cited papers. Most

Table 4.1: Parameters for equation (4.63) obtained by a least–square fit. The parameters for the Pentium IV machine (with 450 MHz) are based on a poorer statistic (i.e. averaged over fewer successful quenches) and are given only for demonstrating the effect of computer power on the performance. The corresponding data for this case are *not* shown in figure 4.10.

CPU type	system	method	A_{lm}	b_{lm}
AMD Athlon	Morse	conjugate gradient	$4.84 \cdot 10^{-5}$	2.62
		L–BFGS method	$1.98 \cdot 10^{-5}$	2.35
AMD Athlon	red. L.-J., tight	L–BFGS method	$6.06 \cdot 10^{-5}$	2.21
	red. L-J., sloppy		$4.26 \cdot 10^{-5}$	2.24
Pentium IV	Morse	conjugate gradient	$1.13 \cdot 10^{-4}$	2.81
		L–BFGS method	$8.08 \cdot 10^{-5}$	2.41

of these comparisons use the set of test functions introduced by Moré et al. (1981):

- Liu & Nocedal (1989) compare the L–BFGS method with a combined conjugate gradient and quasi–Newton algorithm of Buckley & LeNir (1983), and the partitioned quasi–Newton method of Toint (1983). Their results are as follows:

  1. The L–BFGS methods performs better than the combination of conjugate gradient and quasi–Newton of Buckley & LeNir (1983).
  2. In some cases the performance (expressed by the number of function calls) of the limited BFGS algorithm approaches that of the full BFGS method.
  3. The L–BFGS method seems to be preferable to the partitioned quasi–Newton algorithm for large scale problems, where the Hessian matrix is not very sparse.

- Nash & Nocedal (1991) performed a comparison between a truncated Newton method, developed by one of the authors (see Xie & Schlick, 1999, for a detailed description of this algorithm) and the L–BFGS method. They find, that neither algorithm is clearly superior to the other, although the L–BFGS algorithm tends to need fewer evaluations of the function and its gradient. The authors further try to classify the test problems in terms of nonlinearity and their distribution of the eigenvalues of the Hessian matrix. They find *no* correlation between the performance of the algorithms and latter property, but they presume a correlation with the degree of nonlinearity. While the truncated Newton method performs better for quadratic and approximately quadratic functions, the L–BFGS method is the method of choice for highly nonlinear problems. Last but not least they compared both methods with the Polak–Ribière conjugate gradient (see Eq. 4.18) and find, that it is not competitive

with the other two, Newton step related algorithms. The function characteristics introduced by Nash & Nocedal (1991) might be useful for a detailed analysis of the performance of the L–BFGS algorithm for different potential models.

- Zou et al. (1993) compare the limited BFGS quasi–Newton method with a truncated Newton method using the mentioned test set and some large–scale problems in oceanography and meteorology. They find, that the L–BFGS method has the best overall performance, although the truncated Newton algorithms yields better results for some special large–scale meteorological problems.

- Xie & Schlick (1999) compare an improved version of the truncated Newton method (TNPACK) with the L–BFGS algorithm. They find, that both methods are competitive. From their published data (see table 4 in the paper) it can be concluded, that TNPACK generally needs fewer iterations to reach a minimum, then the L–BFGS routine. But since each iteration in the first case is computationally more expensive then in the second, this advantage is cancelled out for small and moderate problem dimensions, and the performance of both methods is comparable. Whereas for large–scale optimization problems with ≈ 6100 variables, the TNPACK proves to be about three–times faster. Xie & Schlick (1999) also considered a conjugate gradient algorithm, which performed notably worse, than the other two methods.

- Baysal et al. (1999) investigated the efficiency of different minimization algorithms applied to peptides and proteins. The algorithms used are i.) a modified version of the conjugate gradient due to Shanno (1978); ii.) the L–BFGS quasi–Newton method and iii.) the truncated Newton method already mentioned. Baysal et al. (1999) considered two cases. At first, they minimized the potential energy Φ_{FF} of a molecule, as described by means of certain force field[15]. As a second test case, they additionally took the effects of the solvent of the protein into account, by adding a term which is proportional to the solvent–accessible surface area of the molecule, i.e. $\Phi_{\mathrm{tot}} = \Phi_{\mathrm{FF}} + \Phi_{\mathrm{solv}}$, which is expected to increase the nonlinearity of the objective function. For the first test case (pure force field) the truncated Newton method performs best, while the incorporation of the solvation effect reverses this picture and makes the L–BFGS algorithm the best method for minimization. Contrary to the results of Nash & Nocedal (1991) the authors presume that the question, which algorithm performs best, mainly depends on the distribution of the eigenvalues and not on the degree of nonlinearity. This point clearly deserves clarification by some future investigations.

- Most recently Morales (2002) demonstrated that the L–BFGS method of Nocedal (1980) clearly outperforms the SNOPT algorithm of Gill et al. (1997) even for large–scale problems with up to 1000 variables.

[15]The authors used the GROMOS force field developed by van Gusteren & Berendsen (1987).

Table 4.2: Storage requirements of different minimization algorithms discussed in the text. Note, that a nowadays computer with approximately 500 MB RAM can store $6.25 \cdot 10^7$ real numbered variables. Using this number, the maximum number of atoms N_{atom}^{max}, that can be treated on such a computer is given in the last row. Remember, that for the case of molecules and clusters the dimension of the problem is $N = 3 \times N_{atom}$. For the L–BFGS routine $M_{up} = 5$ was assumed.

Method	Storage	N_{atom}^{max}
downhill-simplex	$(N+2)\,N$	2635
steepest descent	$2\,N$	$1.04 \cdot 10^7$
Fletcher–Reeves conjugate gradient	$3.\,N$	$6.94 \cdot 10^6$
Polak–Ribière conjugate gradient	$4\,N$	$5.21 \cdot 10^6$
L-BFGS quasi-Newton	$2\,M_{up}\,N + 2\,M_{up} + 4\,N$	$1.49 \cdot 10^6$

From our own investigations and those presented by others it can be concluded, that the L–BFGS minimization algorithm is one of the best and most suitable methods currently at hand for finding the local minima of empirical potential energy functions.

From a practical point of view the storage requirement of a minimization algorithm is also an important information needed to rank its usability. Since in sections 4.1.3 - 4.1.5 this quantity has been specified for each algorithm in detail, we simply repeat them here in 4.2. Except for the downhill simplex method, the L–BFGS algorithm apparently has the largest storage requirement, which is approximately three times as large, as that of the Polak–Ribière conjugate gradient. Thus, one obtains the speed of this algorithm at the expense of a larger storage requirement. Note however, that one still could handle clusters with $\approx 1.49 \cdot 10^6$ atoms on a moderate sized computer. The limiting quantity in this case clearly is the time t_{lm} required to quench such a large structure. Employing the power law found for the size–dependence of t_{lm} in section 4.1.7.2, one can estimate, that it would last more then 50 years to minimize such a huge cluster.

It is generally accepted, that the efficiency of the last three minimization algorithms listed in table 4.2, in terms of function evaluations, and their robustness tends to increase with the storage requirement. Our own calculations presented here confirm this. Although the L–BFGS algorithm needs significantly more memory than e.g. the conjugate gradient, this is clearly compensated by the gain in computational speed. Furthermore is this point of less importance, since modern computer facilities posses enough memory to handle even very large systems with up to 10 thousands of atoms. Thus, the robustness and speed of the limited–memory BFGS algorithm for the local minimization of clusters enables one to address a more demanding problem, namely that of *global optimization*, which will be discussed in the next section.

4.2 Global optimization

While in the last section the problem of *local minimization* was discussed, we shall now turn to the problem of *global minimization*. In section 4.1.2 some theorems about necessary and sufficient conditions for local minima were stated (theorem 4.2 to 4.4). In the case of global minima there exist only the following statement:

Theorem 4.8 Convexity and global minima
When f is convex, any local minimum $\vec{\mathbf{x}}_{\min}$ is a global minimum of f. If in addition f is differentiable, then any stationary point $\vec{\mathbf{x}}_{\mathrm{sp}}$ is a global minimum of f.

The following definition recapitulates the meaning of the term *convex* (Polak, 1997, p. 668):

Definition 4.2 Convexity *A function $f : \mathbb{R}^N \mapsto \mathbb{R}$ is said to be* convex *if, for any $\vec{\mathbf{x}}_1, \vec{\mathbf{x}}_2 \in \mathbb{R}^N$, and $\lambda \in (0, 1)$:*

$$f(\lambda\, \vec{\mathbf{x}}_1 + (1-\lambda)\, \vec{\mathbf{x}}_2) \leq \lambda\, f(\vec{\mathbf{x}}_1) + (1-\lambda)\, f(\vec{\mathbf{x}}_2) \tag{4.64}$$

Unfortunately almost all physically and chemically interesting fitness functions f, e.g. the potential energy surfaces of molecules or clusters, are non-convex. For this general case there exists no analytic criterion which enables to decide, whether a found stationary point is the global minimum or not. Moreover there exists no thread of Ariadne, like the gradient in the case of local minimization, which leads in a deterministic way from an arbitrary point in the search space to the global minimum. Both points have a severe consequence for the development of global minimization algorithms (see section 4.2.2).

In the case of atomic or molecular clusters the problem of global optimization is further aggravated by the sheer number of local minima, which has been discussed in some detail in section 3.2.2. Thus one might say, that global optimization is a *hard* problem, in that sense, that it is difficult to solve. It is possible to give this rather rough term a more concrete and more exact meaning using the theory of computational complexity.

4.2.1 Some words about computational complexity

The theory of computational complexity tries to measure the efficiency of an algorithm in terms of computational resources, typically the time and storage required to solve a problem (see Mertens, 2002, for a good introduction). One distinguishes mainly two important complexity classes named $\mathcal{P}$ and $\mathcal{NP}$, respectively. A problem is called $\mathcal{P}$–hard, if it can be solved by a *polynomial* time algorithm, i.e. an algorithm can find a solution of the problem within a time, that depends polynomial on the size N of the problem. This dependence is usually expressed as $\mathcal{O}(N^k)$ with k typically between 1 and 3. The term $\mathcal{NP}$ stands for '*nondeterministic polynomial*' and its definition is a little bit circumstantial. It assumes, that an algorithm can perform an exponential number of computations in polynomial time, by splitting the computation in each iteration into two parallel processes[16]. Such an algorithm is called *non-deterministic* and a problem is $\mathcal{NP}$–hard, if it can be solved solely by

[16]This could be achieved by an instruction like: `goto both label 1, label 2`.

a non–deterministic algorithm in polynomial time. Since conventional computers can not execute non–deterministic algorithms, the definition implies, that a $\mathcal{NP}$–hard problem is solved in exponential time $\mathcal{O}(2^N)$ by these machines. It is noteworthy, that computational complexity deals with a worst–case scenario and that indeed algorithms might exist, which are able to find a *good* solution of an $\mathcal{NP}$–hard problem within polynomial time. However, there is no guarantee that this solution really is the optimal solution. Such algorithms sometimes are called *heuristics* (Nissen, 1997).

It is well known, that finding the ground state of a homogeneous atomic clusters is an $\mathcal{NP}$–hard problem (Wille & Vennik, 1985). Greenwood (1999) demonstrated, that the proof of Wille & Vennik does not apply to the more general case of heterogeneous clusters. Greenwood then presents a generalised form and thus shows, that finding the minimum energy configuration of a heteronuclear cluster is a $\mathcal{NP}$–hard.

Unfortunately the theory of computational complexity only states, how hard or how easy a certain problem might be solved - in the worst case. Another, more statistically based approach to the complexity of optimization has been presented by Wolpert & Macready (1996, 1997). They prove a so called *no free lunch* theorem for optimization. Wolpert & Macready show, that for any pair of optimization algorithm $\mathfrak{A}$ and $\mathfrak{B}$ it holds:

$$\sum_f P(d_m^y|f,m,\mathfrak{A}) = \sum_f P(d_m^y|f,m,\mathfrak{B}) \tag{4.65}$$

where f is a cost function and m is the number of iterations algorithm $\mathfrak{A}$ performed on that function. The quantity $d_m^y \equiv \{d_m^y(1),\ldots,d_m^y(m)\}$ denotes the set of m cost values visited by the algorithm and ordered according to the time at which they were generated. The sample d_m^y can be used to construct a measure $\Pi(d_m^y)$ for the performance of an algorithm. For example in the case of minimization problems the lowest value of d_m^y is a reasonable measure to assess the efficiency of an algorithm. Another possibility would be, to determine the first occurrence of a certain value within the sample d_m^y - the so called *first passage time*. Wolpert & Macready (1997) chose the conditional probability $P(d_m^y|f,m,\mathfrak{A})$, that a particular sample d_m^y is obtained by performing an algorithm $\mathfrak{A}$ m times on a cost function f, as a performance measure. Thus, the no free lunch theorem (4.65) states[17], that the performance of algorithm $\mathfrak{A}$ equals the performance of algorithm $\mathfrak{B}$, when averaged over all cost functions $f \in \mathcal{F}$, with $\mathcal{F}$ the set of all such functions.

This rather abstract theorem has some interesting consequences, which are of some practical importance. First of all, if an algorithm $\mathfrak{A}$ outperforms a second algorithm $\mathfrak{B}$ on a certain class $\mathcal{F}_A \subset \mathcal{F}$, this second algorithm must perform better on the remaining functions $f \in \mathcal{F}_B = \mathcal{F} \setminus \mathcal{F}_A$. This means, that it is rarely justified, that an algorithm will perform equally well on a broad class of problems. In other words, a general–purpose '*black box*' exploiting only limited knowledge of the optimization problem it tries to solve, will not exist. Instead of this it is indicated by the no free lunch theorem (4.65) to incorporate any a priori knowledge about the optimization problem into the algorithm.

[17]For a proof see the appendix of Wolpert & Macready (1997).

From a physical point of view the latter point is to handle with care, since the incorporation of *too much* knowledge might bias the optimization strategy into a search direction, where it almost certainly will fail to locate the *true* global minimum. An example is discussed in section 3.2, where it is demonstrated, that restricting the global optimization procedure of Lennard–Jones clusters to icosahedral structures in some cases leads to suboptimal solutions, since the global minimum has an FCC structure, as e.g. in the case of LJ_{38} and 13 other species (see page 25). Such preconceptions have been utilised by Northby (1987) and Xie et al. (1989) for the global optimization of Lennard–Jones clusters. Later investigations e.g. by Deaven et al. (1996) or Doye et al. (1995) found new global minima. Thus the incorporation of any knowledge about the particulars of the optimization problem may not lead to a restriction of the search space!

As the discussion demonstrated, that one cannot expect, that a particular algorithm performs equally well on all problems, it seems necessary to define some criteria, a 'good' algorithm for finding the minimum energy configuration of a cluster should fulfil. Since Lennard–Jones clusters are rather well studied, it seems natural to use this system as a (first) test case. In section 3.2 it was shown, that for some cluster sizes the global minimum is particularly difficult to locate. Based on this observation Wales & Doye (1997) recommend, that any method, which claims to be '*useful*' should locate the truncated octahedron of LJ_{38}. As a second hurdle they suggest the location of the Marks' decahedron for LJ_{75}. This poses a much more severe test for a global optimization algorithm. To our knowledge this test has been passed only by the basin–hopping algorithm of Wales & Doye (1997, see next section), and the genetic algorithm developed by Hartke (1999). With this criteria one assumes, that finding the global minimum of any potential energy function (PEF) defines a kind of subclass of global minimization problems, and that the comparison of the performance of two algorithms $\mathfrak{A}$ and $\mathfrak{B}$ on a certain PEF (e.g. Lennard-Jones) yields (approximately) the same result, when one uses another PEF (e.g. Morse).

4.2.2 Different approaches to global optimization

It is generally accepted, that finding the minimum energy configuration of a homo– or heteronuclear cluster is an $\mathcal{NP}$–hard problem, which means that it only can be solved within a time, that depends exponentially on the clusters size N. However, there exist numerous effective algorithms, which are able to locate putative global minima for various clusters systems[18] within reasonable time. As already mentioned for the case of the Lennard–Jones potential probably all global minima for clusters with up to $N = 150$ atoms have been found, although only for $N \leq 7$ this has been proved (Maranas & Floudas, 1992). It is beyond the scope of this section to give an overview over the various approaches introduced to tackle the problem of global optimization of atomic and/or molecular clusters. Recent publications by Wille (2000) and Hartke (2002) give a comprehensive review of this field.

As it was mentioned earlier there is no analytical possibility to determine a suitable

[18] A collection of such global minima for clusters bound by various empirical force fields can be found in the *Cambridge Cluster Database* (Wales et al., 2002).

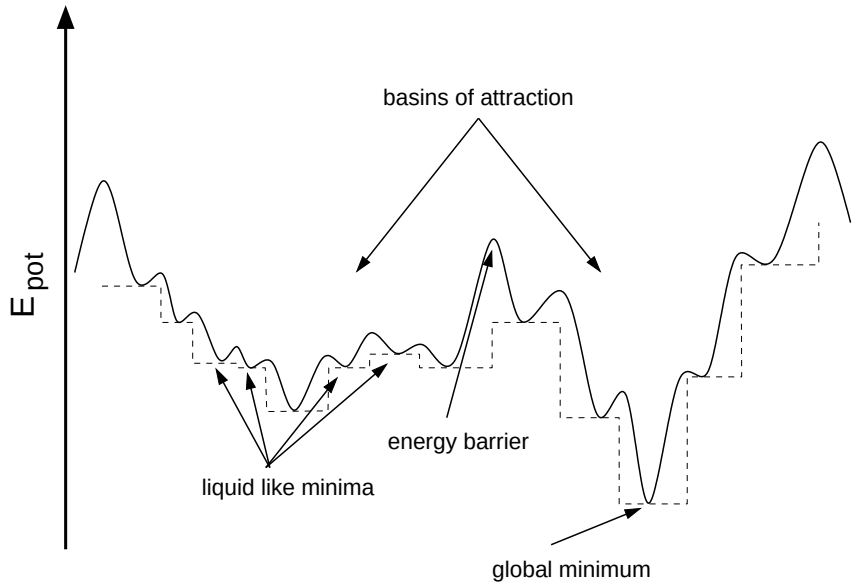

Figure 4.11: Sketch of a potential energy surface. The dashed line indicates the transformed potential energy surface of the basin–hopping algorithm described in section 4.2.3.

direction in search space, where the algorithm should look for the global minimum[19]. Thus, suitable global optimization algorithms must be *stochastic*[20] algorithms, which try to scan the different regions of the energy landscape. Furthermore, a global minimum is a stationary point of the potential energy surface, and it can only be decided by comparison with other local minima found before, whether the new point possibly *is* the global minimum. Thus the scanning of the potential energy surface should be combined with an effective method, to quench a generated candidate configuration[21]. Almost all optimization techniques currently regarded as successful contain these two elements. They differ mainly in the way, the exploration of the potential energy surface is accomplished, although most of these techniques are similar in that sense, that they have been inspired by nature[22] or natural processes:

- Simulated annealing (Kirkpatrick et al., 1983) mimics the annealing and cooling of a solid. The procedure starts with an arbitrary configuration at a prescribed temperature T. At each iteration an atom is displaced by a random distance Δr and

[19]Recall, that the gradient in the case of local minimization defines such a direction!

[20]There exist a few expectations, e.g. the branch-and-bound algorithm developed by Westerburg & Floudas (1999). Unfortunately such deterministic algorithms are rather time consuming, which prohibits their application to larger aggregates.

[21]This point seems to be trivial but the historical development shows, that the early optimization algorithms did not utilise local minimization algorithms and solely build up on the stochastic search either by simulated annealing or evolutionary algorithms. Only when these elements were combined with local minimization techniques, they became *really* effective.

[22]Wille (2000) coined the expression '*new age algorithm*' for such methods.

the energy E of the new configuration is determined. In order to decide, whether the new configuration is accepted, a Metropolis criterion is applied, i.e. the acceptance probability $P_{acc}(\text{old} \rightarrow \text{new})$ is given by:

$$P_{acc}(\text{old} \rightarrow \text{new}) = \begin{cases} 1 & \text{if } \Delta E \leq 0 \\ \exp\left(-\Delta E / k T\right) & \text{if } \Delta E > 0 \end{cases} \tag{4.66}$$

where ΔE is the associated change in the energy of the two configurations. At each iteration the temperature is reduced according to a predefined cooling rate.

Starting with a *liquid like* configuration with a rather high energy, it is hoped, that upon cooling the system reaches the global minimum. Unfortunately the system might get trapped in the basin of attraction around a suboptimal minimum, which is separated by a high energy barrier (c.f. figure 4.11) from the basin of attraction of the global minima. The disconnectivity graph of the LJ_{38} cluster discussed in section 3.2.2 is an example for a cluster, where such difficulties are frequently encountered. A broader discussion of the application of simulated annealing algorithms to the global optimization of clusters can be found in Wille (2000).

- Evolutionary algorithms (e.g. Rechenberg, 1973, 1994, Bäck, 1996) mimic the process of the *survival of the fittest* between putative solutions. Since the potential energy surface is scanned by means of different genetic operators such as mutation or cross–over, a certain diversity within the population of configurations is introduced. Thus, it is hoped, that the algorithm is *not* trapped in a basin of attraction, which does not belong to the global minimum.

  A very successful variant of an evolutionary algorithm has been introduced by Hartke (1999). The key idea of his procedure is the introduction of *niches*, which ensures, that within the population a great variety of structures is present.

Within the framework of this thesis we implemented a version of the *basin–hopping algorithm*, developed by Wales & Doye (1997). It is described in the following section 4.2.3.

4.2.3 Outline of the basin–hopping algorithm

Li & Scheraga (1987) used a 'Monte Carlo plus minimization' algorithm to find the global minimum of polypetides. The description of their method given here is based on the interpretation given by Wales & Doye (1997), who also coined the name '*basin–hopping*' for it. It combines two different approaches. At first it uses a transformation of the potential energy surfaces. Such *surface sculpting* algorithms (Wille, 2000) have been developed e.g. by Stillinger & Weber (1988) or Pillardy & Piela (1995), who proposed different deformations of the potential energy surface in order to reduce the number of local minima. Ideally the deformed PES only has 1 local minimum, which then is mapped back to the original surface. At this it is *hoped*, that this will lead back to the global minimum of the original PES. Unfortunately this hope is not complied with in many cases, because the global minima

depend sensitively on the range of the potential energy function (Doye et al., 1995). The basin–hopping algorithm circumvents this problem by using the following transformation:

$$\widetilde{\Phi}(\vec{\mathbf{R}}_i) = \mathsf{Min}\{\, \Phi(\vec{\mathbf{R}}_i) \,\} \tag{4.67}$$

where $\vec{\mathbf{R}}_i$ is the $3\,N$–dimensional vector representing the coordinates of the cluster during the i–th iteration. The '*operator*' Min signifies that an energy minimization is performed starting from $\vec{\mathbf{R}}_i$, which is usually performed with less tight convergence criterion. This transformation obviously guarantees, that the global minimum of the transformed PES is identical to the global minimum of the original PES. In other words, the energy at any point of the configuration space is mapped onto the energy of the local minimum obtained by the chosen minimization algorithm. Thus, the potential energy surface is transformed into a set of interpenetrating staircases, as it is depicted in figure 4.11. The plateaus correspond to the basins of attraction around each local minimum.

This transformed energy surface $\widetilde{\Phi}$ is then explored by means of a Monte Carlo simulation. Hence, the algorithm can be viewed as combination of a surface sculpting algorithm and a simulated annealing schedule. The advantage of this method is its simplicity and the fact, that it requires only a few parameters: the temperature T, the step size δr, and the required acceptance ratio, which is mostly set to 50 %. Suitable values for T and δr can be easily determined by some preliminary test calculations. As the local minimization methods we implemented the conjugate gradient as well as the L–BFGS algorithm, but since the performance of the latter is clearly superior (see section 4.1.7), this method was chosen in most applications.

4.2.4 Performance of the basin–hopping algorithm

The basin–hopping algorithm has successfully passed the test criteria for a 'useful' global optimization algorithm discussed on page 90. Additionally some new putative global minima have been found, viz. those for $N = 69, 78$, and 107 (Wales & Doye, 1997). More recently a new global minimum for the LJ_{98} cluster has been found by a slightly modified version of the basin–hopping algorithm (Leary & Doye, 1999). The different aspects of the basin–hopping algorithm have been studied quite extensively by Wales and co–workers (e.g. Doye & Wales, 1996, 1998, Doye et al., 1998). A recent review can be found in Doye (2003).

The key aspect of the basin–hopping algorithm, which is responsible for its success, is the exploration of the *transformed* potential energy surface $\widetilde{\Phi}$. As already discussed above, this is a necessary and common feature of (presumably) all '*successful*' global optimization techniques. Hartke's genetic algorithm for example makes also use of a local minimization algorithm. Thus, the only difference between the two algorithms is the way, the transformed PES is explored. One might ask, how big the influence of this aspect on the overall performance of the algorithm is. Below, we will shed some light on this question.

As a consequence of the mentioned transformation, all transition state barriers (see figure 4.11) between the minima on the PES are removed, while the identity of the global

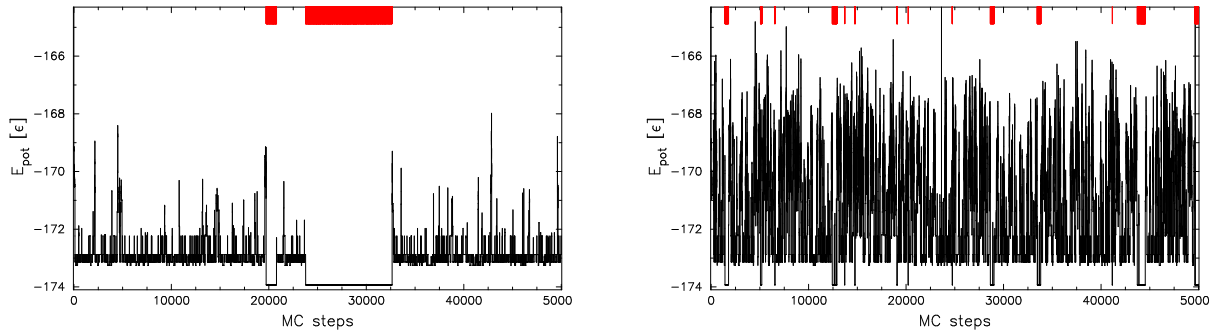

(a) $T = 0.4\ \varepsilon k^{-1}$ (b) $T = 0.8\ \varepsilon k^{-1}$

Figure 4.12: Transformed energy $\widetilde{\Phi}$ as a function of Monte Carlo steps of a basin–hopping run for the LJ_{38} cluster at (a) $T = 0.4\ \varepsilon k^{-1}$ and (b) $T = 0.8\ \varepsilon k^{-1}$. The red bars mark those steps, when the system is in the basin of the global minimum (see figure 3.6). The initial step size was $\delta r_0 = 0.35\ \sigma$.

minimum is preserved. On such a barrierless PES the dynamics is considerably accelerated and the system can hop directly between different minima; hence the name of the algorithm. This hopping is seen in figure 4.12, where we depicted the energy $\widetilde{\Phi}$ as a function of Monte Carlo steps of a basin–hopping run for a LJ_{38} cluster. The simulation comprises 50.000 steps and was performed at reduced temperatures of $T = 0.4\,\varepsilon k^{-1}$, and $T = 0.8\,\varepsilon k^{-1}$, respectively. The red bars in the upper part of the plots indicate those time steps, when the algorithm hit the global minimum (see section 3.2 and figure 3.6). It can be seen, that the cluster is able to pass between the different funnels of LJ_{38} (see figure 3.7) over a broad temperature range. Even at a moderately high temperature of $0.8\ \varepsilon k^{-1}$ the basin around the global minimum is populated considerably. For comparison, it was demonstrated by Doye et al. (1998), that on the *untransformed* PES, the transition between the fcc and icosahedral regions of the configurational space occurs at a reduced temperature of $\approx 0.11\ \varepsilon k^{-1}$. Furthermore, for temperatures above $\approx 0.2\ \varepsilon k^{-1}$ the probability of the cluster being in the fcc funnel reaches zero. Thus on the untransformed PES one has two conflicting requirements: On the one hand side, as a consequence of the Boltzmann distribution, low temperatures are required to allow the global minimum to be populated considerably. On the other hand, such low temperatures hinder the system to pass between different regions of the PES, which are separated by energy barriers. For systems like the LJ_{55} cluster, where only a single funnel with low barriers exists (c.f. figure 3.7), is is possible to satisfy both requirements within a rather broad temperature range. Whereas for the LJ_{38} clusters this is aggravated by the existence of two competing funnels, which are separated by a high barrier (Doye et al., 1999b).

By removing the barriers between the minima, transformation (4.67) effectuates, that the global minimum has a significant probability of occupation even at temperatures, where

it is completely unoccupied on the untransformed PES. Doye et al. (1999b) demonstrated this by means of an elaborate thermodynamic machinery. Here we present a more phenomenological argument, by simply determining the frequency N_{hit}^{tot}, with which the global minimum of LJ_{38} has been found in a basin–hopping run with 50.000 steps. Together with the step number Q_{hit}, when the global minimum has been found for the first time (also called first passage time) in that simulation, the resulting data are shown in table 4.3. Note, that N_{hit}^{tot} corresponds to the total length of the red bars, shown in figure 4.12. It is obvious, that the quantity N_{hit}^{tot} decreases as the temperature is increased. This is also apparent from figure 4.12: For the simulation with $T = 0.4\,\varepsilon k^{-1}$ it lasts approximately one third of the total simulation time, until the global minimum is found for the first time. But after it has been found, the basin–hopping trajectory is confined for some time ($\approx 10\%$) to the corresponding basin of attraction. On the other hand the higher temperature trajectory visits the global minima already at step no. 1420 for the first time, but it always remains only for a short time in its vicinity. For the success of a global optimization algorithm it is indeed advantageous to pass frequently between different basins. The quantity N_{enter} in table 4.3 measures the frequency, the basin around the global minimum is entered. The accelerated dynamics on the transformed PES manifests itself in an increasing value for N_{enter}, as the temperature is increased. Doye et al. (1998) note, that the timescale for the transition between different states of a clusters is much shorter on the transformed than on the untransformed PES. However, due to the necessity to perform a local minimization, each Monte Carlo step on $\widetilde{\Phi}$ is computationally more expensive!

$T\ [\varepsilon k^{-1}]$	Q_{hit}	N_{hit}^{tot}	N_{enter}
0.4	19729	5184	2
0.6	380	2925	7
0.8	1420	1509	14
1.2	5420	379	18

Table 4.3: Summary of 4 different basin–hopping runs for LJ_{38}.

Another requirement for a useful global optimization method, is its ability to visit different regions of the configuration space. In order to demonstrate, how the increasing temperature influences the area, searched by the basin–hopping algorithm, we present in figure 4.13 a scatter plot of $\widetilde{\Phi}(t_{mc})$ and the squared interatomic distances $\langle\, R^2 \,\rangle$ of the structure $\vec{\mathbf{R}}(t_{mc})$. The quantity $\langle\, R^2 \,\rangle$ provides a geometric characterisation of the structure and is discussed in section 4.3.1 (page 103). The location of the two energetically lowest structures, the fcc truncated octahedron and the incomplete Mackay icosahedron (see figure 3.6) are marked in the plot. As expected the number of points in configuration space visited by the basin–hopping algorithm increases as the temperature is increased. This is due to the shorter timescales necessary to leave a certain basin at a higher temperature. Additionally the higher temperature enables the system to surmount the still existing barriers (see figure 4.11) between different funnels or regions of the PES and to visit more high energy minima, which are usually identified as *liquid like*. Note that a kind of grouping of the points seems to be discernible. The border line between the two groups is slightly inclined against the vertical line at $\approx -171\,\varepsilon$. Since on right side of this line the density of points and thus the number of configurations is clearly higher, than on the left hand side, it seems

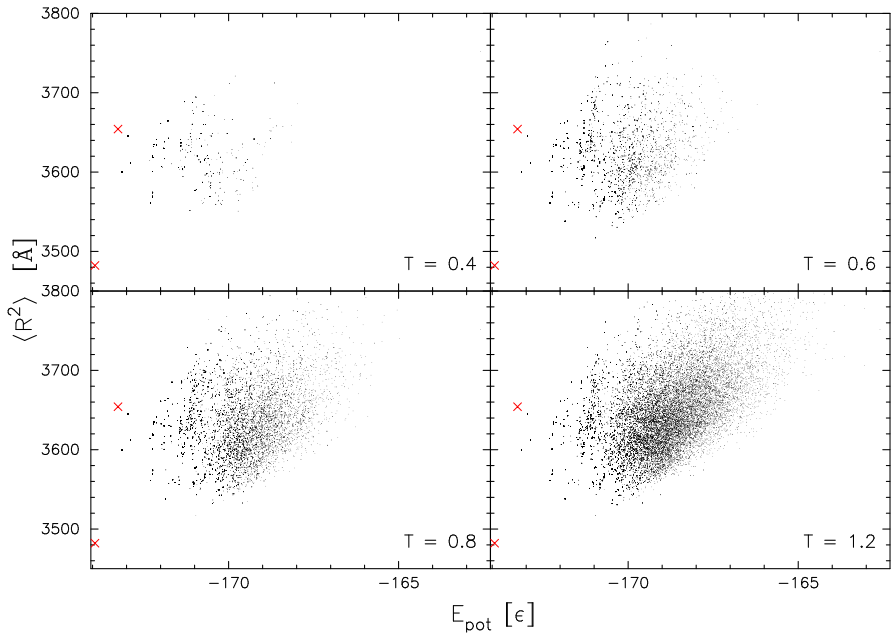

Figure 4.13: Scatter plot of the $\widetilde{\Phi}$ and $\langle R^2 \rangle$ values of four basin–hoping runs at different temperatures. The location of the fcc global minimum and the icosahedral second lowest energy structure (see figure 3.6) are marked with a red cross.

appropriate to associate this region of the $\widetilde{\Phi}\langle R^2 \rangle$–plane with the icosahedral funnel of the disconnectivity graph shown in figure 3.7. However, this assignment is rather tentative since it is not known, where the minima, which belong to a certain basin, are located in this plane.

After having explained why the basin–hopping is successful in locating the global minima of Lennard–Jones and other clusters (see Doye, 2003, for an overview of other clusters optimized with the basin–hopping algorithm), the following discussion will try to quantify the performance of the method. Such benchmark tests for global optimisation algorithms are not a trivial task. The reason for this is twofold. Normally one tries to determine, how long it takes for a particular algorithm to solve a given problem, starting from a randomly chosen initial guess for the solution. While for most numerical problems there exist a well defined *convergence* criterion, measuring whether the solution has been obtained or not, such a criterion is missing for global optimisation problems, as already mentioned. Instead one can only determine, how long a specific algorithm needs, to find the *known* or at least *presumed* solution of a certain optimization problem.

The second reason is simply of practical nature: Benchmark tests for global optimization problems are rather time consuming - already one calculation for a certain cluster size might last several hours. Since it is necessary to average over a significant number of calculations the required CPU time accumulates quickly. The benchmark application presented here has been performed as follows:

- We considered the reduced Lennard–Jones potential and all cluster sizes between $N = 7$ and $N = 120$. The energies for the global minima have been taken from the Cambridge Cluster Database.

- For each cluster we performed 10 basin–hopping runs with $Q_{max} = 10.000$ MC steps at a reduced temperature of $T = 0.8\,\varepsilon k^{-1}$ and an initial step size of $\delta r_0 = 0.4\,\sigma$.

- The convergence criterion for the L–BFGS minimization algorithm was $\varepsilon = 0.01$.

- The calculation stopped, when the global minimum was found. The required number of quenches Q_{hit}, also known as first passage time, was determined and the probability to find the global minimum was determined according to:

$$P_{hit}(N) = \frac{Q_{max} + 1 - Q_{hit}}{Q_{max}} \tag{4.68}$$

  in order to ensure, that for those cases, where the minimum is found in the first step, $P_{hit} = 1$. Note that it should hold, that:

$$\lim_{Q_{hit} \to \infty} P_{hit} = 1 \tag{4.69}$$

  which means that for a never ending search the global minimum *must* be found. A proof of this statement for the *pure random search* can be found in Boender & Romeijn (1995).

The results of this benchmark test are compared with those published by some other authors, namely:

1. The Big Bang algorithm developed by Leary (1997).

2. The *monotonic sequence basin–hopping* (MSBH) proposed by Leary (2000). This algorithm is in principle a basin–hopping algorithm where only those steps are accepted, for which the energy is decreased. This is equivalent to setting the temperature in equation (4.66) to zero. The procedure is restarted at a high energy structure, if for R_{max} consecutive steps no improvement could be obtained. A typical value for R_{max} is 1000. With the help of this algorithm the new global minimum for LJ_{98} was found (Leary & Doye, 1999).

3. The already mentioned genetic algorithm of Hartke (1999) which utilises the biological concept of *niches*.

4. The *parallel fast annealing evolutionary algorithm* (PFAEA) implemented by Cai et al. (2002) borrows concepts from simulated annealing and evolutionary algorithms and is performed on a parallel machine. The authors use the L–BFGS methods as a local minimization algorithm, too.

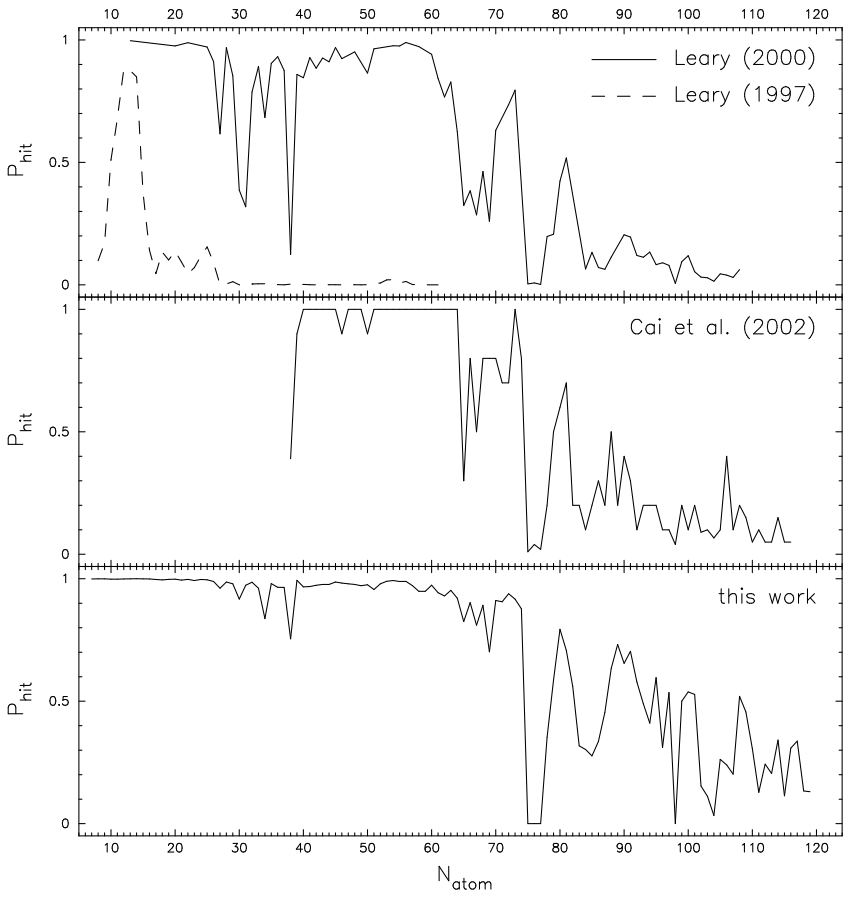

Figure 4.14: Probability to locate the global minimum of the LJ_N cluster compared for different algorithms described in the text.

The last three algorithms can be viewed as an exploration of the transformed PES $\widetilde{\Phi}$. The probability to find the global minimum of a Lennard–Jones cluster by the applied method and our own results for P_{hit} are plotted in figure 4.14. As expected, P_{hit} is not a smooth function of the cluster size N, but shows strong variations. These are caused by the differences in the topology of the underlying potential energy surface. Furthermore, except for the Big Bang algorithm, all methods show a remarkable similar size dependence of P_{hit}. For most clusters with up to 60 atoms, P_{hit} is close to one with a few exceptional hard cases as the LJ_{38} cluster. For clusters with more than 60 atoms the probability to find the global minimum decreases generally. Again one can distinguish between clusters, for which the lowest energy structure is particularly difficult to find (e.g. LJ_{75} to LJ_{77}) and those, for which this task despite the size of the cluster is relatively easy as e.g. LJ_{108} and LJ_{109}. In order to appraise the high value of P_{hit} for these clusters, one should note, that LJ_{108} has approximately $4.5 \cdot 10^{47}$ local minima (c.f. section 3.2.2), whereas for LJ_{77} there are '*only*' $1.6 \cdot 10^{32}$, i.e. **15** orders of magnitude less. As discussed in section 3.2, the Lennard–Jones

clusters with 75 to 77 atoms, belong to those clusters, for which the lowest energy structure is not based on an icosahedron. It is shown by Doye et al. (1999a), that the topology of the LJ_{75} clusters has a similar pathological double–funnel disconnectivity graph, as the LJ_{38} cluster. This comparison gives an interesting clue on the solution of Levinthal's paradox. A key assumption of the paradox discussed on page 27 is, that the search is random, i.e. the topography of the landscape is that of a perfectly flat putting green with no thermodynamical or dynamical bias towards the global minimum (Doye, 2003). The examples discussed above indicate, that this assumption is not true for real clusters. Instead of this, the topography of the PES strongly influences the global optimization process by leading the system towards (in case of a single–funnel landscape) or away (in case of a double–funnel) from the global minimum.

In figure 4.15 we take a closer look on the general performance of the basin–hopping. In the upper panel the data for P_{hit} are repeated for convenience. The middle panel shows the mean first passage time $\langle Q_{hit} \rangle$ as a function of the cluster size. This quantity is contrary to P_{hit}, which means, that high values of P_{hit} correspond to low values of Q_{hit}: The higher the probability to find a minimum, the lower the mean number of quenches required to actually locate it - and vice versa. Again the curve reflects the different topologies of the considered clusters. For example for LJ_{38} $\langle Q_{hit} \rangle$ is as large as for LJ_{69}, while for all intermediate clusters it is clearly lower.

Despite this relative large variations a general trend is discernible. If one uses a double–logarithmic plot, one sees that the data lie approximately along a line. Thus it seems justified to assume, that the mean number of quenches $\langle Q_{hit} \rangle$ to hit the global minimum of a given cluster size follows a polynomial law of the form:

$$\langle Q_{hit} \rangle = A_{hit}\, N^{b_{hit}} \tag{4.70}$$

This number should not depend on the local minimisation algorithm, which is used for the quenches. Using standard techniques for non-linear fits we determined the following coefficients:

$$A_{hit} = 0.11 \qquad \text{and} \quad b_{hit} = 2.37$$

The resulting function is shown in the middle panel of figure 4.15. It can be seen, that the data are reasonably well reproduced. Using this fit we determined the mean CPU time necessary to solve the global optimization time. As discussed in section 4.1.7, the CPU time needed for each quench follows also a polynomial law like equation (4.63). Combining these two equations one finds, that the time required to find the global minimum using the basin–hopping algorithm can also be expressed as a polynomial law:

$$\begin{aligned} t_{glob} &= \langle Q_{hit} \rangle\, t_{lm}(N) = A_{glob}\, N^{b_{glob}} \\ \text{with} \quad A_{glob} &= A_{hit} A_{cpu} \\ \text{and} \quad b_{glob} &= b_{hit} + b_{cpu} \end{aligned} \tag{4.71}$$

Contrary to this indirect way one also can measure the CPU time directly using the appropriate system routines. The resulting values for t_{glob} are depicted in figure 4.15 with a cross

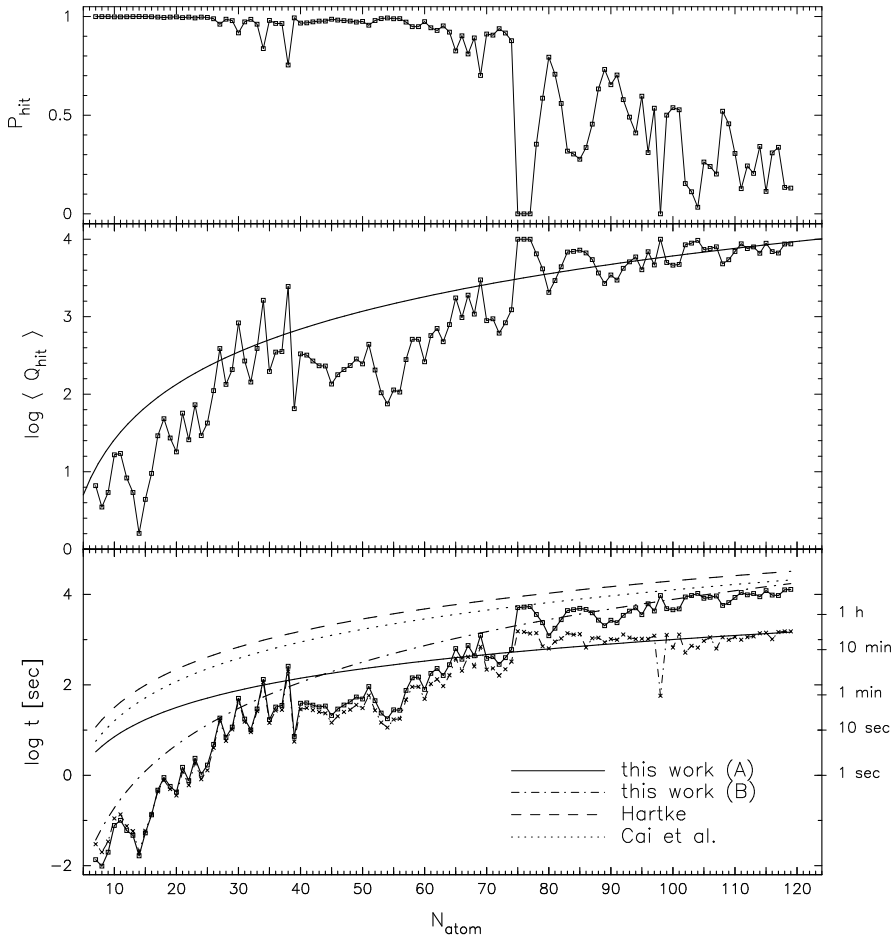

Figure 4.15: Detailed analysis of the performance of the basin–hopping algorithm. The upper panel repeats the data for P_{hit} already shown in figure 4.14. The middle panel shows the mean first passage time $\langle Q_{hit} \rangle$ averaged over 10 independent runs. The lower panel plots the estimated CPU time required to find the global minimum.

($\times$) together with those obtained by using $\langle Q_{hit} \rangle$ and the results of the local optimization benchmark investigation in section 4.1.7, which are marked with a square ($\square$). For clusters with up to ≈ 70 atoms, both data sets fit perfectly well. For larger cluster the directly measured CPU time is considerably lower, then those obtained indirectly. One might think of two different reasons for this. First of all it could be possible, that the CPU time measured by a system routine is erroneous. Especially for longer times different error might accumulate. But a closer look at the results reveals the (possibly) true reason: The start configurations for the benchmark investigation of the local minimization algorithms were generated, by randomly placing the desired number of atoms within a box of appropriate size. For the basin–hopping algorithm on the other hand each trial configuration is based on the stationary point found in the previous step. Thus, in this case the coordinates are closer to a (hopefully new) local minimum and it requires less iterations (approximately

a factor 1/2) to reach it, than in the completely random case. Although the first reason cannot definitely be excluded, we regard the second explanation as the correct one.

The resulting parameters for both approaches together with those given by Hartke (1999) and Cai et al. (2002) are summarised in table 4.4. The parameters obtained on the basis of the directly measured times are given under (A), while indirectly determined data are given under (B). For each of the four parameter sets, function (4.71) has been plotted in the lower panel of figure 4.15. Note however, that this comparison with the results of the other authors is only qualitative, since the results have been obtained on different type of computers. Cai et al. (2002) e.g. use a parallel computer with 8 processors and Hartke a 400 MHZ Pentium II, compared to the 1400 MHz AMD Athlon, used in this work. The type of hardware used for the calculation should mainly influence the value of the preexponential factor A_{glob}, whereas the size dependence of the performance is described by b_{glob}. Parameter set (B) has the highest exponent indicating the worst performance. It is noteworthy, that this rather accidental finding indicates, that an '*intelligent*' technique for generating the next structure might improve a global optimization algorithm. Although using large step sizes accelerates the exploration of large parts of the PES, this might be counteracted by the slowdown of the whole procedure due to the longer time, required for the quenches.

Author	A_{glob}	b_{glob}
this work (A)	0.05	2.15
this work (B)	$4.68 \cdot 10^{-6}$	4.61
Cai et al.	0.02	2.9
Hartke	0.05	2.8

Table 4.4: Fitted parameters for equation 4.71.

On the other hand, it can be seen in table 4.4 and figure 4.15, that the performance of this quite different algorithms is rather similar. For all the exponential factor is between 2 and 3. The concrete values should not be taken too seriously and merely seen as a guiding principle, since it is apparent, that $t_{glob}(N)$ strongly depends on the topography of the cluster's PES. Additionally no attempt has been made to optimize the parameters of the basin–hopping algorithm, e.g. the usage of a higher reduced temperature could improve the performance at least for some clusters. This comparable performance has already been observed for P_{hit} in figure 4.14. Thus, one might answer the question stated above, whether the performance of a global optimization algorithm is influenced by the technique used to explore the (transformed) PES, with: "*No, not really.*" At least for the potential energy surface of Lennard–Jones clusters, each global optimization techniques considered here solves the problem roughly speaking as good as the other. It would be interesting to investigate, whether this is also valid for other systems, like Morse clusters.

We close this section with a short remark about the $\mathcal{NP}$–hardness of global optimization problems. It is noteworthy, that although it was found, that the CPU time required to find the global optimum of a Lennard–Jones cluster depends polynomial on the cluster size N, this does not contradict the fact, that this problem is known to be $\mathcal{NP}$–hard. At first, the theory of computational complexity assumes, that one *proves*, that a certain configuration is indeed a solution of the global optimization problem. This up to now can not be accomplished for clusters, thus all global minima discussed are only *putative* global

minima, until a new, better solution is found. Although this seems unlikely, given the large number of attempts to tackle this problem, it cannot be excluded. This is demonstrated by the recently found new global minimum for LJ_{98} (Leary & Doye, 1999). Secondly computational complexity considers the worst case and makes no assumptions about the topography of the PES, similar to the Levinthal paradox. It was already mentioned, that this assumption is not necessarily valid. As the basin–hopping or Hartke's genetic algorithm demonstrate, it is indeed possible to design algorithms, which do not randomly search the potential energy surface but take advantage of different properties, which bias the search towards the global minimum.

4.3 Analysing cluster geometries

Structure and appearance of a cluster are uniquely described by the Cartesian coordinates of the constituting atoms, defining a $3\ N$-dimensional vector $\vec{\mathbf{R}}$. Because of the translational and rotational degrees of freedom, it is possible to reduce the $3 \times N$ numbers of the Cartesian coordinates to $3 \times N - 6$ numbers of the *internal* coordinates, which describe the structure in terms of bonding lengths, bonding angles and dihedral angles[23]. While these coordinates are needed e.g. for visualizing the structure or determining the symmetry point group, they are on the other hand sometimes not so useful, if one is e.g. interested in possible correlations between the structure and the energy of different isomers. In this case one seeks for a transformation $\mathcal{G}$ to reduce the $3 \times N$ Cartesian coordinates to a scalar:

$$\begin{aligned} \mathcal{G} : \mathbb{R}^{3N} &\longrightarrow \mathbb{R} \\ \vec{\mathbf{R}} &\longmapsto g = \mathcal{G}(\vec{\mathbf{R}}) \end{aligned}$$

One possible approach for this problem is the *sphericity* σ introduced by Chang et al. (2001a), which shall be introduced in section 4.3.2. Another is the *sum of square interatomic distances* $\langle R^2 \rangle$, discussed in section 4.3.1

A related problem concerns the question, how similar two cluster configurations $\vec{\mathbf{R}}_r$ and $\vec{\mathbf{R}}_s$ are, i.e. one is interested in a transformation $\mathcal{S}$ with:

$$\begin{aligned} \mathcal{S} : \mathbb{R}^{3N} \times \mathbb{R}^{3N} &\longrightarrow \mathbb{R} \\ \vec{\mathbf{R}}_r \otimes \vec{\mathbf{R}}_s &\longmapsto s = \mathcal{S}(\vec{\mathbf{R}}_r, \vec{\mathbf{R}}_s) \end{aligned}$$

An important feature of such a measure is, that it should be commutative, i.e.:

$$\mathcal{S}(\vec{\mathbf{R}}_r, \vec{\mathbf{R}}_s) \stackrel{!}{=} \mathcal{S}(\vec{\mathbf{R}}_s, \vec{\mathbf{R}}_r) \tag{4.72}$$

A first ansatz to quantify the similarity of two configurations could be the difference of a geometric measure:

$$s = \mathcal{S}(\vec{\mathbf{R}}_r, \vec{\mathbf{R}}_s) = |\mathcal{G}(\vec{\mathbf{R}}_r) - \mathcal{G}(\vec{\mathbf{R}}_s)|$$

[23] If the structure is linear, there are $3 \times N - 5$ internal coordinates.

where one has to use the absolute value in order to fulfil the requirement of equation (4.72). Of course this might be a rather rough method. Some more elaborate approaches will be discussed in the next sections. Special emphasis will be put on the following properties of the measures:

1. Are they commutative?
2. Are they invariant under rotation and translation of the configurations?
3. Are they sensitive to permutational isomerism, i.e. the exchange of two identical atoms, without any geometric change?

The first two properties are important for establishing a kind of metric in the configurational space. As shall be demonstrated it is rather difficult, to fulfil all three requirements.

Since most methods discussed in the following sections have emerged from the investigation of biomolecules and are usually not used in cluster science, they will be presented in some detail.

4.3.1 Square of the interatomic distances

A simple method for reducing the geometry of a cluster to a single number is to calculate the sum of the square interatomic distances within the cluster (Chandrasekhar et al., 2001):

$$\langle R^2 \rangle = \sum_{i=1}^{N} \sum_{j>i}^{N} r_{ij}^2 \tag{4.73}$$

which can be viewed as a summation of the $N(N-1)/2$ independent elements of the distance matrix $\underline{\mathsf{D}}$ (Huisinga et al., 1999):

$$\mathsf{D}_{ij}^2 = (\vec{\mathbf{r}}_i - \vec{\mathbf{r}}_j)^2 \tag{4.74}$$

This symmetric $N \times N$ matrix is sometimes also called *feature vector* and is invariant under rotations and translations.

The sum of the square interatomic distances $\langle R^2 \rangle$ is a measure for the compactness of the structure: The smaller its $\langle R^2 \rangle$–value, the more compact is the configuration. This is demonstrated in figure 4.16, where three different configurations of a 4-mer are depicted. If the distance between two neighbouring atoms is a, one finds for the $\langle R^2 \rangle$–value of the configurations (a), (b), and (c):

$$\langle R^2 \rangle_a = 10\,a \tag{4.75a}$$

$$\langle R^2 \rangle_b = 5\,a + 2\,a\sqrt{2} \approx 7.8\,a \tag{4.75b}$$

$$\langle R^2 \rangle_c = 4\,a + 2\,a\sqrt{2} \approx 6.8\,a \tag{4.75c}$$

The tetrahedron (see e.g. figure 4.18) is the structure with the lowest possible $\langle R^2 \rangle$–value ($\langle R^2 \rangle_{tetrahedron} = 6\,a$) and therefore the most compact configuration of 4 identical atoms.

Since the permutation of atoms within a structure does not effect the interatomic distances (only their order), the $\langle R^2 \rangle$–value is left unchanged in this case.

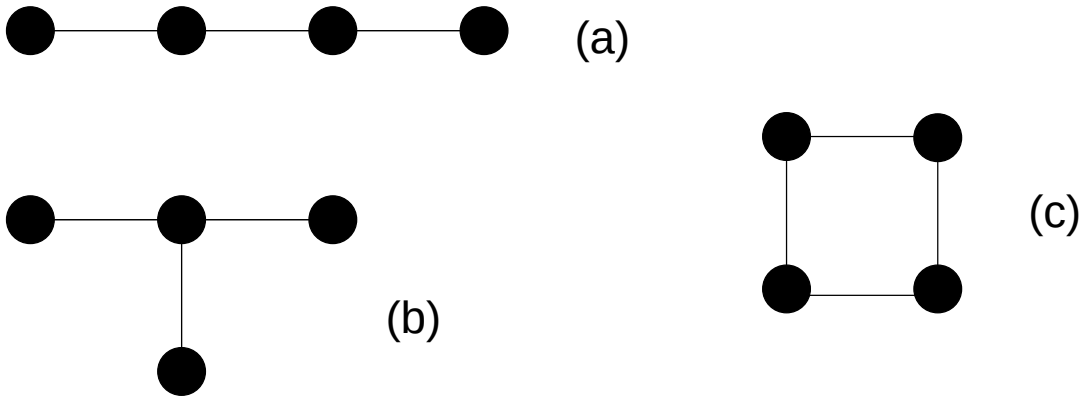

Figure 4.16: Three possible configurations of a cluster with 4 identical atoms, illustrating the sum of the square interatomic distances $\langle R^2 \rangle$. The corresponding values are given in equation (4.75). Note that the tetrahedron, which is shown in figure 4.18, has the lowest value: $\langle R^2 \rangle_{tetra} = 6\,a$

4.3.2 The sphericity of a structure

In an investigation about $(AlN)_n$ clusters ($n = 1, 2, 4, 6, 12$), which for $n \geq 6$ exhibit a cage-like structure, Chang et al. (2001a) argue, that the most reasonable starting geometry for the $(AlN)_{12}$ cluster is a perfect truncated octahedron consisting of six squares and eight hexagons. They observe, that upon optimization these faces of the perfect body loose their planarity and distort in several complex ways, but conserve the point group symmetry (T_h) of the structure. For a detailed analysis of the phenomenon Chang et al. (2001a) view a N-cluster as a purely geometric object, a convex polyhedron $\mathcal{P}_N$. For this set $\mathcal{P}_N$ of N points or vertices in $\mathbb{R}^3$ they calculate the *convex hull* defined as:

$$\mathrm{conv}(\mathcal{P}_N) := \left\{ \sum_{i=1}^{N} \lambda_i\, x_i \;\middle|\; \lambda_i \geq 0 \;\wedge\; \sum_{i=1}^{N} \lambda_i = 1 \right\} \tag{4.76}$$

As a consequence of this definition it is possible to measure the volume and the surface of the considered set of points. Additionally one is able to distinguish between points, lying within the cluster or on its surface. The numerical computation of the convex hull leads to a set of $N_\triangle$ triangles, a so called triangulation of the polyhedron. Each triangle T_i ($i = 1, \ldots, N_\triangle$) with the vertices $\vec{\mathbf{a}}_i$, $\vec{\mathbf{b}}_i$ and $\vec{\mathbf{c}}_i$ has a surface area S_{T_i} given by (see e.g. Pisanski et al., 1997):

$$S_{T_i} = \frac{1}{2}\,|(\vec{\mathbf{a}}_i - \vec{\mathbf{c}}_i) \times (\vec{\mathbf{b}}_i - \vec{\mathbf{c}}_i)| \tag{4.77}$$

The volume of the polyhedron $\mathcal{P}_N$ can be computed by adding the signed(!) volumes V_{T_i} of the irregular tetrahedra spanned by the three vertices of the triangle T_i and the origin. An analytic formula for this expression can be found in Bronstein & Semendjajew (1989,

p. 197) or Pisanski et al. (1997). It holds:

$$V_{T_i} = \frac{1}{6} \begin{vmatrix} a_x & a_y & a_z \\ b_x & b_y & b_z \\ c_x & c_y & c_z \end{vmatrix} \tag{4.78}$$

Using equation (4.77) and (4.78) one finds for the surface $S(\mathcal{P}_N)$ and the volume $V(\mathcal{P}_N)$ of the polyhedron:

$$S(\mathcal{P}_N) = \sum_{i=1}^{N_\triangle} S_{T_i} \tag{4.79}$$

$$V(\mathcal{P}_N) = \left| \sum_{i=1}^{N_\triangle} V_{T_i} \right| \tag{4.80}$$

One might argue, that a shortcoming of this definition of the volume and the surface of a cluster is, that it lacks any physical motivation. So as to elucidate this point, consider the situation depicted in figure 4.17, where 3 atoms, part of the surface of a cluster, form a kind of kink. From the purely mathematical point of view using the convex hull, the

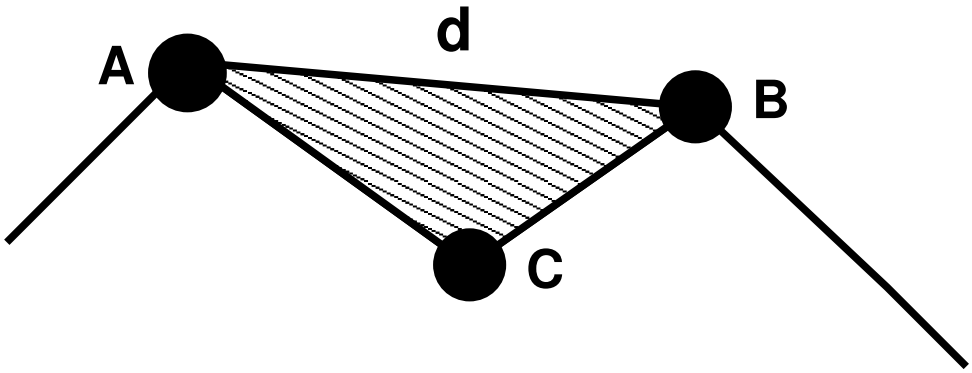

Figure 4.17: Problem of the definition of the volume of a polyhedron via the convex hull

shaded region is part of the cluster and the point C lies within it. From a physical or chemical point of view, this depends on the distance d between the points A and B. If d is greater, then the typical bonding length r_{A-B}, than this region lies *outside* of the cluster. Consequently one might say, that $V_{math} \geq V_{phys}$. Of course, this greatly depends on the type of atoms, positioned in the points A and B and on the value one assigns to what was called a *typical* bond length[24]. Other approaches to the definition of a molecular surface

[24]A similar problem occurs, when one visualizes molecules or clusters using computer programs. Depending on the value defined within the code for a bond length, the program draws or does not draw a stick between two atoms. One should keep in mind, that these sticks are mainly intended to clarify the structure.

can be found under the keyword *van de Waals surface* or *solvent accessible surface* (Leach, 2001).

This discussion demonstrated that the aforementioned shortcoming of the mathematical definition of the cluster volume V_{cluster} can be viewed as an advantage, because any physically motivated definition of V_{cluster} introduces some arbitrariness, due to the necessity, of deciding, whether two atoms are neighbours or not. Chang et al. (2001a) use this pure geometric way of measuring the volume and surface of a cluster, to define a measure of sphericity σ, by comparing the surface area of the polyhedron $\mathcal{P}_N$ with that of a sphere of equal volume, which leads to:

$$\sigma = \sqrt[3]{\frac{36\pi\, V(\mathcal{P}_N)^2}{A(\mathcal{P}_N)^3}} \tag{4.81}$$

where the volume and surface are calculated using the convex hull and equations (4.79) and (4.80). A similar quantity is the so called *isoperimetric quotient* $IQ(\mathcal{P}_N)$, which was first introduced by Lhuilier in 1782 (see Deza et al., 1998, and references therein) and is simply the cube of the sphericity σ, i.e.:

$$IQ(\mathcal{P}) = 36\pi \frac{V(\mathcal{P})^2}{A(\mathcal{P})^3} = \sigma^3 \tag{4.82}$$

For both the so called *isoperimetric inequality* holds:

$$0 \leq IQ(\mathcal{P}) \leq 1 \qquad \text{and} \qquad 0 \leq \sigma \leq 1 \tag{4.83}$$

where only for the sphere, having least surface for any volume, IQ and σ are equal 1. Table 4.5 presents the isoperimetric quotient IQ, the sphericity

Table 4.5: Sphericity, isoperimetric quotient and some further properties of the Platonic solids, depicted in figure 4.18.

Polyhedron	No. of vertices	No. of facets	IQ	σ	PG
tetrahedron	4	4	$\frac{\pi}{6\sqrt{3}} \approx 0.3023$	0.6711	T_d
octahedron	6	8	$\frac{\pi}{3\sqrt{3}} \approx 0.6045$	0.8456	O_h
cube	8	6	$\frac{\pi}{6} \approx 0.5236$	0.8060	O_h
icosahedron[a]	12	20	$\frac{\pi\,\tau^4}{15\sqrt{3}} \approx 0.8288$	0.9393	I_h
dodecahedron[a]	20	12	$\frac{\pi\,\tau^{7/2}}{3\cdot 5^{5/4}} \approx 0.7547$	0.9105	I_h

[a] The variable τ is defined as $\tau = \frac{1+\sqrt{5}}{2}$ (golden ratio).

σ and some other properties of the 5 Platonic solids: the tetrahedron, the octahedron, the cube, the icosahedron and the dodecahedron (see also figure 4.18).

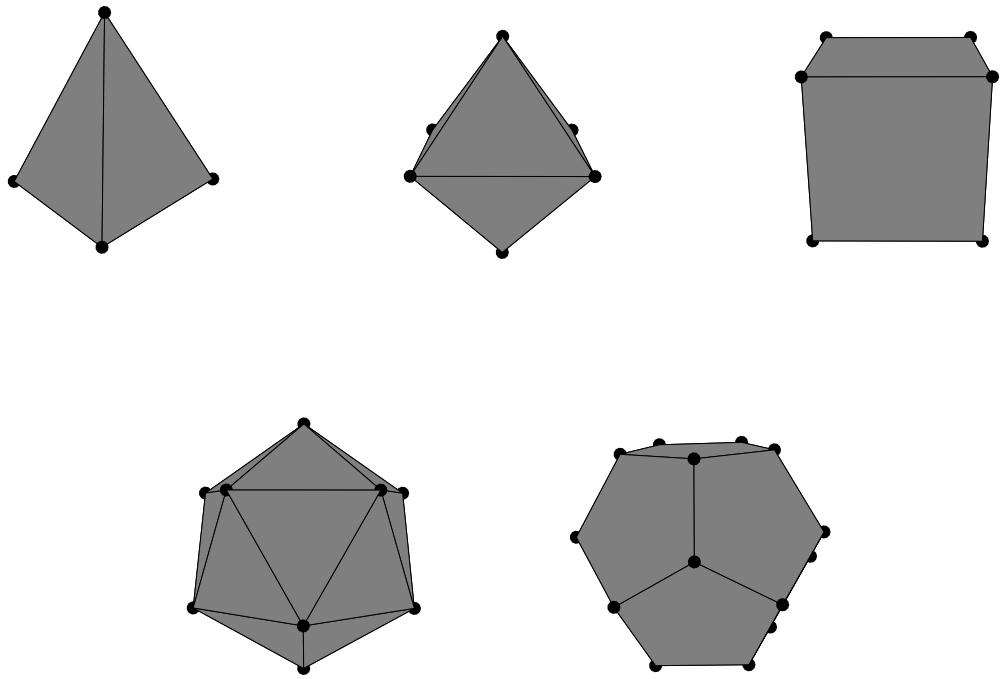

Figure 4.18: The 5 platonic solids, ordered according to the increasing number of vertices: tetrahedron, octahedron, cube, icosahedron and dodecahedron. Some of their properties are listed in table 4.5

In Chang et al. (2001a) the authors observe, that the distortion of the (ideal) starting configuration of the $(AlN)_{12}$ cluster in the course of the optimization process leads to a configuration, which is about 3% more spherical:

$$\sigma_{ideal}((AlN)_{12}) = 0.909918 \quad \xrightarrow{\text{optimization}} \quad \sigma_{real}((AlN)_{12}) = 0.944751$$

The same holds true for the well known C_{60} fullerene molecule (see figure 3.1). The perfect truncated icosahedron has a sphericity of $\sigma_{ideal} = 0.966622$ whereas the real C_{60} structure has a sphericity of $\sigma_{real} = 0.966819$. This slight increase is due to the fact, that the hexagons of the real bucky ball have two alternate edge length ($a = 1.458$ and $b = 1.401$).

A similar increase of the sphericity upon optimization is observed for fullerene-like clusters $(XY)_n$ of ceramic and semiconductor materials (X = Al, Ga, and In; Y = N, As, and Sb; $n = 12$, 24 and 60; see Chang et al., 2001b)). Furthermore the internal rotation of ethane (C_2H_6), hydrogen peroxide (H_2O_2) and hydrazine (N_2H_4) is analysed using the concepts of the convex hull and sphericity σ by Chang et al. (2002). They find, that the minima of the potential energy surfaces for the internal rotation correspond to the maximal values of the sphericity σ.

The examples discussed above demonstrate, that the spherical aspects of molecules and clusters, if seen as convex polyhedra, give rise to another stability criterion apart from minimal energy and high symmetry. One might conclude that under the physical condition of the energy being minimal the system tries to become more spherical (Chang et al., 2002).

Further examples for the application of the concept of sphericity in the field of molecular modelling concern the chemistry and physics of fullerenes (Pisanski et al., 1997, Bokal, 1998, Deza et al., 1998). These species can be seen as a *simple* polyhedron, which means, that each vertex has exactly 3 neighbouring vertices (Deza et al., 1998). It is demonstrated by Pisanski et al. (1997), that polyhedra with the maximal IQ values reproduce well the molecular mechanics geometries of fullerenes.

A similar quantity, the *asphericity* α of a molecular configuration, defined as the inverse of the isoperimetric quotient, is used by Matsumoto et al. (2002) for the analysis of the inherent structure of water clusters in the course of a molecular dynamics simulation.

The introduced measure of the sphericity of a cluster allows one to quantify a statement often found in literature, that certain aggregates are more *spherical* then others. In most cases this statement is guided solely by a visual impression (cf. section 5.3.3).

4.3.3 Root mean square deviation and superposition

The structure of small molecules with 3 or 4 atoms might be easily compared by means of their internal coordinates. For larger molecules like proteins or clusters this becomes difficult, cumbersome or even impractical. A simpler, albeit cruder measure is the root-mean-square (rms) coordinate deviation σ_{rms} (see e.g. Field, 1999, chapter 3), defined as:

$$\sigma_{\mathrm{rms}}(\vec{\mathbf{R}}_r, \vec{\mathbf{R}}_s) = \sqrt{\frac{1}{m_{tot}} \sum_{i=1}^{N} m_i \left(\vec{\mathbf{r}}_i^{\,r} - \vec{\mathbf{r}}_i^{\,s}\right)^2} \tag{4.84}$$

where the superscripts r and s refer to the coordinates of the first and second structure respectively. As it is apparent from this definition, the value of σ_{rms} depends on the orientation of the structures and thus lacks translational or rotational invariance. In order to develop a useful measure for the comparison of structures based on the rms coordinate deviation it is necessary to define a unique orientation of the molecules, using the principal axis transformation for example. However this coordinate transformation is not necessarily the optimal choice in that sense, that there might exist an orientation, for which the σ_{rms}-value can be smaller. Hence one seeks a transformation, which superimposes the two structures in such way, that the rms coordinate deviation is minimal. Mathematically this superposition can be expressed as follows: First one set of coordinates is chosen as the reference structure ($\vec{\mathbf{R}}_r = (\vec{\mathbf{r}}_i^{\,r}, \ldots, \vec{\mathbf{r}}_N^{\,r})$). Then the second structure $\vec{\mathbf{R}}_s$ is superimposed on this reference structure. Any translation of the two structures can always be removed, by shifting the centres of mass of the configurations into the origin. Thereafter the problem is reduced to the computation of a rotation matrix $\underline{\mathsf{U}}$, which minimizes the rms coordinate

deviation σ_{rms}, which now can be written as a function of this matrix:

$$\sigma^2_{\mathrm{rms}}(\underline{\mathsf{U}}) \propto \sum_{i=1}^{N} m_i \left(\vec{\mathbf{r}}_i^{\,r} - \underline{\mathsf{U}}\, \vec{\mathbf{r}}_i^{\,s}\right)^2 \tag{4.85}$$

The rotation matrix $\underline{\mathsf{U}}$ has to be an orthogonal matrix, which means:

$$\underline{\mathsf{U}}^T\, \underline{\mathsf{U}} = \underline{\mathsf{I}} \qquad \Leftrightarrow \qquad \det \underline{\mathsf{U}} = \pm 1 \tag{4.86}$$

where $\underline{\mathsf{I}}$ is the identity matrix (see Fischer, 1989, p. 200). Consequently one faces the solution of the following problem, by defining a new mapping σ_{opt}:

$$\begin{aligned} \sigma_{\mathrm{opt}}: \quad & \mathbb{R}^{3N} \times \mathbb{R}^{3N} \;\rightarrow\; \mathbb{R}_+ \\ & \sigma_{\mathrm{opt}}\left(\vec{\mathbf{R}}_r, \vec{\mathbf{R}}_s\right) = \min_{\underline{\mathsf{U}} \in \mathcal{O}(3,3)} \sigma_{\mathrm{rms}}\left(\underline{\mathsf{U}}; \vec{\mathbf{R}}_r, \vec{\mathbf{R}}_s\right) \end{aligned} \tag{4.87}$$

where $\mathcal{O}(3,3)$ is the set of orthogonal 3×3 matrices. Problem (4.87) is a minimization problem with constraints specified by equation (4.86), and could be solved using an appropriate method for this class of optimization problems (see e.g. Polak, 1997 or Nocedal & Wright, 1999). McLachlan (1982), for example, introduced an iterative algorithm, which is based on the conjugate gradient method, for finding the best rotation matrix $\underline{\mathsf{U}}$. For the analysis of cluster geometries within the scope of this thesis, two algebraic approaches have been used. They are shortly presented in the next two section. In the concluding section 4.3.3.3 their performance and properties are discussed.

4.3.3.1 Superposition with the Kabsch method

One of the first and most widely used methods to solve the minimization problem (4.87) was proposed by Kabsch (1976; see also Kabsch, 1978). He found an expression for the rotation matrix using the standard method of Lagrange multipliers. A good and compact overview of the procedure is given in Kabsch (1978).

4.3.3.2 Superposition with the Kneller algorithm

Kneller (1991) introduced a different parametrisation of the rotation matrix $\underline{\mathsf{U}}$ using four *quaternion* parameters:

$$\vec{\mathbf{q}}^{\,t} := (q_0, \vec{\mathbf{q}}^{\,t}) = (q_0, q_1, q_2, q_3)$$

leading to the following expression for the rotation matrix:

$$\underline{\mathsf{U}} = \begin{pmatrix} q_0^2 + q_1^2 - q_2^2 + q_3^2 & 2(q_1 q_2 - q_0 q_3) & 2(q_0 q_2 + q_1 q_3) \\ 2(q_0 q_3 + q_1 q_2) & q_0^2 - q_1^2 + q_2^2 - q_3^2 & 2(q_2 q_3 - q_0 q_1) \\ 2(q_1 q_3 - q_0 q_2) & 2(q_0 q_1 + q_2 q_3) & q_0^2 - q_1^2 - q_2^2 + q_3^2 \end{pmatrix} \tag{4.88}$$

For the determinant of this matrix one finds the following expression:

$$\det \underline{\mathsf{U}} = \left(q_0^2 + q_1^2 + q_2^2 + q_3^2\right)^3 \tag{4.89}$$

and consequently the requirement (4.86) is equivalent to a normalisation condition for the quaternion parameters:

$$q_0^2 + q_1^2 + q_2^2 + q_3^2 = \vec{\mathbf{q}} \cdot \vec{\mathbf{q}} = 1 \tag{4.90}$$

The algorithm to find the quaternion parameters that solve the minimization problem makes use of the algebraic properties of quaternions (Altmann, 1986). It is outlined in the paper of Kneller (1991) and leads to the analytic computation of a 4×4 matrix $\underline{\mathsf{M}}$ whose eigenvalues finally yield the four quaternion parameters q_i $(i = 0, \ldots, 3)$.

4.3.3.3 A short comparison of the two methods

Both methods give in most cases identical results (up to 4 or 5 digits) as it has been tested in this work on a variety of structures. Remarkable are those cases, where the results differ significantly. This often happens for those cases, where the Kabsch algorithm results in a so called *improper* rotation matrix, i.e. an orthogonal matrix $\underline{\mathsf{U}}$, with

$$\det \underline{\mathsf{U}} = -1$$

Equation (4.89) implies, that this case cannot happen for the Kneller algorithm, because all q_i are assumed to be real valued and thus $\det \underline{\mathsf{U}} > 0$. Fischer (1989, p. 202) points out, that an orthogonal matrix $\underline{\mathsf{U}}$ with $\det \underline{\mathsf{U}} = -1$ can be viewed as mirroring the structure at an axis, which is determined by one of the matrix eigenvectors. It was further observed that in these cases the rms coordinate deviation after superimposing the structure using Kabsch's algorithm is smaller than the one using Knellers algorithm, i.e.:

$$\sigma_{\text{opt,Kabsch}} < \sigma_{\text{opt,Kneller}} \qquad \text{if } \det \underline{\mathsf{U}} = -1$$

Presumably in such cases there exist two minima of $\sigma_{\text{rms}}(\underline{\mathsf{U}})$. While the stronger constraint of the Kneller algorithm ($\det \underline{\mathsf{U}} = 1$) leads to a suboptimal solution of the problem (4.87), the better solution is found by the Kabsch algorithm due to its weaker requirement ($\underline{\mathsf{U}}$ is orthogonal $\Leftrightarrow |\det \underline{\mathsf{U}}| = 1$).

The computational performance of both algorithms should be approximately equal. Each one has to compute a matrix using the coordinates of all atoms, which in the case of big molecules might be the most time-consuming part. A subsequent diagonalisation of a quadratic matrix with 3 and 4 rows respectively, should be computationally inexpensive.

The algorithms for the superposition of structures only cover translation and rotation, but can not describe the permutation of atoms. As a consequence the σ_{opt}–measure is not invariant under this kind of geometric changes. Whether this is a drawback of the measure or not, depends on the type of application. In the case of molecular dynamics calculations, where it might occur that due to the dynamics two atoms exchange their positions, it is of course necessary to quantify this effect. On the other hand when analysing the geometric structure of the stationary points of a cluster on the potential energy surface it might be essential to remove such permutations. As to achieve this, one simply has to order the atoms in a determined fashion, which is invariant under translation and rotation, e.g. according to their distance from the centre of mass.

An important feature of the minimized rms coordinate deviation σ_{opt} is the fact, that it induces a metric in the configuration space as has been proved by Kaindl & Steipe (1997). As a metric σ_{opt} has the following properties:

$$\sigma_{\text{opt}}(\vec{\mathbf{R}}_r, \vec{\mathbf{R}}_s) : \mathbb{R}^{3N} \times \mathbb{R}^{3N} \to \mathbb{R}_+$$

$$\sigma_{\text{opt}}(\vec{\mathbf{R}}_r, \vec{\mathbf{R}}_s) \geq 0 \quad \wedge \quad \sigma_{\text{opt}}(\vec{\mathbf{R}}_r, \vec{\mathbf{R}}_s) = 0 \Leftrightarrow \vec{\mathbf{R}}_s = \vec{\mathbf{R}}_r \tag{4.91a}$$

$$\sigma_{\text{opt}}(\vec{\mathbf{R}}_r, \vec{\mathbf{R}}_s) = \sigma_{\text{opt}}(\vec{\mathbf{R}}_s, \vec{\mathbf{R}}_r) \tag{4.91b}$$

$$\sigma_{\text{opt}}(\vec{\mathbf{R}}_r, \vec{\mathbf{R}}_t) \leq \sigma_{\text{opt}}(\vec{\mathbf{R}}_r, \vec{\mathbf{R}}_s) + \sigma_{\text{opt}}(\vec{\mathbf{R}}_s, \vec{\mathbf{R}}_t) \tag{4.91c}$$

These metric properties are important for the development of an useful procedure for the analysis of e.g. molecular dynamics simulations, which will be presented in a forthcoming section.

4.3.4 The difference distance matrix

Another approach for the comparison of two configurations, which is also based on the distance matrix $\underline{\mathsf{D}}$ (c.f. Eq. (4.74)) is called *difference distance matrix* (DDM) approach and was originally developed for the analysis of protein structures (see e.g. Richards & Kundrot, 1988, Schneider, 2000). An application to the different conformations of myoglobin was presented by Elber & Karplus (1987). As the name suggests, the difference distance matrix $\underline{\Delta}^{r-s}$ is defined as the difference of the distance matrix $\underline{\mathsf{D}}^r$ of a reference structure $\vec{\mathbf{R}}_r$ and of the distance matrix $\underline{\mathsf{D}}^s$ of a second structure $\vec{\mathbf{R}}_s$:

$$\underline{\Delta}^{r-s} := \underline{\mathsf{D}}^r - \underline{\mathsf{D}}^s \qquad \Longleftrightarrow \qquad \Delta_{ij}^{rs} = \mathsf{D}_{ij}^r - \mathsf{D}_{ij}^s \tag{4.92}$$

The matrix $\underline{\Delta}$ is symmetric and the diagonal elements $\Delta_{ii} = \mathsf{D}_{ii}^r - \mathsf{D}_{ii}^s$ are zero. Thus the difference distance matrix for two configurations with N atoms has $\frac{1}{2}N(N-1)$ independent elements. Since distance matrices are invariant under rotation and translation of the molecule, this also holds true for the DDM $\underline{\Delta}$. Additionally the DDM has some advantages over methods based on a rms-fit procedure previously described in section 4.3.3:

1. The DDM approach clearly locates identical parts of the two structures under consideration.
2. The differences are quantified on an atomic level and not added up to a single figure.
3. The approach can accommodate insertions and deletions in the structure.
4. The difference distance matrix $\underline{\Delta}$ can be easily and fast calculated, even for large molecules.

The immense size and complexity of the DDM makes it rather challenging to find an intuitive representation which expedites its interpretation. Following Schneider (2000) we use a two-dimensional plot, where each matrix element is displayed as a colour-coded square

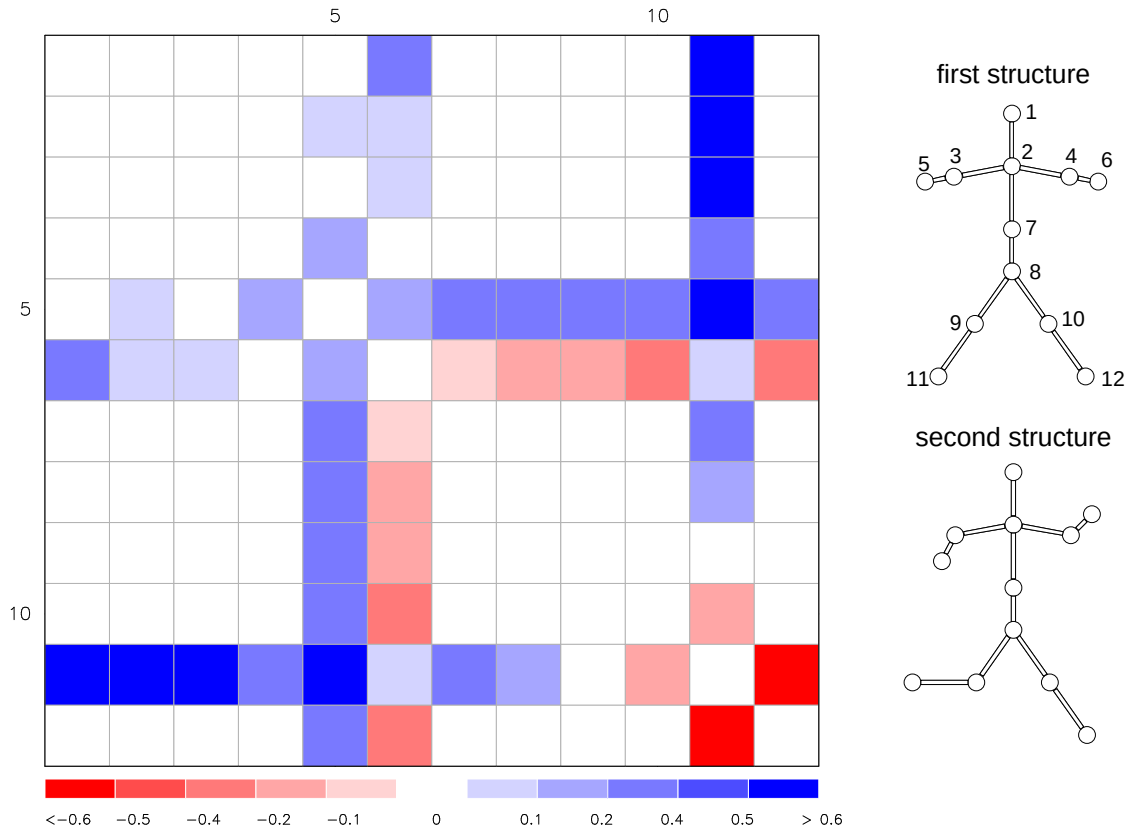

Figure 4.19: Illustration of the difference distance matrix $\underline{\Delta}$. The distances of "*bond*" atoms (e.g. r_{3-5}) in the two structures depicted next to the plot, are kept fixed on distortion. The colours used to encode the changes of the distances are depicted below the plot. Blue squares indicate a contraction and red squares indicate a expansion of the structures. The $\langle R^2 \rangle$-value of the first structure is 537.74Å^2, while for the second it is 498.44Å^2. The rms coordinate deviation after superposition of the two configurations is $\sigma_{\text{opt}} = 0.36828$ for both methods.

representing the distance change between the atoms: Blue stands for positive (contraction) and red for negative (expansion) changes of the interatomic distances r_{ij}. The absolute values are indicated by the intensity of the colour, where full colours (blue or red) represent the largest values. In order to demonstrate the interpretation of the difference distance matrix, figure 4.19 depicts the DDM $\underline{\Delta}$ of two arbitrary chosen structures, which are composed of an *invariant* skeleton and 3 *moving* atoms (No. 5, 6, and 11), as can be seen in the right part. The distances of *bond*[25] atoms are kept fixed, while only the bond angles have been altered, which of course leads to changes of the distances between *non-bond* atoms. The visualization of the difference distance matrix in the left part of figure 4.19

[25]The terms *bond* and *non-bond* are used here only in a descriptive manner and lack any physical or chemical meaning.

clearly reveals certain features, namely:

- The unchanged parts of the configurations are discernible as accumulations of white squares, e.g. in the upper left corner. Due to the possibility to define a threshold, below which distance changes are treated as zero, small (e.g. thermal) fluctuations can be suppressed, while essential changes are emphasised.
- From the pattern of the coloured squares it is also evident, which atoms mainly participate in the structural changes from structure $\vec{\mathbf{R}}_r$ to $\vec{\mathbf{R}}_s$. In the present example, only the elements of the 5-th, 6-th and 10-th column (or row) are coloured, because all other atoms are left unchanged.
- In this case also the type and extent of the changes can be characterised. For example the colours of the movements of atoms 5 and 6 are less intense than that of atom no. 10, indicating the smaller displacements of this atoms.

Additionally it is apparent from this example, that the analysis of different structures by means of the difference distance matrix is applicable only to a limited number of configurations. Huisinga et al. (1999) describe a method to circumvent this drawback of the distance matrix approach, by defining the structural difference of two structures as:

$$\mathrm{dist}(\vec{\mathbf{R}}_r, \vec{\mathbf{R}}_s) = \frac{1}{N(N-1)/2} \left(\sum_{i<j}^{N} \left(\mathsf{D}_{ij}^r - \mathsf{D}_{ij}^s \right)^2 \right)^{1/2} \tag{4.93}$$

This allows the calculation and visualization of the distance matrix of a trajectory, where the distance r_{ij} is not measured between two atoms, but instead between configurations $\vec{\mathbf{R}}(t_i)$ and $\vec{\mathbf{R}}(t_j)$ at different times of a molecular dynamic simulation (see e.g. Best & Hege, 1999, and references therein).

Although the difference distance matrix is sensitive to the permutation of atoms, it should be relatively easy to detect such a case, where simply two atoms have been exchanged. This would result in a characteristic pattern of the DDM–plot, where only the rows and columns of the two exchanged atoms are coloured.

4.4 Molecular Dynamic Simulations

Up to now the discussion solely focused on the local minima of the potential energy surface. But since real clusters have a certain temperature, they are not necessarily trapped in the vicinity of such a minimum. Instead they might overcome a barrier separating two different basins. The collective motion of the atoms within such a cluster are completely determined by Newtons equations of motion, regarded the forces acting on each atom are known. These forces might be calculated using an empirical force field and its gradient or by means of *ab initio* methods. While it is possible to treat clusters with up to 10.000 atoms using potential models, the latter approach is restricted to rather small clusters with only a few

atoms (for an example see Jellinek et al., 1994 or Bonačić-Koutecký et al., 1997). Such molecular dynamics calculations facilitate further insight into the topology of the potential energy surface. For this reason we accomplished some microcanonical molecular dynamics simulations of some clusters at different total energies. The basic equations are shortly presented hereafter.

In a microcanonical ensemble, the total energy E_{sys} of the system, its volume V, and its number N of particles are kept constant[26]. Since Newton's equation of motion conserve the energy, they provide a suitable method for the description of the microcanonical ensemble. For other ensembles, e.g. the canonical or constant–NVT ensemble, one has to use other methods for simulating the motion of the system through the phase space (Allen & Tildesley, 1987, p. 40ff).

A proper algorithm for the integration of Newton's equation of motion is the *Verlet velocity algorithm* (Allen & Tildesley, 1987, Rapaport, 1995, Haberlandt et al., 1995, Frenkel & Smit, 1996), which ensures the conservation of energy to a high accuracy and is easy to implement. In what follows we denote with $\vec{\mathbf{R}}(t) \in \mathbb{R}^{3N}$ the vector with the coordinates of the cluster at a given moment t, called trajectory. Correspondingly $\vec{\mathbf{V}}(t) \in \mathbb{R}^{3N}$ is the vector with the velocities of the atoms. As discussed by Allen & Tildesley (1987, p. 81), the Verlet–velocity takes the following form:

$$\vec{\mathbf{R}}(t+\Delta t) = \vec{\mathbf{R}}(t) + \vec{\mathbf{V}}(t)\,\Delta t + \frac{1}{2m_i}\Delta t^2\,\mathbf{A}(t) \tag{4.94a}$$

$$\vec{\mathbf{V}}(t+\Delta t) = \vec{\mathbf{V}}(t) + \frac{1}{2}\Delta t\,\left(\vec{\mathbf{A}}(t)) + \vec{\mathbf{A}}((t+\Delta t)\right) \tag{4.94b}$$

where $\vec{\mathbf{A}}(t)$ is the acceleration of the atoms. The components of $\vec{\mathbf{A}}$ of the i–th atom are given by:

$$\vec{\mathbf{A}}_i = -\frac{1}{m_i}\,\nabla_{\mathbf{r_i}}\Phi(\mathbf{R}(t)) \tag{4.95}$$

with m_i the mass of that atom, and $\nabla_{\mathbf{r_i}}$ the derivation with respect to the coordinates of the i–th atom.

During the course of a molecular dynamic simulation one essentially monitors 3 different quantities (see e.g. Jellinek & Krissinel, 1999):

1. The potential energy E_{pot} of the system calculating using the force field, which describes the interaction between the atoms in the system.

2. The kinetic energy E_{kin} of the system computed using the velocities $\vec{\mathbf{v}}_i$ of the atoms, according to:

$$E_{kin} = \frac{1}{2}\,\sum_{i=1}^{N} m_i v_i^2 \tag{4.96}$$

This allows one to introduce a kinetic temperature T_k by calculating

$$T_k = \frac{2\,E_{kin}}{k\,(3N-6)} \tag{4.97}$$

[26] One often finds the notion 'constant-NVE' for the microcanonical ensemble.

As noted by Allen & Tildesley (1987) this expression is exact for the canonical ensemble, but differs by $\mathcal{O}(N^{-1})$ from the thermodynamic definition $T^{-1} = \partial S/\partial E$ of the temperature (e.g. Reif, 1987) in the microcanonical ensemble.

3. The coordinates of the cluster, which are typically stored after a certain, prescribed number of time steps.

The potential and kinetic energy are averaged over the whole trajectory, which is denoted by $\langle\, . \,\rangle_t$. Additionally the temporal behaviour of the system can be characterised by means of the so called *short time average* (STA) of any suitable quantity $\mathcal{A}$ (Berry, 1995). It is calculated according to:

$$\langle\, \mathcal{A} \,\rangle_{\mathrm{STA}} = \frac{1}{\mathcal{N}_{\mathrm{STA}}} \sum_{i=1}^{\mathcal{N}_{\mathrm{STA}}} \mathcal{A}(t_i) \tag{4.98}$$

where the number of time steps $\mathcal{N}_{\mathrm{STA}}$ has to be large enough to average over a few vibrations of the cluster without leaving the current basin on the potential energy surface. Most authors (see Berry, 1995, and references therein) identify $\mathcal{A}$ with the kinetic temperature of the system. But since it holds for the total energy of the system

$$E_{tot} = E_{pot} + E_{kin} = E_{pot} + \frac{1}{2}\, k\, (3N - 6)\, T_k \tag{4.99}$$

and we are interested in the topological structure of the potential energy surface, we consider the short time average $\langle\, E_{pot} \,\rangle_{\mathrm{STA}}$ of the potential energy.

The structural changes a cluster undergoes during a simulation at a specific energy is analysed by means of the *root-mean-square bond length fluctuation* δ:

$$\delta = \frac{2}{N\,(N-1)} \sum_{i<j} \frac{\sqrt{\langle\, r_{ij}^2 \,\rangle_t - \langle\, r_{ij} \,\rangle_t^2}}{\langle\, r_{ij} \,\rangle_t} \tag{4.100}$$

This section is closed with a short explanation of the preparation of the initial state of the cluster. As the start configuration a local minimum of the potential energy surface, possibly the global minimum, is chosen. The velocities are initialised randomly and it is required, that the total linear and angular momentum vanish, i.e.:

$$\vec{\mathbf{p}}_{tot} \equiv 0 \qquad \text{and} \quad \vec{\mathbf{L}}_{tot} \equiv 0 \tag{4.101}$$

This is accomplished by the following transformation of the randomly chosen velocities $\vec{\mathbf{v}}_i^{\,r}$:

$$\vec{\mathbf{v}}_i^{\,i} = \vec{\mathbf{v}}_i^{\,r} + \frac{1}{m_{tot}}\, \vec{\mathbf{p}}_{tot} - \vec{\omega} \times \vec{r}_i \qquad \text{with} \quad \vec{\omega} = \underline{\mathrm{I}}^{-1}\, \vec{\mathbf{L}}_{tot} \qquad (i = 1, \ldots N) \tag{4.102}$$

with $\vec{\omega}$ the angular velocity and $\underline{\mathrm{I}}$ the moments of inertia tensor of the cluster. The new velocities $\vec{\mathbf{v}}_i^{\,i}$, fulfilling condition (4.101), are now scaled to yield the desired total energy of the system.

Chapter 5

Inorganic cluster systems - silicon-oxide

5.1 Introduction

Next to water silicon dioxide is the most abundant molecule on earth. Its solid form is either known as *silica* or *quartz*. Although from a chemical point of view SiO_2 is an oxide, the structures and and properties of silica minerals are more closely related to those of silicates, as enstatite ($MgSiO_3$), forsterite (Mg_2SiO_4), or olivine ($(Mg\ Fe)_2SiO_4$), which are all found on earth and in the circumstellar environments of evolved stars (see e.g. Jäger et al., 1998, Demyk et al., 2000). Quartz can be either crystalline or amorphous.

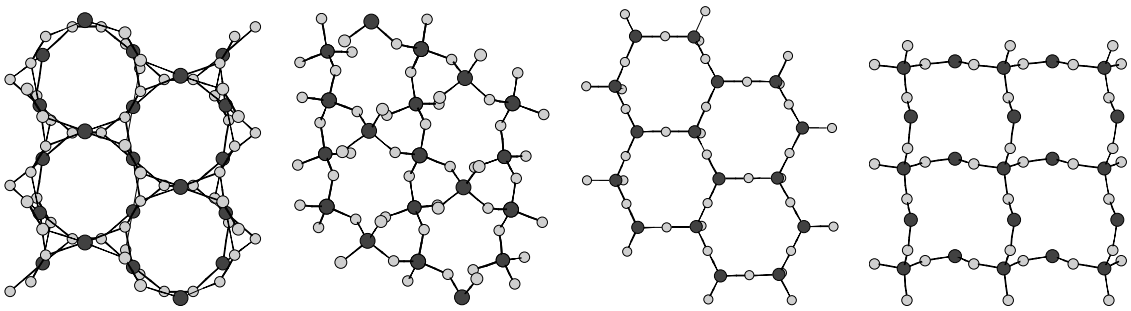

(a) β Quartz (b) α Quartz (c) β Tridymite (d) α Cristobalite

Figure 5.1: Different modifications of solid SiO_2.

In the crystalline case, the SiO_4 tetrahedra is the main building block: The solid consists of a 3–dimensional lattice of such tetrahedra, in which all four oxygen atoms are shared by adjoining tetrahedra. Depending on the temperature and pressure during the crystallisation process, different minerals are formed. One can distinguish between three main forms, namely *Cristobalite*, *Quartz*, and *Tridymite*:

Quartz is the most common form of silicon dioxide. It splits into two different forms,

named α– and β–quartz, shown in figure 5.1(a) and 5.1(b), respectively. β–quartz has a hexagonal crystal structure and is only stable at temperature above 847 K. Below this temperature β–quartz is automatically transformed into α–quartz. Thus, all quartz naturally found on earth is α–quartz, which has a trigonal crystal structure. Pure quartz is colourless, but there exist also coloured quartz minerals like amethyst, which gets is violet colour from the incorporation iron oxide (Mottana et al., 1982).

Tridymite is formed at 1143 K from β–quartz. It has a hexagonal crystal structure, displayed in figure 5.1(c). The mineral tridymite has a white colour and is only rarely found on earth, e.g. in Italy (Mottana et al., 1982).

Cristobalite has also two different forms, α and β. The first form, α–cristobalite, has a tetragonal structure (see figure 5.1(d)). It transforms at temperatures above 543 K into the second form, β–cristobalite. Additionally it is observed, that β–quartz transforms at temperatures above 1079 ± 250 K into β–cristobalite (Chase, 1998). Cristobalite rarely occurs in detectable samples, e.g. in San Cristobal, Mexico, explaining the origin of the name.

It is noteworthy, that the melting temperature of β–quartz ($T_m = 1696 \pm 50$ K) is slightly lower, than that of β–cristobalite ($T_m = 1996 \pm 5$ K, Chase, 1998). Other forms of silica like *coesite* or *stishovite* are only formed under intense heat and pressure, as they occur, when a meteorite strucks the earth. They are only found in the Barringer Crater in Arizona, which was formed by such an event.

Another solid form of oxidised silicon is silicon monoxide SiO(s), which is used as a protective layer and anti-reflection coating in optical applications (Palik, 1985). In a reducing environment SiO(s) acquires additional oxygen and the O–to–Si ratio rises above unity, forming a solid with the stoichiometric composition SiO_x, with $x > 1$. The crystal structure is not known, but presumably SiO(s) forms an amorphous solid, which exhibits only a short range order. Schick (1960) states, that only a few data concerning the properties of SiO are available. Since then, this picture has not changed substantially, e.g. we are not aware of any thermochemical data of SiO(s).

The condensation of silicon oxides has been investigated by several authors. As stated by Schick (1960), the condensation product of SiO(g) might be either SiO(s) or a mixture of Si(s) and SiO_2(s). Hoch & Johnston (1953) observed, that SiO(s) does not exist at temperatures below 1200°C, but that the solid formed consists of a mixture of SiO_2(s) and Si(s). However Hoch & Johnston also demonstrated, that SiO(s) is formed through the reaction of $SiO_2(s) + Si(s) \rightarrow 2\ SiO(s)$ at a temperature of 1300 K by observing the disappearance of the Si diffraction line and the appearance of new lines, attributed to solid SiO. Upon cooling the reverse is seen: the new lines disappear and the Si lines reappear.

Stephens & Bauer (1981) investigated the homogeneous nucleation of Si and SiO_x vapours. They observe, that the condensation of SiO_x occurs in the temperature range between $1200 - 1600$ K, while pure Si condensates at higher temperature between 1800 K and 2100 K. This finding contradicts the predictions of the classical homogeneous nucleation theory. Stephens (1984) confirms these result for gaseous mixture of Si, Fe, O, N

Table 5.1: Different values for the surface tension of SiO and SiO_2.

Ref.	σ [J/m^2]	comment
Silicon monoxide SiO		
Nuth & Donn (1982)	0.5 - 0.65	depending on the used fit formula
Hale et al. (1989)	$0.82 - 2.2 \cdot 10^{-4} T$	data from Nuth & Donn (1982) analysed using scaled nucleation theory
Gail & Sedlmayr (1986)	0.5	estimated
Silicon dioxide SiO_2		
Blander & Katz (1967)	0.85	
Bruce (1965)	$0.925 - 1.93 \cdot 10^{-4}$	values taken from Nuth & Donn

and C with cosmic abundances. Further important experiments about the nucleation of refractory compounds have been carried out by Donn and coworker. They investigated the nucleation of SiO (Nuth & Donn, 1982), amorphous magnesium silicate (Nuth & Donn, 1983), silver (Nuth et al., 1986), magnesium (Fergurson et al., 1996), and lithium (Ferguson & Nuth, 2000). One important finding of their experiment about the condensation of a silicon monoxide is, that the stoichiometric composition of the solid particles formed in their apparatus is SiO_x with $x \approx 1.5$. The experimental data are interpreted in terms of classical homogeneous nucleation rate. Depending on the formula used to express the size dependence of ΔG, they obtain a value of $\sigma = 0.5$ J/m^2 and 0.65 J/m^2, respectively (see also table 5.1). Nonetheless the results cast some doubt on the applicability of the classical homogeneous nucleation theory to the condensation of silicon monoxide. In another experiment Nuth & Donn (1983) investigated the nucleation in the Mg–SiO–H_2 system. They conclude that the onset of nucleation is unaffected by the presence of magnesium and that the critical nuclei are pure $(SiO)_N$ clusters. Hale et al. (1989) presented an analysis of the nucleation data of Nuth & Donn (1982) using the scaled nucleation theory, which is described in Hale (1986). They find a slightly higher value for σ then in the original article (see table 5.1). We are unaware of any publications dealing with the condensation of solid SiO_2.

Spectroscopically the most prominent features of quartz are located approximately at 9.7 μm and 19 μm. They are attributed to the stretching and bending modes of the Si–O bond in the SiO_4–tetrahedron of solid silica (Whittet, 1989). According to Morioka et al. (1998) the exact position of the 9.7 μm feature depends on the temperature of the sample and on its oxygen content. They observe a variation of the peak position due to the Si–O stretching mode between 9.2 μm and 10.2 μm, while the peak attributed to the Si–O bending mode, can be found between 19.5 μm and 22.5 μm. Furthermore they identify a feature positioned between 11.4 μm and 13.5 μm, which is caused by Si–Si stretching modes. The samples investigated by Morioka et al. consisted of a mixture of different

types of silicon microcrystallites (α–, and β–quartz, cristobalite, etc.). Up to now, the possibility that SiO_2 is a component of the dust around evolved stars has been ignored by most authors. Posch et al. (1999) e.g. exclude quartz as being responsible for the 13 μm feature observed in some AGB stars, mainly for two reasons: i.) Posch et al. claim, that the 13 μm feature in this case should always be accompanied by stronger features at 9 and 20.5 μm, which is not observed; ii.) the disagreement in the band position is even more pronounced for SiO_2 then for other substances considered by the authors (e.g. α–Al_2O_3). Contrary Speck et al. (2000) presume that indeed silicon dioxide is responsible for that feature (see also Speck, 1998, for more details). They argue, that due to the possible existence of different polytopes of SiO_2, the discrepancy between the observed 13 μm feature and the peak positions of quartz, should be less then presumed[1] by Posch et al.. Furthermore Speck et al. discuss in detail the possible correlation of the features at 9, 13, and 20 μm and conclude, that such a correlation might exist.

The condensation of silicon oxides in the outflows of AGB stars has been considered within the framework of homogeneous nucleation theory by Fadeev (1994) and more recently by Jeong et al. (2003). Both come to the conclusion, that silicon monoxide probably does *not* serve as the primary dust condensate. Fadeev (1994) e.g. demonstrates, that the radiation pressure acting on the dust does not exceed the gravity force, even in the case of complete condensation of SiO. Thus, the observed outflow velocities of O-rich red giants cannot be explained using these assumptions. As the results of Jeong et al. (2003) have already been mentioned in chapter 1, we just critically note, that the data used for the calculation of the nucleation rate of SiO and SiO_2 – especially the surface tension $\widetilde{\sigma}$ – are not well established. The value estimated by Gail & Sedlmayr (1986, see table 5.1) has been used for silicon monoxide. For SiO_2 the same value has been used (Jeong, private communication). In both cases no attempt has been made to justify the choice on the basis of the physical properties of the corresponding clusters. The values given in table 5.1 are higher then those used by Jeong et al. (2003). Furthermore, higher values for $\widetilde{\sigma}$ tend to decrease the resulting nucleation rate (McDonald, 1962, 1963).

In summary, from an astrophysical point of view, it is worth it to consider the physical properties of Si_xO_y clusters for the following reasons:

1. There is a strong, although not conclusive evidence that silicon dioxide in form of possibly one or more of its different polytopes is an important component of circumstellar dust.

2. The possibility that the dust formation in AGB stars is initiated by the homogeneous nucleation of SiO or SiO_2 has been rejected although the necessary data are not well established. It seems desirable to verify or falsify this on the strength of the molecular properties of the corresponding clusters.

3. All experiments discussed above indicate, that the solid formed during the condensation of Si–O has a stoichiometric composition, which can be written as SiO_x with

[1]Note also the peak positions given by Morioka et al. (1998).

$1 \leq x \leq 2$. Thus, the condensation of Si–O is represents an auspicious test case for the non–stoichiometric nucleation discussed in chapter 2.

Additionally the investigation of silicon–oxides might enable one, to further elucidate the formation of other silicates as e.g. enstatite or olivine. One might think of a scenario, already proposed by Tielens (1990): The onset of dust formation is triggered by the formation of small seeds consisting of a *pure* substance, like SiO_2, which is transparent in the visible and UV spectral region. Such *clean* solids do not absorb much stellar radiation and thus are only slightly accelerated by the radiation pressure. Tielens further conjectures, that consequently such grains remain in the inner regions of the circumstellar environment (within 5 R_*). Upon growing such grains start to incorporate other elements as Fe, Mg, or Al - they become '*dirty*' and increase their absorptivity. Consecutively the radiation pressure on such grains grows and leads to a rapid expansion of the outflow. With this it would be possible to trace back the formation of different silicates (olivine, forsterite of the '*astronomical silicates*' of Draine & Lee, 1984) to the initial condensation of quartz.

It should be mentioned, that silicon oxides are also important for technology and molecular nanotechnology (see Gillett, 1997).

It is the aim of this chapter, to elucidate the physical properties of Si_xO_y clusters and to address the following question: What conclusions can be drawn about the importance of Si_xO_y clusters for the dust formation process in circumstellar environments? To this end, we first performed some empirical force field calculations on homogeneous SiO_2 clusters (c.f. section 5.2). They are accomplished by a density functional study of Si_xO_y clusters, presented in section 5.3.

5.2 Empirical force field calculations

5.2.1 Introduction

We start our investigation of silicon oxide clusters with some empirical force field calculations using the global optimization algorithm described in section 4.2.3. The interaction of the atoms within homogeneous SiO_2 clusters is described by means of the empirical force field introduced by Tsuneyuki et al. (1988, abbreviated as TTAM). This model is quite successful in reproducing several structural features and physical properties of bulk quartz. It combines three kinds of terms: a long–range Coulomb interaction, a short–rang repulsion, and an attractive dispersion interaction. The functional relationship is expressed by the following equation.

$$\phi_{\text{TTAM}}(r_{ij}) = \frac{1}{4\pi\varepsilon_0}\frac{Q_iQ_j}{r_{ij}} + f_0\,(b_i + b_j)\exp\left(\frac{a_i + a_j - r_{ij}}{b_i + b_j}\right) - \frac{C_iC_j}{r_{ij}^6} \tag{5.1}$$

where $f_0 = 1$ kcal Å^{-1} mol^{-1} is a standard force, as usual. Thus the total energy of a SiO_2 cluster with N monomers is given by:

$$\Phi(N) = \sum_{i=1}^{3N-1} \sum_{j=i+1}^{N} \phi_{coul}(r_{ij}) + \phi_{rep}(r_{ij}) - \phi_{disp}(r_{ij}) \tag{5.2}$$

where we identify the terms as follows:

$$\text{Coulomb interaction:} \qquad \phi_{coul}(r_{ij}) = \frac{1}{4\pi\varepsilon_0}\frac{Q_i Q_j}{r_{ij}} \tag{5.3}$$

$$\text{short range repulsion:} \qquad \phi_{rep}(r_{ij}) = f_0\,(b_i + b_j)\exp\left(\frac{a_i + a_j - r_{ij}}{b_i + b_j}\right) \tag{5.4}$$

$$\text{attractive dispersion interaction:} \qquad \phi_{disp}(r_{ij}) = \frac{C_i C_j}{r_{ij}^6} \tag{5.5}$$

The necessary parameters are given in table 5.2 and the formulas required for the calculation of the gradient and Hessian matrix are given appendix A.5. Figure 5.2 gives a plot of the different contributions to the total energy due to the Si–O, Si–Si, and the O–O interaction, respectively. Due to the attractive dispersion contribution $\phi_{disp} \propto r_{ij}^{-6}$ all of them diverge to $-\infty$ as r_{ij} tends to 0. As a result of this divergence the $\phi_{i,j}$ (i,j is Si or O) exhibit an unphysical maximum seen in figure 5.2 for the Si–O interaction at $r_{ij} \approx 1.5$ Å and for the O–O interaction at $r_{ij} \approx 1.7$ Å. For the Si–Si interaction this point is outside the plot range. In order to remove this maximum and make sure that for $r_{ij} \to 0$ the potential energy function tends to $+\infty$, we added at R_{cut} a correction term which reads as follows:

Parameter	Silicon	Oxygen
q_i/e	2.4	-1.2
a_i/Å	0.8688	2.0474
b_i/Å^{-1}	0.0328	0.1756
C_i/(eV$^{1/2}$Å^{3}mol$^{-1/2}$)	4.8268	14.6587
m_i/amu	28.0855	15.9994

Table 5.2: Parameters of the TTAM–potential.

$$\phi_{cor}(r_{ij}) = 500(r_{ij}^2 - (R_{cut}^{ij})^2)^2 \qquad \text{for} \quad r_{ij} < R_{cut}(i,j) \tag{5.6}$$

Appropriate values for R_{cut} have been determined numerically by locating the described maximum:

$$R_{cut}^{Si-Si} = 0.0877 \text{ Å} \qquad R_{cut}^{Si-O} = 1.06122 \text{ Å} \qquad R_{cut}^{O-O} = 1.41497 \text{ Å} \tag{5.7}$$

This addition has no influence on the properties of the stationary point. It ensures the numerical stability of the global optimization procedure, since due to the necessity to create configurations randomly it cannot be excluded, that the distances of two atoms accidentally are smaller then R_{cut}. The corrected curves are plotted in 5.2 as dotted lines. The potential energy curves of a similar force field developed by van Beest et al. (1990)

are also shown in that figure. They use a similar functional form for the potential energy function but deduce the necessary fit parameters for each bond and not for each atom as Tsuneyuki et al. (1988) did, i.e. except for the charges, which are identical, the parameters are given as A_{ij}, B_{ij} etc. Additionally they neglect any short range interactions between two Si atoms, i.e. $\phi_{disp}^{Si-Si} \equiv 0$ and $\phi_{rep}^{Si-Si} \equiv 0$. The Si-Si interaction is thus solely described by the (long range) Coulomb force (Kramer et al., 1991). From figure 5.2 it is apparent, that the two potentials are almost identical.

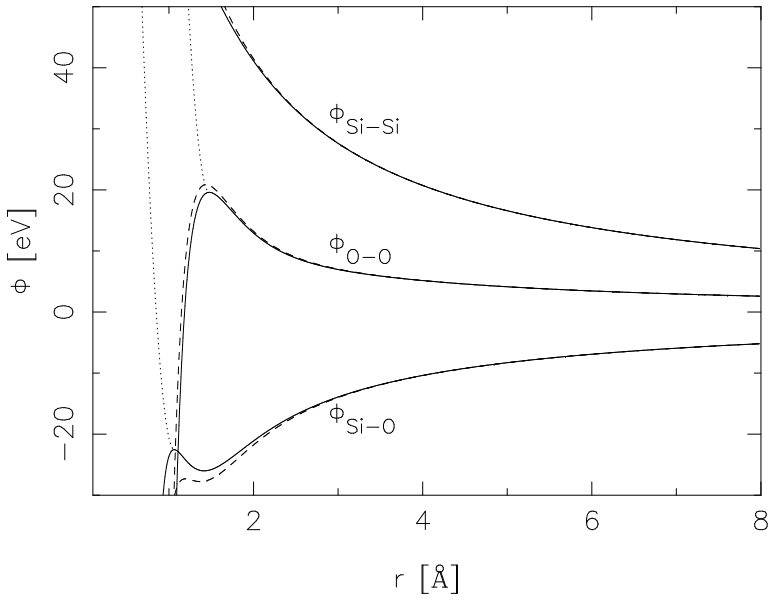

Figure 5.2: Potential energy curve of the TTAM potential. The solid line depicts the original curve. The dotted line gives the modified potential energy curve for $r_{ij} < R_{\text{cut}}$. The dashed curves represent the similar potential model, introduced by van Beest et al. (1990).

Using this potential model we searched for the global minima of $(SiO_2)_N$ clusters with up to 21 monomers by means of the basin–hopping algorithm described in section 4.2.3. This is accomplished in the following way:

- Some preliminary test calculations showed that the suitable temperature range is $0.4 \leq T_{red} \leq 2$ in reduced units.

- Similarly is was found, that the initial step size δr_0 should have a value between 0.5 Å and 1.0 Å.

- As a (sloppy) convergence criterion for the Monte Carlo simulation $\varepsilon_{sloppy} = 0.01$ was used. At the end of the calculation the N_{save} lowest structures were reoptimized with a tighter convergence criterion ($\varepsilon_{tight} = 1 \cdot 10^{-7}$).

Table 5.3: List of candidate global minima for $(SiO_2)_N$ clusters ($N = 1, \ldots, 21$) bound by the TTAM potential.

N_{mono}	PG	Φ_0 [eV]	E_{zp} [eV]	$\langle \nu \rangle_{geo}$ [cm^{-1}]
1	$D_{\infty h}$	-44.7143827	0.1817	563.734
2	D_{2h}	-94.7781039	0.4710	502.175
3	D_{3h}	-145.5384845	0.7525	437.170
4	C_{2v}	-196.1715165	1.1030	514.068
5	C_1	-247.5438447	1.3673	447.514
6	C_2	-300.0602764	1.7165	500.061
7	C_{2v}	-352.1589755	2.0366	504.028
8	C_s	-404.7350409	2.2950	460.167
9	C_1	-456.4201468	2.6166	466.559
10	C_1	-509.1976346	2.9276	465.637
11	C_1	-561.7445389	3.2416	463.723
12	C_{2h}	-615.5826823	3.5892	482.858
13	C_s	-667.6523286	3.9060	478.076
14	C_1	-720.8171244	4.2182	479.806
15	C_1	-773.1948848	4.5322	476.589
16	C_{2h}	-826.3694990	4.8336	471.175
17	C_s	-878.1972176	5.1550	473.191
18	C_1	-931.4228588	5.4608	472.452
19	C_1	-983.7867954	5.7724	469.519
20	C_{2h}	-1037.0760204	6.0794	469.146
21	C_1	-1088.3708279	6.3927	467.668

- For each cluster size we performed a number of up to 15 basin–hopping runs at different temperatures. The length of the Monte Carlo simulation was either 10.000 or 50.000 steps.
- We used three different seeding techniques:
  1. Some calculations were started with a completely random structure.
  2. In some cases the putative global minimum of a smaller cluster was used as a seed. The positions of the missing atoms were generated randomly.
  3. In other cases the calculation started with the lowest energy structure of the same cluster size, found in another run.
  4. It also proved to be useful, to initiate some calculations with a not so tightly bound structure previously found.

- For each stationary point found by the basin–hoping algorithm we performed a vibrational analysis. The necessary Hessian matrix was calculated analytically (see appendix A.5) and the normal modes pertaining to the zero–eigenvalues of rotation and translation were removed by the projection method described e.g. in Field (1999, p. 112ff).

The results are summarised and discussed in section 5.2.2.

5.2.2 Results

Table 5.3 lists the putative minima of the considered SiO_2 clusters with up to 21 monomers. Since each minimum has been found several times it is believed, that the true global minima have been found. Additionally to the energy Φ_0 of the structure, the table lists the point group, the zero point energy of vibration E_{zp} and the geometric mean value of the frequencies $\langle \nu \rangle_{geo}$, which is calculated according to:

$$\langle \nu \rangle_{geo} = \left(\prod_{i=1}^{f_{vib}} \nu_i \right)^{1/fvib} \tag{5.8}$$

with f_{vib} the number of vibrational degrees of freedom.

Harkless et al. (1996) presented a study of the same system. However, they restrict their discussion to rather small aggregates and did not perform an extensive search. Already for the case of the tetramer $(SiO_2)_4$ a new global minimum was found by the basin–hopping algorithm. The structure described by Harkless et al. (1996) is the energetically second lowest structure, denoted with a Roman number II in figure 5.5. Since for all larger clusters we were able to locate energetically more favourable structures, we do not consider this paper further.

We first discuss the energetic aspects of the clusters. It turned out, that the size dependence of the potential energy $\Phi(N)$ is most easily analysed by means of the second energy difference $\Delta_2 E$, introduced in 3.2. The resulting curve is presented in figure 5.3. Beginning with the hexamer $(SiO_2)_6$, a pronounced odd–even–oscillation can be seen. As expedited on page 23 positive $\Delta_2 E$ values indicate cluster sizes, which are particularly stable. Such oscillations are often due to certain (electronic or geometric) shell closure effects. Since even numbered clusters are particularly stable, one might presume, that for these clusters some kind of '*pairing*' occurs. On the other hand, such a '*pairing*' would also explain the reduced stability of odd numbered clusters, as for these numbers one pair is uncompleted.

In order to validate this rather phenomenological explanation of the odd–even–oscillation in figure 5.3 we now discuss the structures of some exemplary SiO_2 clusters shown in figure 5.4. The configurations can be described as some kind of tube with a quadratic cross section. They can be viewed also as stacked rings with 4 silicon atoms bridged by the oxygen atoms. Thus the fourth minimum of the tetramer (isomer IV in

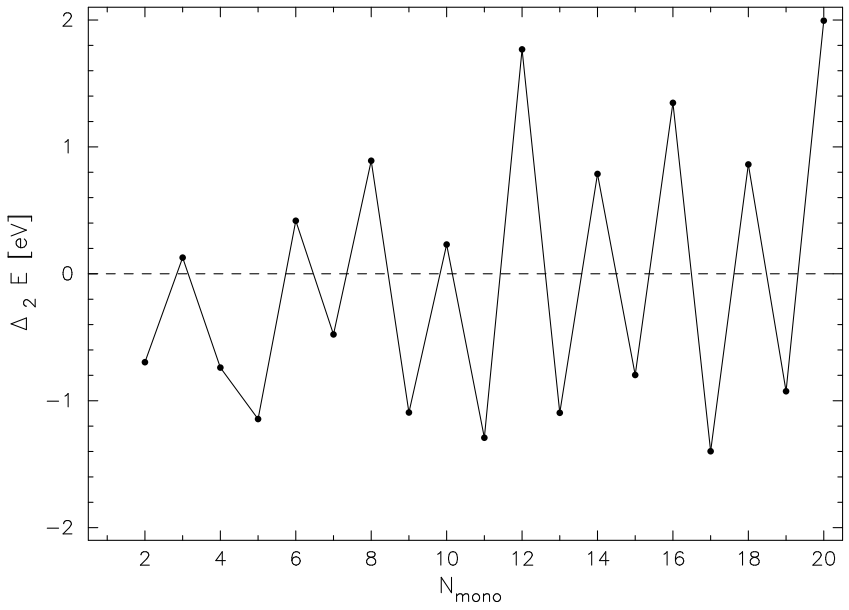

Figure 5.3: Second energy difference $\Delta_2 E$ as a function of the number of monomers for the SiO_2 clusters bound by the TTAM potential energy function.

figure 5.5) would serve as a basic building block. The first clusters for which such a tube–like configuration could be completed is the octamer $(SiO_2)_8$. Although such a structure is *not* the global minimum, it is the 6th lowest isomer. Starting with the 9–mer, this type of structures becomes the global minimum on the TTAM potential energy surface. Since 4 monomers are required to complete a new layer, the next *closed* tubes occur for $N_{mono} = 12, 16$, and 20. These structures are even more stable, than the other even–numbered structures, as the corresponding peaks in the $\Delta_2 E$ curve are quite distinct, compared to the neighbouring peaks. For $N_{mono} = 10, 14$, and 18 the next layer of the tube is half complete, which explains the reduced stability of these clusters compared to the complete tubes: The dislocation in the structure of the tube is associated with some strain energy Φ_{strain}, which leads to a (slight) decrease of $\Phi(N)$. The addition of a monomer to an even numbered cluster leads to the formation a dangling SiO_3 unit, seen e.g. on the right hand side of $(SiO_2)_{19}$, which obviously is responsible for the reduced stability of odd numbered clusters.

Another explanation of this phenomenon can be given in terms of coordination numbers. It is generally accepted, that in silicon oxide the Si atom prefers to be four–fold coordinated with oxygen, while O prefers to have two nearest neighbour Si atoms (e.g. Nayak et al., 1998). As a consequence of this preference, the SiO_4 tetrahedron was identified as the main building block, at least in stoichiometric silica. This tetrahedron indeed can be found also in the tubes discussed above. For the complete tubes ($N = 12, 16, 20, \ldots$) each silicon atom is fully coordinated, i.e. it is surrounded by 4 oxygen atoms. All oxygen atoms have 2 silicon atoms as nearest neighbours, except for the 2 dangling O-atoms at each end of

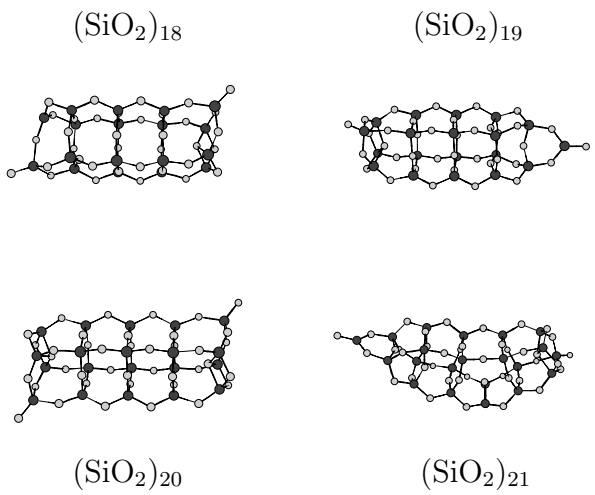

Figure 5.4: Structure of the four largest SiO_2 clusters considered here.

the tube. In cases of the incomplete tubes ($N = 10, 14, 18, \ldots$) and of the odd–numbered tubes one observes, that one Si atom is only three–fold coordinated, while all others are fully–coordinated. This explains the reduced stability of these clusters. The difference between these two types of tubes is, that in case of the even–numbered incomplete tubes the three–fold coordinated Si atom is *almost* four–fold coordinated[2]: The distance r_{nnn} between the Si atom and the next nearest oxygen atom is close to the nearest neighbour distance ($r_{nnn} = 1.99\,\text{Å}$ compared to $r_{nn} \approx 1.61\,\text{Å}$). Contrary for the odd–numbered tubes, this distance for the three–fold coordinated Si atom is clearly larger ($r_{nnn} = 2.96\,\text{Å}$) and hence the contribution of this '*bond*' to the overall potential energy Φ notably smaller. Thus we explained the characteristic odd–even oscillation of the second energy difference $\Delta_2 E$ on two different levels: The first explanation considers the general shape of the structures, while the second explains it on an atomistic level.

5.2.3 The topology of a potential energy surface

We now take a closer look at the topology of the potential energy surface of the tetramer. This is among others motivated by the observation, that it was more difficult to find the global minimum of this clusters, then that of the larger clusters like $(SiO_2)_5$ and $(SiO_2)_6$.

In order to analyse the topology of the PES we conducted some microcanonical molecular dynamics simulations as described in section 4.4. It is the aim of this section to explicate a new technique, which might be useful for the analysis and visualization of such a topology. Therefore we not only needed to know the ground state of the cluster, but at least some of the other isomers with similar energy. The necessary data were taken from

[2]In case of the $(SiO_2)_{18}$ cluster shown in figure 5.4 this concerns the Si atom in the upper left corner of the structure

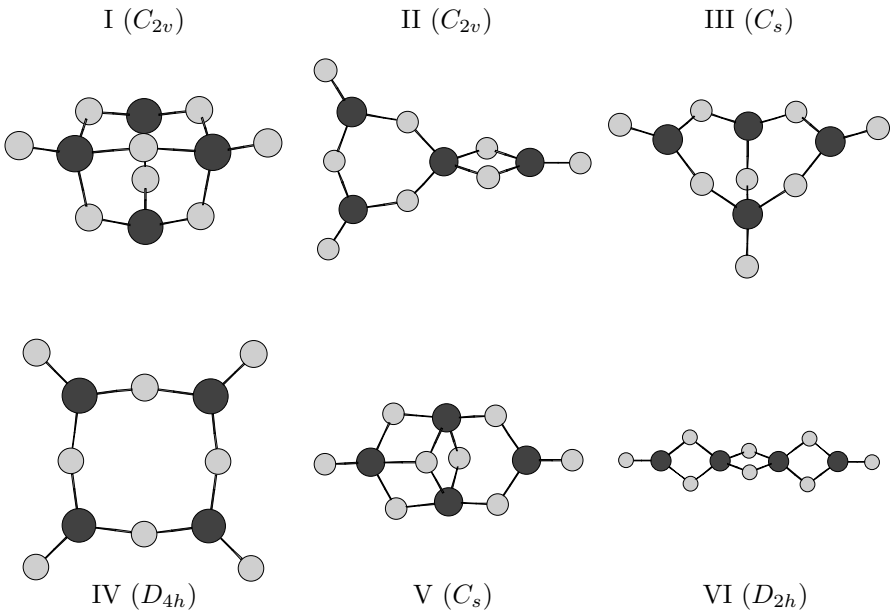

Figure 5.5: The six most stable isomers of $(SiO_2)_4$

a number of basin–hopping calculations. The six energetically lowest structures are visualized in figure 5.5 and their energies are given in table 5.4. For convenience we labelled the structures according to their energetic order using Roman numbers. It can be seen, that they are located within the narrow energy range of about 0.8 eV. All simulations were initialised with the ground state structure. A time step of 0.5 fs was chosen and the total length of a run was 10^7 steps, so each simulation lasted 5 ns. The short time average of the potential energy $\langle E_{pot} \rangle_{\mathrm{STA}}$ (c.f. Eq. 4.98) is calculated by averaging $\Phi(t)$ over $\mathcal{N}_{\mathrm{STA}} = 500$ time steps. After the same number of time steps the actual configuration of the cluster was saved. Additionally the various mean values discussed in 4.4 were calculated. It turned out, that the *relative root mean square (RMS) bond fluctuation* δ is an appropriate and sensitive quantity for monitoring the occurrence of phase transitions or *melting like* events. It was calculated for several trajectories with different total energies. The resulting $\delta(E)$–curve is shown in figure 5.6.

Isomer	Φ [eV]
I (C_{2v})	-196.171516
II (C_{2v})	-195.915927
III (C_s)	-195.871851
IV (D_{4h})	-195.598995
V (C_s)	-195.462840
IV (D_{2h})	-195.422494

Table 5.4: The six lowest isomers of Si_4O_8.

For small energies the rms bond fluctuation rises only slowly, nearly linearly until at an energy of $\approx -16.15\,\mathrm{eV/atom}$ a sudden increase is is observed in figure 5.6. This sharp rise of δ is generally interpreted as an indication of a solid–liquid–like transition (e.g. Berry, 1995, 1999). In order to elucidate the reason for this jump in the δ–curve, we try to determine, to which isomers the basins belong, in which the cluster moves at a given instant of time. This *inherent structure approach* was originally introduced by

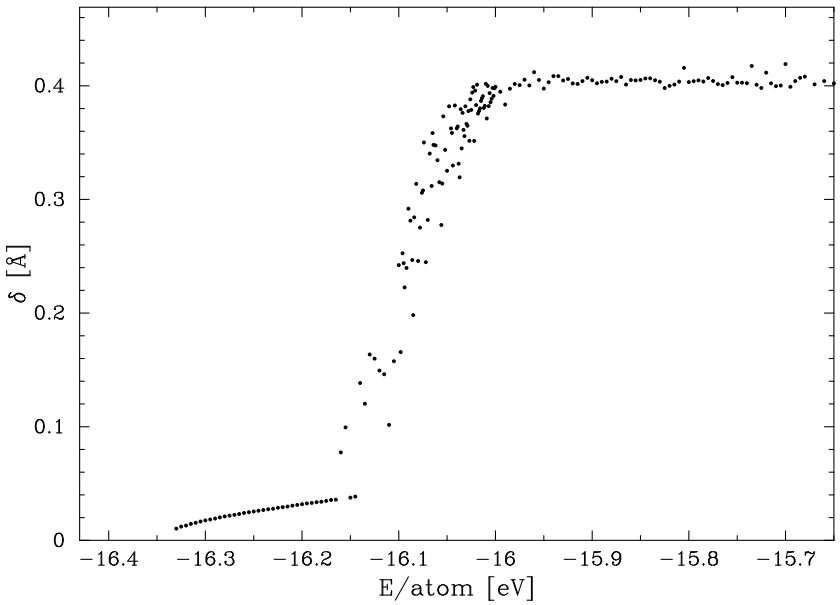

Figure 5.6: RMS bond fluctuation δ as a function of the energy per atom for $(SiO_2)_4$. The onset of *melting* is clearly discernible at $\approx -16.15\,\mathrm{eV/atom}$.

Stillinger & Weber (1982, 1983) for the analysis of dynamic transition in liquids. It has been applied to analyse the molecular dynamic simulations of clusters by e.g. Rose & Berry (1991, 1993a,b) for the case of KCl, or by Calvo & Labastie (1998) for NaF. Using the configurations saved along the trajectory every 500 steps, each of them was quenched using the L–BFGS minimization algorithm. For each considered trajectory the number of occurrences of the different isomers is counted and plotted as a function of the energy in figure 5.7. It can be seen, that the trajectory for energies below $\approx -16.15\mathrm{eV/atom}$ is solely confined to the basin of the ground state isomer I. Thus, the fluctuations are only due to the vibrational motions of the cluster, which explains the low δ values. At energies above this value different other isomers become accessible, at first - of course - isomer II and III. Hence, the dynamic of the cluster is no longer solely due to vibrational motions but additionally isomerisations happen. This results in an increasing δ–value in figure 5.6. As soon as all isomers are accessible, and these rearrangements are fast, the δ–curve flattens again.

The results presented in figure 5.7 also suggest an answer to the question stated at the beginning of this section. As it is apparent from this figure, the relative abundance of the ground state drops to very low values as soon as other isomers become accessible. There is only a relatively small energy range, in which the ground state and the other isomers coexist. Animations of such molecular dynamic trajectories reveal, that isomer I transforms never directly into isomer II, which would require several rearrangement steps (compare the structure shown in figure 5.5). Instead, the ground state transforms easily into the 3rd isomer by opening only a single Si–O bond. Obviously the energy barrier between isomer

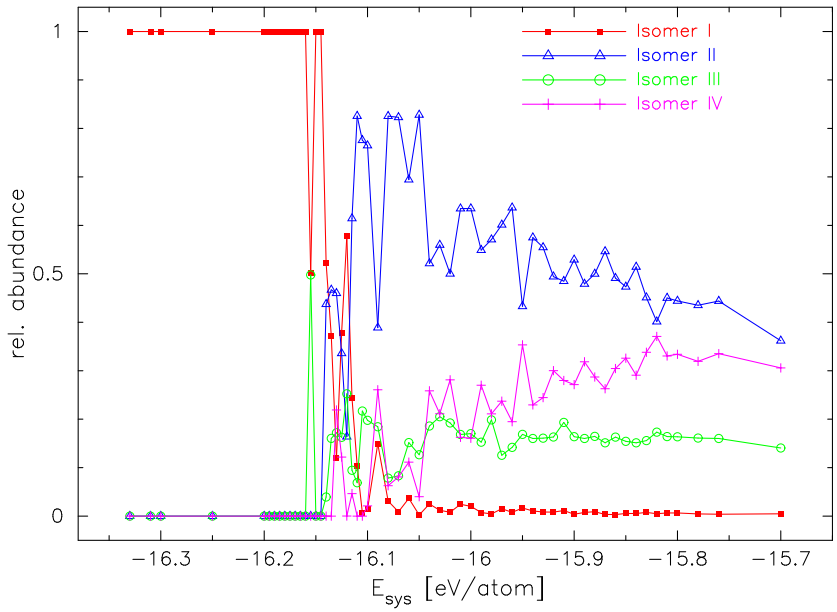

Figure 5.7: Relative abundance of isomers found along a MD trajectory of $(SiO_2)_4$ as a function of the energy of the trajectory. The *inherent structure approach* used to determine the abundances is described in the text.

I and III is higher than that between isomer II and III. It would be intriguing, to verify or falsify this conclusion, which is solely based on an analysis of the dynamics, by means of appropriate methods for locating transition states.

We now propose a method, which accesses directly the informations gained during a molecular dynamic simulations, without the detour, to perform local minimization calculations as in case of the inherent structure approach. Instead, the new technique tries to correlate the dynamical behaviour of a cluster directly to its structural changes. To this end, we calculated for each of the saved structures of a MD trajectory the root mean square deviation σ_{opt} relative to two different *reference configurations*, after they have been superpositioned by means of the algorithm described in section 4.3.3.1. In doing so one assumes, that the saved structures are representative for the corresponding time interval of $\mathcal{N}_{STA}$ time steps. In view of the large number of saved structures (typically about 20.000), this seems to be justified. Thus, one might correlate the calculated σ_{opt} values with the instantaneous value of the short time averaged potential energy $\langle E_{pot} \rangle_{\mathrm{STA}}$. As it was realised in section 4.3.3.3, σ_{opt} defines a metric in the configuration space. It seems natural to assign to each configuration a point in the plane defined by the rms deviations σ^1_{opt} and σ^2_{opt} relative to the first and second reference structure. The $\langle E_{pot} \rangle_{\mathrm{STA}}$–value for that structure is depicted by colour code. The resulting plot[3] is shown in figure 5.8. For this example, the coordinates of isomer I and II have been used as reference structures.

[3]Since it reminds one of a cat, which waddles with her paws first through colour pots and then across a canvas, the name *catwalk* plot is suggested for plots like 5.8.

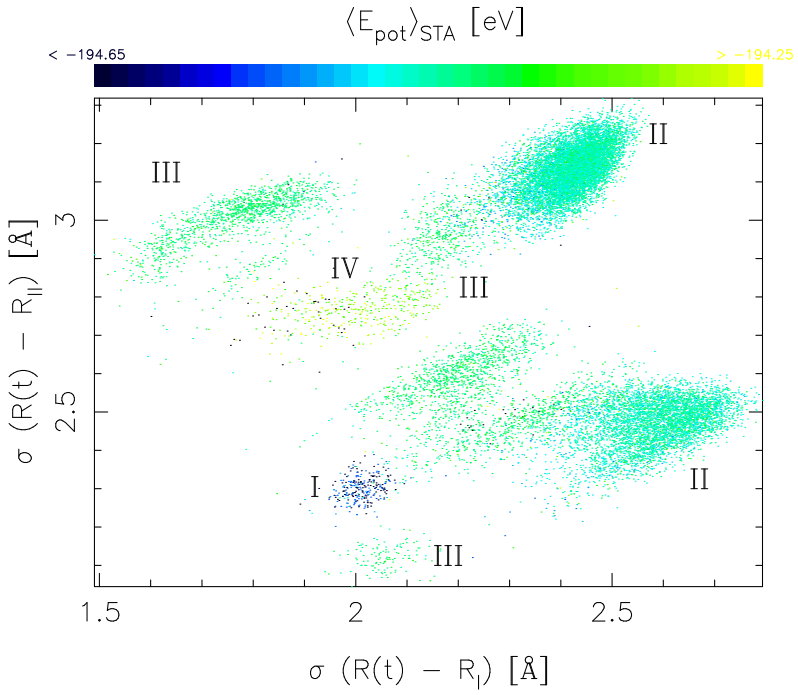

Figure 5.8: Configurational analysis of a MD trajectory of $(SiO_2)_4$ at an energy of $-16.10\,eV/atom$. As reference structures the coordinates of isomer I and II have been used.

Figure 5.8 represents a direct visualization of the PES with its basins of attraction around different minima, which are discernible by their different colours. As the rms deviation is *not* invariant under the exchange of two atoms (see section 4.3.3), more then one basin might belong to each isomer. From the density of points it becomes apparent, that the trajectory spends most of its time in the basin around isomer II, while those around isomer I and IV are a only rarely visited.

In conclusion this type of plots provides a tool, which might be useful for the analysis of molecular dynamic simulations and the visualization of the underlying potential energy surface. The key idea of this method, namely the correlation of a measure for the structural similarity of different configurations and their energies, could be applied to stationary points (minima and transition states), too. We are not aware, that such methods have been applied to inorganic clusters before.

5.3 Quantum mechanical investigation of silicon oxide clusters

In the previous section the structures and energies of SiO_2 clusters have been investigated using an empirical potential model developed by Tsuneyuki et al. (1988). One drawback

of this approach is, that the sum of the fractional charges used to describe the Coulomb interaction within the cluster, does not yield zero for non-stoichiometric aggregates, leading to a non-vanishing net-charge of the cluster. Thus, this approach is only applicable to stoichiometric SiO_2 clusters. But due to the discussion about non–stoichiometric nucleation (see chapter 2) in general, and the condensation of silicon oxide in particular (see this chapter, page 117 ff) it can be concluded, that it is indeed important for the understanding of this process, to consider also the general case of Si_xO_y clusters. Thus, we performed density functional calculations on small and intermediate sized Si_xO_y clusters with up to 45 atoms. As discussed in section 3.1, density functional methods offer the possibility to achieve a particular level of accuracy at lower cost than other *ab initio* methods, thus enabling, to treat larger clusters, than usual. Furthermore it is the aim of this section to answer the following questions:

1. How good are the properties of SiO_2 clusters reproduced by the TTAM potential?

2. Is it possible to utilise the informations gained from molecular mechanics calculations for the computational more demanding quantum-mechanical methods?

Before the results of the DFT calculations are discussed in section 5.3.2, some short remarks about the applied techniques are given in the following section.

5.3.1 Methods

It is beyond the scope of this thesis to give an introduction of the density functional method. Instead of this the reader might refer to the numerous existing introductions given for example by Parr & Yang (1989), Jones (1995), Chrétien & Salahub (2001), or Cramer (2002, p. 233ff). In this section mainly some practical aspects of the calculations are discussed.

5.3.1.1 Accuracy of the method

At first the very well known electronic structure of the SiO molecule was studied in order to assess the quality of the level of theory used in this work. To this end the silicon monoxide molecule has been optimized using different levels of theory, namely simple Hartree-Fock (HF), the more demanding Møller-Plesset second order-perturbation (MP2) theory, and different density functional methods. These either use Becke's exchange functional (B or B88; see Becke, 1988) or his three parameter hybrid functional B3 (Becke, 1993). Both are combined with three different correlation functionals, namely that of Perdew (1986, P86), Lee et al. (1988, LYP), or Perdew & Wang (1992, PW91). Thus, we considered 6 different DFT methods in total. Additionally we used 4 different standard, split–valence basis sets: 6-31G, 6-31G(d), 6-311G, and 6-311G(d). For each of these $8 \times 4 = 32$ different combinations, the spectroscopic constants (D_0, r_{eq}, and ω_e) have been calculated using the Gaussian98 suite of programs (Frisch et al., 1998). The results have been compared with

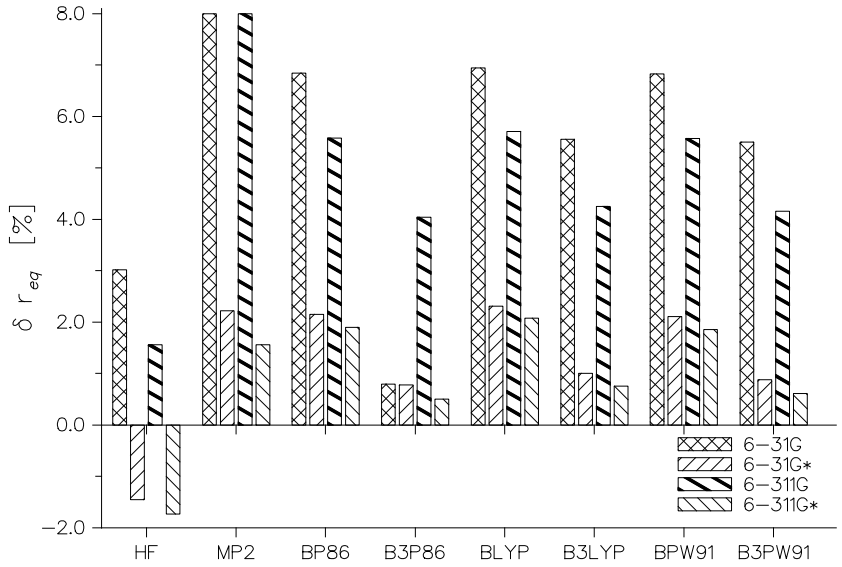

Figure 5.9: Relative error of the calculated equilibrium distance r_{eq} using different levels of theory.

the experimental values given in Chase (1998):

$$D_0 = 8.26 \text{ eV} \qquad r_e = 1.5097 \text{ Å} \qquad \omega_e = 1241.5 \text{ cm}^{-1}$$

by calculating the relative error of the quantities:

$$\delta X = \frac{X_{calc} - X_{exp}}{X_{exp}} \tag{5.9}$$

They are visualized in figures 5.9 to 5.11 and summarised in table B.4 on page 183. We now discuss how well each of the three quantities are reproduced by the different theoretical methods.

Equilibrium distance r_{eq} Figure 5.9 displays the relative error δr_{eq} of the equilibrium distance of the SiO molecule, which is overestimated by most methods. The lowest error is achieved by the B3P86/6- 311G(D) method ($\approx 0.5\%$). Furthermore it is apparent, that the additional consideration of polarisation effects in the 6-31G(D) and 6-311G(D) basis sets leads to a significant improvement of the calculated r_{eq} values. On the other hand one observes, that going from the 6-31G to the (slightly) larger basis 6-311G, yields only

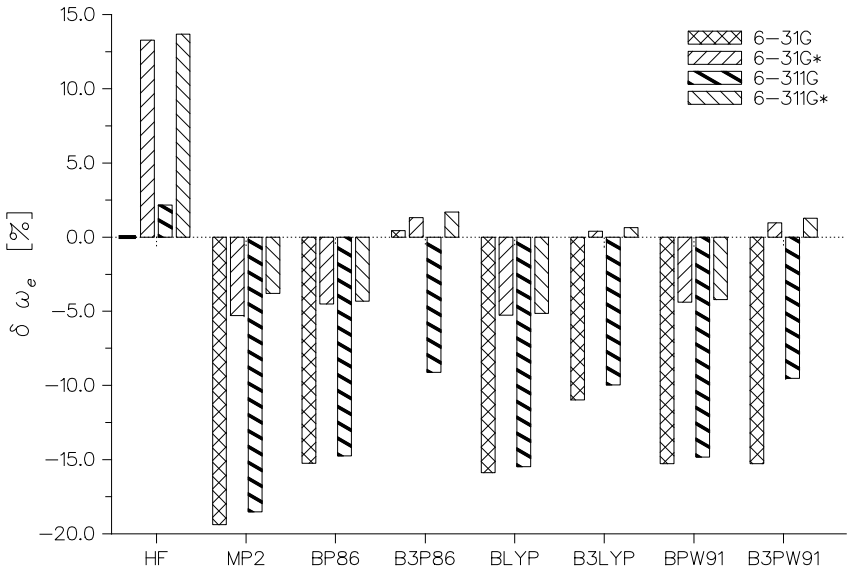

Figure 5.10: Relative error of the calculated vibrational frequency ω_e using different levels of theory.

slightly better results. It is important to note, that these effects can be also observed for the harmonic frequency (figure 5.10) and the dissociation energy (figure 5.11), respectively.

Vibrational frequency ω_e The result of the comparison for the calculated and experimental frequencies ω_e are depicted in figure 5.10. The most apparent outcome is the fact, that this quantity is *underestimated* by almost all methods. Furthermore it must be regarded as a fortuitous result, that the HF/6-31G level of theory reproduces the measured frequency almost exactly (the error $\delta\omega_e = 0.02\%$). Both findings are surprising, since it is generally accepted, that vibrational frequencies are *overestimated* by quantum chemistry methods. This is principally due to the neglect of anharmonicity, and the inadequacies in the calculations arising from an incomplete treatment of electron correlations and the use of finite basis sets (Hehre et al., 1985). As a result, one often scales calculated harmonic vibrational frequencies by an appropriate scale factor in order to compensate for this systematic error. Most of these empirical determined factors are between 0.8 and 1.0. For the HF/6-31G(D) level of theory e.g. one uses a factor 0.8953, while for MP2/6-31G(D) 0.9434 is appropriate (Cramer, 2002, p. 305). For the case of density functional methods some scaling factors have been determined by Scott & Radom (1996). They recommend

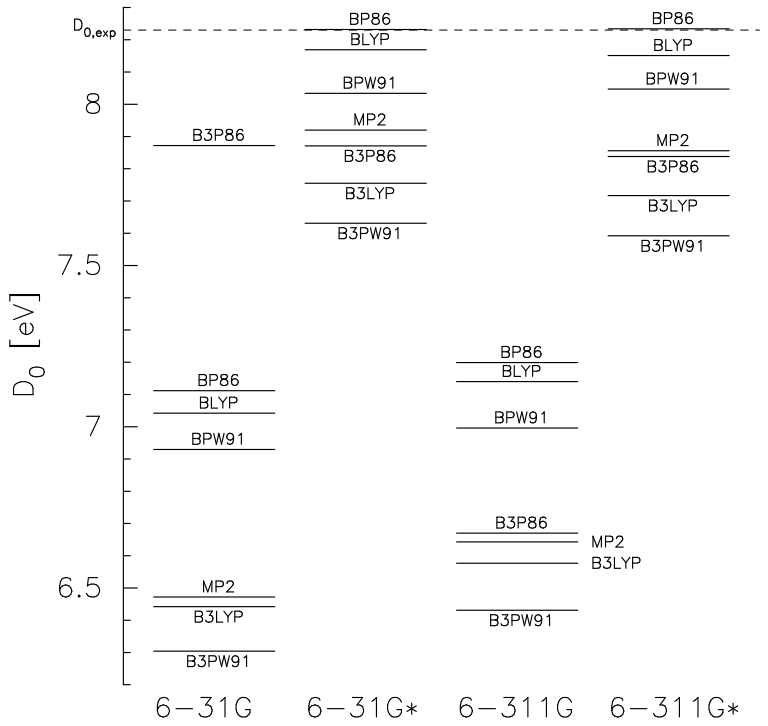

Figure 5.11: Comparison of the calculated dissociation energies D_0 with the experimental value $D_{0,exp} = 8.26$ eV using the unscaled vibrational frequencies.

for the scaling of theoretical harmonic frequencies and the calculation of the zero–point vibrational energy scaling factors, which are all lower than one for each considered method, e.g. 0.9914 for BP86/6-31G(d), or 0.9945 for B-LYP/6-31G(d). Thus, one would aggravate the error, if one would apply these scaling factors to the calculated values for the frequency of SiO. Apart from exceptional and fortuitous result for HF/6-31G, the B3LYP/6-31G(d) method shows the lowest error ($\approx 0.4\%$).

Dissociation energy D_0 In figure 5.11 we compare the resulting values for the dissociation energy D_0, calculated using the *unscaled* frequencies, with the experimental value, which is marked by a dashed line. The results for the Hartree–Fock method have been omitted from this plot, since they are totally erroneous (see table B.4 on page 183). It turns out, that the BP86 DFT method in combination with the 6-31G(d) and the 6-311G(d) basis sets yield the most accurate values for the dissociation energy with errors well below 1%. Note that all methods give dissociation energies, which are lower, then the experimental value. Interestingly the values of the MP2 method are in combination with all four used basis sets distinctively worse then those, calculated on the BP86 level of theory.

Additionally the results obtained by means of the BP86/6-31G(d) level of theory for the spectroscopic constants of 4 silicon containing species listed in Chase (1998), namely SiO, SiO_2, Si_2, and Si_3 are summarised in table 5.5. It becomes clear, that the chosen level

of theory not only yields good results for the monomer, but also for the larger molecule SiO_2 and the solely silicon-containing molecules Si_2, and Si_3. For all quantities the absolute error is lower then 10% in most cases even lower then 2%. While the atomization energy of the mixed species is reproduced very well, the observed error for the Si_N species is slightly larger, but still acceptable (see section 5.3.3 for more details about pure silicon clusters). Another important result of the comparison is the fact, that for all species considered here the vibrational frequencies are lower then the measured values. As already mentioned above, this is against the general trend and clearly would deserve some further investigations.

Table 5.5: Comparison of calculated and experimental spectroscopic constants of some further silicon containing molecules. The experimental values for the frequencies of SiO_2 and Si_3 have been taken from the compilation of Jacox (2003), since they are more accurate then those given in Chase (1998). The theoretical values have been obtained using the BP86/6-31G(d) level of theory.

molecule	method	D_{at}[eV]	δD_{at} [%]	r_{eq}[Å]	δr_{eq} [%]	ω_e[cm$^-$1]	$\delta\omega_e$ [%]
SiO	calc.	8.23	-0.36	1.5415	2.11	1186	-4.51
	exp.	8.26		1.5097		1242	
SiO_2	calc .	12.67	-1.71	1.537	-0.84	$^{246.1}/_{1393.7}$	$^{-9.69}/_{-1.60}$
	exp.	12.89		1.55		$^{272.5}/_{1416.4}$	
Si_2	calc.	3.36	6.67	2.309	2.8	468	-8.41
	exp.	3.15		2.246		511	
Si_3	calc.	7.42	1.64	2.308	2.58	$^{309}/_{487}$	$^{-8.31}/_{-2.79}$
	exp.	7.30		2.25		$^{337}/_{501}$	

These results confirm the findings of Chang et al. (1998, 2000) and Jeong et al. (2000), that the P86 functional yields better predictions for the atomization energy, then other, later developed methods as e.g. the PW91 functional. Thus, one might conjecture, that the atomization energies of inorganic oxide compounds are most accurately determined, using the P86 correlation functional, either in combination with Beckes exchange functional (B) or his 3 parametric hybrid functional (B3). Unfortunately we are not aware of any publication addressing this question in a systematic way. Martell et al. (1997) for example consider both organic and inorganic compounds and compare their atomization energies using different density functional methods and basis set. They come to the conclusion, that the B3P86 level of theory yields indeed good results for most molecules containing *no* carbon, while BP86 accurately describes those species, which involve singly bonded oxygen atoms. Since in the context of this thesis we are mainly interested in the thermodynamic properties of the silicon oxide species and their resulting gas phase abundances, we regard

the dissociation energy as the key quantity, which should be determined as accurate as possible. Consequently the BP86/6-31G(d) level of theory was chosen to determine the structure, energies and frequencies of Si_xO_y clusters. Since the scaling factor given by Scott & Radom (1996) for this method is lower than one, the calculated frequencies are *not* scaled for the calculation of the thermodynamic data.

5.3.1.2 Some further details of the calculations

In what follows it is described, which methods has been applied in the present investigation of silicon-oxide clusters, concentrating on clusters with up to eight silicon atoms, although some larger aggregates have been studied, too. A rather extensive survey of small silicon oxide clusters has been published by Chu et al. (2001), which served as a starting point. The most important dissimilarity between the work of Chu et al. and this thesis is the different density functional method used. Chu et al. used the B3LYP functional in combination with a smaller basis set, namely 3-21G and 6-31G(d) for silicon and oxygen, respectively (see also Zhang et al., 2001b). The authors claim, that this level of theory predicts quite accurately the geometric parameters of Si-O-compounds. However the given equilibrium distance for SiO (Zhang et al., 2001a) equals the value obtained by our chosen method. Furthermore it is apparent from figure 5.9, that the consideration of polarisation in the basis for silicon, significantly improves the results for the calculated geometry, contrary to the assumption made by Zhang et al. (2001b). Although the usage of the small mixed basis set is computationally less demanding, than using the larger basis, this speed-up is obtained at the expense of less accurate binding energies, as can be seen in the following table[4]:

	exp.	this work	small basis set
molecule	D_e [eV]	D_e [eV]	D_e [eV]
SiO	8.34	8.31	7.32
SiO_2	13.07	12.84	10.68

Thus this method is inferior to the approach chosen in this thesis, though we used the configurations depicted in Chu et al. (2001) as starting points. These authors discussed only Si_xO_y clusters with less then 16 atoms, i.e. $x, y = 1 \ldots 8$ with $x + y \leq 16$ and did not treat pure silicon clusters. In this work we expanded the range of treated cluster sizes considerably (see table 5.6). Furthermore we succeeded in optimizing the silicon rich clusters Chu et al. failed to optimize due to convergence problems, namely: Si_5O_1, Si_6O_1, Si_7O_y ($y = 1, 2$), and Si_8O_y ($y = 1 - 3$). In some cases we found presumably new global minima, which have not yet been described by Chu et al. (2001), e.g. Si_7O_3, Si_7O_4, Si_7O_5[5]. Furthermore it is noteworthy, that Chu et al. did not treat pure silicon clusters.
Additionally we applied the following techniques:

[4]The data for the small basis set have been taken from Zhang et al. (2001a), while the experimental value for D_e has been calculated using the mentioned values for D_0 and ω_e.

[5]New global minima are also marked in table B.1.

- For homogeneous SiO_2 clusters we used some of the isomers found on the corresponding TTAM potential energy surface as starting points.

- For non–stoichiometric cluster the semi-empirical PM3 method (see e.g. Cramer, 2002, p.136 ff) has been used to obtain "*good*" initial geometries. This method has been applied by Chu et al. (2001), too. Its advantage is its computational inexpensiveness and the ability to yield quite reliable geometries.

- In some cases, e.g. Si_2O_7 and Si_2O_8, possible ground state structures have been obtained by applying certain building or *aufbau* principles, which will be described below.

- We tried to find the global minima of some silicon rich clusters (e.g. Si_6O, and Si_7O) by means of the *vertical energy surface hopping* (VESH) procedure (Sülzle & Chang, 1999), which proved to be useful for various systems, e.g. Al_2O_3 (Chang et al., 1998), and $MgSiO_3$ (Patzer et al., 2002). The main idea of this technique is to escape from a certain basin of attraction of a molecular system by shifting it to other (higher or lower) spin and/or charge states. Each of these "*shifts*" is followed by a geometry optimization. Thus, the procedure systematically scans the potential energy surface of different spin *and* charge states (see Sülzle & Chang, 1999, for further details). Again the PM3 method has been used to describe the molecular system.

  Unfortunately the VESH procedure did not prove to be very useful for the aggregates considered here, since it only swapped between two similar configurations. Obviously the mechanism developed to escape the basin around a certain minimum fails for the silicon-rich clusters, since changing the spin and/or charge state leads only to minor changes of the cluster's geometry. Liu et al. (1998) observe the same for pure silicon clusters and their cations: The geometries of neutral Si_N and charged Si_N^+ clusters remain (almost) identical, at least until $N = 7$. The results of the present work, summarised in table B.1, also demonstrate, that in most cases there are only small differences between singlet and triplet configurations.

- Due to the unsuccessful application of the VESH algorithm, a simpler search heuristic was developed. It is motivated by the observation, that in most cases within the geometry of a Si_xO_y cluster structural motifs of the previous cluster Si_xO_{y-1} are discernible[6]. Thus, in order to create a set of possible start configurations for a Si_xO_y cluster, we generated a configuration by seeding it with the structure of a Si_xO_{y-1} cluster, placing the "*missing*" atom randomly within a sphere of certain radius around the centre of mass of the seed, and performing a local optimization using the PM3 method. From this set of stationary points the most probable configurations were selected by physical intuition and then optimized on the BP86/6-31G(d) level of theory. This procedure was successfully applied to the Si_7O_y ($y = 1 - 4$), and the Si_8O_y ($y = 1 - 3$) clusters.

[6]For the transition from a $Si_{x-1}O_y$ to a Si_xO_y cluster this similarity is less distinct.

- For each stationary point found a vibrational analysis was performed, in order to decide, whether it is a true minimum with no imaginary frequencies or a transition state of order N_{imag}, where N_{imag} is the number of imaginary frequencies.

- In some cases the local optimization of a chosen start configuration lead to a transition state. At such a stationary point of the potential energy surface one could initiate a eigenvector following calculation (Cerjan & Miller, 1981), in order to find the minima connected with the transition state. Since such a calculation requires at *each* step the knowledge of the Hessian matrix (at least in an approximate form), it is computationally rather expensive and prohibitive for larger systems. However, since the vibrational analysis also yields the Cartesian displacement vectors of each vibrational mode, it is possible to utilise these informations by distorting the structure at the transition state by a certain amount along the displacement vector of the imaginary mode. The geometry of a potential energy surface implies, that the energy *decreases* with respect to the displacement parallel to the eigenvector pertaining to the negative eigenvalue of the Hessian matrix (Heidrich et al., 1991). Thus, it is hoped, and confirmed by practical applications, that such a *eigenvector distortion* moves the structure into the basin of attraction of the neighbouring minimum. A subsequent local minimization procedure will then, mostly within a few iterations, move the structure to that local minimum. In table B.1 we marked the isomers found by this technique[7].

As a consequence of the unsuccessful application of the VESH procedure one might identify two components of a "*good*" global minimization algorithm for *ab initio* potential energy surfaces. At first it seems useful, to introduce some kind of randomness in order to make the scanning of the PES more effective. Additionally, although the shifting of the spin and/or charge states proved to be efficient, it seems necessary to allow also a *geometric shifting*. A short sketch of such an algorithm will be given in chapter 6.

5.3.2 Results

Using the methods described above, an extensive survey of small and medium sized silicon and silicon oxide clusters has been performed, considering 117 different clusters and 274 different isomers in total. The results are summarised in table B.1, which due to its length is printed in appendix B. For convenience a quick overview over the cohesive energy E_{coh} of the clusters is given in table 5.6.

Different isomers of a cluster are labelled by ${}^{M}K(P)$, where K counts the isomers in energetic order, M indicates the spin multiplicity, and P the point group, which might be omitted sometimes within the text. In the last row of table B.1 we try to give a description of the structure of the clusters. In some cases we used the following abbreviations:

- **BP** stands for bipyramid

[7] Transition states have been omitted from that table.

Table 5.6: Cohesive energies E_{coh} (in eV) of silicon oxide clusters Si_xO_y ($x = 1, -10$, $y = 0, -20$) calculated on the BP86/6-31G(d) level of theory

O \ Si	**1**	**2**	**3**	**4**	**5**	**6**	**7**	**8**	**9**	**10**
no O	–	1.68	2.47	2.97	3.14	3.31	3.44	3.36	3.45	
1	4.12	3.55	3.53	3.47	3.47	3.64	3.69	3.65		
2	4.22	4.59	4.18	4.06	3.91	3.96	4.01	3.86		
3	3.88	4.82	4.81	4.43	4.27	4.10	4.09	4.14		
4	3.79	4.87	5.09	4.83	4.57	4.36	4.37	4.18		
5	3.63	4.62	5.12	5.13	4.84	4.61	4.52	4.44		
6	3.59	4.42	5.13	5.25	5.15	4.87	4.70	4.56		
7		4.29	4.92	5.26	5.26	5.11	4.88	4.71		
8		4.18	4.75	5.25	5.34	5.26	5.08	4.88		
9			4.62	5.08	5.34	5.33	5.20	5.06	4.91	
10			4.51	4.94	5.33	5.40	5.33			
11				4.82	5.19	5.39	5.43			
12				4.72	5.06	5.38	5.43	5.50		
13					4.96	5.26	5.42	5.50		
14					4.86	5.15	5.41	5.50		
15						5.05	5.31	5.49		
16						4.97	5.21	5.49	5.48	
17							5.12	5.39	5.47	
18							5.05	5.30	5.46	5.50
19								5.22		5.49
20								5.15		5.48

- **FC** stands for face capped (an atom is more or less centred above the face of a cluster)
- **EC** stands for edge capped (an atom is more or less centred above an edge of a cluster)
- **TBP** stands for the trigonal bipyramid

Furthermore we introduced a short notation to describe different types of chain–like configuration, depending on the number of oxygen atoms at the end of the chain. If the chain does not terminate with an oxygen atom, the respective end is denoted by **A**. If at the end of the chain there are one or two *non–bridging oxygen atoms*, which are not connected with a second silicon atom, the end of the chain is denoted by $\mathbf{B}_1$ or $\mathbf{B}_2$, respectively.

If finally the two oxygen atoms are connected with a third oxygen atom, the particular ending is denoted by **C**. Each of the two ends of a chain is denoted by the corresponding letter, e.g. the ground state of the Si_4O_8 cluster is a B_1B_1–chain. Note that going from an AA–chain to a CC–chain defines a kind of *Aufbau* principle. Some examples for such chain–like configurations are depicted in 5.15 for the case of Si_2O_y ($y = 2 - 8$).

Table 5.6 gives a good overview over all clusters treated with the above described methods. For a better orientation we underlay the entries for the homogeneous $(SiO)_N$ and $(SiO_2)_N$ clusters with a dark and a light grey background, respectively. Beginning with the pure silicon clusters, we discuss the results now in some detail.

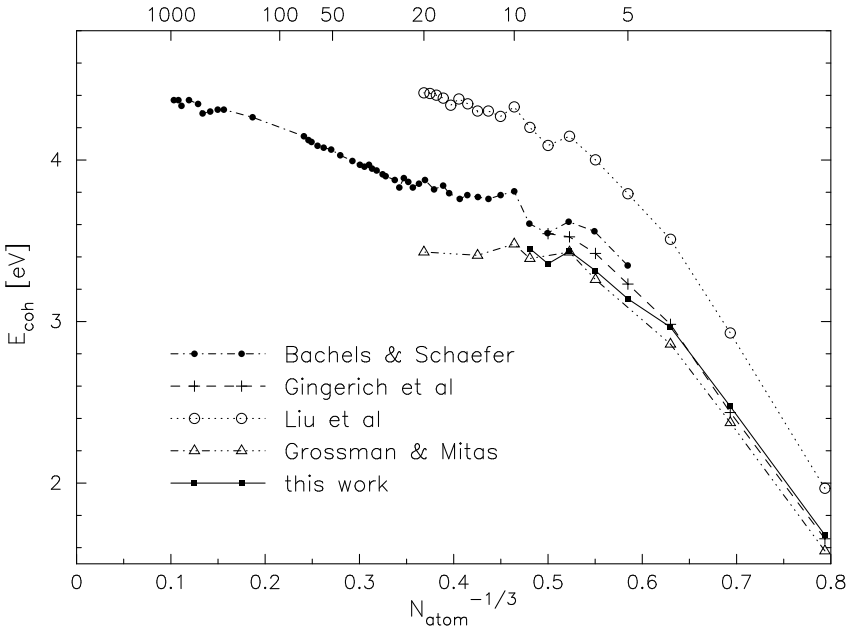

Figure 5.12: Cohesive energy E_{coh} of pure silicon clusters as a function of $N^{-1/3}$. The data from Bachels & Schäfer (2000) contain also those measured by Jarrold & Honea (1991). These data have been digitalized from the paper using an appropriate program (see appendix D). The other sources are discussed in the text.

5.3.3 Pure silicon clusters

Pure silicon clusters have been studied by numerous authors using many different approaches ranging from empirical force fields (Gong, 1993, Gong et al., 1995) and tight–binding method (Jo & Lee, 1999) up to G2 (Curtiss et al., 1992) and density functional studies (e.g. Fournier et al., 1992). Additionally they have been investigated by means of different experimental approaches. Gingerich and co–workers used mass spectrometric techniques to determine the atomization enthalpie of Si_2 and Si_3 (Schmude et al., 1995), Si_4 (Schmude et al., 1993), Si_5 (Ran et al., 1994), Si_6 (Gingerich et al., 1996), and most

recently Si_7 and Si_8 (Meloni & Gingerich, 2001). (Jarrold & Honea, 1991) studied the collision induced dissociation of silicon cluster anions with up to 70 atoms. Together with the ionization potentials measured by Fuke et al. (1993), one can deduce the atomization energy of neutral clusters (see section 3.3.1). Even larger clusters have been studied calorimetrically by Bachels & Schäfer (2000). The resulting cohesive energy is plotted as a function of $N^{-1/3}$ in figure 5.12 where we also depicted some exemplary data based on quantum mechanical calculations. The plot clearly reveals three different regions in the size dependence of the cohesive energy. For small clusters ranging from the dimer up to clusters with $N \approx 7-10$ atoms, E_{coh} increases rapidly. For clusters with $N \approx 10$ to $N \approx 25$ atoms the cohesive energy is nearly constant and for larger clusters it becomes proportional to $N^{-1/3}$ (Bachels & Schäfer, 2000). The described size dependence of E_{coh} can be explained by different growth patterns of the aggregates. While small clusters have compact polyhedral geometries (see figure 5.13), they adopt prolate or elongated structures in the intermediate size range (see Ho et al., 1998, for details). If the clusters become larger, they prefer a compact, spherical like structure (Bachels & Schäfer, 2000).

In figure 5.12 we also compared the results of various theoretical approaches with each other. As can be seen in that figure, there is a reasonable agreement between the experimental data and those obtained either by means of quantum Monte–Carlo (QMC) calculations (Grossman & Mitáš, 1995) or the BP86/6-31G(d) level of theory used in this work. Instead of this the density functional theory in the local density approximation[8] (Liu et al., 1998) clearly overestimates the binding energies[9] of pure silicon clusters.

We now discuss some further geometric aspects of small silicon clusters using the concept of sphericity introduced in section 4.3.2. It has been presumed recently by Zhu & Zeng (2003) that the lowest energy structure of small silicon clusters are all sphere–like, since this shape would minimize the surface area and reduce the number of dangling bonds. In order to elucidate this conjecture, the sphericity of the various isomers of small Si_N clusters ($N = 6-9$) has been calculated using the convex hull (see section 4.3.2). Together with the atomization energy D_{at} the resulting data are plotted in figure 5.14. The bars shown in that figure give the maximal sphericity attainable by a structure with the corresponding number of points. These values have been obtained using a simple evolutionary algorithm. Apparently there is no correlation between the sphericity σ of an isomer and its energetic order. In the case of the silicon heptamer e.g. the most stable cluster has the lowest sphericity.

5.3.4 Silicon oxide clusters - some general trends

We now focus the discussion on the mixed silicon oxide clusters. Unfortunately we are not aware of any experiments, which try to determine the dissociation energy of Si_xO_y clusters. The photoelectron spectroscopical studies of silicon oxide anions of Wang et al.

[8]The BP86 functional used throughout this thesis is a generalized gradient and not a local (spin) density approximation.

[9]It is noteworthy, that the published data by Grossman & Mitáš (1995) and Liu et al. (1998) do not include the zero-point vibrational energy. This would lower the energy values slightly by ≈ 0.4eV/atom.

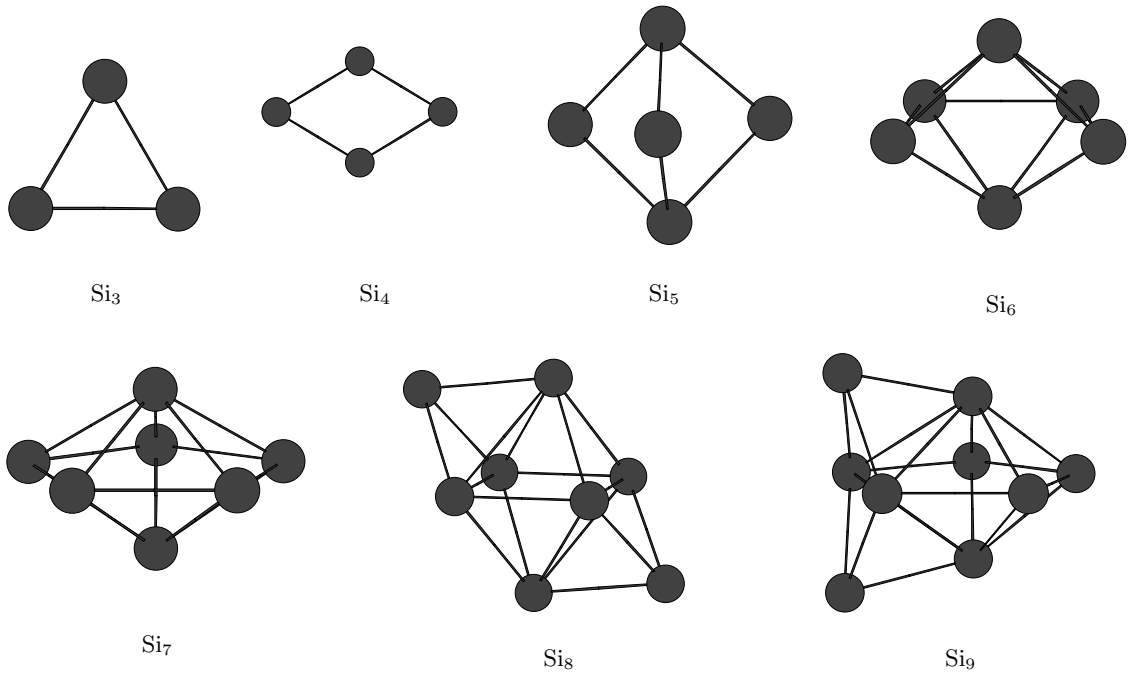

Figure 5.13: Ground state structures of pure Si_N clusters

(1996, 1997a,b) yield mainly information about the electron affinity and the structure of the species. It is noteworthy, that all structures identified experimentally by Wang et al. were reproduced by the chosen level of theory, as e.g. the B_1B_1–chain of Si_2O_4 (Wang et al., 1997a, see figure 5.15), or the ring like structure of homogeneous $(SiO)_N$ clusters ($N = 3 - 5$). Some structures of silicon oxide clusters will be presented in the course of the discussion but since we think, that the presentation of 117 different ground state configurations plus some interesting isomers is beyond the scope of this work, we abstain from this.

As the aim of this work is to elucidate the condensation process of solids and the effectiveness of this process is partly governed by the stability of the intermediate products between the atom and the solid, we focus the following discussion on the energies of small silicon oxide clusters.

The cohesive energy of the considered Si_xO_y clusters is plotted in figure 5.16 as a function of $N^{-1/3}$. For convenience the data for the pure silicon clusters are connected with a blue line, and those for the $(SiO)_N$ and $(SiO_2)_N$ species with a green and red line, respectively. The same data are presented in figure 5.17 in another way. The idea behind this plot is to view the a Si_xO_y cluster as an oxidised Si_x cluster. Hence we plotted for a fixed number of silicon atoms, the cohesive energy for as a function of N_O, the number of oxygen atoms in the cluster. The resulting curves for clusters with up to 8 silicon atoms have been shifted by a constant factor, in order to clarify the plot.

One important property of silicon oxide clusters evident from both plots, is the sta-

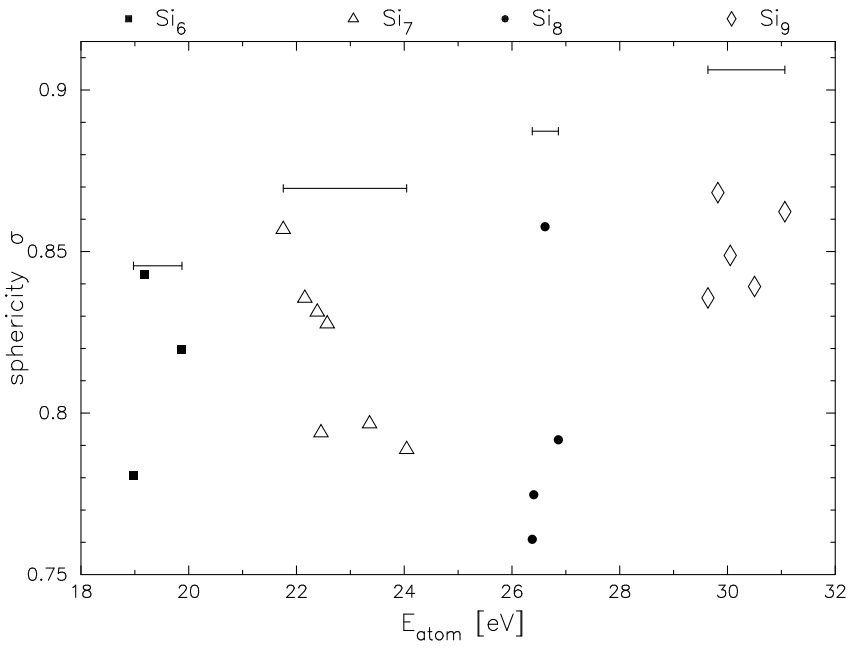

Figure 5.14: Sphericity of small Si_N–clusters.

bilising effect of an increasing oxygen content. While pure silicon clusters are clearly the least stable species in this series, the stability increases as the clusters successively take up more oxygen. The most stable aggregates are the $(SiO_2)_N$ clusters (connected with a red line in figure 5.17) and those with a slight oxygen deficit, i.e. with approximately up to 3 oxygen atoms less, than required by a stoichiometric composition. These oxygen deficient clusters can be viewed as $(Si_2O_3)_M$ clusters. They are connected with a blue line in figure 5.17. Between these two lines the clusters are of comparable stability, as it is discernible from the plateaus seen in figure 5.17, especially for the series with 7 and 8 silicon atoms. The addition of even more oxygen atoms then destabilises the clusters. Thus, the region between the series of the Si_2O_3 and the SiO_2 clusters define a '*valley of stability*', where the clusters are considerable more stable than outside of this region. In case of the other, well studied inorganic cluster system of Al_xO_y clusters this '*valley of stability*' is more or less reduced to a straight line where $x = y$ (Patzer, priv. comm.). It is important to note, that this '*valley of stability*' explains the stoichiometric composition of the solids formed in the condensation experiments of silicon monoxide discussed in section 5.1: Although the experiment of Nuth & Donn (1982) started with the evaporation of solid SiO, the enhanced stability of clusters with a stoichiometric composition between $(Si_2O_3)_M$ and $(SiO_2)_N$ favour the formation of a solid with a composition of SiO_x with $x \approx 1.5$, which is between the borders of the '*valley of stability*'. Thus, it is indeed possible to substantiate the results of a macroscopic condensation experiment by means of the properties of the molecular clusters, which are formed as intermediate products of this process. Note, that the formation process is also influenced by the abundances of the condensating species.

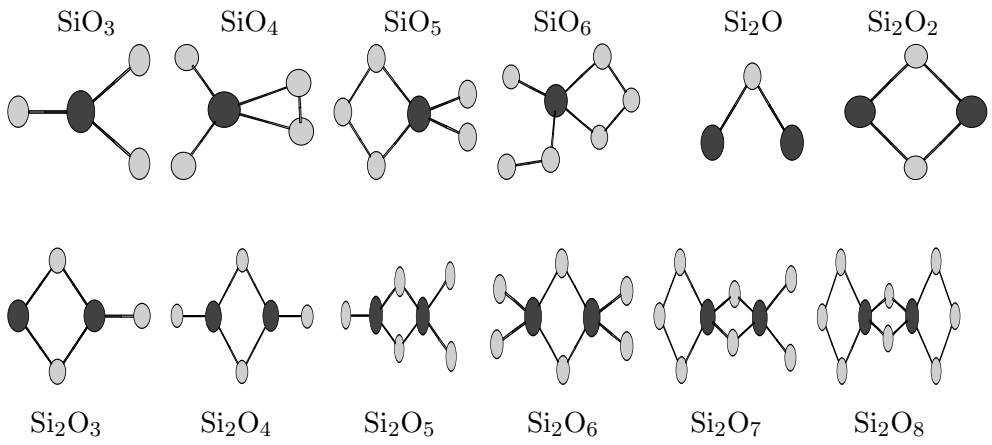

Figure 5.15: Ground state geometries of small Si_xO_y clusters ($x = 1, 2$, $y = 1 - 8$). The structures of the Si_2O_y ($y = 2 - 8$) represent the different types of chains introduced in the text.

Additionally, the calculated properties of Si_xO_y clusters confirm, that the nucleation of Si–O is more accurately described by a non–stoichiometric nucleation theory as it was outlined in chapter 2.

In section 3.1 it was discussed, that it is possible to describe the properties of clusters by means of *cluster size equations*, which interpolate between the bulk properties and those for the monomer. For the cohesive energy E_{coh} one often makes the following *ansatz* (Bachels & Schäfer, 2000):

$$E_{coh} = E_{coh}(\text{bulk}) - 4\,\pi\, r_1^2\, \widetilde{\sigma}\, N^{-1/3} \tag{5.10}$$

where $\widetilde{\sigma}$ is the surface tension. The hypothetical radius of the monomer r_1 is given by:

$$r_1 = \left(\frac{m}{4\pi\rho}\right)^{1/3} \tag{5.11}$$

with m the mass of the monomer and ρ the density of the solid. For SiO_2 one finds with $\rho = 2.648\,\text{g/cm}^3$ and $m = 60.084\,\text{amu}$ that $r_1 = 2.0797 \cdot 10^{-10}\,\text{m}$. Using the thermodynamic data listed in Chase (1998) for solid SiO_2, we find for the cohesive energy of the solid:

$$E_{coh}(\text{bulk}) = 6.37\ \text{eV}$$

Using these prerequisites the cohesive energy of the homogeneous SiO_2 clusters has been fitted using equation (5.10). For the parameter $\widetilde{\sigma}$ we obtained a value of

$$\widetilde{\sigma} = 0.809\ \text{J/m}^2$$

which is in reasonable agreement with the value given in table 5.1. However, this result should be handled with cautiousness. The graph of function (5.10) would describe a straight line in figure 5.16, which is obviously not true. The discussion in section 5.3.5 will clarify,

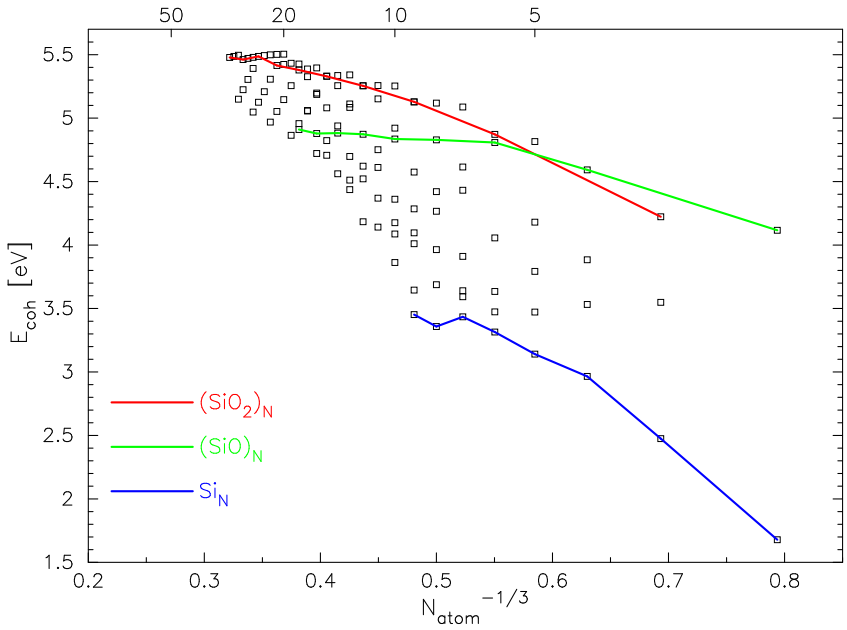

Figure 5.16: Cohesive energy of Si_xO_y clusters as a function of $N^{-1/3}$.

the reason for this deviation. We will deliver strong support for the assumption that for homogeneous SiO_2 clusters with more than 8 monomers the ground state structure has not yet been found.

5.3.5 Rings, chains, and crosses

The dominant structure type of silicon dioxide clusters is a chain like configuration build up of the two–ring unit of the Si_2O_2 cluster (see figure 5.15). Within in chain, each of these rings is planar and has a 90° orientation relative to its neighbour (see figure 5.18(c)). Alternatively the chain can be viewed as a linear arrangement of N SiO_4 tetrahedra, where the terminating two tetrahedra have a missing oxygen atom, which is often described as *non–bridging oxygen* atom (NBO, see Bromley et al., 2003). Thus, in a chain all Si atoms, except for the two at both ends of the chain, are four–fold coordinated, which is the preferred coordination for silicon. By bending the chain in such a way, that the ends come together, one obtains a ring–like (or crown–like) structure shown in figure 5.18(a) and 5.18(b). The Si atoms within such a ring are fully coordinated as the two terminal oxygen atoms now form another bridge.

For small SiO_2 clusters the chain–like configuration represents the ground state, while for larger clusters it is observed, that the ring–like configuration becomes energetically more favourable (Bromley et al., 2003). Since there was no evidence published by other authors (e.g. Nayak et al., 1998, Chu et al., 2001), that there might appear a deviation from this structural motif, it was a surprise, that we found for $(SiO_2)_8$ a structure, which turned out to be more stable, then the corresponding chain. The configuration reminds of a (bent)

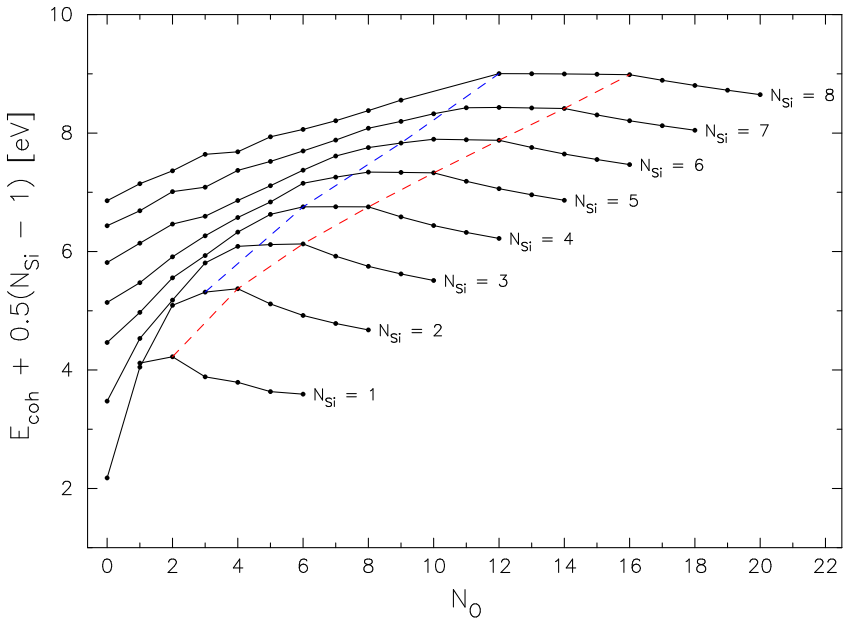

Figure 5.17: Cohesive energy of silicon oxide clusters as a function of the number of oxygen atoms. The positions of the $(SiO_2)_N$ and $(Si_2O_3)_N$ clusters are connected with a red and blue line, respectively.

cross and is shown in figure 5.20 together with other clusters, which were constructed on the basis of this first found configuration. All these structures turned out to be of particular stability compared to those structures of equal size, that are based on the chain-like configuration (the AA–chains to CC–chains in table B.1). The cross–like configuration has an atomization energy, which is about 1 eV larger than that of the chain. The initial configuration was found on the TTAM potential energy surface, where it is isomer number 47 of the energy scale[10]. It was mainly chosen for aesthetic reasons, since it possesses a high symmetry (D_{2d}). Although the finding of this minimum is some how accidental, the following discussion will demonstrate, that it is not unexpected in retrospect.

But at first, we discuss further some energetic aspects of the chain- and ring–like configuration. In order to determine for which cluster size the ring becomes more stable than the chain, we calculated the energies of such structures with up to $N = 15$ SiO_2 units. The first ring, which becomes stable against the dissociation into smaller fragments has 4 such units (Bromley et al., 2003). For clusters with more then 9 units, it became necessary to use a different *ab initio* program for the computations, which can be executed on a parallel computer. We used the program NWChem (Harrison et al., 2000). By some preliminary test calculation we assured, that both programs (Gaussian and NWChem) yield the same results within the numerical accuracy. For the larger clusters a vibrational analysis was not performed, since it would have been too time consuming. Hence, we solely discuss the

[10]This number is a lower bound, since it is not known how complete the sample of minima found with the different basin–hopping runs is.

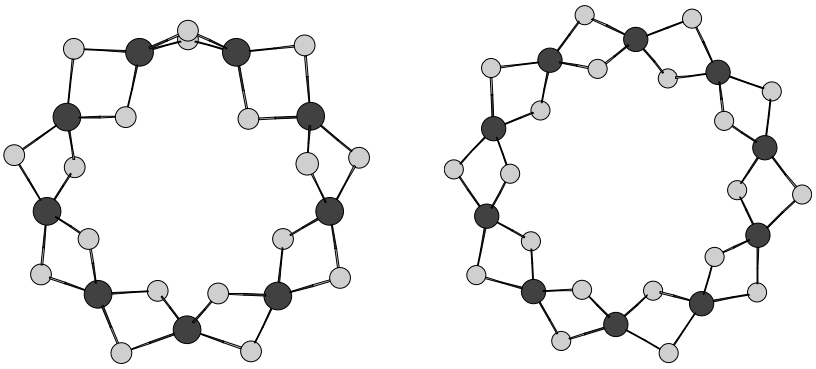

(a) Ring with 9 SiO_2 units (b) Ring with 10 SiO_2 units

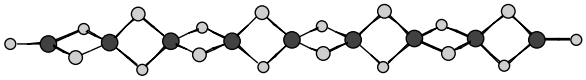

(c) Chain with 9 SiO_2 units

Figure 5.18: Ring and chain–like structures of SiO_2 clusters.

bond energy D_e of the structures. The results for the clusters calculated using NWChem are listed in table B.2, while all others can be found in table B.1. From that table and figure 5.19 it can be concluded, that the ring with 12 SiO_2 units is the first ring, which is energetically more stable, than the commensurate ring, which agrees with the findings of Bromley et al. (2003).

We try to explain the binding energy of both types of structures by means of a simple model, which decomposes D_e into different contributions due to different types of bonds. For the chain one easily distinguishes between two different bond types. The first (E_{nbo}) is due to the non-bridging oxygen at both ends of the chains. The second arises from the bond within the tetrahedron and is abbreviated with E_{tet}. By simply counting the number of occurrences of each type, one gets the following expression for the binding energy D_e^c of a chain with N_{Si} SiO_2 units:

$$D_e^c(N_{Si}) = 4\,(N_{Si} - 1)\,E_{tet}^c + 2\,E_{nbo} \tag{5.12}$$

which thus depends linearly on the number of atoms. Using a least-square-fit procedure we determined the following values for the two parameters:

$$E_{tet}^c = 4.292 \text{ eV} \qquad \text{and} \quad E_{nbo} = 6.278 \text{ eV} \tag{5.13}$$

The relative deviation between of the fitted data is below 0.2%.

For the ring–like configuration a different *ansatz* has to be made. In this case, there is no contribution due to the terminal oxygen atom. On the other hand, ring like structures possess some structural strain (Bromley et al., 2003), which is expected to decrease with increasing size of the ring. Thus, one can calculate the binding energy D_e^r of a ring by the following equation:

$$D_e^r = 4\, N_{Si}\, E_{tet}^r + E_{strain}\, N_{Si}^{-1} \tag{5.14}$$

where the parameters result in:

$$E_{tet}^c = 4.290 \text{ eV} \qquad \text{and} \quad E_{strain} = -50.956 \text{ eV} \tag{5.15}$$

As expected, the strain energy E_{strain} is negative, as it destabilises the configuration. The relative error of the fitted data is below 1%. The consistency of this model can be also inferred from the fact, that the energy E_{tet}, which appears in both models, is almost identical for chains and rings.

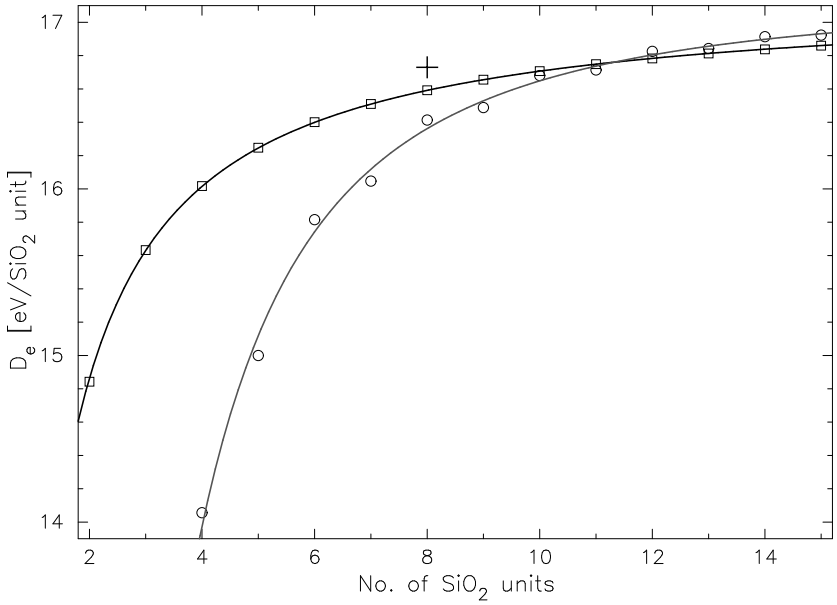

Figure 5.19: Binding energy D_e per SiO_2 unit of rings and chains. The lines give the energy calculated using equations 5.12 and 5.14. The cross marks the value of D_e of the cross–like structure.

The values of the binding energy D_e per number of SiO_2–units of these types of clusters are plotted in figure 5.19. It is apparent, that equation 5.14 reproduces the binding energies of chains perfectly well. For the case of the rings, one observes a pronounced odd–even oscillation, which is caused by the different geometries of odd and even numbered rings. The latter ones have a high symmetry (S_N), since they are able to mimic the favoured alternating orientation of the Si_2O_2 as in the chains. For odd numbered rings, such a arrangement would not lead to a closed structure. Thus, the ring has to distribute some

extra strain throughout the ring. In other words, for odd numbered rings E_{strain} is larger than for even numbered rings (Bromley et al., 2003). This explains, why equation (5.14) underestimates the the binding energy D_e^r of an even numbered ring and overestimates D_e^r for an odd numbered ring. This effect could be modelled, if one introduces a kind of Kronecker symbol $\delta_{eo}(N_{Si})$, which distinguishes between odd and even numbers:

$$\delta_{eo}(N_{Si}) = \begin{cases} 1 & \text{if } N_{Si} \text{ is even} \\ 0 & \text{if } N_{Si} \text{ is odd} \end{cases} \tag{5.16}$$

With the help of this, one can describe the binding energy of ring–like silicon oxide clusters by:

$$D_e^r(N_{Si}) = 4\,N_{Si}\,\widetilde{E}_{tet}^r + \widetilde{E}_{strain}\,N_{Si}^{-1} + E_{cor}\,(1 - 2\,\delta_{eo}(N_{Si})) \tag{5.17}$$

The parameters for this equation are:

$$\widetilde{E}_{tet}^r = 4.291\,\text{eV} \qquad \widetilde{E}_{strain} = -51.516\,\text{eV} \qquad E_{cor} = -0.342\,\text{eV} \tag{5.18}$$

and the relative error is now below $\approx 0.2\%$!

Using equation (5.12) and noticing, that $N = 3\,N_{Si}$, one finds for the cohesive energy of a chain:

$$E_{coh}^c(N) = \frac{4}{3}\,E_{tet}^c - (4\,E_{tet}^c + 2\,E_{nbo})\frac{1}{N} \tag{5.19}$$

Note, that the parameters are fitted using the data for D_e^c not those for D_{at}^c, since for larger clusters a vibrational analysis was prohibitive. Thus, the given values for E_{coh} in the following discussion are slightly overestimated by $\approx 0.08\,\text{eV/atom}$. Note further, that $N^{-1} = (N^{-1/3})^3$, thus equation 5.19 provides an explanation, why the E_{coh}–data for homogeneous SiO_2 clusters in figure 5.16, do *not* lie along a straight line, as it would be expected on the basis of equation (5.10): The possibility to describe the binding energy of chain–like configurations by means of a simple bond additivity scheme, leads to a size dependence, that differs from that expected for spherical clusters. Of course, one expects also, that for some cluster size another structural motif becomes dominating, because it is not clear, how a solid could be formed on the basis of a 1–dimensional growth pattern, as it is represented by the chain–like configurations. This can be deduced also from the fact, that for $N \to \infty$ equation (5.19) yields:

$$\lim_{N\to\infty} E_{coh}^c(N) = E_{coh}(\text{bulk}) = \frac{4}{3}\,E_{tet}^c = 5.722\,\text{eV}$$

which clearly does not match the experimental value of $E_{coh}(\text{bulk}) = 6.37\,\text{eV}$ given above. Note, that similar arguments apply to the ring configurations. Thus, one strongly expects, that for some $(SiO_2)_N$ clusters configurations other than rings or chains represent the ground state configurations. As already mentioned, for $N = 8$ such a configuration has been found. As depicted in figure 5.20 it is possible to use the Si_8O_{16} cross–like structure as a

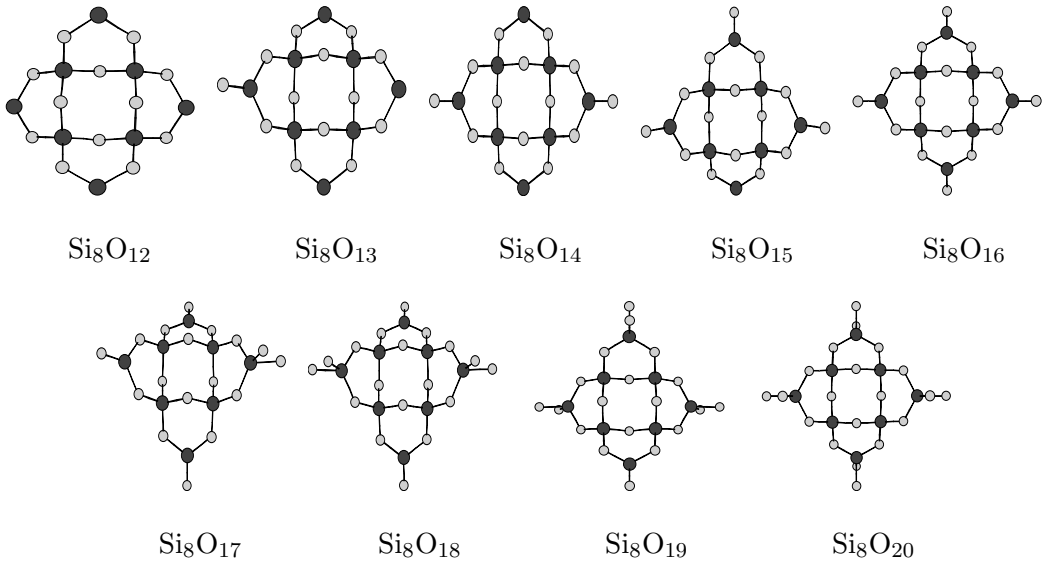

Figure 5.20: Ground state structures of Si_8O_y ($y = 12-18$) based on the cross-like structure of Si_8O_{16}.

building block from which further structures can be obtained. It is again based on the SiO_4–tetrahedron, which seems to be the ubiquitous structural motif in silicon oxide clusters[11]. As can be seen in figure 5.20, the cross–like structure consists of four such tetrahedra in the centre of the structure. We now analyse this tetrahedron, by measuring the torsion angle δ of its four oxygen atoms in different structures. For the ideal tetrahedron it turns out, that the torsion angle is $\delta = \arccos 1/3 \approx 70.52°$. The results of this comparison are given in 5.7. One recognises, that the cross–like structure resembles the bulk structure of α–quartz more, then the chains and rings discussed above, although these are also based on the tetrahedron. For the chain this angle does not vary significantly with the cluster size, where for the rings it reaches the bulk value with increasing size. It is noteworthy, that for odd numbered rings, δ shows a strong variation within the structure. Both findings

Table 5.7: Comparison of the torsion angle of the tetrahedra in different types of silica.

ideal	Si_8O_{16}	Si_8O_{16}	$Si_{12}O_{24}$	Si_8O_{16}	solid	solid	solid
tetrahedron	chain	ring	ring	cross	α-quartz	β-quartz	β-tridymite
70.5°	78.2°	95.5°	72.3°	70.6°	70.5°	68.0°	70.5°

confirm the assumption, that a.) the strain energy is proportional to N_{Si}^{-1} and b.) that

[11] A detailed analysis of this and the derivation of different *aufbau* principles has to be postponed to future works.

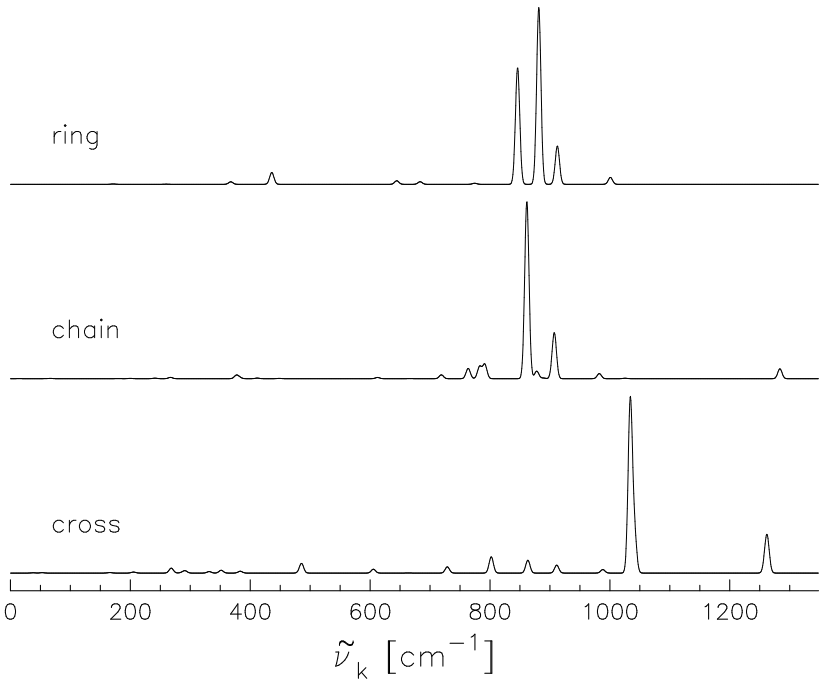

Figure 5.21: Calculated spectrum of the 3 different isomers of Si_8O_{16}. The spectral lines are illustrated with an artificial Gauss profile. The infrared intensities are scaled to the maximum value of the actual cluster.

this energy is larger in odd numbered rings, than in even numbered ones. Thus, this geometric consideration also motivates, why the cross is slightly more stable than the other configurations: The tetrahedron is almost "*relaxed*" possessing almost no strain. Furthermore, it allows for building up three dimensional structures. We thus conjecture, that the structure of larger clusters are mostly based on this building block, as it has already been confirmed for some other Si_xO_y species, which are shown in figure 5.20.

One might notice, that there is a certain similarity between the structure and energies of pure silicon (c.f. section 5.3.3) and silicon oxide clusters. In both circumstances one observes, that the growth pattern changes as the clusters become larger. It might be intriguing to conduct some drift tube experiments, as they have been performed for silicon clusters (Jarrold & Honea, 1991). The three different cluster structures discussed above should be clearly discernible by this experimental technique.

It is intriguing to ask, whether it would be possible to distinguish the different isomers (chain, cross or ring) on the basis of a measured spectrum, either in the gas phase or in a matrix. Figure 5.21 shows an calculated spectrum for these three different types of configurations for the Si_8O_{16} cluster. Obviously the spectrum of the cross–like configuration is different from the other two spectra and it could be possible to identify this species on the basis of the strong feature at about 1040 cm^{-1}. On the other hand a clear identification of a ring– or a chain–like configuration on the basis of a spectrum seems to be difficult, since

both species exhibit lines at roughly the same position. Since both structures are quite similar, this is not surprising: if one inspects an animation of the vibrational modes of the dominant peaks around $870 - 900\,\mathrm{cm}^{-1}$ for both species, one observes, that the motions of the atoms are very similar. The vibrational projection analysis developed by Grafton & Wheeler (1998) might provide a suitable tool for the quantitative comparison of the vibrational modes of different isomers. On the other hand the simultaneous occurrence of three lines between 850 and $950\,\mathrm{cm}^{-1}$ for the ring–like isomers, where for the chain only two lines are seen, might allow an identification of the corresponding structure. Additionally the line due to the stretching mode of the non–bridged oxygen atom at $\approx 1280\,\mathrm{cm}^{-1}$ may permit a discrimination between the chain and ring like configuration. Note, that due to the symmetry of these structures, the spectra of other cluster sizes should be similar. Of course, at the current time it seems difficult to isolate such large clusters in a sufficient amount, to measure reliable spectra.

5.3.6 Comparison between force-fields and ab initio calculations

At last we compare the results obtained using the density functional method with those of the force field calculations presented in section 5.2. The discussion is focused on two aspects, namely the geometry and the energetics of the tetramer. From table B.1 it can be seen, that each of the six lowest isomers of the TTAM potential energy surface corresponds to a stationary point on the DFT PES. Additionally all configurations found with the help of the force field turned out to be a stationary point, when treated with the BP86/6-31G(d) level of theory (see the corresponding marks in table B.1). Thus, the TTAM potential provides reasonable well configurations for the initialisation of DFT calculations. In most cases the structure is already close to the minimum, so only a few further optimization steps with the DFT method are necessary.

As already noted by several other authors (Nayak et al., 1998, Chu et al., 2001), the energies calculated with the TTAM potential significantly differ from those calculated by *ab initio* methods or measured experimentally. For example the potential energy Φ of the SiO_2 molecule is about a factor 4 higher, than the measured and calculated value (see table 5.3 and 5.5). However, in most cases it is ignored, that the calculated energy Φ of the TTAM potential refers to a different reference point, than the energy given by *ab initio* methods. The latter one refers to the ground state of the free, infinitely separated atoms (see section 3.3.1). For the TTAM potential however, the charged atoms define the zero point of the energy scale. Thus, in order to compare the energies, one has to correct for the charging of the atoms. This is done by means of a Born–Haber cycle, as discussed in Köhler et al. (1997) for the case of MgO clusters. One finds that the bond energy D_e of a $(SiO_2)_N$ clusters is given by:

$$D_e = -\Phi_0 + 2\,N\,E_a - N\,I_p \tag{5.20}$$

where the term $N\,I_p$ accounts for the ionization of the N silicon atoms (I_p is the ionization potential). The energy required for charging the $2N$ oxygen atoms is the electron affinity

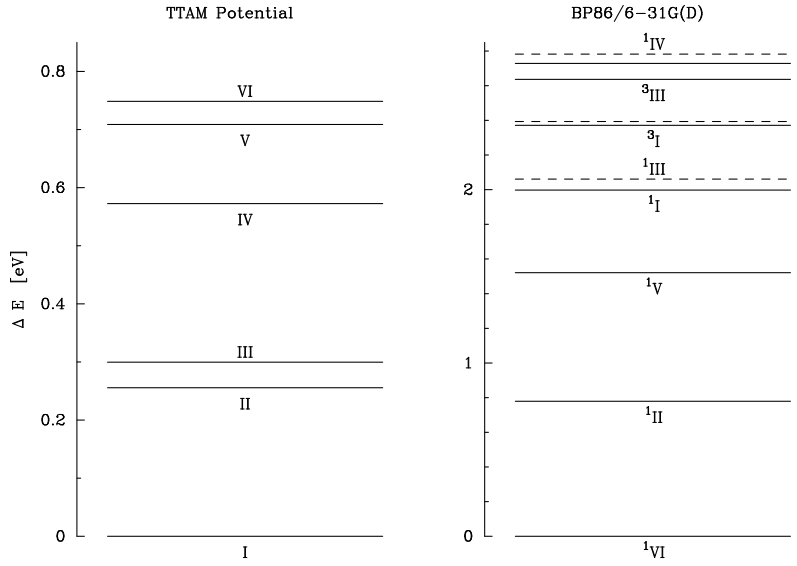

Figure 5.22: Energetic order of the isomers of Si_4O_8 with respect to the actual ground state of the TTAM PES (left) and the BP86/6-31G(d) level of theory (right). Transition states are marked with dashed lines.

E_a. Unfortunately it is not clear, how to take the fractional charges of the Si and the O atom into account. While one might think of a simple interpolation of the ionization potential between the known data for Si^{2+} and Si^{3+}, the problem is severely aggravated by the fact, that the free O^{2-} ion is not stable (Hotop & Lineberger, 1985). On the other hand it is known to exist within in a solid, where it is stabilised by the environment (Wilson, 1997). At the moment it is not clear how to take these different effects into account.

If one considers the relative energies between the different isomers, as they are shown in figure 5.22, one notices that a.) the energetic order of the isomers is not the same for the TTAM and the DFT method; and b.) the energy difference between the different conformers is underestimated by the TTAM potential. To summarise one might state:

1. The TTAM potential provides good start configurations, which simplify the search for the ground state of $(SiO_2)_N$ clusters considerably.

2. The energetic aspects are only poorly described by the TTAM potential.

The latter point should be addressed in future works in order to develop an improved potential model, which should at least reproduce the correct relative energies of the isomers.

5.3.7 A first application - the homogeneous condensation of SiO_2

Using the molecular data calculated by means of the BP86/6-31G(d) level of theory, the thermodynamic data of the $(SiO)_M$ $(M = 2 - 9)$ and $(SiO_2)_N$ clusters $(N = 2 - 10)$ have been calculated as described in section 3.3. The resulting values for $S^{\ominus}$, $\Delta_f G^{\ominus}$, and $\Delta_f H^{\ominus}$

are listed in table C.2. Based on these data the equilibrium constants have been fitted using a fourth–order polynomial (c.f. Eq. 3.51). The resulting coefficients are listed in table C.3.

The data for the Gibbs free energy of a cluster are required for the calculation of the evaporation rates in the master equation, that describes either a homogeneous or a non–stoichiometric nucleation process (see section 2). Since the latter one would require the solution of differential equation system, we concentrate here on the possibility of homogeneous nucleation. In the *classical* homogeneous nucleation theory a kind of cluster size equation is used to describe the size dependence of $\Delta_f G^{\ominus}$, which then allows a analytical calculation of the nucleation rate J_*. Starting with the following expression for the equilibrium size distribution $\overset{\circ}{f}(N)$ of a cluster (Patzer, 1998):

$$\overset{\circ}{f}(N) = \overset{\circ}{f}(1) \left(-\frac{\Delta \widetilde{G}}{RT} \right) \tag{5.21}$$

one finds for the Gibbs free energy change associated with the formation of a cluster with N monomers from the gas phase:

$$\Delta \widetilde{G}(N) = \Delta_f G^{\ominus}(N) - \Delta_f G^{\ominus}(1) - (N-1)\, \Delta_f G^{\ominus}(\text{solid}) \tag{5.22}$$

On the other hand, $\Delta \widetilde{G}$ is often expressed by means of a cluster size equation, which uses a parameter $\widetilde{\sigma}$, which has the physical meaning of a surface tension. It is a matter of debate, whether using the macroscopic bulk value for this quantity is applicable to the description of the properties of microscopic clusters. By attempting to determine this parameter on the basis of the microphysical properties of the clusters, one circumvents this discussion. From equations (5.21) and (5.22) it follows, that any physical meaningful fit formula for $\Delta \widetilde{G}$ must fulfil the condition, that $\Delta \widetilde{G} \equiv 0$ for $N = 1$. A profound discussion of the various attempts, to establish a suitable fit formula, the reader might refer to Patzer (1998) or Patzer et al. (1998). A widely used approach, was introduced by Gail et al. (1984):

$$\left(\frac{\Delta \widetilde{G}(N)}{RT} \right) = \Theta_\infty \frac{(N-1)}{(N-1)^{1/3} + N_f^{1/3}} \qquad \text{with} \quad \Theta_\infty = \frac{4\,\pi\, r_1\, \widetilde{\sigma}}{kT} \tag{5.23}$$

where the radius of the monomer r_1 is defined in equation (5.11). The parameter N_f is a further fit parameter. However, Patzer (1998) points out, that for high supersaturation ratio S and $N_f \neq 0$, this parameter leads to *negative* values for the size of the critical cluster, which is defined by the maximum of $\Delta \widetilde{G}(N)$. In order to prevent this unphysical behaviour, $N_f = 0$ is used. Using the calculated thermodynamic data for the SiO_2 clusters we determined the fit parameter $\widetilde{\sigma}$ by means of a non linear least square fit of the quantity $\Delta_f G^{\ominus}(N)/N$ using equations (5.22) and (5.23). The resulting value is

$$\widetilde{\sigma} = 0.977 \text{ J/m}^2 = 977 \text{ erg/cm}^2$$

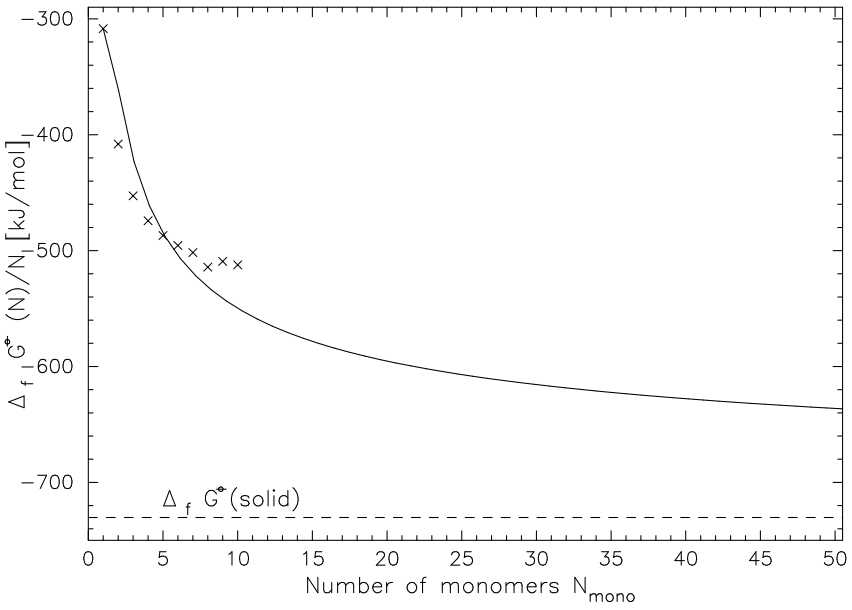

Figure 5.23: Plot of the $\Delta_f G^{\ominus}(N)/N$ values for $(SiO_2)_2$ clusters. The full line gives the calculated values using the fit formula (5.23) with $N_f = 0$ and $\widetilde{\sigma} = 0.977$ J/m^2. Note, that the enhanced stability of the $(SiO_2)_8$ cluster is clearly discernible.

The resulting curve for $\Delta_f G^{\ominus}(N)/N$ together with the thermodynamic data are plotted in figure 5.23. Clearly, the agreement between the fit and the data is only qualitative. It seems, as if the $\Delta_f G^{\ominus}(N)/N$ values do not converge to the bulk value. The reasons for this have been extensively discussed in the previous section. As this discussion suggests, that for principle reasons the data of the currently known ground states of the $(SiO_2)_N$ clusters do *not* converge against the bulk value, the result must be considered as preliminary. For the problem of the primary dust condensate in M–stars this result implies, that the homogeneous nucleation of silicon dioxide is not likely to initiate the dust formation process, since our calculated value for $\widetilde{\sigma}$ is higher, than that used by Jeong et al. (2003), the resulting nucleation rates will be lower and thus it seems unlikely, that the homogeneous nucleation of SiO_2 is important in astrophysical environments. On the other hand it was demonstrated in the previous section, that the condensation of silicon oxide is possibly a non–stoichiometric nucleation process.

We close this section with an application of the calculated thermodynamic data and consider the chemical equilibrium abundances of silicon monoxide and dioxide clusters in a stationary wind model, as it was already used in section 3.3.6. The necessary stellar parameters for the model are the same as above, viz.:

$$L_* = 1 \cdot 10^4\ L_\odot \qquad T_{\rm eff} = 2500\ \mathrm{K}$$
$$\dot{M} = 1 \cdot 10^{-6}\ M_\odot/\mathrm{yr} \qquad v_{\rm wind} = 1\ \mathrm{km/s}$$

Up to now, only the data of the $(SiO)_M$ $(M = 1-9)$ and $(SiO_2)_N$ $(N = 1-10)$ clusters are

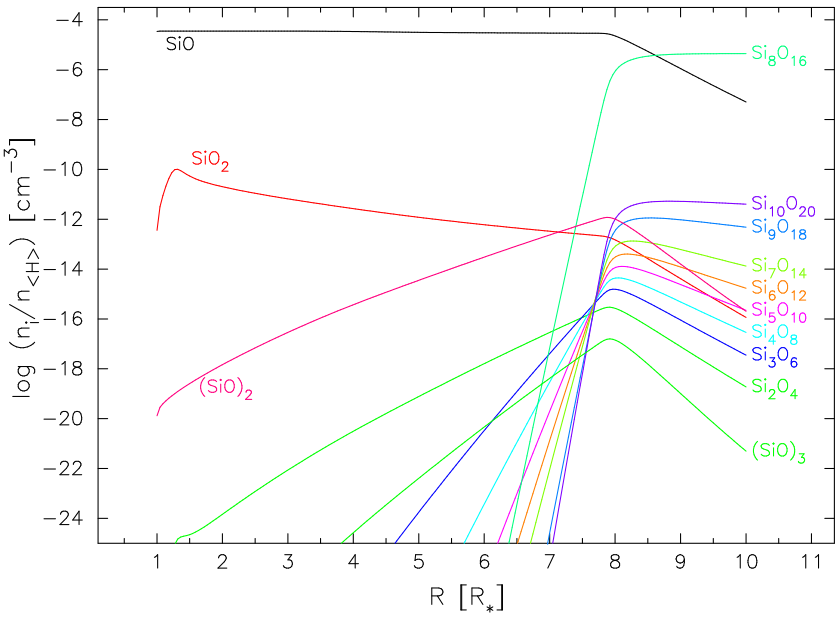

Figure 5.24: Chemical equilibrium abundances of silicon oxide clusters in a stationary wind model. The stellar parameters for the model are the same, as in section 3.3.6.

used for the calculation. The resulting equilibrium densities of the clusters are presented in figure 5.24. At approximately $7.8\,R_*$ the cluster distribution function reaches a maximum, which one might interpret as the onset of effective nucleation. The critical cluster at this point, defined as the aggregate with the lowest abundance, is the dimer $(SiO_2)_2$. Note, that the Si_8O_{16} cluster becomes at $\approx 8.5\,R_*$ the most abundant silicon oxide species - even more abundant the SiO molecule.

Except for the dimer and trimer of SiO, all other silicon monoxide clusters have abundances, which are outside the plot range. In a rather small window at around $6.5\,R_*$ the dimer becomes the second most abundant silicon oxide species, which is consistent with the fact, that for small cluster sizes the SiO monomer and dimer are the most stable silicon oxide clusters (see the crossing of the red and green line in figure 5.16).

The next chapter will summarise the results of the work presented in the previous sections. We will further try to sketch, in which directions future work should go.

Chapter 6

Conclusion and outlook

Denn mit dem Warum der Dinge kommt niemand zu Ende. Die Ursachen alles Geschehens gleichen den Dünenkulissen am Meere: eine ist immer der anderen vorgelagert, und das Weil, bei dem sich ruhen ließe, liegt im Unendlichen. *Thomas Mann,* Joseph der Ernährer

In the course of this thesis we elucidated some microphysical aspects of the dust formation process in oxygen-rich environments by means of various theoretical approaches. Thereby special attention has been payed to the physical properties of silicon oxide clusters, which were treated either by an empirical force field or by density functional methods. A major result of the latter investigation is, that the homogeneous nucleation of either silicon monoxide or silicon dioxide is likely not to be responsible for the onset of dust formation in M–stars. On the other hand it was demonstrated, that the enhanced stability of silicon oxide clusters with a stoichiometric composition between $(Si_2O_3)_M$ and $(SiO_2)_N$ - the *valley of stability* - quite naturally explains, why the macroscopic particles formed in condensation experiments of Si–O all have a composition, which is between that of silicon monoxide and silicon dioxide. Thus, solid silicon oxide grains are probably formed via a *non–stoichiometric* nucleation process in astrophysical situations.

In chapter 2 we derived a master equation, which describes the non–stoichiometric nucleation of two substances. Although the outlined theory is not yet complete, a direction, in which future work should go, is clearly given. Irrespective of the clarification of the question concerning the definition of an appropriate equilibrium state, it seems necessary to implement in a next step a suitable numerical algorithm for the solution of the differential equation system. The data, required for such calculations, namely the values for the Gibbs free energy of formation $\Delta_f G^{\ominus}$ are now known for different Si_xO_y clusters. The covered range of varying stoichiometric compositions seems to be suitable to perform a meaningful investigation of the the non-stoichiometric nucleation of silicon oxide clusters. The aim of such a study should be a simplification of the equation system by identifying the most effective nucleation path through the cluster space. Such a reduced description of the nucleation process then might be coupled with the hydrodynamic and radiative transfer equation system, which describe the physical processes in AGB stars (e.g. Fleischer, 1994)

or brown dwarfs (Lüttke, 2002).

Additionally, the mentioned thermodynamic data for homogeneous SiO_2 clusters have been used to determine a value for the parameter $\widetilde{\sigma}$, which is used in the fit formulas for the Gibbs free energy in the framework of homogeneous nucleation theory. The resulting value:

$$\widetilde{\sigma} = 0.977 \text{ J/m}^2 = 977 \text{ erg/cm}^2$$

is in reasonable agreement with other values given in the literature. On the other hand it is argued, that the fit would be improved considerably, if the correct ground state configurations of clusters with more then 8 monomers were known. It was further demonstrated, that starting with Si_8O_{16} the configurations of Si_xO_y clusters are governed by a new structural motif which more closely resembles the bulk properties, then the chain configurations, which dominate up to $N = 8$. For the latter class of configurations a simple bond additivity scheme was proposed, which explains the size dependence of the binding energy of these structures. A similar approach was successfully applied to ring–like configurations. Both bond additivity formulas lead for $N \to \infty$ to cohesive energy values, which are perspicuously lower than the experimental value. This in turn confirms the qualitative impression, that the calculated values for the currently known $\Delta_f G^{\ominus}$–values of SiO_2 clusters, do not converge to the bulk value. Until this crossover between the two competing structural motifs is not fully understood, the given value for $\widetilde{\sigma}$ should be regarded as preliminary.

Next to these results, some further aspects are clearly worth mentioning. Since we applied methods from different fields of physics and numerics, we discuss each part in turn.

Global optimization played an important role in the course of this thesis. In section 4.2.4 two key components of a '*good*' global optimization algorithm were identified: a.) a fast local minimization technique (see section 4.1) and b.) an effective scheme for searching different regions of the potential energy surface. It was further demonstrated, that for the case of Lennard–Jones clusters, each of the discussed global optimization techniques performs roughly speaking as good as the other. In view of the discussion of the 'no free lunch' theorem, it is intriguing to ask, whether this is also valid for other cluster systems, e.g Morse or heterogeneous clusters, consisting of two or more different atoms.

In section 4.3 we introduced some geometric measures, which allow a simple, quantitative description of the geometric structure of a cluster configuration. It was further demonstrated, that one of these quantities, the root mean square deviation σ_{opt}, can be used, to establish a new method for the direct visualization of the basins of attraction of the local minima on a potential energy surface. Up to now, the method, has only been applied to the analysis of molecular dynamic simulations, but it seems promising, to analyse the basin hopping trajectory by means of this method, too.

Next to the potential energy such geometric measures provide a simple and computational fast method, to determine the current "*position*" of the algorithm on the potential energy surface. If one now introduces a kind of *memory* for the algorithm, implemented through a histogram of this geometric measure and/or the energy, one can *penalise* the algorithm for revisiting different parts of the PES. This can be accomplished by a modifi-

cation of the acceptance probability (4.66), viz.:

$$P_{acc}(i \to j) = \min\left(1, \widetilde{P}_{acc}(i \to j)\right) \tag{6.1}$$

with

$$\widetilde{P}_{acc}(i \to j) = \exp\left(-\frac{\widetilde{\Phi}_j - \{\widetilde{\Phi}_i + H(Q_i, t)\ \delta E\}}{k\ T}\right) \tag{6.2}$$

and $H(Q_i, t)$ the histogram of an order parameter Q_i (either the energy, a geometric measure or both), which is updated after each iteration. The parameter δE determines the strength of that penalty. As a consequence the PES now has a *time dependent* topography, since it is deformed by the algorithm itself according to the previously visited points of the configuration space. It is hoped, that this kind of penalty accelerates the passing of the system between different basins. Since for the shift parameter $\delta E = 0$, the usual basin hopping algorithm is reconstructed, we call this algorithm *penalty basin–hopping*. Some preliminary applications of this algorithm to the LJ_{38} and LJ_{55} cluster show, that this newly developed *ansatz* is promising but not yet ripe.

Furthermore it was demonstrated, that the VESH algorithm, might be insufficient for some systems (see section 5.3.1) and that the introduction of a random component and additional geometric distortions of the structures, might be important for a *better* global optimization algorithm. There exist various techniques for the generation of such new configurations in the context of genetic algorithms (see e.g. Deaven & Ho 1995 or Roberts et al. 2000). They can be described as *genetic operators* (Bäck, 1996), which are applied to a configuration with a certain prescribed probability. Thus, it seems natural to view the changing of the spin and charge states, introduced by Sülzle & Chang (1999) for the VESH algorithm, as a new kind of genetic operator. In doing so, it becomes straight forward, to develop a new optimization algorithm utilising this enhanced set of genetic operators[1]. The regular seeding of (shorter) VESH runs with cluster structures, which are drawn from a pool of possible start configurations obtained from (simpler and faster) force field calculations, would be another possibility of an improved global optimization algorithm.

Force fields proved to be a useful instrument for the investigations presented here, since they allowed the location of some new isomers of $(SiO_2)_N$ cluster. One of these proved to be a up to now unknown global minimum and possible building block for the transition from molecules to solids. However, the detailed comparison of the $(SiO_2)_N$ clusters calculated by means of the TTAM potential model and the BP86/6-31G(d) level of theory revealed two main aspects:

1. The structures resulting from force field calculations using the TTAM potential agree reasonable well with those, obtained by the computational more demanding DFT calculations. Thus, the generation of an extensive sample of isomers of the TTAM force field combined with some *physical insight* into the building principles of silicon

[1]Note, that the changing of the spin state has no counterpart in force field calculations.

oxide clusters, gives a selection of configurations, which are good candidates for the ground state of the cluster. This kind of strategy located successfully the previously unknown ground state of the SiO_2 octamer.

2. On the other hand, the energetic properties are only poorly described by the TTAM potential, even if one takes into account, that the energy scale of this model refers to a different zero point. A shift of this point should not affect the energetic order of different isomers and their relative energies. Both effects can be observed (c.f. Fig. 5.22).

As it is additionally not possible to treat silicon oxide clusters with a non–stoichiometric composition with the help of the TTAM potential, it is strongly suggested to develop an improved or even new potential model for the Si–O system. The calculated molecular properties of 117 different clusters with 274 isomers should provide a reasonable large data set for such a derivation. Since it comprises clusters with a varying oxygen content between 0% (pure silicon clusters) and $\approx$ 87% (SiO_6), it provides a suitable base for the design of a potential model, that accurately describes the Si–Si as well as the Si–O interaction in different molecular environments (either almost pure silicon or highly oxidised clusters). This, for example, would allow for the first time the direct modelling of the non–stoichiometric nucleation process by means of molecular dynamic simulations. This can be accomplished by two different approaches:

1. A huge system with a large number of (> 5000) particles is studied directly by means of a molecular dynamic simulation and the onset of nucleation is monitored using appropriate properties of the system. Such an approach has been applied e.g. by Toxvaerd (2001) and Yasuoka & Matsumoto (1998a) to the homogeneous nucleation of Lennard–Jones particles and by Yasuoka & Matsumoto (1998b) to the homogeneous nucleation of water.

2. Only the microphysical aspects of a single growth and/or evaporation reactions are considered in order to determine the corresponding reaction rates. A similar approach has been applied Meißner et al. (1996) to the growth reaction of small alkali halide clusters.

Finally, such a potential model would also allow the atomic–level modelling of the Si/SiO_2 interface and the oxidation process of silicon surfaces, which are of some practical importance in the field of material science (Wang et al., 1997b, and references therein).

In order to verify or falsify the existence of silicon oxide as an important component of circumstellar dust, it is necessary, to investigate the optical properties of such grains in greater detail. Such an investigation must take into account, that the structure of a grain possibly consists of different polytopes and that its stoichiometric composition might vary continuously between that of silicon monoxide and of silicon dioxide, respectively. The works of Müller (2002) and Tamanai (1998) could serve as good starting points for such a study.

Appendix A

Formulas for the potential models

In this appendix the required formulas of the potentials are summarised, i.e. the definition and the first and second derivatives are given for each potential used in this thesis.

A.1 Some preliminary equations

Here we collect some expressions, which are needed for the calculations in the consecutive sections. With the help of these equations it should be straight forward, to verify the given formulas.

The distance r_{ij} between the i–th atom and the j–th atom in a cluster is given by the euclidian norm of the difference vector:

$$r_{ij} = |\vec{r_i} - \vec{r_j}| = \sqrt{\sum_{\alpha=1}^{3} (x_i^\alpha - x_j^\alpha)^2} \tag{A.1}$$

The first partial derivative of the n-th power of r_{ij} with respect to x_i is given by:

$$\frac{\partial}{\partial x_i} r_{ij}^n = n(x_i - x_j)\, r_{ij}^{n-2} \tag{A.2}$$

The obvious substitutions of Cartesian coordinates (y_i and z_i) yield the other equations for the gradient (A.2) and the Hessian matrix (A.4). For the derivative with respect to the other index j one finds:

$$\frac{\partial}{\partial x_j} r_{ij}^n = -n(x_i - x_j)\, r_{ij}^{n-2} = -\frac{\partial}{\partial x_i} r_{ij}^n \tag{A.3}$$

The second derivative of r_{ij}^n yields:

$$\frac{\partial^2}{\partial x_i \partial y_i} r_{ij}^n = n(n-2)(x_i - x_j)(y_i - y_j)\, r_{ij}^{n-4} \tag{A.4a}$$

$$\frac{\partial^2}{\partial x_i \partial y_j} r_{ij}^n = -n(n-2)(x_i - x_j)(y_i - y_j)\, r_{ij}^{n-4} \tag{A.4b}$$

$$\frac{\partial^2}{\partial x_i^2} r_{ij}^n = n\, r_{ij}^{n-2} \left\{ (n-2)\frac{(x_i - x_j)^2}{r_{ij}^2} + 1 \right\} \tag{A.4c}$$

$$\frac{\partial^2}{\partial x_i \partial x_j} r_{ij}^n = -n\, r_{ij}^{n-2} \left\{ (n-2)\frac{(x_i - x_j)^2}{r_{ij}^2} + 1 \right\} \tag{A.4d}$$

Note, that $\frac{\partial^2}{\partial x_i \partial y_j} r_{ij}^n = -\frac{\partial^2}{\partial x_i \partial y_i} r_{ij}^n$ (see also section next section).

Next to terms containing powers of the distance r_{ij} one often meets exponential terms for the repulsive part of the potential energy function. Consider a term of the type:

$$f_{\text{rep}}(r_{ij}) = C \exp\left(\frac{A - r_{ij}}{B}\right) \tag{A.5}$$

For the elements of the gradient one obtains:

$$\frac{\partial}{\partial x_i} f_{\text{rep}}(r_{ij}) = -\frac{C}{B}\, \frac{x_i - x_j}{r_{ij}} \exp\left(\frac{A - r_{ij}}{B}\right) \tag{A.6}$$

and for the contributions to the Hessian matrix it holds:

$$\frac{\partial^2}{\partial x_i \partial y_i} f_{\text{rep}}(r_{ij}) = \frac{C}{B}\, \frac{(x_i - x_j)(y_i - y_j)}{r_{ij}^2} \left[\frac{1}{r_{ij}} + \frac{1}{B}\right] \exp\left(\frac{A - r_{ij}}{B}\right) \tag{A.7a}$$

$$\frac{\partial^2}{\partial x_i \partial y_j} f_{\text{rep}}(r_{ij}) = -\frac{C}{B}\, \frac{(x_i - x_j)(y_i - y_j)}{r_{ij}^2} \left[\frac{1}{r_{ij}} + \frac{1}{B}\right] \exp\left(\frac{A - r_{ij}}{B}\right) \tag{A.7b}$$

$$\frac{\partial^2}{\partial x_i^2} f_{\text{rep}}(r_{ij}) = \frac{C}{B\, r_{ij}} \left[\left(\frac{x_i - x_j}{r_{ij}}\right)^2 + \frac{1}{B}\frac{(x_i - x_j)^2}{r_{ij}^2} - 1\right] \times \exp\left(\frac{A - r_{ij}}{B}\right) \tag{A.7c}$$

$$\frac{\partial^2}{\partial x_i \partial x_j} f_{\text{rep}}(r_{ij}) = -\frac{C}{B\, r_{ij}} \left[\left(\frac{x_i - x_j}{r_{ij}}\right)^2 + \frac{1}{B}\frac{(x_i - x_j)^2}{r_{ij}^2} - 1\right] \times \exp\left(\frac{A - r_{ij}}{B}\right) \tag{A.7d}$$

With the help of the equations (A.2) - (A.7) the computation of the necessary expressions for different potential energy functions is quite easy. The following sections we collect the results for the (reduced) Lennard–Jones, the Morse and the TTAM potential respectively.

A.2 Properties of the Hessian matrix

The Hessian matrix is a matrix with $3N \times 3N$ elements. Due to the symmetry, i.e.:

$$\mathsf{H}_{ij} = \mathsf{H}_{ji} \tag{A.8}$$

only $\frac{3}{2}N\ (3N+1)$ are independent. But under some special circumstances there exists another symmetry property. Assume that, the potential energy function depends only on the internuclear distances between atom i and atom j, viz $\phi = \phi(r_{ij})$. This means that 3-body contributions to the potential energy are neglected, and the energy of an N–cluster can be written as:

$$\Phi(N) = \sum_{i<j}^{N} \phi(r_{ij})$$

Without any further assumption about the functional form of ϕ one finds for one elements of the Hessian matrix:

$$\frac{\partial^2 \Phi}{\partial x_i \partial y_j} = \frac{\partial^2 \phi}{\partial r_{ij}^2} \frac{\partial r_{ij}}{\partial x_i} \frac{\partial r_{ij}}{\partial y_j} + \frac{\partial \phi}{\partial r_{ij}} \frac{\partial^2 \phi}{\partial x_i \partial y_j} \tag{A.9}$$

and for the case $i = j$:

$$\frac{\partial^2 \Phi}{\partial x_i \partial y_i} = \sum_{\substack{j=1 \\ j\neq i}}^{N} \left(\frac{\partial^2 \phi}{\partial r_{ij}^2} \frac{\partial r_{ij}}{\partial x_i} \frac{\partial r_{ij}}{\partial y_i} + \frac{\partial \phi}{\partial r_{ij}} \frac{\partial^2 \phi}{\partial x_i \partial y_i} \right) \tag{A.10}$$

Utilising the fact, that $\frac{\partial}{\partial y_j} r_{ij} = -\frac{\partial}{\partial y_i} r_{ij}$ (see appendix A.1 equation (A.2)) one finds that:

$$\frac{\partial^2 \Phi}{\partial x_i \partial y_i} = -\sum_{\substack{j=1 \\ j\neq i}}^{N} \frac{\partial^2 \Phi}{\partial x_i \partial y_j} \tag{A.11}$$

which is a consequence of the vanishing net force in a free cluster (Köhler, 1989). Equation (A.11) can be used to verify the correctness of the analytic formulas, one obtains for the elements of the Hessian matrix. Furthermore it can be utilised to simplify the practical computation of the matrix (John, 2002)

A.3 Lennard–Jones potential

As already mentioned in section 3.2 the reduced form of the Lennard–Jones potential energy function is defined as follows:

$$\phi_{\mathrm{rLJ}} = 4 \left(\frac{1}{r_{ij}^{12}} - \frac{1}{r_{ij}^{6}} \right) \tag{A.12}$$

accordingly it follows for the energy of an N–cluster:

$$\Phi_{\mathrm{rLJ}} = 4 \sum_{i<j}^{N} \left(\frac{1}{r_{ij}^{12}} - \frac{1}{r_{ij}^{6}} \right) \tag{A.13}$$

Using equation (A.2) one finds for the gradient:

$$\frac{\partial}{\partial x_i} \Phi_{\mathrm{rLJ}} = -24 \sum_{\substack{j=1 \\ j\neq i}}^{N} \left(\frac{2(x_i - x_j)}{r_{ij}^{14}} - \frac{x_i - x_j}{r_{ij}^{8}} \right) \tag{A.14}$$

and with the help of equation (A.4) the Hessian matrix is given by:

$$\frac{\partial^2}{\partial x_i \partial y_i} \Phi_{\mathrm{rLJ}} = 96 \sum_{\substack{j=1 \\ j\neq i}}^{N} (x_i - x_j)(y_i - y_j) \left(\frac{7}{r_{ij}^{16}} - \frac{2}{r_{ij}^{10}} \right) \tag{A.15a}$$

$$\frac{\partial^2}{\partial x_i \partial y_j} \Phi_{\mathrm{rLJ}} = -96\,(x_i - x_j)(y_i - y_j) \left(\frac{7}{r_{ij}^{16}} - \frac{2}{r_{ij}^{10}} \right) \tag{A.15b}$$

$$\frac{\partial^{\,2}}{\partial x_i^2} \Phi_{\mathrm{rLJ}} = 24 \sum_{\substack{j=1 \\ j\neq i}}^{N} \left[\frac{2}{r_{ij}^{14}} \left(\frac{14(x_i - x_j)^2}{r_{ij}^2} - 1 \right) - \frac{1}{r_{ij}^{8}} \left(\frac{8(x_i - x_j)^2}{r_{ij}^2} - 1 \right) \right] \tag{A.15c}$$

$$\frac{\partial^2}{\partial x_i \partial x_j} \Phi_{\mathrm{rLJ}} = -24 \left[\frac{2}{r_{ij}^{14}} \left(\frac{14(x_i - x_j)^2}{r_{ij}^2} - 1 \right) - \frac{1}{r_{ij}^{8}} \left(\frac{8(x_i - x_j)^2}{r_{ij}^2} - 1 \right) \right] \tag{A.15d}$$

A.4 Morse potential

For completeness also the Morse potential (Morse, 1929) is recalled here. However, it plays only a minor role in this thesis. It has been extensively used for the development and evaluation of the source code for OPOSSUM. The following form of the potential has been used:

$$\phi_{\mathrm{M}}(r_{ij}) = D \left[\exp\left\{ -2\alpha(r_{ij} - r_{eq}) \right\} - \exp\left\{ -\alpha(r_{ij} - r_{eq}) \right\} \right] \tag{A.16}$$

where D, α and r_{eq} are parameters[1], which can be calculated analytically using the spectroscopic constants D_0, ω_e and r_e of a diatomic molecule (see e.g. Atkins, 1989).

Because of the analytic properties of the exponential function, the following definition, first introduced by Braier et al. (1990), is quite useful:

$$g_{ij}(r_{ij}) = \exp\left(-\alpha(r_{ij} - r_{eq}) \right) \tag{A.17}$$

With this definition equation (A.16) can be rewritten as:

$$\phi_{\mathrm{M}}(r_{ij}) = D\; g_{ij}\,(g_{ij} - 2) \tag{A.18}$$

[1] In a heterogeneous cluster occur different parameters D^{ij}, α^{ij} and r_{eq}^{ij}, which depend on the atom type of the i–th and j–th atom. For the sake of convenience we omit these indices.

and the total energy of Morse cluster with N atoms is given by:

$$\Phi_{\mathrm{M}} = \sum_{i<j} D\, g_{ij}\,(g_{ij} - 2) \tag{A.19}$$

Comparing equation (A.5) and (A.17), it is obvious that $A = r_{eq}$, $B = 1/\alpha$ and $C = 1$. So equations (A.6) and (A.7) can be used, to calculate the gradient and the Hessian matrix of the Morse potential.
The gradient can be written as:

$$\frac{\partial}{\partial x_i}\,\Phi_{\mathrm{M}} = -2 \sum_{\substack{j=1 \\ j\neq i}}^{N} D\, \frac{\alpha\,(x_i - x_j)}{r_{ij}}\, g_{ij}\,(g_{ij} - 1) \tag{A.20}$$

and for the elements of the Hessian matrix it follows:

$$\frac{\partial^2}{\partial x_i \partial y_i}\,\Phi_M = 2\sum_{\substack{j=1 \\ j\neq i}}^{N} D\, g_{ij}\, \frac{\alpha\,(x_i - x_j)(y_i - y_j)}{r_{ij}^2}\, \left(\frac{g_{ij} - 1}{r_{ij}} + \alpha(2g_{ij} - 1)\right) \tag{A.21a}$$

$$\frac{\partial^2}{\partial x_i \partial y_j}\,\Phi_{\mathrm{M}} = -2D\, g_{ij}\, \frac{\alpha\,(x_i - x_j)(y_i - y_j)}{r_{ij}^2}\, \left(\frac{g_{ij} - 1}{r_{ij}} + \alpha(2g_{ij} - 1)\right) \tag{A.21b}$$

$$\frac{\partial^{\,2}}{\partial x_i^2}\,\Phi_{\mathrm{M}} = 2\sum_{\substack{j=1 \\ j\neq i}}^{N} \frac{D\, g_{ij}\,\alpha}{r_{ij}} \left\{ \left[\left(\frac{x_i - x_j}{r_{ij}} \right)^2 - 1 \right] (g_{ij} - 1) + \frac{\alpha\,(x_i - x_j)^2}{r_{ij}} (2g_{ij} - 1) \right\} \tag{A.21c}$$

$$\frac{\partial^2}{\partial x_i \partial x_j}\,\Phi_{\mathrm{M}} = -2\frac{D\, g_{ij}\,\alpha}{r_{ij}} \left\{ \left[\left(\frac{x_i - x_j}{r_{ij}} \right)^2 - 1 \right] (g_{ij} - 1) + \frac{\alpha\,(x_i - x_j)^2}{r_{ij}} (2g_{ij} - 1) \right\} \tag{A.21d}$$

The Morse potential can be transformed to reduced units (e.g. Miller et al., 1999, Braier et al., 1990). If one introduces the following quantities:

$$\rho_{ij} = \alpha\; r_{ij} \qquad \rho_0 = \alpha\, r_{eq} \qquad \widehat{x}_{ij} = \alpha\,(x_i - x_j) \tag{A.22}$$

and sets $D = 1$, the reduced form of the Morse potential is:

$$\phi_{\mathrm{redM}} = \exp\left(2\,(\rho_0 - \rho_{ij})\right) - 2\exp\left(\rho_0 - \rho_{ij}\right) \tag{A.23}$$

where ρ_0 is the only remaining parameter of the potential, describing the range of the interaction. Its influence on the various properties of Morse clusters is investigated e.g. by Braier et al. (1990), Mainz & Berry (1996), and Moseler & Nordiek (1999). In order to obtain equations for the gradient and the Hessian matrix of the reduced Morse potential, it is convenient to use the following rules of substitution (see also Braier et al., 1990):

1. g_{ij} in equation (A.17) is redefined: $g_{ij} = \exp(\rho_0 - \rho_{ij})$
2. omit the factors D and α
3. in all equations the term $(x_i - x_j)$ should be replaced by $\widehat{x}_{ij}$, accordingly for the other coordinates.
4. replace r_{ij} and r_{ij}^2 with ρ_{ij} and ρ_{ij}^2 respectively.

It is noteworthy, that the equations obtained in this way, do *not* agree with the all equations given in Braier et al. (1990) for the Hessian matrix of the reduced Morse potential. In contrast their equations (A5) and (A6), which give the second derivative with respect to different indices of the atoms, do not match the corresponding equations (A.21b) and (A.21d) given here. Since the equations given by Braier et al. (1990) do not obey the symmetric property described in section A.2 (see equation (A.11)), it seems plausible, that in the mentioned paper a typo occurred and the equations given here are correct.

A.5 TTAM potential

The TTAM potential energy function introduced by Tsuneyuki et al. (1988) is defined as follows:

$$\phi_{\mathrm{TTAM}}(r_{ij}) = \frac{1}{4\pi\varepsilon_0}\frac{q_i q_j}{r_{ij}} + f_0\,(b_i + b_j)\exp\left(\frac{a_i + a_j - r_{ij}}{b_i + b_j}\right) - \frac{C_i C_j}{r_{ij}^6} \tag{A.24}$$

For a detailed discussion of the parameters and the underlying physics see section 5.2. Here we present the first and second partial derivatives of the TTAM-potential (eq. A.24). For convenience we define the following new constants:

$$A^{ij} = a_i + a_j \tag{A.25a}$$
$$B^{ij} = b_i + b_j \tag{A.25b}$$
$$C^{ij} = C_i\, C_j \tag{A.25c}$$
$$Q^{ij} = \frac{q_i\, q_j}{4\pi\varepsilon_0} \tag{A.25d}$$

and a new function $\hat{g}_{ij}$:

$$\hat{g}_{ij}(r_{ij}) = f_0\,\exp\left(\frac{A^{ij} - r_{ij}}{B^{ij}}\right) \tag{A.26}$$

thus writing for the potential energy of an N–clusters:

$$\Phi_{\mathrm{TTAM}} = \sum_{i<j}^{N} \frac{Q^{ij}}{r_{ij}} + B^{ij}\,\hat{g}_{ij} - \frac{C^{ij}}{r_{ij}^6} \tag{A.27}$$

With these simplifications one finds for the gradient the following equation:

$$\frac{\partial}{\partial x_i}\,\phi_{\mathrm{TTAM}} = \sum_{\substack{j=1\\ j\neq i}}^{N} \frac{(x_i - x_j)}{r_{ij}}\,\left\{\frac{6C^{ij}}{r_{ij}^7} - \frac{Q^{ij}}{r_{ij}^2} - \hat{g}_{ij}\right\} \tag{A.28}$$

Using the above given equations (A.4) and (A.7) one obtains the following expression for the Hessian matrix:

$$\begin{aligned}
\frac{\partial^2}{\partial x_i^2}\Phi_{\mathrm{TTAM}} = & \sum_{\substack{j=1\\ j\neq i}}^{N} \left[\frac{Q^{ij}}{r_{ij}^3} \left(3 \left(\frac{x_i - x_j}{r_{ij}} \right)^2 - 1 \right) \right. \qquad \text{(A.29a)} \\
& + \frac{\hat{g}_{ij}}{r_{ij}} \left\{ \left(\frac{x_i - x_j}{r_{ij}} \right)^2 + \frac{(x_i - x_j)^2}{B^{ij}\, r_{ij}} - 1 \right\} \\
& - \left. 6\, \frac{C^{ij}}{r_{ij}^8} \left\{ 8 \left(\frac{x_i - x_j}{r_{ij}} \right)^2 - 1 \right\} \right] \\
\frac{\partial^2}{\partial x_i \partial x_j}\Phi_{\mathrm{TTAM}} = & - \frac{Q^{ij}}{r_{ij}^3} \left\{ 3 \left(\frac{x_i - x_j}{r_{ij}} \right)^2 - 1 \right\} \qquad \text{(A.29b)} \\
& - \frac{\hat{g}_{ij}}{r_{ij}} \left\{ \left(\frac{x_i - x_j}{r_{ij}} \right)^2 + \frac{(x_i - x_j)^2}{B^{ij}\, r_{ij}} - 1 \right\} \\
& + 6\, \frac{C^{ij}}{r_{ij}^8} \left\{ 8 \left(\frac{x_i - x_j}{r_{ij}} \right)^2 - 1 \right\}
\end{aligned}$$

Now the second derivative with respect to different coordinates yields:

$$\frac{\partial^2}{\partial x_i \partial y_i}\Phi_{\mathrm{TTAM}} = \sum_{\substack{j=1\\ j\neq i}}^{N} \frac{(x_i - x_j)(y_i - y_j)}{r_{ij}^2} \left[3\frac{Q^{ij}}{r_{ij}^3} + \hat{g}_{ij} \left(\frac{1}{r_{ij}} + \frac{1}{B^{ij}} \right) - 48\frac{C^{ij}}{r_{ij}^8} \right] \qquad \text{(A.30a)}$$

$$\frac{\partial^2}{\partial x_i \partial y_j}\Phi_{\mathrm{TTAM}} = -\frac{(x_i - x_j)(y_i - y_j)}{r_{ij}^2} \left[3\frac{Q^{ij}}{r_{ij}^3} + \hat{g}_{ij} \left(\frac{1}{r_{ij}} + \frac{1}{B^{ij}} \right) - 48\frac{C^{ij}}{r_{ij}^8} \right] \qquad \text{(A.30b)}$$

A.6 Rosenbrock's function

At last the definition, gradient and Hessian matrix of Rosenbrock's test function, which has been used for the discussion of the performance of local minimization algorithms in section 4.1.6, are presented here.

The original form of Rosenbrock's function is defined in two dimension[2] and reads as follows:

$$f_{\mathrm{R}}(x,y) = 100\left(x^2 - y\right)^2 + (1-x)^2 \tag{A.31}$$

A 3-dimensional and contour plot is shown in figure A.1. For the gradient it holds:

$$\frac{\partial}{\partial x} f_{\mathrm{R}} = 400\, x\, (x^2 - y) + 2(x-1) \tag{A.32a}$$

$$\frac{\partial}{\partial y} f_{\mathrm{R}} = -200\, (x^2 - y) \tag{A.32b}$$

With this one easily shows, that the minimum is at the point $\vec{\mathbf{x}}_{\min} = (1,1)$ and the

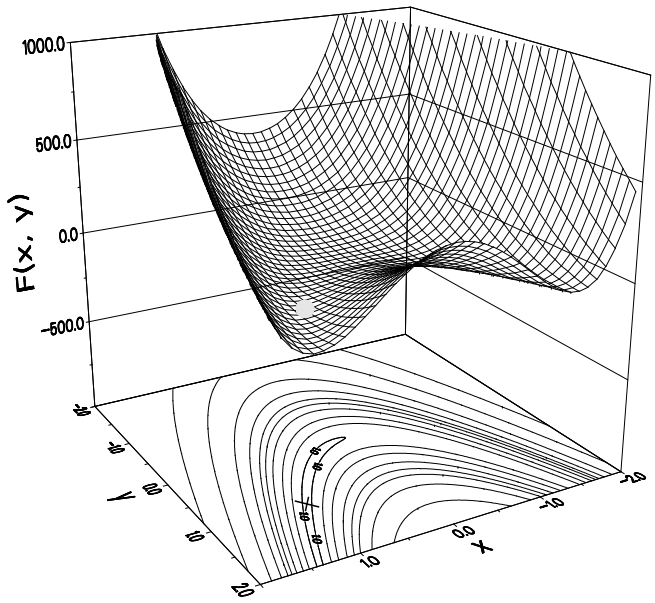

Figure A.1: Three-dimensional and contour plot of Rosenbrock's test function. The position of the minimum is marked with a cross and circle. The contour lines start with a function value $f(x,y) = 1$ (annotated) and the following contours are for $f = 10$, 25, 50, 75, 100, 150, 250, 500 and 1000, respectively.

corresponding function value is $f_{\mathrm{R}}(\vec{\mathbf{x}}_{\min}) = 0$, which is marked in figure A.1. The elements

[2]It is possible to generalise this definition to N dimensions, if N is an even integer value.

of the Hessian matrix are given by:

$$\frac{\partial^2}{\partial x^2} f_{\mathrm{R}} = 1200\,x^2 + 2\,x - 400\,y \tag{A.33a}$$

$$\frac{\partial^2}{\partial y^2} f_{\mathrm{R}} = 200 \tag{A.33b}$$

$$\frac{\partial^2}{\partial x \partial y} f_{\mathrm{R}} = -400\,x \tag{A.33c}$$

With this it follows for the Hessian matrix at the minimum:

$$\underline{\mathsf{H}}(f_{\mathrm{R}}(\vec{\mathbf{x}}_{\mathrm{min}})) = \begin{pmatrix} 802 & -400 \\ -400 & 200 \end{pmatrix}$$

By solving the characteristic polynomial one obtains for the 2 eigenvalues:

$$\lambda_1 = 0.3994 \qquad \wedge \qquad \lambda_2 = 1001.6006 \tag{A.34}$$

which yields for the condition number κ:

$$\kappa = \frac{\lambda_{max}}{\lambda_{min}} = 2.508 \cdot 10^3$$

The rather high value for κ is an indication of the slow convergence of the steepest descent minimisation discussed in section 4.1.6.

Appendix B

DFT results

The following table gives the result of the DFT calculation of Si_xO_y clusters. It comprises 117 different clusters and 274 different isomers in total. We recall, that different isomers of a cluster are labelled by ${}^{M}K(P)$, where K counts the isomers in energetic order, M indicates the spin multiplicity, and P the point group. The abbreviations used to describe the geometry are explained on page 139.

Table B.1: Results of the calculations. The description of the structure is only for a first orientation. The table lists only true minima, transition states are omitted.

cluster	isomer	D_e [eV]	E_{zp} [eV]	E_{coh} [eV]	ΔE_{H-L} [eV]	description
SiO	${}^{1}\mathbf{1}(C_{\infty v})$	8.31	0.07	4.12	4.69	$r_{eq} = 1.541$Å
	${}^{3}\mathbf{2}(C_{\infty v})$	4.25	0.06	2.10	0.12	$r_{eq} = 1.600$Å
	${}^{3}\mathbf{3}(C_{\infty v})$	4.18	0.05	2.07	0.54	$r_{eq} = 1.765$Å
SiO_2	${}^{1}\mathbf{1}(D_{\infty h})$	12.84	0.18	4.22	3.66	inserted dioxo O–Si–O
	${}^{3}\mathbf{2}(C_{2v})$	10.90	0.13	3.59	4.34	bent
	${}^{1}\mathbf{3}(C_{\infty v})$	9.27	0.16	3.04	2.38	side-on peroxo Si–O–O
SiO_3	${}^{1}\mathbf{1}(C_{2v})$	15.79	0.25	3.88	2.43	Y-shaped
	${}^{1}\mathbf{2}(C_{2v})$	13.89	0.25	3.41	3.59	rhombus
SiO_4	${}^{3}\mathbf{1}(C_{2v})$	19.26	0.30	3.79	5.12	tetrahedron [c] (B_2B_2–chain)
	${}^{1}\mathbf{2}(C_{2v})$	19.22	0.36	3.77	2.27	kite-shaped (B_1C–chain)
	${}^{1}\mathbf{3}(D_{2d})$	18.88	0.34	3.71	3.30	B_2B_2–chain
	${}^{3}\mathbf{4}(C_2)$	16.86	0.29	3.31	3.71	distorted B_2B_2–chain [b]
SiO_5	${}^{1}\mathbf{1}(C_{2v})$	22.24	0.44	3.63	2.24	B_2C–chain
SiO_6	${}^{3}\mathbf{1}(C_s)$	25.63	0.48	3.59	3.80	distorted CC–chain[c]
	${}^{1}\mathbf{2}(D_{2d})$	25.57	0.53	3.57	3.25	CC–chain
	${}^{1}\mathbf{3}(C_2)$	25.46	0.51	3.56	1.82	2-4-chain[b]

Table B.1: (continued)

cluster	isomer	D_e [eV]	E_{zp} [eV]	E_{coh} [eV]	ΔE_{H-L} [eV]	description
Si_2	$^3\mathbf{1}(D_{\infty h})$	3.39	0.03	1.68	2.09	$r_{eq} = 2.309$Å
	$^3\mathbf{2}(D_{\infty h})$	3.32	0.03	1.65	2.20	$r_{eq} = 2.184$Å
Si_2O	$^1\mathbf{1}(C_{2v})$	10.76	0.11	3.55	0.94	triangle
	$^3\mathbf{2}(D_{\infty h})$	10.25	0.11	3.42	1.09	linear Si–O–Si
	$^3\mathbf{3}(C_{2v})$	10.01	0.09	3.34	0.70	triangle like $^1\mathbf{1}$
	$^3\mathbf{4}(C_{\infty h})$	9.56	0.11	3.19	2.69	linear Si–Si–O
Si_2O_2	$^1\mathbf{1}(D_{2h})$	18.59	0.22	4.59	2.55	rhombus (AA-chain)
	$^1\mathbf{2}(C_s)$	16.60	0.20	4.10	1.62	zigzag line
	$^3\mathbf{3}(D_{2h})$	16.43	0.22	4.05	1.20	rhombus
	$^3\mathbf{4}(C_1)$	15.56	0.19	3.84	0.80	zigzag line
Si_2O_3	$^1\mathbf{1}(C_{2v})$	24.42	0.34	4.82	3.75	AB_1–chain
	$^3\mathbf{2}(C_{2v})$	21.14	0.33	4.16	1.87	AB_1–chain
Si_2O_4	$^1\mathbf{1}(D_{2h})$	29.68	0.45	4.87	3.75	B_1B_1–chain [a]
	$^3\mathbf{2}(C_1)$	27.18	0.39	4.46	3.82	dist. B_1B_1–chain
Si_2O_5	$^1\mathbf{1}(C_{2v})$	32.85	0.54	4.62	2.41	B_1B_2–chain
	$^1\mathbf{2}(C_{2v})$	31.86	0.52	4.48	1.98	
Si_2O_6	$^1\mathbf{1}(D_{2h})$	36.00	0.63	4.42	2.36	B_2B_2–chain
Si_2O_7	$^1\mathbf{1}(C_{2v})$	39.29	0.72	4.29	2.20	B_2C–chain
Si_2O_8	$^1\mathbf{1}(D_{2h})$	42.58	0.82	4.18	2.96	CC–chain
Si_3	$^3\mathbf{1}(D_{3h})$	7.49	0.07	2.47	2.55	equilateral triangle
	$^1\mathbf{2}(C_{2v})$	7.45	0.07	2.46	1.16	triangle
	$^3\mathbf{3}(C_{2v})$	6.14	0.06	2.03	0.52	triangle
Si_3O	$^1\mathbf{1}(C_{2v})$	14.30	0.17	3.53	1.15	distorted rhombus
	$^3\mathbf{2}(C_s)$	13.89	0.16	3.43	2.06	buckled rhombus
Si_3O_2	$^3\mathbf{1}(C_{2v})$	21.16	0.25	4.18	2.16	irregular pentagon
	$^1\mathbf{2}(C_s)$	20.25	0.24	4.00	0.71	EC trig. pyramid
Si_3O_3	$^1\mathbf{1}(D_{3h})$	29.20	0.35	4.81	3.07	planar ring
	$^3\mathbf{2}(C_s)$	26.86	0.32	4.42	1.58	buckled ring [b]
Si_3O_4	$^1\mathbf{1}(D_{2d})$	36.12	0.51	5.09	3.85	AA–chain
	$^1\mathbf{2}(C_{2v})$	34.94	0.48	4.92	2.95	ring-like
	$^3\mathbf{3}(C_{2v})$	32.89	0.50	4.62	0.64	AA–chain
	$^3\mathbf{4}(C_{2v})$	32.39	0.45	4.56	0.73	ring-like
Si_3O_5	$^1\mathbf{1}(C_{2v})$	41.57	0.63	5.12	3.95	AB_1–chain
	$^1\mathbf{2}(C_{2v})$	40.56	0.60	4.99	3.49	ring-like
	$^3\mathbf{3}(C_{2v})$	38.25	0.62	4.70	1.44	AB_1–chain

Table B.1: (continued)

cluster	isomer	D_e [eV]	E_{zp} [eV]	E_{coh} [eV]	ΔE_{H-L} [eV]	description
Si_3O_6	$^1\mathbf{1}(D_{2d})$	46.90	0.74	5.13	4.10	B_1B_1–chain [a]
	$^1\mathbf{2}(D_{3h})$	45.95	0.72	5.03	3.54	planar ring [a]
	$^1\mathbf{3}(C_s)$	44.92	0.70	4.91	0.80	cube like [a]
	$^3\mathbf{4}(C_s)$	43.43	0.64	4.75	3.16	buckled ring (similar $^1\mathbf{2}$)
Si_3O_7	$^1\mathbf{1}(C_{2v})$	50.04	0.83	4.92	2.42	B_1B_2–chain
	$^1\mathbf{2}(C_{2v})$	49.19	0.81	4.84	2.42	ring–like
Si_3O_8	$^1\mathbf{1}(D_{2d})$	53.18	0.91	4.75	2.42	B_2B_2–chain
	$^1\mathbf{2}(C_{2v})$	52.42	0.90	4.68	2.39	ring–like
	$^1\mathbf{3}(C_{2v})$	51.11	0.87	4.57	0.52	ring–like
Si_3O_9	$^1\mathbf{1}(C_{2v})$	56.47	1.01	4.62	2.17	B_2C–chain
	$^1\mathbf{2}(D_{3h})$	55.66	0.98	4.56	2.39	ring-like
	$^1\mathbf{3}(C_1)$	51.36	0.88	4.21	1.17	ring-like
Si_3O_{10}	$^1\mathbf{1}(D_{2d})$	59.76	1.10	4.51	3.10	CC–chain
Si_4	$^1\mathbf{1}(D_{2h})$	11.99	0.13	2.97	1.17	rhombus
	$^3\mathbf{2}(D_{2d})$	11.06	0.12	2.76	2.23	buckled rhombus
Si_4O	$^1\mathbf{1}(C_1)$	17.56	0.19	3.47	1.34	irreg. pentagon [b]
	$^3\mathbf{2}(C_s)$	16.74	0.19	3.31	0.67	irreg. pentagon
Si_4O_2	$^1\mathbf{1}(C_{2v})$	24.64	0.31	4.06	1.63	irreg. hexagon
Si_4O_3	$^1\mathbf{1}(C_2)$	31.40	0.37	4.43	2.17	buckled irreg. heptagon
Si_4O_4	$^1\mathbf{1}(D_{2d})$	39.10	0.47	4.83	2.42	buckled ring [b]
	$^1\mathbf{2}(T_d)$	38.65	0.50	4.77	3.49	cube
	$^1\mathbf{3}(C_{2v})$	38.30	0.54	4.72	0.24	
	$^3\mathbf{4}(D_{2d})$	37.04	0.44	4.57	1.07	buckled ring
Si_4O_5	$^1\mathbf{1}(C_{2v})$	46.80	0.65	5.13	3.11	two joined ring (2 + 3)
Si_4O_6	$^1\mathbf{1}(D_{2h})$	53.33	0.80	5.25	4.03	AA–chain
Si_4O_7	$^1\mathbf{1}(C_{2v})$	58.73	0.91	5.26	4.10	AB_1–chain
Si_4O_8	$^1\mathbf{1}(D_{2h})$	64.07	1.02	5.25	4.19	B_1B_1–chain [a] (VI)
	$^1\mathbf{2}(C_{2v})$	63.29	1.00	5.19	3.79	rhombus + ring [a] (II)
	$^1\mathbf{3}(C_{2h})$	62.55	1.01	5.13	2.26	two joined rings [a] (V)
	$^1\mathbf{4}(C_{2v})$	62.07	0.99	5.09	1.99	cage–like [a] (I)
	$^3\mathbf{5}(C_s)$	61.70	0.97	5.06	1.70	cage–like [a,b] (I)
	$^3\mathbf{6}(C_s)$	61.43	0.95	5.04	4.12	two joined Si_3O_2 units [a] (III)
	$^1\mathbf{7}(D_2)$	61.34	0.96	5.03	3.45	buckled ring [a,b] (IV)
	$^1\mathbf{8}(S_4)$	56.22	0.94	4.61	0.51	crown–like ring

Table B.1: (continued)

cluster	isomer	D_e [eV]	E_{zp} [eV]	E_{coh} [eV]	ΔE_{H-L} [eV]	description
Si_4O_9	$^1\mathbf{1}(C_{2v})$	67.21	1.11	5.08	2.42	B_1B_2–chain
	$^1\mathbf{2}(C_s)$	66.52	1.09	5.03	2.43	AB_1–chain+ 3–ring
	$^1\mathbf{3}(C_{2v})$	66.42	1.09	5.02	2.42	AB_2–chain+ 3–ring
Si_4O_{10}	$^1\mathbf{1}(D_{2h})$	70.34	1.20	4.94	2.42	B_2B_2–chain
	$^1\mathbf{2}(C_{2v})$	69.75	1.18	4.90	2.39	AB_1–chain+ 3–ring
	$^1\mathbf{3}(C_s)$	69.65	1.18	4.89	2.42	AB_2–chain+ 3–ring
Si_4O_{11}	$^1\mathbf{1}(C_{2v})$	73.64	1.29	4.82	2.16	B_2C–chain
	$^1\mathbf{2}(C_{2v})$	72.88	1.27	4.77	2.39	
Si_4O_{12}	$^1\mathbf{1}(D_{2h})$	76.93	1.38	4.72	3.09	CC–chain
	$^1\mathbf{2}(D_{2h})$	74.33	1.31	4.56	2.34	ring-like
Si_5	$^1\mathbf{1}(D_{3h})$	15.89	0.19	3.14	2.08	trigonal bipyramid
	$^3\mathbf{2}(C_{2v})$	15.26	0.17	3.02	2.5	dist. trigonal bipyramid
Si_5O_1	$^1\mathbf{1}(C_s)$	21.08	0.23	3.47	1.18	EC trigonal bipyramid
	$^3\mathbf{2}(C_s)$	21.03	0.24	3.47	2.26	AC trigonal bipyramid
	$^1\mathbf{3}(C_2)$	20.74	0.25	3.42	1.31	dist. pentagon + appending O
	$^3\mathbf{4}(C_s)$	20.35	0.24	3.35	1.99	dist. tetra. + appending O
Si_5O_2	$^1\mathbf{1}(C_1)$	27.72	0.34	3.91	1.27	irreg. pentag. + rhombus
	$^1\mathbf{2}(C_1)$	27.41	0.34	3.87	0.58	similar to $^1\mathbf{1}$
	$^3\mathbf{3}(C_1)$	27.11	0.32	3.83	1.26	similar to $^1\mathbf{1}$
Si_5O_3	$^1\mathbf{1}(C_{2v})$	34.56	0.43	4.27	1.24	planar double ring
	$^3\mathbf{2}(C_{2v})$	33.70	0.40	4.16	0.80	similar to $^1\mathbf{1}$
Si_5O_4	$^1\mathbf{1}(C_1)$	41.69	0.51	4.57	2.49	two joined rings (6 + 6)
	$^1\mathbf{2}(C_s)$	41.45	0.50	4.55	1.74	two joined rings (6 + 6)
	$^1\mathbf{3}(C_s)$	41.19	0.53	4.52	0.90	two joined rings (4 + 6)
Si_5O_5	$^1\mathbf{1}(C_1)$	48.95	0.59	4.84	2.76	buckled ring
	$^1\mathbf{2}(C_s)$	48.61	0.61	4.80	2.36	based on a cube
	$^3\mathbf{3}(C_1)$	46.67	0.57	4.61	0.60	buckled ring
Si_5O_6	$^1\mathbf{1}(D_{2d})$	57.46	0.79	5.15	3.02	two joined rings (3 + 3)
Si_5O_7	$^1\mathbf{1}(C_{2v})$	64.00	0.93	5.26	3.11	AA–chain+ Si_3O_3–ring
	$^1\mathbf{2}(C_{2v})$	63.47	0.93	5.21	3.16	two joined rings (3 + 5)
Si_5O_8	$^1\mathbf{1}(C_1)$	70.51	1.08	5.34	4.12	AA–chain
	$^1\mathbf{2}(C_{2v})$	69.02	1.05	5.23	2.96	two joined rings (3 + 5)
	$^3\mathbf{3}(D_{2d})$	67.20	1.07	5.09	0.85	AA–chain
	$^3\mathbf{4}(C_s)$	66.44	1.03	5.03	1.12	two joined rings (3 + 5)

Table B.1: (continued)

cluster	isomer	D_e [eV]	E_{zp} [eV]	E_{coh} [eV]	ΔE_{H-L} [eV]	description
Si_5O_9	$^1\mathbf{1}(C_1)$	75.89	1.19	5.34	4.16	AB_1–chain
Si_5O_{10}	$^1\mathbf{1}(D_{2d})$	81.24	1.31	5.33	4.27	B_1B_1–chain [a]
	$^1\mathbf{2}(C_{2v})$	80.45	1.28	5.28	3.85	AB_1–chain+ ring [a]
	$^1\mathbf{3}(C_1)$	80.19	1.30	5.26	2.46	2 dist. joined rings (3 + 4) [a]
	$^1\mathbf{4}(C_{2v})$	79.91	1.29	5.24	3.32	two joined rings (3 + 4) [a]
	$^1\mathbf{5}(D_{2d})$	79.70	1.27	5.23	3.71	two joined rings (3 + 3) [a]
	$^1\mathbf{6}(C_1)$	75.00	1.27	4.92	1.42	crown like structure
Si_5O_{11}	$^1\mathbf{1}(C_{2v})$	84.38	1.39	5.19	2.42	B_1B_2–chain
Si_5O_{12}	$^1\mathbf{1}(D_{2d})$	87.51	1.48	5.06	2.43	B_2B_2–chain
Si_5O_{13}	$^1\mathbf{1}(C_{2v})$	90.80	1.57	4.96	2.15	B_2C–chain
Si_5O_{14}	$^1\mathbf{1}(D_{2d})$	94.09	1.68	4.86	3.10	CC–chain
Si_6	$^1\mathbf{1}(C_{2v})$	20.11	0.22	3.31	2.04	dist. octahedron
	$^3\mathbf{2}(D_{4h})$	19.41	0.22	3.20	2.00	octahedron
	$^3\mathbf{3}(C_s)$	19.20	0.22	3.16	1.21	dist. octahedron
Si_6O	$^1\mathbf{1}(C_s)$	25.80	0.32	3.64	1.95	octahedron based
	$^1\mathbf{2}(C_{2v})$	24.82	0.26	3.51	1.76	pentag. bipyramid
	$^3\mathbf{3}(C_s)$	24.68	0.30	3.48	1.52	octahedron based
	$^3\mathbf{4}(C_1)$	24.64	0.27	3.48	2.17	FC octahedron
Si_6O_2	$^1\mathbf{1}(C_s)$	32.11	0.40	3.96	1.32	rhombus + Si_3O_2
	$^1\mathbf{2}(C_1)$	31.39	0.37	3.88	1.45	
	$^1\mathbf{3}(C_1)$	30.99	0.36	3.83	1.57	octahedron based
	$^1\mathbf{4}(C_s)$	30.90	0.37	3.82	1.04	bi–FC octahedron
	$^3\mathbf{5}(C_1)$	30.36	0.35	3.75	0.88	cage–like
Si_6O_3	$^1\mathbf{1}(C_1)$	37.31	0.45	4.10	1.47	
Si_6O_4	$^1\mathbf{1}(C_1)$	44.14	0.53	4.36	1.57	cage–like
Si_6O_5	$^1\mathbf{1}(C_1)$	51.35	0.63	4.61	1.52	cage–like
	$^1\mathbf{2}(C_s)$	51.19	0.66	4.59	1.28	two joined rings (6 + 8)
Si_6O_6	$^1\mathbf{1}(C_1)$	59.24	0.77	4.87	2.06	two joined rings (3 + 4)
	$^1\mathbf{2}(D_{3d})$	58.95	0.73	4.85	3.06	buckled ring
Si_6O_7	$^1\mathbf{1}(C_1)$	67.37	0.91	5.11	2.59	two joined rings (6 + 8)
Si_6O_8	$^1\mathbf{1}(D_{2h})$	74.65	1.07	5.26	3.07	rhombus + 2 rings
Si_6O_9	$^1\mathbf{1}(C_{2v})$	81.19	1.21	5.33	3.11	chain + ring
Si_6O_{10}	$^1\mathbf{1}(D_{2h})$	87.68	1.36	5.40	4.14	AA–chain
	$^1\mathbf{2}(C_{2v})$	86.59	1.33	5.33	3.12	chain + ring
	$^1\mathbf{3}(C_1)$	86.04	1.32	5.30	2.32	three joined rings
	$^1\mathbf{4}(C_1)$	85.55	1.28	5.20	0.86	three joined rings

Table B.1: (continued)

cluster	isomer	D_e [eV]	E_{zp} [eV]	E_{coh} [eV]	ΔE_{H-L} [eV]	description
Si_6O_{11}	$^1\mathbf{1}(C_{2v})$	93.06	1.47	5.39	4.16	AB_1–chain
Si_6O_{12}	$^1\mathbf{1}(D_{2h})$	98.40	1.59	5.38	4.31	B_1B_1–chain [a]
	$^1\mathbf{2}(C_s)$	97.57	1.60	5.33	1.38	cage–like [a]
	$^1\mathbf{3}(C_2)$	97.13	1.59	5.31	0.90	cage–like [a]
	$^1\mathbf{4}(D_{2h})$	96.89	1.55	5.30	3.65	two joined rings (8 + 8) [a]
	$^1\mathbf{5}(C_i)$	95.83	1.54	5.24	3.02	ring + two rhombuses
	$^1\mathbf{5}(S_6)$	94.89	1.60	5.18	2.71	crown like structure
	$^1\mathbf{6}(C_{2v})$	93.29	1.54	5.09	1.54	cross–based structure
Si_6O_{13}	$^1\mathbf{1}(C_{2v})$	101.54	1.68	5.26	2.42	B_1B_2–chain
Si_6O_{14}	$^1\mathbf{1}(D_{2h})$	104.68	1.76	5.15	2.42	B_2B_2–chain
Si_6O_{15}	$^1\mathbf{1}(C_{2v})$	107.97	1.86	5.05	2.13	B_2C–chain
Si_6O_{16}	$^1\mathbf{1}(D_{2h})$	111.26	1.95	4.97	3.10	CC–chain
Si_7	$^1\mathbf{1}(D_{5h})$	24.32	0.28	3.44	2.11	pentag. bipyramid
	$^1\mathbf{2}(C_{3v})$	23.64	0.28	3.34	1.78	bi-FC TBP
	$^3\mathbf{3}(C_{2v})$	22.83	0.26	3.22	1.29	distorted pentag. BP
	$^1\mathbf{4}(C_{3v})$	22.71	0.25	3.21	0.86	bi-FC tetrahedron
	$^3\mathbf{5}(C_s)$	22.64	0.25	3.20	0.42	bi-FC TBP
	$^1\mathbf{6}(C_s)$	22.40	0.24	3.17	1.35	bi-EC TBP
	$^3\mathbf{7}(C_{2v})$	21.76	0.24	3.11	1.83	bi-EC TBP
Si_7O	$^1\mathbf{1}(C_{3v})$	29.88	0.38	3.69	1.96	tri–FC trig. BP
	$^1\mathbf{2}(C_1)$	29.80	0.36	3.68	1.54	dist. EC BP
	$^1\mathbf{3}(C_s)$	29.06	0.34	3.59	1.15	dist. FC pent. BP
	$^1\mathbf{4}(C_1)$	28.48	0.34	3.52	0.99	
	$^3\mathbf{5}(C_1)$	28.43	0.33	3.51	1.38	based on FC tetrahedron
	$^3\mathbf{6}(C_1)$	28.17	0.33	3.48	1.51	bi-FC & EC tetrahedron
Si_7O_2	$^1\mathbf{1}(C_{2v})$	36.57	0.48	4.01	2.25	FC tetrahedron + Si_2O_3
	$^1\mathbf{2}(C_1)$	35.57	0.44	3.90	1.44	tetrahedron + buckled Si_2O_3
	$^1\mathbf{3}(C_1)$	35.20	0.42	3.86	0.93	tetrahedron + Si_2O_3
	$^3\mathbf{4}(C_1)$	35.06	0.42	3.84	1.00	based on octahedron
Si_7O_3	$^1\mathbf{1}(C_1)$	41.36	0.50	4.09	0.87	based on octahedron [b,c]
	$^3\mathbf{2}(C_1)$	40.99	0.50	4.05	1.25	
	$^1\mathbf{3}(C_1)$	40.77	0.52	4.03	1.07	
	$^1\mathbf{4}(C_s)$	40.75	0.48	4.03	1.43	
Si_7O_4	$^1\mathbf{1}(C_s)$	48.67	0.61	4.37	1.82	two sandwiched rings [c]
	$^1\mathbf{2}(C_1)$	47.83	0.59	4.29	1.02	structure of Chu et al.
	$^3\mathbf{3}(C_1)$	47.57	0.59	4.27	1.05	

Table B.1: (continued)

cluster	isomer	D_e [eV]	E_{zp} [eV]	E_{coh} [eV]	ΔE_{H-L} [eV]	description
Si_7O_5	$^1\mathbf{1}(C_1)$	54.97	0.71	4.52	1.05	joined cube + ring [b,c]
	$^1\mathbf{2}(C_1)$	54.61	0.69	4.49	1.24	structure of Chu et al.
	$^1\mathbf{3}(C_1)$	54.39	0.68	4.48	1.95	
Si_7O_6	$^1\mathbf{1}(C_{2v})$	61.86	0.79	4.70	1.26	two joined rings (8 + 8)
Si_7O_7	$^1\mathbf{1}(C_s)$	69.25	0.91	4.88	1.91	two joined rings (3 + 4)
	$^1\mathbf{2}(C_1)$	69.23	0.90	4.88	1.61	two joined rings (5 + 2)
	$^1\mathbf{3}(C_2)$	68.73	0.84	4.84	2.98	buckled ring
Si_7O_8	$^1\mathbf{1}(C_2)$	77.25	1.03	5.08	2.65	two twisted rings (8 + 8)
	$^1\mathbf{2}(C_1)$	76.24	1.07	5.01	1.67	three joined rings
Si_7O_9	$^1\mathbf{1}(C_1)$	84.38	1.22	5.20	1.72	three joined rings
	$^1\mathbf{2}(C_1)$	83.83	1.20	5.16	1.67	four joined rings
Si_7O_{10}	$^1\mathbf{1}(C_1)$	91.90	1.35	5.33	1.61	three joined rings
Si_7O_{11}	$^1\mathbf{1}(C_s)$	99.21	1.53	5.43	3.67	four joined rings (cross based)
Si_7O_{12}	$^1\mathbf{1}(C_s)$	104.85	1.64	5.43	4.15	AA–chain
	$^1\mathbf{2}(C_s)$	102.62	1.62	5.32	3.12	cross-based structure
Si_7O_{13}	$^1\mathbf{1}(C_s)$	110.22	1.76	5.42	4.16	AB_1–chain
Si_7O_{14}	$^1\mathbf{1}(D_{2d})$	115.57	1.87	5.41	4.34	B_1B_1–chain [a]
	$^1\mathbf{2}(C_{2v})$	115.02	1.91	5.39	1.38	glob. min. on TTAM PES [a]
	$^1\mathbf{3}(C_1)$	114.07	1.86	5.34	1.09	TTAM structure [a]
	$^1\mathbf{4}(C_2)$	112.33	1.88	5.26	3.05	ring
Si_7O_{15}	$^1\mathbf{1}(C_{2v})$	118.71	1.96	5.31	2.42	B_1B_2–chain
Si_7O_{16}	$^1\mathbf{1}(D_{2h})$	121.84	2.04	5.21	2.44	B_2B_2–chain
Si_7O_{17}	$^1\mathbf{1}(C_{2v})$	125.13	2.14	5.12	2.13	B_2C–chain
Si_7O_{18}	$^1\mathbf{1}(D_{2h})$	128.42	2.23	5.05	3.10	CC–chain
Si_8	$^1\mathbf{1}(C_{2h})$	27.17	0.31	3.36	1.89	dist. bi–FC octahedron
	$^1\mathbf{2}(C_{2v})$	26.93	0.32	3.33	1.11	dist. bi–FC octahedron
	$^1\mathbf{3}(C_s)$	26.70	0.30	3.30	0.66	FC pentagonal BP
	$^3\mathbf{4}(D_{3d})$	26.68	0.30	3.39	1.45	bi–FC octahedron
Si_8O_1	$^1\mathbf{1}(C_1)$	33.21	0.40	3.65	0.94	based on tri–FC tetrahedron
	$^1\mathbf{2}(C_2)$	33.18	0.39	3.64	1.16	based on dist. pent. BP
	$^1\mathbf{3}(C_1)$	33.05	0.40	3.63	1.19	dist. tri-FC octahedron
Si_8O_2	$^1\mathbf{1}(C_{2v})$	39.12	0.50	3.86	0.91	based on bi-FC octahedron
	$^1\mathbf{2}(C_1)$	39.07	0.47	3.86	1.62	based on an octahedron
	$^1\mathbf{3}(C_s)$	38.86	0.50	3.84	1.09	dist. 4-FC octahedron
	$^1\mathbf{4}(C_s)$	38.56	0.46	3.81	0.89	based on an octahedron

Table B.1: (continued)

cluster	isomer	D_e [eV]	E_{zp} [eV]	E_{coh} [eV]	ΔE_{H-L} [eV]	description
Si_8O_3	$^1\mathbf{1}(C_1)$	46.14	0.59	4.14	1.64	
	$^1\mathbf{2}(C_1)$	45.76	0.57	4.11	1.25	based on an octahedron
	$^1\mathbf{3}(C_1)$	45.71	0.57	4.10	1.22	
	$^1\mathbf{4}(C_1)$	44.77	0.54	4.02	1.27	bi-FC tetra. + rhombus
	$^1\mathbf{5}(C_1)$	44.37	0.54	3.98	0.71	
Si_8O_4	$^1\mathbf{1}(C_1)$	50.83	0.62	4.18	1.21	cage–like
Si_8O_5	$^1\mathbf{1}(C_1)$	58.41	0.73	4.44	1.41	cage–like
Si_8O_6	$^1\mathbf{1}(C_1)$	64.68	0.82	4.46	1.32	cage–like
Si_8O_7	$^1\mathbf{1}(C_1)$	71.52	0.90	4.71	1.49	two joined rings (8 + 10)
	$^3\mathbf{2}(C_1)$	70.81	0.89	4.66	0.80	two joined rings (8 + 10)
Si_8O_8	$^1\mathbf{1}(C_2)$	79.07	1.01	4.88	1.98	two joined rings (8 + 8)
Si_8O_9	$^1\mathbf{1}(C_1)$	87.15	1.20	5.06	2.20	cage + ring
	$^1\mathbf{2}(C_1)$	87.06	1.18	5.05	1.75	two joined rings (8 + 10)
Si_8O_{12}	$^1\mathbf{1}(D_{2d})$	111.78	1.70	5.50	3.75	bent cross
Si_8O_{13}	$^1\mathbf{1}(C_s)$	117.37	1.82	5.50	3.72	bent cross
Si_8O_{14}	$^1\mathbf{1}(C_{2v})$	122.91	1.93	5.50	3.67	bent cross
	$^1\mathbf{2}(D_{2h})$	122.02	1.92	5.46	4.15	AA–chain
Si_8O_{15}	$^1\mathbf{1}(C_s)$	128.40	2.06	5.49	3.71	bent cross
	$^1\mathbf{2}(C_{2v})$	127.38	2.04	5.45	4.16	AB_1–chain
Si_8O_{16}	$^1\mathbf{1}(D_{2d})$	133.84	2.18	5.49	3.83	bent cross [a]
	$^1\mathbf{2}(D_{2h})$	132.74	2.15	5.44	4.36	B_1B_1–chain [a]
	$^1\mathbf{3}(C_1)$	132.14	2.13	5.42	1.13	cage–like [a]
	$^1\mathbf{4}(S_8)$	131.31	2.19	5.38	3.89	crown like structure
	$^1\mathbf{5}(C_{2h})$	131.30	2.19	5.38	1.03	cube–like [a]
Si_8O_{17}	$^1\mathbf{1}(C_s)$	137.06	2.26	5.39	2.43	bent cross
	$^1\mathbf{2}(C_{2v})$	135.87	2.24	5.35	2.42	B_1B_2–chain
Si_8O_{18}	$^1\mathbf{1}(C_{2v})$	140.27	2.35	5.30	2.43	bent cross
	$^1\mathbf{2}(D_{2h})$	139.01	2.33	5.26	2.42	B_2B_2–chain
Si_8O_{19}	$^1\mathbf{1}(C_s)$	143.49	2.43	5.22	2.43	bent cross
	$^1\mathbf{2}(C_{2v})$	142.30	2.42	5.18	2.13	B_2C–chain
Si_8O_{20}	$^1\mathbf{1}(D_{2d})$	146.70	2.52	5.15	2.43	bent cross
	$^1\mathbf{2}(D_{2h})$	145.59	2.51	5.11	3.11	CC–chain

Table B.1: (continued)

cluster	isomer	D_e [eV]	E_{zp} [eV]	E_{coh} [eV]	ΔE_{H-L} [eV]	description
Si_9	$^1\mathbf{1}(C_{2v})$	31.42	0.36	3.45	1.97	bi–FC pentag. bipyramid
	$^1\mathbf{2}(C_1)$	31.09	0.36	3.41	1.73	
	$^1\mathbf{3}(C_{2v})$	30.83	0.33	3.39	1.60	bi–FC pentag. bipyramid
	$^3\mathbf{4}(C_s)$	30.40	0.35	3.34	1.66	dist. tri-capped prism
	$^3\mathbf{5}(D_1)$	30.15	0.32	3.31	1.41	tri-capped prism
	$^3\mathbf{6}(C_2)$	29.97	0.33	3.29	0.94	
Si_9O_9	$^1\mathbf{1}(C_1)$	89.58	1.19	4.91	2.19	cage + ring
	$^1\mathbf{2}(C_1)$	88.93	1.16	4.88	1.99	cage–like
	$^1\mathbf{3}(C_1)$	88.40	1.13	4.85	1.37	joined rings
Si_9O_{16}	$^1\mathbf{1}(C_s)$	139.19	2.21	5.48	4.16	AA–chain
Si_9O_{17}	$^1\mathbf{1}(C_s)$	144.55	2.32	5.47	4.16	AB_1–chain
Si_9O_{18}	$^1\mathbf{1}(D_{2d})$	149.90	2.43	5.46	4.37	B_1B_1–chain[a]
	$^1\mathbf{2}(C_2)$	148.40	2.46	5.40	3.87	crown–like structure
$Si_{10}O_{18}$	$^1\mathbf{1}(D_{2h})$	156.35	2.49	5.50	4.16	AA–chain
$Si_{10}O_{19}$	$^1\mathbf{1}(C_{2v})$	161.71	2.60	5.49	4.16	AB_1–chain
$Si_{10}O_{20}$	$^1\mathbf{1}(D_{2h})$	167.07	2.72	5.48	4.38	B_1B_1–chain[a]

[a] Similar configurations exist for the TTAM potential.
[b] Found by an eigenvector distortion of a transition state.
[c] Putative global minimum not found by Chu et al. (2001)

The following table lists the results of the calculations for large chain– and ring–like configurations of SiO_2 clusters. They have been obtained using the program NWCHEM (Harrison et al., 2000).

Table B.2: Results of the NWChem calculations for large clusters.

	chain		ring	
cluster	D_e [eV]	PG	D_e [eV]	PG
$(SiO_2)_{10}$	167.07	D_{2h}	166.80	S_8
$(SiO_2)_{11}$	184.23	D_{2d}	183.86	C_2
$(SiO_2)_{12}$	201.40	D_{2h}	201.91	S_{12}
$(SiO_2)_{13}$	218.57	D_{2d}	218.96	C_1
$(SiO_2)_{14}$	235.73	D_{2h}	236.80	S_{14}
$(SiO_2)_{15}$	252.90	D_{2d}	253.86	C_1

The data for the smaller ring– and chain–like clusters can be found in table B.1. Note, that

the ring–like structures are described as crown–like in that table in order not to confuse them with other, ring–like structures.
For completeness the *ab initio* data calculated for the benchmark test presented in section 5.3.1.1 are tabulated below. Table B.3 contains the energies of the Si and O atom in their respective ground states, calculated using the four different basis sets (6-31G, 6-31G(d), 6-311G(d)and 6-311G(d)) and the methods mentioned in section 5.3.1.

Table B.3: Total energies of the atoms Si($^3P_0$) and O($^3P_2$) for various DFT methods and basis sets. Energies are given in Hartree.

method	atom	basis set			
		6-31G	6-31G(d)	6-311G	6-311G(d)
HF	O	-74.780307	-74.783931	-74.802491	-74.805207
	Si	-288.828432	-288.831785	-288.847780	-288.850346
MP2	O	-74.830064	-74.880037	-74.861051	-74.918145
	Si	-288.842993	-288.872030	-288.864358	-288.892196
BP86	O	-75.047856	-75.050214	-75.074044	-75.075206
	Si	-289.371898	-289.375399	-289.397123	-289.396603
B3P86	O	-75.194538	-75.194485	-75.216896	-75.218145
	Si	-289.620355	-289.620451	-289.640537	-289.641577
BLYP	O	-75.044549	-75.046947	-75.072328	-75.073373
	Si	-289.352424	-289.354961	-289.379005	-289.378211
B3LYP	O	-75.058320	-75.060611	-75.084241	-75.085374
	Si	-289.368887	-289.371734	-289.392934	-289.393821
BPW91	O	-75.028875	-75.031325	-75.053501	-75.054803
	Si	-289.352776	-289.356790	-289.378366	-289.377387
B3PW91	O	-75.028874	-75.031325	-75.053501	-75.054803
	Si	-289.316103	-289.318866	-289.338903	-289.35000

Finally table B.4 lists the calculated spectroscopic constants of the SiO ground state for the different levels of theory and basis sets.

Table B.4: Summary of the calculated spectroscopic constants for the SiO molecule. All frequencies are unscaled! The last row gives the experimental values taken from Chase (1998) and Huber & Herzberg (1979).

Method	Basis set	E_{tot} [H]	D_e [eV]	r_e[Å]	ω_e [cm^{-1}]	D_0 [eV]
HF	6-31G	-363.703120138	2.568	1.5545	1241.2820	2.491
HF	6-31G(D)	-363.778844691	4.439	1.4871	1406.3905	4.352
HF	6-311G	-363.752025049	2.769	1.5325	1268.5437	2.690
HF	6-311G(D)	-363.816543617	4.381	1.4829	1411.1678	4.293
MP2	6-31G	-363.913187716	6.534	1.6297	1000.9930	6.472
MP2	6-31G(D)	-364.045810808	7.993	1.5425	1175.9753	7.920
MP2	6-311G	-363.971822096	6.705	1.6065	1011.5766	6.643
MP2	6-311G(D)	-364.101747714	7.930	1.5325	1194.5747	7.856
BP86	6-31G	-364.683496281	7.177	1.6122	1052.3272	7.112
BP86	6-31G(D)	-364.730838970	8.306	1.5415	1185.5043	8.232
BP86	6-311G	-364.738148290	7.265	1.5932	1058.3976	7.199
BP86	6-311G(D)	-364.777111300	8.308	1.5376	1188.0049	8.234
B3P86	6-31G	-365.107017867	7.949	1.5210	1246.8957	7.872
B3P86	6-31G(D)	-365.107042191	7.949	1.5207	1257.9908	7.871
B3P86	6-311G	-365.105128759	6.740	1.5700	1128.3123	6.670
B3P86	6-311G(D)	-365.150646880	7.916	1.5166	1262.5220	7.838
BLYP	6-31G	-364.658138632	7.107	1.6138	1044.3611	7.042
BLYP	6-31G(D)	-364.704798675	8.242	1.5439	1176.1271	8.169
BLYP	6-311G	-364.716125501	7.205	1.5952	1049.5210	7.140
BLYP	6-311G(D)	-364.753810520	8.224	1.5403	1177.8112	8.151
B3LYP	6-31G	-364.666480585	6.511	1.5929	1105.2834	6.442
B3LYP	6-31G(D)	-364.720026634	7.828	1.5241	1246.3889	7.755
B3LYP	6-311G	-364.721408687	6.646	1.5732	1117.8944	6.577
B3LYP	6-311G(D)	-364.765527246	7.792	1.5204	1249.3646	7.717
BPW91	6-31G	-364.654983919	6.995	1.6121	1051.8475	6.930
BPW91	6-31G(D)	-365.702404064	8.108	1.5408	1186.9273	8.03
BPW91	6-311G	-364.708936060	7.062	1.5931	1057.6360	6.996
BPW91	6-311G(D)	-364.748108385	8.121	1.5370	1189.1417	8.047
B3PW91	6-31G	-364.579190543	6.373	1.5920	1109.7876	6.304
B3PW91	6-31G(D)	-364.633468889	7.708	1.5223	1253.5994	7.631
B3PW91	6-311G	-364.631281436	6.500	1.5718	1123.3544	6.431
B3PW91	6-311G(D)	-364.676650572	7.670	1.5183	1257.4048	7.592
experimental values				1.5097	1241.5	8.26

Appendix C

Thermodynamic data

In this appendix we summarise some informations and results concerning the thermodynamic properties of molecules and clusters considered in this thesis.

Rotational symmetry number The following table gives the rotational symmetry number σ (see section 3.3.2.2) for some molecular point groups.

Table C.1: Rotational symmetry number of certain molecular point groups. The numbers are taken from Cramer (2002).

Point Groups	Symmetry number σ
C_1, C_i, C_s, $C_{\infty v}$	1
$D_{\infty h}$	2
S_n, $n = 2, 4, 6, \ldots$	$n/2$
C_n, $n = 2, 3, 4, \ldots$	n
C_{nh}, $n = 2, 3, 4, \ldots$	n
C_{nv}, $n = 2, 3, 4, \ldots$	n
D_n, $n = 2, 3, 4, \ldots$	$2n$
D_{nd}, $n = 2, 3, 4, \ldots$	$2n$
D_{nh}, $n = 2, 3, 4, \ldots$	$2n$
T, T_d	12
O_h	24
I_h	60

Determining the degeneracy of the ground state: The degeneracy of the molecular ground state can be inferred from its term symbol, like $^3\Sigma$ or $^4\Phi$. The term symbol is constructed according to $^{2S+1}\Lambda$, where Λ is generally expressed using greek symbols Σ

($\Lambda = 0$), Π ($\Lambda = 1$), Δ ($\Lambda = 2$), ... In such a case the degeneracy of the molecule is given by (Sauval & Tatum, 1984):

$$g_e = (2 - \delta_{0,\Lambda})\,(2\,S + 1) \tag{C.1}$$

where δ is the Kronecker symbol. As an example, the $^1\Sigma^+$ ground state of SiO has an degeneracy $g_e = 1$, while the $^4\Phi$ state of TiH has $g_e = 8$.

Thermodynamic Data: Since space is limited, it is not possible to list the thermodynamic data between 100 K and 4000 K in steps of 100 K for all molecules and clusters treated in this thesis. On the other hand such data might be useful for other in interpreting experimental or theoretical results. To this end table C.2 list the entropy, the enthalpy of formation and the Gibbs free energy of formation at the reference temperature $T_r = 298.15$ K. The molecular data needed as an input for the calculations have been discussed in section 3.3.3 and 5.3.2, respectively.

Table C.2: Calculated thermodynamic data of molecules and clusters considered in this thesis. The table gives the values for the entropy $S^{\ominus}$, enthalpy of formation $\Delta_f H^{\ominus}$ and the Gibbs free energy of fromation $\Delta_f G^{\ominus}$ at the reference temperature $T_r = 298.15$K.

Molecule	$S^{\ominus}(T_r)$ [J K^{-1} mol^{-1}]	$\Delta_f H^{\ominus}(T_r)$ [kJ mol^{-1}]	$\Delta_f G^{\ominus}(T_r)$ [kJ mol^{-1}]
Transition metal hydrides			
TiH	213.420	485.878	450.898
VH	215.377	522.511	486.405
CrH	210.950	425.540	389.168
FeH	213.772	471.808	435.699
Other titanium compounds			
TiC	226.669	842.542	785.843
TiN	223.013	468.558	439.801
TiS	246.577	292.101	237.313
Ti_2	245.434	793.067	738.233
Corrected phosphorus compounds			
PH	196.344	233.611	206.800
PH_2	212.652	108.500	96.307
PH_3	210.241	-0.758	7.249
Silicon compounds			
AlSi	240.380	532.588	474.961
MgSi	239.086	502.385	446.453
SiB	224.280	694.396	634.877
SiP	236.748	414.185	361.457
$MgSiO_3$	297.597	-617.330	-598.959

Table C.2: (continued)

Molecule	$S^{\ominus}(T_r)$ [J K^{-1} mol^{-1}]	$\Delta_f H^{\ominus}(T_r)$ [kJ mol^{-1}]	$\Delta_f G^{\ominus}(T_r)$ [kJ mol^{-1}]
$(SiO)_N$ clusters			
Si_2O_2	275.109	-389.285	-398.922
Si_3O_3	336.841	-708.526	-700.375
Si_4O_4	427.291	-958.667	-941.290
Si_5O_5	529.646	-1203.769	-1180.716
Si_6O_6	491.955	-1493.389	-1422.904
Si_7O_7	555.403	-1753.738	-1665.977
Si_8O_8	630.843	-1997.251	-1895.789
Si_9O_9	610.432	-2306.605	-2162.864
$(SiO_2)_N$ clusters			
Si_2O_4	317.770	-947.466	-908.658
Si_3O_6	383.667	-1645.773	-1559.836
Si_4O_8	450.084	-2339.918	-2207.008
Si_5O_{10}	516.295	-3033.870	-2853.925
Si_6O_{12}	582.533	-3727.856	-3500.884
Si_7O_{14}	649.428	-4421.460	-4147.656
Si_8O_{16}	674.899	-5219.837	-4886.852
Si_9O_{18}	778.234	-5809.188	-5440.236
$Si_{10}O_{20}$	845.625	-6502.906	-6087.272

Equilibrium constants For the computation of the equilibrium constant K_p (c.f. Eq. 3.49) one has to chose an appropriate value for the standard pressure $p^{\ominus}$. Since the reference system of the JANAF tables has been used throughout this work, it follows that $p^{\ominus} = 1$ bar. Additionally one has to decide, in which units this pressure should be expressed, e.g. SI units ($\mathrm{N\,m^{-2}}$) or CGS units ($\mathrm{dyn\,cm^{-2}}$), which are commonly used in an astrophysical context. Since it holds that

$$1 \text{ bar} = 1 \cdot 10^5 \text{ N m}^{-2} = 1 \cdot 10^6 \text{ dyn cm}^{-2}$$

one finds, that the $\ln K_p$ curve using SI units is shifted to higher values compared to the $\ln K_p$ curve in CGS units. Assuming that the standard pressure can be expressed using two different units, namely A and B, one finds for the difference in $\ln K_p$:

$$(\ln K_p)_{\mathsf{A}} - (\ln K_p)_{\mathsf{B}} = (1-b) \ln \left(\frac{p^{\ominus}_{\mathsf{A}}}{p^{\ominus}_{\mathsf{B}}} \right) \tag{C.2}$$

which allows one to obtain the equilibrium constant in any desired pressure unit by applying this correction[1]. Because equation (C.2) does not depend on the temperature T, the same correction has to be applied to the coefficient a_0 of equation (3.51). Here the partial pressure is expressed in SI units, so one has to add the term $(1-b)\ \ln 0.1 \approx -(1-b)\, 2.302585$, to obtain the equilibrium constant in CGS units.

As already mentioned in section 3.3.5 the equilibrium constant $\ln K_p$ has been fitted using a 5-th order polynomial (3.51) by means of a least-square fit procedure. The resulting coefficients are listed in table C.3. The last column gives the mean absolute error of the fit, viz.:

$$\langle\, \delta_{abs} \,\rangle = \langle\, |(\ln K_p)_{fit} - \ln K_p| \,\rangle \tag{C.3}$$

in order to demonstrate the quality of the fit.

[1]Note, that the correction defined by equation (C.2) depends on the number of atoms in the molecule ($b > 0$).

Table C.3: Fit coefficients for the equilibrium constant $\ln K_p$.

molecule	a_0	a_1	a_2	a_3	a_4	$\langle\, \delta_{abs} \,\rangle$
Transition metal hydrides						
TiH	-2.37991e+01	5.41773e+00	-3.70313e-02	1.09227e-03	-1.09675e-05	$5.79126 \cdot 10^{-2}$
VH	-2.44943e+01	5.69245e+00	-4.82682e-02	1.42670e-03	-1.42734e-05	$5.34691 \cdot 10^{-2}$
CrH	-2.30870e+01	4.98579e+00	-3.33024e-02	9.87686e-04	-9.89311e-06	$4.90577 \cdot 10^{-2}$
FeH	-2.42230e+01	4.43039e+00	-4.00195e-02	1.14080e-03	-1.11694e-05	$4.38134 \cdot 10^{-2}$
Other titanium compounds						
TiC	-2.70230e+01	8.73696e+00	-3.27956e-02	9.86203e-04	-1.00356e-05	$5.97016 \cdot 10^{-2}$
TiN	-2.70183e+01	1.18588e+01	-3.37455e-02	1.00345e-03	-1.01434e-05	$5.78372 \cdot 10^{-2}$
TiS	-2.58551e+01	1.13906e+01	-3.35289e-02	1.00670e-03	-1.02374e-05	$6.08290 \cdot 10^{-2}$
Ti_2	-2.75447e+01	4.18037e+00	-3.99327e-02	1.25483e-03	-1.30539e-05	$9.03227 \cdot 10^{-2}$
Corrected phosphorus compounds						
PH	-2.59460e+01	7.63148e+00	-3.14731e-02	8.93436e-04	-8.72854e-06	$2.43963 \cdot 10^{-2}$
PH_2	-5.37961e+01	1.62217e+01	-5.76697e-02	1.59278e-03	-1.53603e-05	$4.14520 \cdot 10^{-2}$
PH_3	-8.34480e+01	2.42470e+01	-6.46012e-02	1.60351e-03	-1.45889e-05	$2.05802 \cdot 10^{-2}$
Silicon compounds						
AlSi	-2.62812e+01	6.19604e+00	-2.26991e-02	6.89360e-04	-7.05918e-06	$3.38056 \cdot 10^{-2}$
MgSi	-2.44510e+01	2.55114e+00	-2.25047e-02	6.92316e-04	-7.10605e-06	$3.41988 \cdot 10^{-2}$
SiB	-2.71098e+01	7.86254e+00	-2.41073e-02	7.09993e-04	-7.15927e-06	$3.36418 \cdot 10^{-2}$
SiP	-2.67225e+01	8.73596e+00	-2.49151e-02	7.52068e-04	-7.67195e-06	$3.98350 \cdot 10^{-2}$
$MgSiO_3$	-1.17938e+02	4.70433e+01	-1.83935e-03	-2.59991e-04	3.64695e-06	$1.75401 \cdot 10^{-2}$
$(SiO)_N$ clusters						
Si_2O_2	-8.97361e+01	4.29796e+01	-1.51941e-02	2.71999e-04	-2.24474e-06	$1.64489 \cdot 10^{-2}$
Si_3O_3	-1.48579e+02	6.69649e+01	1.52968e-02	-7.83708e-04	8.80231e-06	$2.81056 \cdot 10^{-2}$
Si_4O_4	-2.03921e+02	8.92996e+01	4.54226e-02	-1.81873e-03	1.96470e-05	$7.11719 \cdot 10^{-2}$
Si_5O_5	-2.57889e+02	1.11522e+02	7.52215e-02	-2.84961e-03	3.04762e-05	$1.14558 \cdot 10^{-1}$
Si_6O_6	-3.28577e+02	1.34764e+02	1.09153e-01	-4.02114e-03	4.25650e-05	$1.57808 \cdot 10^{-1}$

Table C.3: (continued)

molecule	a_0	a_1	a_2	a_3	a_4	$\langle\, \delta_{abs} \,\rangle$
Si_7O_7	-3.87252e+02	1.57349e+02	1.39399e-01	-5.07301e-03	5.35924e-05	$2.01260 \cdot 10^{-1}$
Si_8O_8	-4.44249e+02	1.79502e+02	1.70841e-01	-6.13733e-03	6.46781e-05	$2.44665 \cdot 10^{-1}$
Si_9O_9	-5.12934e+02	2.03225e+02	2.04207e-01	-7.29797e-03	7.66820e-05	$2.87877 \cdot 10^{-1}$
$(SiO_2)_N$ clusters						
Si_2O_4	-1.51128e+02	6.80343e+01	7.57569e-03	-6.43490e-04	7.86066e-06	$3.54697 \cdot 10^{-2}$
Si_3O_6	-2.43064e+02	1.06965e+02	4.91953e-02	-2.19614e-03	2.45085e-05	$1.04940 \cdot 10^{-1}$
Si_4O_8	-3.34916e+02	1.45794e+02	9.09677e-02	-3.75178e-03	4.11836e-05	$1.74464 \cdot 10^{-1}$
Si_5O_{10}	-4.26796e+02	1.84618e+02	1.32708e-01	-5.30651e-03	5.78486e-05	$2.44012 \cdot 10^{-1}$
Si_6O_{12}	-5.18680e+02	2.23445e+02	1.74384e-01	-6.85991e-03	7.45031e-05	$3.13569 \cdot 10^{-1}$
Si_7O_{14}	-6.10476e+02	2.62261e+02	2.16156e-01	-8.41572e-03	9.11789e-05	$3.83102 \cdot 10^{-1}$
Si_8O_{16}	-7.07349e+02	3.03624e+02	2.52881e-01	-9.78610e-03	1.05916e-04	$4.52040 \cdot 10^{-1}$
Si_9O_{18}	-7.94677e+02	3.39906e+02	2.99624e-01	-1.15255e-02	1.24512e-04	$5.22197 \cdot 10^{-1}$
$Si_{10}O_{20}$	-8.86423e+02	3.78726e+02	3.41303e-01	-1.30790e-02	1.41168e-04	$5.91738 \cdot 10^{-1}$

Appendix D

Some technical remarks

In this appendix some more or less technical aspects of the thesis are shortly presented. The reader, who is not so interested in these types of problems, might easily skip it. But due to the importance of computational aspects in the corse of the work, some words about the "*How-I-have-done-it*" might be of some interest.

The algorithms described in the chapter 4 have been implemented into a computer program called OPOSSUM – an acronym for **O**ptimization **P**rogramm **O**ffering **S**ome **S**trategies **U**sually **M**entionend[1]. The main parts of this program are written in C, mainly because Fortran misses some useful features, namely:

1. the ability of dynamical memory allocation
2. the ability to handle pointer to functions
3. the definition of structures

which allow a more flexible and more extensible design of the code. Three different tasks are covered by the program:

1. minimization of some test functions, e.g Rosenbrock, Rastrigin, etc. Some of these functions are discussed in Bäck (1996) or Schöneburg et al. (1994, chapter 4).
2. local minimization and (optional) subsequent vibrational analysis of clusters
3. global minimization of clusters

The program OPOSSUM is highly modular and relatively easy to extend. For example, the implemented minimization algorithms use a well defined interface for the calculation of the potential energy and its gradient, so it is straight forward to add new potential models without the necessity to change or even recompile the minimization routines. The

[1]The *opossum* is a marsupial and related to kangaroos, koalas etc. Opossums, e.g the Virginia opossum (*Didelphis marsupialis virginana*) are the only marsupials to be found not only in Australia, but also in (north and south) America (see e.g. Grzimek et al., 1979, chapter 4)

same is true for the routines performing the vibrational analysis and the routines for the minimization of some test functions (see section 4.1.6). Moreover many routines, especially for IO purposes, can be reused in other programs, e.g. the molecular dynamic code[2] and are linked together in an extra library.

Nevertheless it is worth mentioning, that the routine, for performing the LBFGS minimization algorithm is a slightly modified version of the original code, developed by Nocedal (1980) and is written in Fortran[3] (see also Liu & Nocedal, 1989). The modifications concern only the organisation of the output.

For the subsequent analysis and interpretation of the data a bunch of Perl programs and subroutines (Wall et al., 1996) was developed. The standard Perl installation was supplemented with PGPERL (Glazebrook, 2000), the Perl interface for the PGPLOT plotting library (Pearson, 2001), and PDL, the **P**erl **D**ata **L**anguage, which adds some *number crunching* capabilities to Perl (see `http://pdl.perl.org` for more details).

For completeness the programs and libraries used and not already mentioned are listed below:

- Meschach is a linear algebra C library written by D. E. Stewart and Z. Leyk (obtainable at `ftp://ftpmaths.anu.edu.au/pub/meschach/meschach.html`)
- BLAS is a standard collection of basic linear algebra subroutines, written in Fortran (Lawson et al., 1979).
- The Lapack library provides routines for solving systems of linear equations, linear least-squares problems, eigenvalue problems, and singular value problems (Anderson et al., 1999). OPOSSUM actually uses Clapack, a translated version of Lapack.
- The program xmakemol developed by Matt Hodges (2001) has been used to visualize the cluster configurations.
- The Gnu Scientific Library GSL, is a collection of routines for numerical computing, published under the terms of the GNU general public license (Galassi et al., 2001).
- DISLIN is a high-level plotting library for the visualization of data as curves, bar charts, 3 dimensional plots etc. DISLIN is maintained by H. Michels at the Max-Planck-Institute for aeronomie (see `http://www.dislin.de`).
- R is a language and environment for statistical computing and graphics published under the GNU public license, providing a wide variety of statistical and graphical techniques. It was originally written by Ihaka & Gentleman (1996).
- Geomview is an interactive, three-dimensional viewing programme, originally developed at the Geometry Center at the University of Minnesota between 1992 and 1996. Details can be found at `http://www.geomview.org`

[2]The code was named WOMBAT - another marsupila (Grzimek et al., 1979, chapter 8).
[3]The Fortran code was incorporated into the C code using the translation program `f2c`.

- g3data was used to extract data from publications, where only graphs are included and the actual data are missing. The program was developed by J. Frantz and is published under the GNU public license (see `http://beam.helsinki.fi/~frantz/software/g3data.php`).

- The program hull used to calculate the convex hull of set of points (see section 4.3.2) was developed by K. L. Clarkson at Bell Labs. For a description of the used algorithms see `http://cm.bell-labs.com/netlib/voronoi/hull.html`.

The calculations were preformed on the computers of the Zentrum für Astronomie und Astrophysik, TU Berlin and on the CRAY T3E computer of the Konrad–Zuse–Zentrum für Informationstechnik Berlin (ZIB).

Bibliography

C.W. Allen (1973). *Astrophysical Quantities*. Athlone Press, London, 3 edition.

M. P. Allen & D. J. Tildesley (1987). *Computer Simulation of Liquids*. Oxford University Press, Oxford.

S. L. Altmann (1986). *Rotations, quaternions, and double groups*. Clarendon Press, Oxford.

L. M. Amon & W. P. Reinhardt (2000). Development of reference states for use in absolute free energy calculations of atomic clusters with application to 55-atom Lennard-Jones clusters in the solid and liquid states. *J. Chem. Phys.*, **113**, 3573–3590.

E. Anderson, Z. Bai, C. Bischof, S. Blackford, J. Demmel, J. Dongarra, J. Du Croz, A. Greenbaum, S. Hammarling, A. McKenney, & D. Sorensen (1999). *LAPACK Users' Guide*. Society for Industrial and Applied Mathematics, Philadelphia, PA, third edition.

N. Andersson, W. J. Balfour, P. F. Bernath, B. Lindgren, & R. S. Ram (2003). Emission spectra of TiH and TiD near 938 nm. *J. Chem. Phys.*, **118**, 3543.

C. D. Andriesse, B. D. Donn, & R. Viotti (1978). The condensation of dust around η Car. *MNRAS*, **185**, 771.

J. Anglada, P. J. Bruna, & S. D. Peyerimhoff (1990). Theoretical investigation of the low-lying electronic states of TiH. *Molec. Phys.*, **69**, 281–303.

P. W. Atkins (1989). *Physical Chemistry*. Oxford University Press, Oxford, 4. edition.

T. Bachels & R. Schäfer (2000). Binding energies of neutral silicon clusters. *Chem. Phys. Lett.*, **324**, 365–372.

Thomas Bäck (1996). *Evolutionary Algorithms in Theory and Praxis*. Oxford University Press, New York.

C. J. Barden, J. C. Rienstra-Kiracofe, & H. F. Schaefer III (2000). Homonuclear 3*d* transition-metal diatomics: A systematic density functional theory study. *J. Chem. Phys.*, **113**, 690–700.

V. Barone & C. Adamo (1997). First-row transition-metal hydrides: A challenging playground for new theoretical approaches. *Int. J. Quantum Chemistry*, **61**, 443.

C. Barrón, S. Gómez, D. Romero, & A. Saavedra (1999). A genetic algorithm for Lennard-Jones atomic clusters. *Appl. Math. Lett.*, **12**, 85–90.

Ingo Barth. Untersuchung von Schlüsselreaktionen im anorganischen Staubbildungsprozeß. Master's thesis, Technical University Berlin, Berlin, 2004. **in preperation**.

C. W. Bauschlicher (1999). TiCl, TiH, and TiH^+ bond energies: a test of a correlation-consistent Ti basis set. *Theor. Chem. Acc.*, **103**, 141–145.

C. W. Bauschlicher, H. Partridge, S. R. Langhoff, & M. Rosi (1991). A theoretical study of the low-lying states of Ti_2 and Zr_2. *J. Chem. Phys.*, **95**, 1057–1063.

C. W. Bauschlicher, R. S. Ram, P. F. Bernath, C. G. Parsons, & D. Galehouse (2001). The $A\,^6\Sigma^+ - X\,^6\Sigma^+$ transition of CrH, Einstein coefficients, and an improved description of the A state. *J. Chem. Phys.*, **115**, 1312.

C. W. Bauschlicher & P. E. Siegbahn (1984). On the low–lying states of TiC. *Chem. Phys. Lett.*, **104**, 331.

C. Baysal, H. Meirovitch, & I. M. Navon (1999). Performance of efficient minimization algorithms as applied to models of peptides and proteins. *J. Comput. Chem.*, **20**, 354.

A. D. Becke (1988). Density–functional exchange–energy approximation with correct asymptotic behavior. *Phys. Rev. A*, **38**, 3098.

A. D. Becke (1993). Density–functional thermochemistry. III. The role of exact exchange. *J. Chem. Phys.*, **98**, 5648.

O. M. Becker & M. Karplus (1997). The topology of multidimensional potential energy surfaces: Theory and application to peptide structure and kinetics. *J. Chem. Phys.*, **106**, 1495–1517.

R. S. Berrry (1993). Potential surfaces and dynamics: What clusters tell us. *Chem. Rev.*, **93**, 2779.

R. S. Berry (1995). Melting and freezing of clusters: How they happen and what they mean. In H. Haberland, editor, *Clusters of Atoms and Molecules I*, volume 52 of *Springer Series in Chemical Physics*, page 187. Springer, Berlin.

R. S. Berry (1996). Many-dimensional potential surfaces: What they imply and how to think about them. *Int. J. Quantum Chemistry*, **58**, 657–670.

R. S. Berry (1999). Phases and phase changes of small systems. In Jellinek (1999), pages 1–26.

R. S. Berry, S. A. Rice, & J. Ross (2000). *Physical Chemistry*. Oxford University Press, New York, second edition.

Ch. Best & H.-C. Hege. Visualizing conformations in molecular dynamics. Technical Report SC 98-42, Konrad-Zuse-Zentrum für Informationstechnik Berlin (ZIB), Berlin, 1999.

M. Blander & J. L. Katz (1967). Condensation of primordial dust. *Geochim. Cosmochim Acta*, **31**, 1025.

C. G. E. Boender & H. E. Romeijn (1995). Stochastic methods. In R. Horst & P. M. Pardalos, editors, *Handbook of Global Optimization*, page 829. Kluwer Academic, Dordrecht.

D. Bokal. Evolutionary algorithms for cluster geometry. preprint, Inst. of Mathematics, Physics & Mechanics, Dep. of Mathematics, Univ. of Ljubljana, Ljubljana, 1998. URL: `http://citeseer.nj.nec.com/442553.html`.

A. I. Boldyrev, N. Gonzales, & J. Simons (1994). Periodicity and peculiarity in 120 first- and second-row diatomic molecules. *J. Phys. Chem.*, **98**, 9931.

A. I. Boldyrev & J. Simons (1993a). Ab initio study of low-lying electronic states of XP (X = Li-B, Na-Si). *J. Phys. Chem.*, **97**, 6149.

A. I. Boldyrev & J. Simons (1993b). Diatomic molecules containing electropositive atoms favor high-spin states. *J. Phys. Chem.*, **97**, 1526.

V. Bonačić-Koutecký, J. Jellinek, M. Wiechert, & P. Fantucii (1997). *Ab initio* molecular dynamics study of solid- to liquidlike transitions inf Li_9^+, Li_{10}, and Li_{11}^+ clusters. *J. Chem. Phys.*, **107**, 6321.

P. A. Braier, R. S. Berry, & D. J. Wales (1990). How the range of pair interaction governs features of multidimensional potentials. *J. Chem. Phys.*, **93**, 8745–8756.

C. Bréchignac (1995). Akali Clusters. In H. Haberland, editor, *Clusters of Atoms and Molecules I*, volume 52 of *Springer Series in Chemical Physics*, page 255. Springer, Berlin.

S. T. Bromley, M. A. Zwijnenburg, & Th. Maschmeyer (2003). Fully coordinated silica nanoclusters: $(SiO_2)_N$ molecular rings. *Phys. Rev. Lett.*, **90**, 035502.

I.N. Bronstein & K.A. Semendjajew (1989). *Taschenbuch der Mathematik*. Harri Deutsch Verlag, Frankfurt am Main, 24. edition.

C. G. Broyden (1970). The convergence of a class of double rank minimization algorithms: 2. The new algorithm. *J. Inst. Math. Appl.*, **6**, 222.

R. H. Bruce (1965). In G. H. Stewart, editor, *Science of Ceramics*, volume 2, chapter 24. Academic.

A. Buckley & A. LeNir (1983). QN–like variable storage conjugate gradients. *Molec. Phys.*, **27**, 155.

A. Burrows & C. M. Sharp (1999). Chemical equilibrium abundances in brown dwarf and extrasolar giant planet atmospheres. *ApJ.*, **512**, 843–863.

R. H. Byrd, J. Nocedal, & Y. Yuan (1987). Global convergence of a class of quasi–Newton methods on convex problems. *SIAM J. Numer. Anal.*, **24**, 1171.

W. Cai, H. Jiang, & X. Shao (2002). Global optimization of Lennard–Jones clusters by a parallel fast annealing evolutionary algorithm. *J. Chem. Inf. Comput. Sci.*, **42**, 1099.

F. Calvo & P. Labastie (1998). Melting and phase space transitions in small ionic clusters. *J. Phys. Chem. B*, **102**, 2051–2059.

C. J. Cerjan & W. H. Miller (1981). On finding transition states. *J. Chem. Phys.*, **75**, 2800–2800.

J. Chandrasekhar, M. Saunders, & W. L. Jorgensen (2001). Efficient exploration of conformational space using the stochastic search method: Application to β-peptide oligomers. *J. Comput. Chem.*, **22**, 1646.

Ch. Chang, A. B. C. Patzer, E. Sedlmayr, T. Steinke, & D. Sülzle (2000). Electronic structure investigation of the Al_4O_4 molecule. *Chem. Phys. Lett.*, **324**, 108–114.

Ch. Chang, A. B. C. Patzer, E. Sedlmayr, T. Steinke, & D. Sülzle (2001a). A density functional study of small $(AlN)_x$ clusters: structures, energies, and frequencies. *Chem. Phys.*, **271**, 283–292.

Ch. Chang, A. B. C. Patzer, E. Sedlmayr, T. Steinke, & D. Sülzle (2001b). Computational evidence for stable inorganic fullerene-like structures of ceramic and semiconductor materials. *Chem. Phys. Lett.*, **350**, 399.

Ch. Chang, A. B. C. Patzer, E. Sedlmayr, & D. Sülzle (1998). Ab initio studies of stationary points of the Al_2O_3 molecule. *Eur. Phys. J. D*, **2**, 57–62.

Ch. Chang, A. B. C. Patzer, E. Sedlmayr, & D. Sülzle (2002). Sphericity: a geometric approach to the internal rotation of C_2H_6, H_2O_2, and N_2H_4. *J. Mol. Struct. (THEOCHEM)*, **594**, 71.

M. W. Chase (1998). *NIST–JANAF Thermochemical Tables*, volume 9 of *Journal of Physical and Chemical Reference Data, Monograph*. American Institute of Physics, Woodbury, NY, 4th edition.

M.W. Chase, C.A. Davies, J.R. Downey, D.J. Frunip, R.A. MacDonald, & A.N. Syverud (1985). JANAF Thermochemical Tables. Third Edition. *J. Phys. Chem. Ref. Data*, **14**(Supl. No. 1).

Y.-M. Chen, D. E. Clemmer, & P. B. Armentrout (1991). The gas-phase thermochemistry of TiH. *J. Chem. Phys.*, **95**, 1228–1233.

Y.-M. Chen, D. E. Clemmer, & P. B. Armentrout (1993). Gas-phase thermochemistry of VH and CrH. *J. Chem. Phys.*, **98**, 4929.

G. V. Chertihin & L. Andrews (1994). Reactions of laser ablated Ti atoms with hydrogen during condensation in excess argon. Infrared spectra of the TiH, TiH_2 , TiH_3 , and TiH_4 molecules. *J. Am. Chem. Soc.*, **116**, 8322.

D. P. Chong, S. R. Langhoff, C. W. Bauschlicher, S. P. Walch, & H. Partridge (1985). Theoretical dipole moments of the first–row transition metal hydrides. *J. Chem. Phys.*, **2850**, 1986.

E. K. P. Chong & S. Żak (1996). *An Introduction to Optimization*. Wiley, New York.

S. Chrétien & D. R. Salahub (2001). Density functional theory, methods, techniques, and applications. In Guet, C. and Hobza, P and Spiegelman, F. and David, F., editor, *Atomic clusters and nanoparticles*, volume LXXIII of *Summer School in Les Houches*, page 105. Springer, Berlin.

T. S. Chu, R. Q. Zhang, & H. F. Cheung (2001). Geometric and electronic structures of silicon oxide clusters. *J. Phys. Chem. B*, **105**, 1705–1709.

W. A. Chupka & J. Berkowitz (1958). Thermodynamic study of some gaseous metallic carbides. *J. Phys. Chem.*, **62**, 611.

K. Clemenger (1985). Ellipsoidal shell structure in free–electron metal clusters. *Phys. Rev. B*, **32**, 1359.

C. Corliss & J. Sugar (1982). Energy levels of iron, Fe I throgh Fe XXVI. *J. Phys. Chem. Ref. Data*, **11**, 135.

C. Cossé, M. Fouassier, T. Mejean, M. Tranquille, D. P. DiLella, & M. Moskovits (1980). Dititanium and divanadium. *J. Chem. Phys.*, **73**, 6075.

A. N Cox, editor (1999). *Allen's Astrophysical Quantities*. Springer, Berlin, 4th edition.

Christopher J. Cramer (2002). *Essentials of Computational Chemistry. Theory and Models*. Wiley, Chichester.

L. A. Curtiss, P. W. Deutsch, & K. Raghavachari (1992). Binding energies and electron affinities of small silicon clusters ($n = 2 - 5$). *J. Chem. Phys.*, **96**, 6868.

Y.-H. Dai (2002). Convergence properties of the BFGS algorithm. *SIAM J. Optim.*, **13**, 693.

Charles Darwin (1859). *On the Origin of Species by Means of Natural Selection.* London.

W. C. Davidon. Variable metric method for minimization. Technical Report ANL–5990, Argonne National Laboratory, Argonne, Il., 1959.

W. C. Davidon (1991). Variable metric methods for minimization. *SIAM J. Optim.*, **1**, 1.

D. M. Deaven & K. M. Ho (1995). Molecular geometry optimization with a genetic algorithm. *Phys. Rev. Lett.*, **75**, 288–291.

D. M. Deaven, N. Tit, J. R. Morris, & K. M. Ho (1996). Structural optimization of Lennard-Jones clusters by a genetic algorithm. *Chem. Phys. Lett.*, **256**, 195–200.

K. Demyk, E. Dartois, H. Wiesenmeyer, A. P. Jones, & L. d'Hendecourt (2000). Structure and chemical composition of the silicate dust around OH/IR stars. *A&A*, **364**, 170–178.

J. E. Dennis & J. J. Moré (1974). A characterization of superlinear convergence and its application to quasi–Newton methods. *Math. Comp.*, **28**, 549.

A. Deza, M. Deza, & V. Grishukhin (1998). Fullerenes and coordination polyhedra versus half-cube embeddings. *Discrete Mathematics*, **192**, 41.

L. d'Hendecourt, C. Joblin, & A. Jones, editors (1999). *Solid interstellar matter: The ISO revolution*, volume 11 of *Les Houches Workshop*. Springer, Berlin.

P. A. M. Dirac (1929). Quantum mechanics of many–electron systems. *Proc. Royal Soc. London A*, **123**, 714.

B. Diu, C. Guthmann, D. Lederer, & B. Roulet (1994). *Grundlagen der statistischen Physik*. Walter de Gruyter, Berlin, New York.

Carsten Dominik. *Formation of dust grains in the wind of cool giants.* PhD thesis, Technische Universit"at Berlin, Berlin, 1992.

M. Doverstål, L. Karlsson, B. Lindgren, & U. Sassenberg (1997). The $^3\Delta_u - X^3\Delta_g$ band system of jet-cooled Ti_2. *Chem. Phys. Lett.*, **270**, 273–277.

M. Doverstål, B. Lindgren, U. Sassenberg, C. A. Arrington, & M. D. Morse (1992). The $^3\Pi_{0u} \leftarrow X^3\Delta_{1g}$ band system of jet-cooled Ti_2. *J. Chem. Phys.*, **97**, 7087–7092.

J. P. K. Doye (2003). Physical perspectives on the global optimization of atomic clusters. In J. D. Pinter, editor, *Global Optimization – Selected Case Studies*, page **in press**. Kluwer Academic, Dordrecht. URL: `cond-mat/0007338`.

J. P. K. Doye & F. Calvo (2001). Entropic effects on the size dependence of cluster structure. *Phys. Rev. Lett.*, **86**, 3570–3573.

J. P. K. Doye & F. Calvo (2002). Entropic effects on the structure of Lennard–Jones clusters. *J. Chem. Phys.*, **116**, 8307.

J. P. K. Doye, M. A. Millar, & D. J. Wales (1999a). Evolution of the potential energy surface with size for Lennard-Jones clusters. *J. Chem. Phys.*, **111**, 8417–8428.

J. P. K. Doye, M. A. Miller, & D. J. Wales (1999b). The double-funnel energy landscape of the 38-atom Lennard-Jones cluster. *J. Chem. Phys.*, **110**, 6896–6906.

J. P. K. Doye & D. J. Wales (1995). An order parameter approach to coexistence in atomic clusters. *J. Chem. Phys.*, **102**, 9673–9688.

J. P. K. Doye & D. J. Wales (1996). On potential energy surfaces and relaxation to the global minimum. *J. Chem. Phys.*, **105**, 8428–8445.

J. P. K. Doye & D. J. Wales (1998). Thermodynamics of global optimization. *Phys. Rev. Lett.*, **80**, 1357–1360.

J. P. K. Doye & D. J. Wales (1999a). Structural transitions and global minima of sodium chloride clusters. *Phys. Rev. B*, **59**, 2292–2300.

J. P. K. Doye & D. J. Wales (1999b). The dynamics of structural transitions in sodium chloride clusters. *J. Chem. Phys.*, **111**, 11070–11079.

J. P. K. Doye & D. J. Wales (2002). Saddle points and dynamics of Lennard-Jones clusters, solids, and supercooled liquids. *J. Chem. Phys.*, **116**, 3777.

J. P. K. Doye, D. J. Wales, & R. S. Berry (1995). The effect of the range of the potential on the structures of clusters. *J. Chem. Phys.*, **103**, 4234–4249.

J. P. K. Doye, D. J. Wales, & M. A. Miller (1998). Thermodynamics and the global optimization of Lennard-Jones clusters. *J. Chem. Phys.*, **109**, 8143–8153.

B. T. Draine & H. M. Lee (1984). Optical properties of interstellar graphite and silicate grains. *ApJ.*, **285**, 89–108.

R. Elber & M. Karplus (1987). Multiple conformational states of proteins: A molecular dynamics analysis of myoglobin. *Sci.*, **235**, 318.

Ş. Erkoç (1997). Empirical many-body potential energy functions used in computer simulations of condensed matter properties. *Phys. Rep.*, **278**, 79–105.

Y. A. Fadeev (1994). Homogeneous nucleation, growth, and evaporation of dust grains in oxygen–rich red giants. *Astronomy Reports*, **38**, 882.

R. Faller, H. Schmitz, O. Biermann, & F. Müller-Plathe (1999). Automatic parameterization of force fields for liquids by simplex optimization. *J. Comput. Chem.*, **20**, 1009–1017.

B. Fegley & K. Lodders (1994). Chemical models of the deep atmospheres of Jupiter and Saturn. *Icarus*, **110**, 117.

F. T. Fergurson, J. A. Nuth, & L. U. Lilleleht (1996). Experimental studies of the vapor phase nucleation of refractory compounds. IV. The condensation of magnesium. *J. Chem. Phys.*, **104**, 3205.

F. T. Ferguson & J. A. Nuth (2000). Experimental studies of the vapor phase nucleation of refractory compounds. V. The condensation of lithium. *J. Chem. Phys.*, **113**, 4093.

Martin J. Field (1999). *A practical introduction to the simulation of molecular systems.* Cambridge University Press, Cambridge.

Gerd Fischer (1989). *Lineare Algebra.* Vieweg, Braunschweig, 9. edition.

A.J. Fleischer. *Hydrodynamics and Dust Formation in the Circumstellar Shells of Miras and Long-Period Variables.* PhD thesis, Technische Universität Berlin, Berlin, 1994.

R. Fletcher (1970). A new approach to variable metric algorithms. *Computer J.*, **13**, 317.

R. Fletcher & M. J. D. Powell (1963). A rapidly convergent descent method for minimization. *Computer J.*, **6**, 163.

R. Fletcher & C. Reeves (1964). Function minimization by conjugate gradients. *Computer J.*, **7**, 149.

C. A. Floudas & P. M. Pardalos, editors (2001). *Encyclopedia of Optimization.* Kluwer Academic Publishers, Dordrecht.

R. Fournier, S. B. Sinnott, & A. E. DePristo (1992). Density functional study of the bonding in small silicon clusters. *J. Chem. Phys.*, **97**, 4149.

D. D. Frantz (2001). Magic number behavior for heat capacities of medium-sized classical Lennard-Jones clusters. *J. Chem. Phys.*, **115**, 6136.

D. Frenkel & B. Smit (1996). *Understanding Molecular Simulation.* Academic Press, San Diego.

M. J. Frisch, G. W. Trucks, H. B. Schlegel, G. E. Scuseria, M. A. Robb, J. R. Cheeseman, V. G. Zakrzewski, J. A. Montgomery, Jr., R. E. Stratmann, J. C. Burant, S. Dapprich, J. M. Millam, A. D. Daniels, K. N. Kudin, M. C. Strain, O. Farkas, J. Tomasi, V. Barone, M. Cossi, R. Cammi, B. Mennucci, C. Pomelli, C. Adamo, S. Clifford, J. Ochterski, G. A. Petersson, P. Y. Ayala, Q. Cui, K. Morokuma, D. K. Malick, A. D. Rabuck, K. Raghavachari, J. B. Foresman, J. Cioslowski, J. V. Ortiz, B. B. Stefanov, G. Liu, A. Liashenko, P. Piskorz, I. Komaromi, R. Gomperts, R. L. Martin, D. J. Fox, T. Keith, M. A. Al-Laham, C. Y. Peng, A. Nanayakkara, C. Gonzalez, M. Challacombe, P. M. W. Gill, B. Johnson, W. Chen, M. W. Wong, J. L. Andres, C. Gonzalez, M. Head-Gordon, E. S. Replogle, & J. A. Pople. *Gaussian 98, Revision A.6.* Gaussian Inc., Pittsburgh PA, 1998.

K. Fuke, K. Tsukamoto, F. Misaizu, & M. Sanekata (1993). Near threshold photoionization of silicon clusters in the 248 - 146 nm region: Ionization potentials for Si_n. *J. Chem. Phys.*, **99**, 7807.

H.-P. Gail, R. Keller, & E. Sedlmayr (1984). Dust formation in stellar winds I. A rapid computational method and application to graphite condensation. *A&A*, **133**, 320–332.

H.-P. Gail & E. Sedlmayr (1986). The primary condensation process for dust around late M-type stars. *A&A*, **166**, 225–236.

H. P. Gail & E. Sedlmayr (1998). Dust formation in M stars. In T. W. Hartquist & D. A. Williams, editors, *The Molecular Astrophysics of Stars and Galaxies*, pages 285–312. Oxford Science Pub., Oxford.

Mark Galassi, Jim Davies, James Theiler, Brian Gough, Gerard Jungman, Michael Booth, & Fabrice Rossi (2001). *GNU Scientific Library Reference Manual.* Network Theory, Bristol. URL: `http://sources.redhat.com/gsl/`.

I. L. Garzón, M. A. Borja, & E. Blaisten-Barojas (1989). Phenomenological model of melting in Lennard-Jones clusters. *Phys. Rev. B*, **40**, 4749–4759.

Marcus Gastreich. *Werkzeuge zur Modelierung von Siliciumbornitrid–Keramiken.* PhD thesis, Rheinische Friedrich–Wilhelms–Universität, Bonn, 2001.

P. E. Gill, W. Muarry, & M. A. Saunders. SNOPT: An SQP algorithm for large–scale constrained optimization. Technical Report NA 97-2, Dept. of Mathematics, University of California, San Diego, 1997.

S. L. Gillett (1997). Toward a silicate-based molecular nanotechnology I. background and review. In R. C. Merkle & A. Globus, editors, *Fifth Foresight Conference on Molecular Nanotechnology*, Palo Alto, California. Foresight Institute. URL: `http://www.foresight.org/Conferences/MNT05/Papers/Gillett1/index.html`.

K. A. Gingerich, Q. Ran, & R. W. Schmude (1996). Mass spectrometric investigation of the thermodynamic properties of the Si_6 molecule. *Chem. Phys. Lett.*, **256**, 274.

K. Glazebrook. PGPERL, Version 2.18, 2000. URL: `http://www.aao.gov.au/local/www/kgb/pgperl`.

D. Goldfarb (1970). A family of variable metric methods derived by variational means. *Math. Comp.*, **24**, 23.

G. H. Golub & C. F. van Loan (1996). *Matrix Computations*. John Hopkins University Press, Baltimore, 3rd edition.

X. G. Gong (1993). Empirical-potential studies on structural properties of small silicon clusters. *Phys. Rev. B*, **47**, 2329–2332.

X. G. Gong, Q. Q. Zheng, & Y.-Z. He (1995). Structural properties of silicon clusters: an empirical potential study. *J. Phys.: Condes. Matter*, **7**, 577–584.

A. K. Grafton & R. A. Wheeler (1998). Vibrational projection analysis: New tool for quantitatively comparing vibrational noraml modes of similar molecules. *J. Comput. Chem.*, **19**, 1663.

G. W. Greenwood (1999). Revisiting the complexity of finding globally minimum energy configurations in atomic clusters. *Z. Phys. Chem.*, **211**, 105–114.

J. C. Grossman & L. Mitáš (1995). Quantum Monte Carlo determination of electronic and structural properties of Si_n clusters. *Phys. Rev. Lett.*, **74**, 1323.

B. Grzimek et al., editors (1979). *Säugetiere 1*, volume 10 of *Grzimeks Tierleben; Enzyklopädie des Tierreichs*. Deutscher Taschenbuch Verlag, München.

C. Guet, P. Hobza, F. Spiegelman, & F. David, editors (2001). *Atomic clusters and nanoparticles*, volume LXXIII of *Summer School in Les Houches*. Spinger, Berlin.

H. Haberland, editor (1995a). *Clusters of Atoms and Molecules I, Theory, Experiment, and Clusters of Atoms*, volume 52 of *Springer Series in Chemical Physics*. Springer, Berlin.

H. Haberland (1995b). Rare gas clusters. In H. Haberland, editor, *Clusters of Atoms and Molecules I*, volume 52 of *Springer Series in Chemical Physics*, page 374. Springer, Berlin.

R. Haberlandt, S. Fritzsche, G. Peinel, & K. Heinzinger (1995). *Molekulardynamik; Grundlagen und Anwendungen.* Vieweg, Braunschweig.

M. D. Hack, R. G. A. R. Maclagan, G. E. Scuseria, & M. S. Gordon (1996). An *ab initio* study of TiC: A comparison of different levels of theory including density funcitonal methods. *J. Chem. Phys.*, **104**, 6628–6630.

J. A. Hackwell, R. D. Gehrz, & G. L. Grasdalen (1979). Dust formation around HD 193793. *ApJ.*, **234**, 133.

W. Hagen (1978). Circumstellar gas and dust shells of M giants and supergiants. *ApJS*, **38**, 1.

B. N. Hale (1986). Application of a scaled homogeneous nucleation–rate formalism to experimental data at $T \ll T_c$. *Phys. Rev. A*, **33**(6), 4156.

B.N. Hale, P. Kemper, & J.A. Nuth (1989). Analysis of experimental nucleation data for silver and SiO using scaled nucleation theory. *J. Chem. Phys.*, **91**, 4314–4317.

J. A. W. Harkless, D. K. Stillinger, & F. H. Stillinger (1996). Structures and energies of SiO_2 clusters. *J. Phys. Chem. A*, **100**, 1098–1103.

I. A. Harris, R. S. Kidwell, & J. A. Northby (1984). Structure of charged argon clusters formed in a free jet expansion. *Phys. Rev. Lett.*, **53**, 2390.

J. F. Harrison (2000). Electronic structure of diatomic molecules composed of a first-row transition metal and main-group element (H-F). *Chem. Rev.*, **100**, 679–716.

R. J. Harrison, J. A. Nichols, T. P. Straatsma, M. Dupuis, E. J. Bylaska, G. I. Fann, T. L. Windus, E. Apra, J. Anchell, D. Bernholdt, P. Borowski, T. Clark, D. Clerc, H. Dachsel, B. de Jong, M. Deegan, K. Dyall, D. Elwood, H. Fruchtl, E. Glendenning, M. Gutowski, A. Hess, J. Jaffe, B. Johnson, J. Ju, K. Kendall, R. Kobayashi, R. Kutteh, Z. Lin, R. Littlefield, X. Long, B. Meng, J. Nieplocha, S. Niu, M. Rosing, G. Sandrone, M. Stave, H. Taylor, G. Thomas, J. van Lenthe, K. Wolinski, A. Wong, & Z. Zhang. *NWChem, A Computational Chemistry Package for Parallel Computers, Version 4.0.* Pacific Northwest National Laboratory, Richland, Washington, 2000.

B. Hartke (1999). Global cluster geometry optimization by a phenotype algorithm with niches. Location of elusive minima, and low-order scaling with cluster size. *J. Comput. Chem.*, **20**, 1752–1759.

B. Hartke (2002). Strukturübergänge in Clustern. *Angew. Chemie*, **114**, 1534.

W. J. Hehre, L. Radom, R. v. R. Schleyer, & J. A. Pople (1985). *Ab initio molecular orbital theory.* Wiley, New York.

D. Heidrich, W. Kliesch, & W. Quapp (1991). *Properties of Chemically Interesting Potential Energy Surfaces*, volume 56 of *Lecture Notes in Chemistry*. Springer, Berlin.

Ch. Helling, J. M. Winters, & E. Sedlmayr (2000). Circumstellar dust shells around long–period variables. VII. The role of molecular opacities. *A&A*, **358**, 651.

M. R. Hestenes & E. L. Stiefel (1952). Methods of conjugate gradients for solving linear systems. *J. Res. Nat. Bureau Standards (B)*, **49**, 409.

H. Heuser (1990). *Lehrbuch der Analysis, Teil 2*. Teubner, Stuttgart, 5. edition.

J. O. Hirschfelder, C. F. Curtiss, & R. B. Bird (1954). *Molecular Theory of Gases and Liquids*. Wiley, New York.

K.-M. Ho, A. A. Shvartsburg, B. Pan, Z.-Y. Lu, C.-Z. Wang, J. G. Wacker, J. L. Fye, & M. F. Jarrold (1998). Structures of medium-sized silicon clusters. *Nature*, **392**, 582–585.

M. Hoch & H. L. Johnston (1953). Formation, stability and crystal structure of solid silicon monoxide. *J. Am. Chem. Soc.*, **75**, 5224.

Matt Hodges. XMakemol:A program for visualizing atomic and molecular systems, version 5 2001. URL: `http://vegemite.chem.nottingham.ac.uk/~xmakemol/`.

J. D. Honeycutt & H. C. Andersen (1987). Molecular dynamics study of melting and freezing of small Lennard-Jones clusters. *J. Phys. Chem.*, **91**, 4950–4963.

H. Hotop & W. C. Lineberger (1985). Binding energies in atomic negative ions: II. *J. Phys. Chem. Ref. Data*, **14**, 732–750.

K. P. Huber & G. Herzberg (1979). *Constants of Diatomic Molecules*, volume IV of *Molecular spectra and Molecular Structure*. van Nostrand, New York.

Renate Huber (2000). *Einstein und Poincaré; Die philosophische Beurteilung physikalischer Theorien*. Mentis, Paderborn. Philosophie, Wissenschaftstheorie.

W. Huisinga, Ch. Best, R. Roitzsch, Ch. Schütte, & F. Cordes (1999). From simulation data to conformational ensembles: Structure and dynamics-based methods. *J. Comput. Chem.*, **20**, 1760–1774.

A. R. Hyland & G. Neugebauer (1970). Infrared observations of Nova Serpentis 1970. *ApJ.*, **160**, L177.

R. Ihaka & R. Gentleman (1996). R: A language for data analysis and graphics. *Journal of Computational and Graphical Statistics*, **5**(3), 299–314. URL: `http://www.r-project.org/`.

A. W. Irwin (1981). Polynomial partition function approximations of 344 atomic and molecular species. *ApJS*, **45**, 621–633.

A. W. Irwin (1988). The partition functions of JANAF polyatomic molecules that significantly affect the stellar atmospheric equation of state. *A&AS*, **74**, 145–160.

M. E. Jacox (2003). Vibrational and electronic energy levels of polyatomic transient molecules. Supplement B. *J. Phys. Chem. Ref. Data*, **32**, 1.

C. Jäger, F. J. Molster, J. Dorschner, Th. Henning, H. Mutschke, & L.B.F.M. Waters (1998). Steps toward interstellar silicate mineralogy. IV. The crystalline revolution. *A&A*, **339**, 904–916.

Z. J. Jakubek, S. G. Nakhate, & B. Simard (2002). The SiP molecule: The first observation and spectroscopic characterization. *J. Chem. Phys.*, **116**, 6513.

M. F. Jarrold & E. C. Honea (1991). Dissociation of large silicon clusters: the approach to bulk behavior. *J. Phys. Chem.*, **95**, 9181.

J. Jellinek, editor (1999). *Theory of Atomic and Molecular Clusters*. Springer Series in Cluster Physics. Springer, Berlin.

J. Jellinek, V. Bonačić-Koutecký, P. Fantucci, & M. Wiechert (1994). *Ab initio* Hartree-Fock self-consistent-field molecular dynamics study of structure and dynamics of Li_8. *J. Chem. Phys.*, **101**, 10092.

J. Jellinek & E. B. Krissinel (1999). Alloy clusters: Structural classes, mixing, and phase changes. In Jellinek (1999), page 277.

K. S. Jeong. *Dust shells around oxygen-rich Miras and long-period variables*. PhD thesis, Technical University Berlin, Berlin, 2000.

K. S. Jeong, Ch. Chang, E. Sedlmayr, & D. Sülzle (2000). Electronic structure investigation of neutral titanium oxide molecules Ti_xO_y. *J. Phys. B.*, **33**, 3417–3430.

K. S. Jeong, J. M. Winters, T. Le Bertre, & E. Sedlmayr (2003). Self–consistent modeling of the outflow from O–rich Mira IRC -20197. *A&A*, **407**, 191.

C. Jo & K. Lee (1999). Ionization potentials and cohesive energies of silicon clusters from the semi-empirical total energy tight binding method. *Phys. Lett. A*, **263**, 376.

M. John. Bildung von Eisen–Clustern in k"uhlen Sternwinden. Master's thesis, Technische Universiät, Berlin, 1995.

M. John. Dokumentation zum Programm OPOSSUM, Version **1.0**. Technische Universität Berlin, 2002.

Roy. L. Johnston (2002). *Atomic and Molecular Clusters*. Taylor & Francis, London.

R. O.. Jones (1995). Density functional calculations for clusters. In H. Haberland, editor, *Clusters of Atoms and Molecules I*, volume 52 of *Springer Series in Chemical Physics*, page 67. Springer, Berlin.

U. G. Jørgensen & M. Larsson (1990). Molecular opacities of astrophysical interest: the $A^2\Pi - X^2\Sigma^+$ system of CN. *A&A*, **238**, 424–434.

J. Jortner (1992). Clusters as a key to the understanding of properties as a function of size and dimensionality. In P. Jena, S. N. Khanna, & B. K. Rao, editors, *Physics and chemistry of finite systems: from clusters to crystals. Volume I*, pages 1–18, Dordrecht. Kluwer Academic Publishers.

W. Kabsch (1976). A solution for the best rotation to relate two sets of vectors. *Acta Cryst.*, **A32**, 922.

W. Kabsch (1978). A discussion of the solution for the best rotation to relate two sets of vectors. *Acta Cryst.*, **A34**, 827–828.

K. Kaindl & B. Steipe (1997). Metric properties of the root-mean-square deviaton of vector sets. *Acta Cryst.*, **A 53**, 809.

A. Kalemos & A. Mavridis (2002). Theoretical investigation of titanium carbide, TiC: $X^3\Sigma^+$, $a^1\Sigma^+$, $A^3\Delta$, and $b^1\Delta$ states. *J. Phys. Chem. A*, **106**, 3905.

J. D. Kirkpatrick, I. N. Reid, J. Liebert, R. M. Cutri, B. Nelson, C. A. Beichman, C. C. Dahn, D. G. Monet, J. E. Gizis, & F. Skrutskie (1999). Dwarfs cooler than "M": The definitio of spectral type "L" using discoveries from the 2-micron all-sky survey (2MASS). *ApJ.*, **519**, 803.

S. Kirkpatrick, C. D. Gelatt, & M. P. Vecchi (1983). Optimization by simulated annealing. *Sci.*, **220**, 671.

G. R. Kneller (1991). Superposition of molecular structures using quaternions. *Molec. Simul.*, **7**, 113–119.

F. J. Kohl & C. A. Stearns (1974). Vaporization and dissociation energies of the molecular carbides of titanium, zirconium, hafnium, and thorium. *High. Temp. Sci.*, **6**, 284.

Michael Köhler. Gleichgewichtskonfigurationen astrophysikalisch relevanter kleiner anorganischer Cluster. Master's thesis, Technische Universität Berlin, Berlin, 1989.

T. M. Köhler, H.-P. Gail, & E. Sedlmayr (1997). MgO dust nucleation in M–Stars: Calculation of cluster properties and nucleation rates. *A&A*, **320**, 553–567.

G. J. Kramer, N. P. Farragher, B. W. H. van Beest, & R. A. van Santen (1991). Interatomic force fields for silicas, aluminophasphates, and zeolites: Derivation based on *ab initio* calculations. *Phys. Rev. B*, **43**, 5068–5080.

U. Kreibig & M. Vollmer (1995). *Optical properties of metal clusters*, volume 25 of *Springer Series in Materials Science*. Springer, Berlin.

H. Kroto (1997). Symmetry, space, stars and C_{60}. *Rev. Mod. Phys.*, **69**, 703.

H. W. Kroto, J. R. Heath, S. C. O'Brien, R. F. Curl, & R. E. Smalley (1985). C_{60}: Buckminsterfullerene. *Nature*, **318**, 162.

R. E. Kunz & R. S. Berry (1993). Coexistence of multiple phases in finite systems. *Phys. Rev. Lett.*, **71**, 3987–3990.

R. E. Kunz & R. S. Berry (1994). Multiple phase coexistence in finite systems. *Phys. Rev. E*, **49**, 1895–1908.

R. E. Kunz & R. S. Berry (1995). Statistical interpretation of topographies and dynamics of multidimensional potentials. *J. Chem. Phys.*, **103**, 1904–1912.

J. C. Lagarias, J. A. Reeds, M. H. Wright, & P. E. Wright (1998). Convergence properties of the Nelder-Mead simplex method in low dimensions. *SIAM J. Optim.*, **9**, 112.

L.D. Landau & E.M. Lifschitz (1987). *Statistische Physik, Teil I*, volume 5 of *Lehrbuch der theoretischen Physik*. Akademie Verlag, Berlin, 8. edition.

O. Launila & B. Lindgren (1996). Spectroscopy of TiH: Rotational analysis of the $^4\Gamma \rightarrow X^4\Phi(0,0)$ band at 530 nm. *J. Chem. Phys.*, **104**, 6418–6422.

C. L. Lawson, R. J. Hanson, D. R. Kincaid, & F. T. Krogh (1979). Basic Linear Algebra Subprograms for Fortran usage. *ACM Transactions on Mathematical Software*, **5**, 308–323. URL: `http://www.netlib.org/blas/index.html`.

Andrew. R. Leach (2001). *Molecular Modelling: Principles and Applications*. Prentice Hall, Harlow, 2nd edition.

R. H. Leary (1997). Global optima of Lennard-Jones clusters. *J. Global Opt.*, **11**, 35.

R. H. Leary (2000). Global optimization on funneling landscapes. *J. Global Opt.*, **18**, 367.

R. H. Leary & J. P. K. Doye (1999). Tetrahedral global minimum for the 98-atom Lennard-Jones cluster. *Phys. Rev. E*, **60**, 6320–6322.

C. Lee, W. Yang, & R. G. Parr (1988). Development of the Colle-Salvetti correlation-energy formula into a functional of the electron density. *Phys. Rev. B*, **37**, 785.

J. E. Lennard-Jones (1924). . *Proc. Roy. Soc.*, **A106**, 441.

I. N. Levine (2000). *Quantum Chemistry*. Prentice Hall, London.

C. Levinthal (1969). How to fold graciously. In J. T. P. DeBrunner & E. Munck, editors, *Mössbauer Spectroscopy in Biological Systems*, pages 22–24, Urbana. University of Illinois Press.

G. N. Lewis & M. Randall (1961). *Thermodynamics*. McGraw-Hill, New York, 2nd edition.

D.-H. Li & M. Fukushima (2001). On the global convergence of the BFGS method for nonconvex unconstrained optimization problems. *SIAM J. Optim.*, **11**, 1054.

Z. Li & H. A. Scheraga (1987). Monte Carlo-minimization approach to the multiple-minima problem in protein folding. *Proc. Natl. Acad. Sci.*, **84**, 6611–6615.

Li Lian, C.-X. Su, & P.B. Armentrout (1992). Collision induced dissociation of Fe_n^+ ($n = 2 - 19$) with Xe: Bond energies, geometric structures, and dissociation pathways. *J. Chem. Phys.*, **97**(6), 4072.

B. Liu, Z.-Y. Lu, B. Pan, C.-Z. Wang, K.-M. Ho, A. A. Shvartsburg, & M. F. Jarrold (1998). Ionization of medium-sized silicon clusters and the geometries of the cations. *J. Chem. Phys.*, **109**, 9401–9401.

D. C. Liu & J. Nocedal (1989). On the limited memory BFGS method for large scale optimization. *Mathematical Programming*, **45**, 503–528.

S.K. Loh, D.A. Hales, Li Lian, & P.B. Armentrout (1989). Collision-induced dissociation of Fe_n^+ ($n = 2 - 10$) with Xe: Ionic and neutral iron binding energies. *J. Chem. Phys.*, **90**(10), 5466.

S.K. Loh, Li Lian, D.A. Hales, & P.B. Armentrout (1988). Collision-induced dissociation processes of Nb_4^+ and Fe_4^+: Fission vs evaporation. *J. Chem. Phys.*, **89**(5), 3378.

S.-I. Lu (2003). Performance of Ornstein–Uhlenbeck diffusion quantum Monte Carlo for first–row diatomic dissociation energies and dipole moments. *J. Chem. Phys.*, **118**, 6152.

M. Lüttke. *Dust in the Atmospheres of Brown Dwarfs*. PhD thesis, Technical University Berlin, Berlin, 2002.

D. T. Mainz & R. S. Berry (1996). Effect of potential energy topography on dynamics and phase behaviour of cluster. *Molec. Phys.*, **88**, 709–726.

Thomas Mann (1943). *Joseph, der Ernährer*. Bermann-Fischer, Stockholm.

C. D. Maranas & C. A. Floudas (1992). A global optimization approach for Lennard–Jones microclusters. *J. Chem. Phys.*, **97**, 7667.

J. M. Martell, J. D. Goddard, & L. A. Eriksson (1997). Assessment of basis set and functional dependencies in density functional theory: Studies of atomization and reaction energies. *J. Phys. Chem. A*, **101**, 1927–1934.

M. Matsumoto, S. Saito, & I. Ohmine (2002). Molecular dynamics simulation of the ice nucleation and growth process leading to water freezing. *Nature*, **416**, 409.

J. E. Mayer & M. G. Mayer (1977). *Statistical Mechanics*. Wiley-Intersience, New York.

Ernst Mayr (1988). *Toward a new philosophy of biology. Observations of an evolutionist*. Harvard University Press, Cambridge.

J. E. McDonald (1962). Homogeneous nucleation of vapor condensation. I. Thermodynamic aspects. *Am. J. Phys.*, **30**, 870–877.

J. E. McDonald (1963). Homogeneous nucleation of vapor condensation. II. Kinetic aspects. *Am. J. Phys.*, **31**, 31–41.

J. S. McFeaters, R. L. Stephens, P. Schwerdtfeger, & M. Liddell (1994). Numerical modeling of titanium carbide synthesis in thermal plasma reactors. *Plasma Chem. Plasma Proc.*, **14**, 333–360.

K. I. M. McKinnon (1998). Convergence of the Nelder–Mead simplex method to a nonstationary point. *SIAM J. Optim.*, **9**, 148.

A. D. McLachlan (1982). Rapid comparision of protein structures. *Acta Cryst.*, **A38**, 871–873.

B. Meissner, B. Schmidt, & R. S. Berry (1996). Cluster growth from the gas phase: Associative collisions of small alkali halide aggregates. *Z. Phys. Chem.*, **195**, 237–251.

G. Meloni & K. A. Gingerich (2001). Thermodynamic investigation of the Si_7 and Si_8 clusters by Knudsen cell mass spectrometry. *J. Chem. Phys.*, **115**, 5470.

S. Mertens (2002). Computational Complexity for Physicists. *Computing in Science and Engineering*, **4**, 31. URL: `http://arXiv.org/abs/cond-mat/0012185`.

Arthur Miller (1949). *Death of a salesman; certain private conversations in two acts and a requiem*. Viking Press, New York.

M. A. Miller, J. P. K. Doye, & D. J. Wales (1999). Structural relaxations in Morse clusters: Energy landscapes. *J. Chem. Phys.*, **110**, 328–334.

R. E. Miller (2000). *Optimization; Foundations and Applications*. Wiley, New York.

B. G. Moore & A. A. Al-Quraishi (2000). The structure of liquid clusters of Lennard-Jones atoms. *Chem. Phys.*, **252**, 337–347.

J. L. Morales (2002). A numerical study of limited memory BFGS methods. *Appl. Math. Lett.*, **15**, 481.

J. J. Moré, B. S. Garbow, & K. E. Hillstrom (1981). Testing unconstrained optimization software. *ACM Trans. Math. Software*, **7**, 17.

J. J. Moré & D. J. Thuente (1994). Line search algorithms with guaranteed sufficient decrease. *ACM Trans. Math. Software*, **20**, 286–307.

T. Morioka, S. Kimura, N. Tsuda, C. Kaito, Y. Saito, & C. Koike (1998). Study of the structure of silica film by infrared spectroscopy and electron diffraction analysis. *MNRAS*, **299**, 78–82.

P. M. Morse (1929). Diatomic molecules according to the wave mechanics. II. Vibrational levels. *Phys. Rev.*, **34**, 57.

M. Moseler & J. Nordiek (1999). Influence of the potential range on the heat capacity of 13-atom Morse clusters. *Phys. Rev. B*, **60**, 11734.

S. H. Moseley, E. Dwek, W. Glaccum, J. R. Graham, & R. F. Loewenstein (1989). Far–infrared observations of thermal dust emission from supernova 1987A. *Nature*, **340**, 697.

A. Mottana, R. Crespi, & G. Liborio (1982). *Der große BLV Mineralienführer*. BLV Verlagsgesellschaft, München, 2nd edition.

Erich Müller. Optische Eigenschaften heterogener Staubkörner in zirkumstellaren Hüllen. Master's thesis, Zentrum für Astronomie & Astrophysik, Technische Universität Berlin, Berlin, 2002.

H. Müller, H.-G. Frische, & L. Skala (1995). Analytic clustermodels and interpolation formulae for cluster properties. In H. Haberland, editor, *Cluster of atoms and Molecules*, volume 52 of *Springer Series in Chemical Physics*, pages 114–140. Springer, Berlin.

S. G. Nash & J. Nocedal (1991). A numerical study of the limited memory BFGS method and the truncated-newton method for large scale optimization. *SIAM J. Optim.*, **1**, 358.

S. K. Nayak, B. K. Rao, S. N. Khanna, & P. Jena (1998). Atomic and electronic structure of neutral and charged Si_nO_m clusters. *J. Chem. Phys.*, **109**, 1245–1250.

J. P. Neirotti, F. Calvo, D. L. Freeman, & J. D. Doll (2000). Phase changes in 38-atom Lennard-Jones clusters. I. A parallel tempering study in the canonical ensemble. *J. Chem. Phys.*, **112**, 10340–10349.

J. A. Nelder & R. Mead (1964). A simplex method for function minimization. *Computer J.*, **7**, 308–313.

Volker Nissen (1997). *Einführung in Evolutionäre Algorithmen; Optimierung nach dem Vorbild der Evolution.* Vieweg, Braunschweig.

L. R. Nittler, C. M. Alexander, X. Gao, R. M. Walker, & E. Zinner (1997). Stellar sapphires: The properties and origins of presolar Al_2O_3 in meteorites. *ApJ.*, **483**, 475–495.

L. R. Nittler, C.M. Alexander, X. Gao, R. M. Walker, & E. Zinner (1994). Interstellar corundum and spinel from the Tieschitz ordinary chondrite. *Nature*, **370**, 443–446.

J. Nocedal (1980). Updating quasi-Newton matrices with limited storage. *Math. Comp.*, **35**, 773–782. URL: `http://www.ece.nwu.edu/~nocedal/lbfgs.html`.

Jorge Nocedal (1992). Theory of algorithms for unconstrained optimization. *Acta Numerica*, **1**, 199–242.

Jorge Nocedal & Stephen J. Wright (1999). *Numerical Optimization.* Springer Series in Operations Research. Springer, New York.

J. A. Northby (1987). Structure and binding of Lennard-Jones clusters: $13 \leq N \leq 147$. *J. Chem. Phys.*, **87**, 6166.

J. A. Northby, J. Xie, D. L. Freeman, & J. D. Doll (1989). Binding energy of large icosahedral and cuboctahedral Lennard-Jones clusters. *Z. Phys. D*, **12**, 69–71.

J. A. Nuth & B. Donn (1982). Experimental studies of the vapor phase nucleation of refractory compounds I. The condensation of SiO. *J. Chem. Phys.*, **77**, 2639–2346.

J. A. Nuth & B. Donn (1983). Experimental studies of the vapor phase nucleation of refractory compounds II. The condensation of an amorphous magnesium silicate. *J. Chem. Phys.*, **78**, 1618–1620.

J. A. Nuth, K. A. Donnelly, B. Donn, & L. U. Lilleleht (1986). Experimental studies of the vapor phase nucleation of refractory compounds. III. The condensation of silver. *J. Chem. Phys.*, **85**, 1116.

F. Ornellas & S. Iwata (1997). A theoretical study of the electronic structure and spectroscopic properties of the low-lying electronic states of the molecule SiB. *J. Chem. Phys.*, **107**, 6782.

F. R. Ornellas, C. M. Andreazza, & A. A. de Almeida (2000). A theoretical sutdy of the $A\,^2\Sigma^+ - X\,^2\Pi$ system of the SiP molecule. *ApJ.*, **538**, 675–683.

F. R. Ornellas & S. Iwata (1998). A theoretical study of the electronic structure and spectroscopic properties of the low–lying electronic states of the molecule AlSi. *Chem. Phys.*, **232**, 95.

E. D. Palik, editor (1985). *Handbook of Optical Constants of Solids*. Academic Press, Orlando.

I. Pápai (2000). The Ti_2H_2 molecule: terminal or bridging hydrogens? *Theor. Chem. Acc.*, **104**, 131–139.

R. G. Parr & W. Yang (1989). *Density Functional Theory of Atoms and Molecules*. Oxford University Press, Oxford.

A. B. C. Patzer, Ch. Chang, M. John, U. Bolick, & D. Sülzle (2002). Theoretical study of stationary points of the $MgSiO_3$ molecule. *Chem. Phys. Lett.*, **363**, 145.

A. B. C. Patzer, Ch. Chang, E. Sedlmayr, & D. Sülzle (1999). Ab initio thermodynamic properties for different isomers of the Al_2O_3 molecule. *Eur. Phys. J. D*, **6**(57–62).

B. Patzer. *Non–Equilibrium Effects on Chemistry and Dust Formation in Circumstellar Outflows*. PhD thesis, Technical University Berlin, Berlin, 1998.

B. Patzer, A. Gauger, & E. Sedlmayr (1998). Dust formation in stellar winds VII. Kinetic nucleation theory for chemical non-equilibrium in the gas phase. *A&A*, **337**, 847–858.

T. Pearson. PGPLOT, Version 5.2.2. California Institute of Technology, 2001. URL: `http://www.astro.caltech.edu/~tjp/pgplot/`.

J. P. Perdew (1986). Density-functional approximation for the correlation energy of the inhomogeneous electron gas. *Phys. Rev. B*, **33**, 8822.

J. P. Perdew & Y. Wang (1992). Accurate and simple analytic representation of the electron gas correlation energy. *Phys. Rev. B*, **45**, 13244.

J. Pillardy & L. Piela (1995). Molecular dynamics on deformed potential energy hypersurfaces. *J. Phys. Chem.*, **99**, 11805.

T. Pisanski, M. Kaufman, D. Bokal, E. C. Kirby, & A. Graovac (1997). Isoperimetric quotient for fullerenes and other polyhedral cages. *J.Chem.Inf.Comput.Sci.*, **37**, 1028.

E. Polak & G. Ribière (1969). Note sur la convergence de methode de directions conjuguées. *Rev. Franc. Inform. Rech. Oper.*, **16**, 35.

Elijah Polak (1997). *Optimziation, Algorithms and Consistent Approximations*, volume 124 of *Applied Mathematical Sciences*. Springer, New York.

T. Posch, F. Kerschbaum, H. Mutschke, D. Fabian, J. Dorschner, & J. Hron (1999). On the origin of the 13 μm feature. A study of ISO-SWS spectra of oxygen-rich AGB stars. *A&A*, **352**, 609–618.

W. H. Press, S. A. Teukolsky, W. T. Vetterling, & B. P. Flannery (1992). *Numerical Recipes in C*. Cambridge University Press, Oxford, 2nd. edition.

A. A. Radzig & B. M. Smirnov (1985). *Referenz data on atoms, molecules and ions*, volume 31 of *Springer Series in Chemical Physics*. Springer, Berlin.

Q. Ran, R. W. Schmude, M. Miller, & K. A. Gingerich (1994). Mass spectrometric investigation of the thermodynamic properties of the Si_6 molecule. *Chem. Phys. Lett.*, **230**, 337.

D. C. Rapaport (1995). *The art of molecular dynamics simulation*. Cambridge University Press, Cambridge.

Ingo Rechenberg (1973). *Evolutionsstrategie*. F. Frommann Verlag, Stuttgart.

Ingo Rechenberg (1994). *Evolutionsstrategie '94*, volume 1 of *Werkstatt Bionik und Evolutionstechnik*. Frommann–Holzboog, Stuttgart.

Frederick Reif (1987). *Statistische Physik und Theorie der Wärme*. de Gruyter, Berlin, New York, 3. edition.

F. M. Richards & C. E. Kundrot (1988). Identification of structural motifs from protein coordinate data: Secondary structure and first-level supersecondary structure. *Proteins: Structure, Function and Genetics*, **3**, 71.

C. Roberts, R. L. Johnston, & N. T. Wilson (2000). A genetic algorithm for the structural optimization of Morse clusters. *Theor. Chem. Acc.*, **104**, 124–130.

E.A. Rohlfing, D.M. Cox, A. Kaldor, & K.H. Johnson (1984). Photoionization spectra and electronic structure of small iron clusters. *J. Chem. Phys.*, **81**(9), 3846–3851.

J. P. Rose & R. S. Berry (1991). Towards elucidating the interplay of structure and dynamics in clusters: Small KCl clusters as models. *J. Chem. Phys.*, **96**, 517–538.

J. P. Rose & R. S. Berry (1993a). Freezing, melting, nonwetting, and coexistence in $(KCl)_3 2$. *J. Chem. Phys.*, **98**, 3246–3261.

J. P. Rose & R. S. Berry (1993b). $(KCl)_3 2$ and the possibilities for glassy clusters. *J. Chem. Phys.*, **93**, 3262–3273.

H. N. Russel (1934). Molecules in the sun and stars. *ApJ.*, **79**, 317–342.

L. M. Russon, S. A. Heidecke, M. K. Birke, J. Conceicao, M. D. Morse, & P. B. Armentrout (1994). Photodissociation measurements of bond dissociation energies: Ti_2^+, V_2^+, Co_2^+, and Co_3^+. *J. Chem. Phys.*, **100**, 4747.

U. A. Salian, S. N. Behera, & V. S. Ramamurthy (1996). Relaxation of collective excitations in LJ-13 cluster. *J. Chem. Phys.*, **105**, 3679–3685.

A. J. Sauval & J. B. Tatum (1984). A set of partition functions and equilibrium constants for 300 diatomic molecules of astrophysical interest. *Ap. J. Sup.*, **56**, 193–209.

H. Schick (1960). A thermodynamic analysis of the high–temperature vaporization properties fo silica. *Chem. Rev.*, **60**, 331.

Friedrich Schlögl (1989). *Probability and Heat, Fundamentals of Thermostatistics*. Vieweg, Braunschweig.

R. W. Schmude, Q. Ran, & K. A. Gingerich (1993). Atomization enthalpy and enthalpy of formation of gaseous Si_4 from mass spectrometric equilibrium measurements. *J. Chem. Phys.*, **99**, 7998.

R. W. Schmude, Q. Ran, K. A. Gingerich, & J. E. Kingcade (1995). Atomization enthalpy and enthalpy of formation of gaseous Si_2 and Si_3 from mass spectrometric equilibrium measurements. *J. Chem. Phys.*, **102**, 2574.

T. R. Schneider (2000). Objective comparison of protein structures: error-scaled difference distance matrices. *Acta Cryst.*, **D56**, 714.

E. Schöneburg, F. Heinzmann, & S. Feddersen (1994). *Genetische Algorithmen und Evolutionsstrategien*. Addison-Wesley, Bonn.

R. H. Schultz & P. B. Armentrout (1991). The gas-phase thermochemistry of FeH. *J. Chem. Phys.*, **94**, 2262.

A. P. Scott & L. Radom (1996). Harmonic vibrational frequencies: An evaluation of Hartree-Fock, Møller-Plesset, quadratic configuration interaction, density functional theory, and semiempirical scale factors. *J. Phys. Chem.*, **100**, 16502–16513.

E. Sedlmayr (1997). Circumstellar dust condensation scenarios. *Ap&SS*, **251**, 103.

D. F. Shanno (1970). Conditioning of quasi-Newton methods for function minimization. *Math. Comp.*, **24**, 647.

D. F. Shanno (1978). Conjugate gradient methods with inexact searches. *Math. Oper. Res.*, **3**, 244.

C. M. Sharp & W. F. Huebner (1990). Molecular equilibrium with condensation. *ApJS*, **72**, 417–431.

I. Shim & K. Gingerich (1982). *Ab initio* HF-CL calculations of the electronic "band structure" in the Fe_2 molecule. *J. Chem. Phys.*, **77**, 2490.

Boris M. Smirnov (1999). *Clusters and small particles in gases and plasmas*. Springer, New York.

S. Sokolova & A. Lüchow (2000). An ab initio study of TiC with the diffusion quantum Monte Carlo method. *Chem. Phys. Lett.*, **320**, 421–424.

R. M. Sosa, P. Gardiol, & G. Beltrame (1997). A theoretical study of the electronic structure of transition-element carbides M_nC (M = Fe, Ni, Cu, $n = 1, 5$; and M = Ti, $n = 1, 7$) and their interactions with an O atom by DFT methods. *Int. J. Quantum Chemistry*, **65**, 919.

A. K. Speck. *The Mineralogy of Dust Around Evolved Stars*. PhD thesis, University College London, London, 1998.

A. K. Speck, M. J. Barlow, R. J. Sylvester, & A. M. Hofmeister (2000). Dust features in the 10–μm infrared spectra of oxygen–rich evolved stars. *A&AS*, **146**, 437.

J. R. Stephens (1984). Homogeneous condensation of gaseous mixtures of Si, Fe, O, N, and C in relative cosmic abundance and implications for the astronomical condensation. *Meteoritics*, **19**, 316.

J. R. Stephens & S. H. Bauer (1981). On the homogeneous condensation of Fe, Si, FeO_x and SiO_x vapors, and implications for astronomical condensation. *Meteoritics*, **16**, 388.

A. E. Stevens, C. S. Feigerle, & W. C. Lineberger (1983). Laser photoelectron spectroscopy of MnH^- and FeH^-: Electronic stuctures of the metal hydrides, identification of a low–spin excited state of MnH, and evidence for a low–spin ground state of FeH. *J. Chem. Phys.*, **78**, 5420.

A. E. Stevens Miller, C. S. Feigerle, & W. C. Lineberger (1987). Laser photoelectron spectroscopy of CrH^-, CoH^-, and NiH^-: Periodic trends in the electronic structure of the transition metal hydrides. *J. Chem. Phys.*, **87**, 1549.

F. Stillinger (1999, 48–51). Exponential multiplicity of inherent structures. *Phys. Rev. E*, **59**.

F. H. Stillinger & T. A. Weber (1982). Hidden structure in liquids. *Phys. Rev. A*, **25**, 978–989.

F. H. Stillinger & T. A. Weber (1983). Dynamics of structural transitions in liquids. *Phys. Rev. A*, **28**, 2408–2416.

F. H. Stillinger & T. A. Weber (1988). Nonlinear optimization simplified by hypersurface deformation. *J. Stat. Phys.*, **52**, 1429.

D. R. Stull & H. Prophet (1971). Janaf *Thermochemical Tables*. National Bureau of Standards, Washington, 2 edition.

S. Sugano & H. Koizumi (1998). *Microclusters Physics*, volume 20 of *Springer series in materials science*. Springer, Berlin, 2nd edition.

D. Sülzle & Ch. Chang (1999). VESH: A vertical energy surface hopping procedure for determining stable isomers of polyatomic molecular systems. *Int. J. Mod. Phys. C*, **10**, 1229–1236.

A. Tamanai. Low Temperature Opacity. Master's thesis, Wichita State University, Wichita, Kansas, USA, 1998.

K. Tanaka, M. Sekiya, & M. Yoshimine (2001). *Ab initio* study of the lower few states of FeH: Application of the multireference coupled pair approximation. *J. Chem. Phys.*, **115**, 4558.

P. R. ten Wolde, M. J. Ruiz-Montero, & D. Frenkel (1999). Numerical calculation of the rate of homogeneous gas-liquid nucleation in a Lennard-Jones system. *J. Chem. Phys.*, **110**, 1591–1599.

A. G. G. M. Tielens (1990). Towards a circumstellar silicate mineralogy. In M.O. Mennessier & A. Omont, editors, *From Miras to Planetary Nebulae: Which Path for Stellar Evolution?*, pages 186–200, Gif sur Yvette Cedex. Editions Frontières.

Ph. L. Toint. *VE08AD, a routine for partially separable optimization with bounded variables*. Harwell Subroutine Library, 1983.

V. Torczon (1991). On the convergence of the multidirectional search algorithm. *SIAM J. Optim.*, **1**, 123.

I. M. Torrens (1972). *Interatomic potentials*. Academic Press, London, New York.

S. Toxvaerd (2001). Molecular–dynamics simulation of homogeneous nucleation in the vapor phase. *J. Chem. Phys.*, **115**, 8913.

C. J. Tsai & K. D. Jordan (1993). Use of an eigenmode method to locate the stationary points on the potential energy surfaces of selected argon and water clusters. *J. Phys. Chem.*, **97**, 11227.

T. Tsuji (1973). Molecular abundances in stellar atmospheres. II. *A&A*, **23**, 411–431.

S. Tsuneyuki, M. Tsukada, H. Aoki, & Y. Matsui (1988). First–principles interatomic potential of silica applied to molecular dynamics. *Phys. Rev. Lett.*, **61**, 869–872.

B. W. H. van Beest, G. J. Kramer, & R. A. van Santen (1990). Force fields for silicas and aluminophosphates based on *ab initio* calculations. *Phys. Rev. Lett.*, **64**, 1955–1958.

W. F. van Gusteren & H. J. Berendsen. *Groningen Molecular Simulation (GROMOS) Library Manual*. Biomos, Groningen, NL, 1987.

S. P. Walch & C. W. Bauschlicher (1983). CASSCF/CI calculations for the first row transition metal hydrides: The TiH ($^4\Phi$), VH ($^5\Delta$), CrH ($^6\Sigma^+$), MnH ($^7\Sigma^+$), FeH ($^{4,6}\Delta$), and NiH ($^2\Delta$) states. *J. Chem. Phys.*, **78**, 4597.

D. J. Wales (2001). Energy landscapes. In Guet, C. and Hobza, P. and Spiegelman, F. and David, F., editor, *Atomic clusters and nanoparticles*, volume LXXIII of *Summer School in Les Houches*, page 437. Springer, Berlin.

D. J. Wales & J. P. K. Doye (1997). Global optimization by Basin-Hopping and the lowest energy structrues of Lennard–Jones clusters containing up to 110 atoms. *J. Phys. Chem. A*, **101**, 5111–5116.

D. J. Wales, J. P. K. Doye, A. Dullweber, M. P. Hodges, F. Y. Naumkin, F. Calvo, J. Hernández-Rojas, & T. F. Middleton. The Cambridge Cluster Database, 2002. URL: `http://www-wales.ch.cam.ac.uk/CCD.html`.

D. J. Wales, J. P. K. Doye, M. A. Miller, P. N. Mortenson, & T. R. Walsh (2000). Energy landscapes: From clusters to biomolecules. In I. Prigogine & S. A. Rice, editors, *Advances in Chemical Physics*, volume 115, pages 1–111. Wiley.

D. J. Wales, M. A. Miller, & T. R. Walsh (1998). Archetypal energy landscapes. *Nature*, **394**, 758–760.

Larry Wall, Tom Christiansen, & Randal L. Schwartz (1996). *Programming Perl*. O'Reilly, Cambridge, 2nd edition.

L.-S. Wang, S. R. Desai, & J. B. Nicholas (1997a). Small silicon oxide clusters: chains and rings. *Z. Phys. D*, **40**, 36–39.

L.-S. Wang, J. B. Nicholas, M. Dupuis, H. Wu, & D. Colson (1997b). Si_3O_y ($y = 1 - 6$) clusters: Models for oxidation of silicon surfaces and defect sites in bulk oxide materials. *Phys. Rev. Lett.*, **78**, 4450–4453.

L.-S. Wang, H. Wu, S. R. Desai, J. Fan, & S. D. Colson (1996). A photoelectron spectroscopic study of small silicon oxyde clusters: SiO_2, Si_2O_3, and Si_2O_4. *J. Phys. Chem.*, **100**, 8697–8700.

K. M. Westerburg & C. A. Floudas (1999). Locating all transition states and studying the reaction pathways of potential energy surfaces. *J. Chem. Phys.*, **9259–9295**.

D. C. B. Whittet (1989). The composition of dust in stellar ejecta. In L. J. Allamandola & A. G. G. M. Tielens, editors, *Interstellar Dust*, pages 455–466, Dordrecht. Kluwer Academic Publishers.

L. T. Wille (2000). Lennard-Jones clusters and the multiple-minima problem. In D. Stauffer, editor, *Annual Reviews of Computational Physics*, volume VII, pages 25–60. World Scientific, Singapore.

L. T. Wille & J. Vennik (1985). Computational complexity of the ground-state determination of atomic clusters. *J. Phys. A: Math. Gen.*, **18**, L419–L422.

M. Wilson (1997). Stability of small MgO nanotube clusters: Predictions of a transferable ionic potential model. *J. Phys. Chem. B*, **101**, 4917–4924.

P. Woitke. *Radiative heating and cooling in circumstellar envelopes.* PhD thesis, Technische Universität Berlin, Berlin, 1997.

P. Woitke (1999). Dust formation in radioactive environments. In R. Diehl & D. Hartmann, editors, *Astronomy with Radioactivities*, pages 163–174, Schloß Ringberg, Germany. MPE Report 274.

D. H. Wolpert & W. G. Macready. No free lunch theorems for search. Technical Report SFI-TR-95-02-010, Santa Fe Institute, Santa Fe, 1996.

D. H. Wolpert & W. G. Macready (1997). No free lunch theorems for optimization. *IEEE Trans. Evol. Comput.*, **1**, 67–82.

D. Xie & T. Schlick (1999). Efficient implemention of the truncated–Newton algorithm for large–scale chemistry applications. *SIAM J. Optim.*, **10**, 132.

J. Xie, J. A. Northby, D. L. Freeman, & J. D. Doll (1989). Theoretical studies of the energetics and structures of atomic clusters. *J. Chem. Phys.*, **91**, 612.

S. Yanagisawa, T. Tsuneda, & K. Hirao (2000). An investigation of density functionals: The first-row transition metal dimer calculations. *J. Chem. Phys.*, **112**, 545.

Shihe Yang & M. B. Knickelbein (1990). Photoionization studies of transition metal clusters: Ionization potentials for Fe_n and Co_n. *J. Chem. Phys.*, **93**(3), 1533.

K. Yasuoka & M. Matsumoto (1998a). Molecular dynamics of homogeneous nucleation in the vapor phase. I. Lennard–Jones fluid. *J. Chem. Phys.*, **109**, 8451.

K. Yasuoka & M. Matsumoto (1998b). Molecular dynamics of homogeneous nucleation in the vapor phase. I. Water. *J. Chem. Phys.*, **109**, 8463.

R. Yerle (1979). TiH in M-type stars and sunspots. *A&A*, **73**, 346–351.

M. R. Zachariah & C. F. Melius (1997). Theoretical calculation of thermochemistry for molecules in the Si–P–H system. *J. Phys. Chem. A*, **101**, 913.

R. Q. Zhang, T. S. Chu, H. F. Cheung, N. Wang, & S. T. Lee (2001a). High reactivity of silicon suboxide clusters. *Phys. Rev. B*, **64**, 113304.

R. Q. Zhang, T. S. Chu, & S. T. Lee (2001b). Computation of large systems with an economic basis set: *Ab initio* calculations of silicon oxide clusters. *J. Chem. Phys.*, **114**, 5531–5536.

X. Zhu & X. C. Zeng (2003). Structures and stabilities of small silicon clusters: *Ab initio* molecular–orbital calculations of Si_7 - Si_{11}. *J. Chem. Phys.*, **118**, 3558.

X. Zou, I. M. Navon, M. Berger, K. H. Phua, T. Schlick, & F. X. Le Dimet (1993). Numerical experience with limited–memory quasi–Newton and truncated Newton methods. *SIAM J. Optim.*, **3**, 582.

Danksagung

Keine wissenschaftliche Arbeit entsteht im luftleeren Raum. Jede ist stattdessen auf den kritischen Dialog mit der Umwelt angewiesen. Und auch wenn eben dieser Dialog im vorliegenden Fall durch die äußeren Umstände erschwert war, so haben doch viele Menschen, wissentlich oder unwissentlich zum Gelingen dieser Arbeit beigetragen. Es ist eine gute Sitte, sich am Ende einer solchen Arbeit bei allen Beteiligten zu bedanken.

Mein Dank gilt zunächst Prof. Dr. A. Knorr, der sich sofort und ohne Umstände bereit erklärt hat, den Vorsitz der Prüfungskommission zu übernehmen.

Prof. Dr. E. Sedlmayr danke ich für die Unterstützung und die vielen Freiheiten, die er mir bei der Bearbeitung dieses spannenden und aktuellen Themas ließ. Bei Herrn Dr. J. P. Kaufmann möchte ich mich für die Anfertigung des Zweitgutachtens bedanken.

Den *3 Doktores* Beate Patzer, Christian Chang und Detlev Sülzle bin ich zu tiefstem Dank für zahlreiche Gespräche über die Feinheiten quantenmechanischer *ab initio* Methoden, die Benutzung von Gaussian, das Problem der Potentialparameter usw. usf. verpflichtet. Neben der Vermittlung von Informationen war dieser Austausch mit Euch immer auch eine Quelle der Motivation und Inspiration für mich. Es zählt zu den positiven Erfahrungen der letzten Jahre, daß Ihr Euch ohne Umstände auf meine veränderten Kommunikationskanäle eingestellt habt. Dafür danke ich Euch!

Die Durchführung dieser Arbeit wäre ohne das Vorhandensein moderner Computertechnologie nicht möglich gewesen. Deswegen möchte ich Uwe Bolick und Marcus Lüttke dafür danken, daß sie dafür sorgten, daß die Computer (meistens `;-)`) liefen und sie mich bei der Durchführung der nötigen Rechnungen unterstützten, auch wenn es mal wieder hieß: „Ich hab da noch ein schönes Programm, das man installieren könnte ...“.

Ein ganz spezielles Dankeschön geht an die mir freundschaftlich verbundenen Kollegen bzw. Exkollegen am Institut Beate Patzer, Marcus Lüttke, Jürgen Buchhammer und Erich Müller. Der Austausch mit Euch über physikalische aber auch nicht-physikalische Probleme war mir immer wichtig.

Einigen Mitarbeitern am Institut, die noch nicht genannt wurden, bin ich zu Dank verpflichtet, weil sie mir durch ihre Mitschriften den Besuch des Institutsseminars und anderer Veranstaltungen ermöglicht haben. Namentlich genannt seien Christine Krumrey, Šime Pervan und Vasco Schirrmacher.

Meine Versuche, mich in einer Sprache auszudrücken, die nicht meine Muttersprache ist, wurden unterstützt von Stuart Wolfe und Christian Chang, die mir wertvolle Tips gaben, wie man sich *gewählt* ausdrückt. Einige Personen, namentlich Beate Patzer, Christian

Chang und Michael Hegmann, haben bereits vor der Fertigstellung dieser Arbeit den Text oder Teile daraus gelesen und mit kritischen Anmerkungen versehen. Ihnen allen gebührt ein herzliches Dankeschön für Ihre Mühen. Alle verbliebenen Fehler und Unzulänglichkeiten im Text gehen allein auf den Autor zurück.

Ich möchte die Gelegenheit nutzen, um mich auch bei all jenen Freunden (S.N.R.W, J.F., C.M., C.W., F.S. und F.L.) zu bedanken, die nicht unmittelbar mit dieser Arbeit zu tun hatten, sondern die mir durch ihre Freundschaft in den letzten Jahren klar gemacht haben, daß diese auch *ohne Ohren* weiter existiert.

Meine Eltern, Großeltern und Schwiegereltern, meine Schwester und mein Schwager habe mich auch in schwierigen Zeiten immer bedingungslos und in jeder Hinsicht, in kleinen wie in großen Dingen, unterstützt. Dafür möchte ich mich an dieser Stelle bedanken.

Und schließlich, meiner Frau - Ihren Anteil am Gelingen dieser Arbeit zu beschreiben hieße den Rahmen dieser Seiten sprengen, weswegen ich mich mit einem *einfachen* Danke bescheiden möchte.

Lebenslauf

Name	Marcus John
Geburtsdatum	20. Juni 1970
Geburtsort	Berlin Tempelhof
Familienstand	verheiratet seit 17.10.1997 mit Petra John, geb. Lockenvitz
Anschrift	Ludwigkirchstr 2 10719 Berlin
Staatsangehörigkeit	deutsch
Schulbesuch	1976 - 1977 Albert-Schweitzer-Grundschule in Köln
	1977 - 1980 Karl-Ernst-Osthaus Grundschule in Hagen
	1980 - 1989 Theodor-Heuss Gymnasium in Hagen Abschluß: Allgemeine Hochschulreife
Studium	Oktober 1989 Beginn des Physikstudiums an der Technischen Universität Berlin
	Dezember 1995 Abschluß des Physikstudiums: Diplom Thema der Diplomarbeit angefertigt am Institut für Astronomie & Astrophysik bei Prof. Sedlmayr: *Bildung von Eisen-Cluster in kühlen Sternwinden*
Beruflicher Werdegang	
	ab Juli 1995 freie Mitarbeit am Institut für Astronomie & Astrophysik
	1.7. 1998 - 30.6 2001 von der DFG geförderter wissenschaftlicher Mitarbeiter am Zentrum für Astronomie & Astrophysik; Thema des Projektes: *Nukleations- und Staubwachstumsprozesse in sauerstoffreichen, astrophysikalischen Situationen*
	seit Juli 2001 freier Mitarbeiter am Institut für Astronomie & Astrophysik

Berlin, den 20.Juni 2003